

https://dspace.org/

Calibration of discrete element modelling parameters for bulk materials handling applications

Guya, Solomon Ramas

2018

https://hdl.handle.net/10539/26654

Guya, Solomon Ramas (2018) Calibration of discrete element modelling parameters for bulk materials handling applications, University of the Witwatersrand, Johannesburg, <http://hdl.handle.net/10539/26654>

Downloaded from a DSpace repository. https://dspace.org/

CALIBRATION OF DISCRETE ELEMENT MODELLING PARAMETERS FOR BULK MATERIALS HANDLING APPLICATIONS

Solomon Ramas Guya



A dissertation submitted to the Faculty of Engineering and the Built Environment, University of the Witwatersrand, Johannesburg in fulfilment of the requirements for the degree of Master of Science in Engineering

Johannesburg, 2018

Declaration

I, the undersigned, am registered for the course **MECN8000-Master of Science in Engineering** in the year 2018. I herewith submit the following dissertation **'Calibration of Discrete Element Modelling Parameters for Bulk Materials Handling Applications'** in fulfilment of the above course.

I hereby declare the following:

- I am aware that plagiarism (the use of someone's work without their permission and/or without acknowledging the original source) is wrong.
- I confirm that the work submitted herewith for assessment in the above course is my own unaided work except where I have stated explicitly otherwise.
- This dissertation has not been submitted before, either individually or jointly, for any course requirement, examination or degree at this or any other tertiary education institution.
- I have followed the required conventions in referencing the thoughts and ideas of others.
- I understand that the University of the Witwatersrand may take disciplinary action against me if it can be shown that this dissertation is not my own unaided work or that I failed to acknowledge the sources of the ideas or words in my writing in this dissertation.

Signed this.....day of .....

S.R Guya

Abstract

The Discrete Element Method (DEM) models and simulates the flow of granular material through confining geometry. The method has the potential to significantly reduce the costs associated with the design and operation of bulk materials handling equipment. The challenge, however, is the difficulty of determining the required input parameters. Previous calibration approaches involved direct measurements and random parameter search. The aim of this research was to develop a sequential DEM calibration framework, identify appropriate calibration experiments and validate the framework on real flows in a laboratory-scale silo and chute.

A systematic and sequential DEM calibration framework was developed. The framework consists of categorising the DEM input parameters into three categories of determining the directly measured input parameters, obtaining the literature acquired input parameters, and linking physical experiments with DEM simulations to obtain the calibrated parameter values. The direct measurement parameters comprised the coefficients of restitution and the particle to wall surface coefficient of rolling friction. Literature obtained parameters were the Young's Modulus and Poisson's ratio. The calibrated parameters comprised the particle to wall surface coefficient of sliding friction calibrated from the wall fiction angle, the particle to particle friction coefficients (sliding and rolling) calibrated from two independent angles of repose, particle density calibrated from bulk density, and adhesion and cohesion energy densities. The framework was then tested using iron ore with a particle size distribution between +2mm and - 4.75 mm in LIGGGHTS DEM software.

Validation of the obtained input parameter values in the silo and chute showed very good qualitative comparisons between the measured and simulated flows. Quantitative predictions of flow rate were found to be particularly sensitive to variations in the particle to particle coefficient of sliding friction. It was concluded that due to their inherent limitations, angle of repose tests were not totally reliable to calibrate the particle to particle coefficient of sliding friction.

Sensitivity tests conducted showed that in the quasi-static flow regime, only the frictional parameters were dominant, while both the frictional and collisional parameters were dominant in the dynamic flow regime. These results are expected to lay a solid foundation for further research in systematic DEM calibration and greatly increase the effectiveness of DEM models in bulk materials handling applications.

Dedication

To my late father and aunt, my wife and two daughters.

Acknowledgements

The author would like to heartily thank his supervisors Mr T Frangakis and Professor T.J Sheer for their excellent support and guidance. The author would also want thank all the staff at TUNRA Bulk Solids Africa and Australia in general, and Dr Lamos in particular, for giving him access to their vast knowledge base of bulk materials handling field in general. Finally, the author would like to thank his family members for their patience and support throughout the duration of the research.

Contents

List of Figures xii

List of Tables xviii

List of Symbols xxii

1 Introduction 1

1.1 Background 1

1.2 Motivation 5

1.3 Research Questions 5

1.4 Objectives 5

1.5 Adopted Software 6

2 Literature Review 7

2.1 Bulk Materials Flow Regimes 7

2.2 DEM Process Overview 9

2.3 DEM Contact Models 11

2.3.1 Contact stiffness models 12

2.3.2 Bonding models 16

2.4 DEM Particle Shape and Size Distribution 17

2.5 DEM Energy Dissipation 19

2.6 DEM Timestep and Simulation Time 20

2.7 DEM Simulation Software 22

2.7.1 DEM simulation in LIGGGHTS 23

2.8 Calibration of DEM Input Parameters 24
2.8.1 DEM input parameters 24
2.8.2 Approaches to DEM calibration 26
2.9 DEM Calibration Experiments 29
2.9.1 Direct Shear Test 30
2.9.2 Angle of repose tests 33
2.9.3 Bulk density test 37
2.9.4 Inclined plane test 39
2.9.5 Coefficient of restitution test 39
2.10 Response Surface Methodology 40
2.10.1 Experimental Strategy 41
2.10.2 Empirical Statistical Modelling 42
2.10.3 Optimisation Methods and Numerical Computing 46

3 Experimental Methods and Apparatus 47

3.1 Flow Regimes Categorisation 48
3.2 DEM Calibration Framework 48
3.3 Physical Calibration Experimental Methods 50
3.3.1 Coefficient of restitution test procedure 51
3.3.2 Inclined plane test procedure 52
3.3.3 Particle size distribution test procedure 55
3.3.4 Particle shape analysis procedure 56
3.3.5 Bulk density measurement procedure 57
3.3.6 Wall friction test procedure 58
3.3.7 Full pipe angle of repose test procedure 61
3.3.8 Split pipe angle of repose test procedure 62
3.3.9 Double cell angle of repose test procedure 63
3.4 DEM Calibration Experimental Methods 65
3.4.1 DEM default input parameters 66
3.4.2 DEM particle shape and size distribution 68
3.4.3 DEM bulk density test procedure 69

3.4.4 DEM wall friction test procedure 71
3.4.5 DEM pipe filling procedure 75
3.4.6 DEM full pipe angle of repose procedure 76
3.4.7 DEM split pipe angle of repose procedure, dry 78
3.4.8 DEM particle to particle friction coefficients calibration procedure 80
3.4.9 DEM double cell angle of repose procedure 81
3.4.10 DEM inclined plane test procedure, moist 83
3.4.11 DEM split pipe angle of repose procedure, moist 85
3.5 Physical Validation Experimental Methods 88
3.5.1 Validation test equipment 88
3.5.2 Physical silo flow test procedure 90
3.5.3 Physical chute flow test procedure 92
3.6 DEM Validation Experimental Methods 94
3.6.1 DEM silo flow test procedure 94
3.6.2 DEM chute flow test procedure 96

4 Data Processing and Results 99

4.1 Physical Calibration Experimental Results 99
4.1.1 Coefficient of restitution test results 99
4.1.2 Inclined plane test results, dry 101
4.1.3 Particle size distribution test results 103
4.1.4 Particle shape analysis results 104
4.1.5 Bulk density test results 104
4.1.6 Wall friction test results 105
4.1.7 Full pipe angle of repose test results 107
4.1.8 Split pipe angle of repose test results 108
4.1.9 Double cell angle of repose test results 109
4.1.10 Inclined plane test results, moist 110
4.1.11 Split pipe angle of repose test results, moist 111

4.2 DEM Calibration Experimental Results 112
4.2.1 DEM particle size and shape model 112
4.2.2 DEM bulk density test results 114
4.2.3 DEM bulk density verification results 116
4.2.4 DEM bulk density sensitivity results 117
4.2.5 DEM wall friction test results 119
4.2.6 DEM wall friction results verification 121
4.2.7 DEM wall friction sensitivity results 123
4.2.8 DEM full pipe angle of repose results 124
4.2.9 DEM split pipe angle of repose results 128
4.2.10 DEM particle to particle friction calibration results . . . 131
4.2.11 DEM angles of repose results verification 133
4.2.12 DEM angles of repose sensitivities 134
4.2.13 DEM inclined plane test results, moist 136
4.2.14 DEM split pipe angle of repose test results, moist 139
4.2.15 DEM moist split pipe angle of repose verification 141
4.3 Physical Validation Experimental Results 142
4.3.1 Silo flow, dry material 142
4.3.2 Silo flow, moist material 146
4.3.3 Chute flow, dry material 150
4.3.4 Chute flow, moist material 151
4.4 DEM Validation Experimental Results 153
4.4.1 DEM silo flow test results, dry material 153
4.4.2 DEM silo flow sensitivity results 162
4.4.3 DEM silo flow test results, moist material 164
4.4.4 DEM chute flow test results, dry material 170
4.4.5 DEM chute flow sensitivity results 171
4.4.6 DEM chute flow test results, moist material 173

5 Discussion **176**

5.1 Calibration Framework 176

5.2 Calibration Experiments . . . 179
5.2.1 Coefficient of restitution . . . 180
5.2.2 Particle to wall coefficient of rolling friction . . . 180
5.2.3 Particle shape and size distributions . . . 181
5.2.4 Particle to wall coefficient of sliding friction . . . 182
5.2.5 Particle to particle coefficients of friction . . . 184
5.2.6 Particle density . . . 187
5.2.7 Adhesion energy density . . . 189
5.2.8 Cohesion energy density . . . 190
5.2.9 Practical DEM calibration . . . 191
5.3 Calibrated Parameters Validation . . . 193
5.3.1 Silo flow . . . 194
5.3.2 Chute flow . . . 197

6 Conclusions **199**
6.1 Summary of main findings . . . 199
6.2 Recommendations for Further Research . . . 201

References **202**

Appendix A Python Programs **209**
A.1 Particle Density Calibration Code . . . 209
A.2 Physical Wall Shear Data Processing . . . 210
A.3 DEM Wall Shear Data Processing . . . 212
A.4 Double Cell Response Surface . . . 214
A.5 Full Pipe Response Surface . . . 215
A.6 Split Pipe Response Surface . . . 216
A.7 Response Surface Equations Solver . . . 217
A.8 Response Surfaces Calculations and Plotting Module . . . 219
A.9 Adhesion Data Processing . . . 221
A.10 Adhesion Solution . . . 223
A.11 Quadratic Equations Solution Module . . . 224

A.12 Cohesion Solution 225

Appendix B LIGGGHTS Input Files 229

B.1 Bulk Density Test 229

B.2 Wall Shear Test 232

B.3 Double Cell Repose 235

B.4 Full Pipe Repose 237

B.5 Split Pipe Repose 239

B.6 Adhesion Inclined Plane 242

B.7 Cohesion Split Pipe Repose 244

Appendix C Drawings 248

Appendix D Moisture Content procedures 252

D.1 Bulk Material Moisture Elevation Procedure 252

D.2 Bulk Material Moisture Elevation Test Results 253

D.3 Bulk Material Moisture Elevation Calculations 254

Appendix E Coefficient of Restitution 256

Appendix F Inclined Plane Tests 258

F.1 Coefficient of Sliding and Rolling Friction Results 258

F.2 Moist Iron Ore Sliding Angle 259

Appendix G Bulk Density Test Results 260

Appendix H DEM Wall Friction Test Results 261

Appendix I Central Composite Design Sampling 269

I.1 Central Composite Design Sampling Procedure 269

I.2 Central Composite Design Sampling Results 271

Appendix J Full Pipe Angle of Repose Results 272

J.1 Full Pipe Physical Calibration Test Results 272

J.2 Full Pipe DEM Calibration Test Results 274

J.3 Full Pipe DEM Verification Test Results 277
J.4 Full Pipe DEM Sensitivity Test Results 277

Appendix K Split Pipe Angle of Repose Results, Dry Material 279
K.1 Split Pipe Physical Calibration Test Results 279
K.2 Split Pipe DEM Calibration Test Results 280
K.3 Split Pipe DEM Verification Test Results 283

Appendix L Double Cell Angle of Repose Results 284
L.1 Double Cell physical Calibration Test Results 284
L.2 Double Cell DEM Verification Test Results 287
L.3 Double Cell DEM Sensitivity Test Results 287

Appendix M Split Pipe Angle of Repose Results, Moist Material 289
M.1 Cohesion Energy Physical Calibration Results 289
M.2 Cohesion Energy DEM Calibration Results 290
M.3 Cohesion Energy DEM Verification Results 291

Appendix N Loadcell Information 292
N.1 Loadcell Linearity Checking Procedure 292
N.2 Loadcell Linearity Checking Results 293
N.3 Loadcell Specifications 295

Appendix O Silo Flow Validation Results 297
O.1 Physical Silo Flow of Dry Iron Ore 297
O.2 Physical Silo Flow of Moist Iron Ore 299

Appendix P Simulation Time 300

Appendix Q LIGGGHTS Installation 301

List of Figures

2.1 Spring dashpot model 12
2.2 Walton-Braun model 15
2.3 Contacting DEM particles with overlap 15
2.4 Parallel bond 17
2.5 Direct shear test experiment 30
2.6 Shear stress evolution during shearing 31
2.7 Bulk material failure envelope 31
2.8 Variation of friction angle with coefficient of friction 32
2.9 Poured angle of repose 34
2.10 Drained angle of repose 35
2.11 Split pipe angle of repose 36
2.12 Dynamic angle of repose 36
2.13 CCD sample points for 2 independent variables 42

3.1 Calibration framework 49
3.2 Calibration framework, physical experiments procedures 51
3.3 Particle drop test setup 53
3.4 Inclinometer in raised position 54
3.5 Jenike wall shear tester 61
3.6 Split pipe angle of repose equipment setup 64
3.7 Calibration framework, DEM experimental procedures 67
3.8 Silo and chute setup 89

4.1 Calibration framework, physical experimental results 100

4.2 Iron particle shapes 104
4.3 Shear stress evolution with time, physical tests 106
4.4 Angle of wall friction, physical tests 107
4.5 Calibration framework, DEM experimental results 113
4.6 Clumped spheres particle 113
4.7 DEM bulk density as a function of DEM particle density 115
4.8 DEM wall friction angle as a function of sliding friction, second order 120
4.9 Shear stress evolution with displacement, $\mu_{pw,s} = 0.47$ 122
4.10 Angle of wall friction, $\mu_{pw,s} = 0.47$ 123
4.11 Full pipe angle of repose, second order response surface 125
4.12 Variation of full pipe angle of repose with particle to particle sliding friction 126
4.13 Variation of full pipe angle of repose with particle to particle rolling friction 127
4.14 Split pipe angle of repose, second order response surface 129
4.15 Variation of split pipe angle of repose with particle to particle sliding friction 130
4.16 Variation of split pipe angle of repose with particle to particle rolling friction 131
4.17 Kinetic energy of particles as a function of inclination angle . . 137
4.18 Adhesion energy density, first order polynomial 138
4.19 Cohesion energy density, first order polynomial 140
4.20 Mass variation with time, dry iron ore silo flow 143
4.21 Profile of physical silo full of dry iron ore 144
4.22 Profile of physical silo three quarters full of dry iron ore 144
4.23 Profile of physical silo half full of dry iron ore 145
4.24 Profile of physical silo one quarter full of dry iron ore 145
4.25 Profile of physical silo one eighth full of dry iron ore 146
4.26 Mass variation with time, moist iron ore silo flow 147
4.27 Profile of physical silo full of moist iron ore 148

4.28 Profile of physical silo half full of moist iron ore 148
4.29 Profile of physical silo one quarter full of moist iron ore 149
4.30 Profile of physical silo one eighth full of moist iron ore 149
4.31 Profile of physical dry iron ore, chute steady flow 150
4.32 Profile of physical dry iron ore remaining in chute 151
4.33 Profile of physical moist iron ore, chute steady flow 152
4.34 Profile of physical moist iron ore remaining in chute 152
4.35 Silo flow mass variation with time, DEM dry 154
4.36 Flow profiles comparison, full silo, dry 155
4.37 Flow profiles comparison, three quarters full silo, dry 156
4.38 Flow profiles comparison, half full silo, dry 157
4.39 Flow profiles comparison, one quarter full silo, dry 158
4.40 Flow profiles comparison, one eighth full silo, dry 159
4.41 Silo flow mass variation with time, DEM $\mu_{pp,s} = 0.80$ 160
4.42 Silo flow mass variation with time, DEM $\mu_{pp,r} = 0.31$ 161
4.43 Silo flow mass rate sensitivity 162
4.44 Silo flow mass variation with time, DEM moist 165
4.45 Flow profiles comparison, full silo, moist 166
4.46 Flow profiles comparison, half full silo, moist 167
4.47 Flow profiles comparison, one quarter full silo, moist 168
4.48 Flow profiles comparison, one eighth full silo, moist 169
4.49 Chute flow profiles comparison, steady flow, dry 171
4.50 Chute flow profiles comparison, stationary, dry 172
4.51 Chute flow profiles comparison, steady flow, moist 174
4.52 Chute flow profiles comparison, stationary, moist 175

5.1 Structured DEM calibration framework 177

C.1 Steel frame drawings 248
C.2 Silo drawings 249
C.3 Chute drawings 250
C.4 Double Cell Angle of Repose Tester 251

H.1 Variation of shear stress with displacement for $\mu_{pw,s} = 0.2$ 261
H.2 Variation of shear stress with normal stress for $\mu_{pw,s} = 0.2$ . . . 262
H.3 Variation of shear stress with displacement for $\mu_{pw,s} = 0.4$ 263
H.4 Variation of shear stress with normal stress for $\mu_{pw,s} = 0.4$ . . . 264
H.5 Variation of shear stress with displacement for $\mu_{pw,s} = 0.6$ 265
H.6 Variation of shear stress with normal stress for $\mu_{pw,s} = 0.6$ . . . 266
H.7 Variation of shear stress with displacement for $\mu_{pw,s} = 0.9$ 267
H.8 Variation of shear stress with normal stress for $\mu_{pw,s} = 0.9$ . . . 268

J.1 Full pipe angle of repose, dry, physical test 1 @ 94 mm 272
J.2 Full pipe angle of repose, dry, physical test 2 @ 94 mm 272
J.3 Full pipe angle of repose, dry, physical test 3 @ 94 mm 273
J.4 Full pipe angle of repose, dry, physical test 1 @ 110 mm 273
J.5 Full pipe angle of repose, dry, physical test 2 @ 110 mm 273
J.6 Full pipe angle of repose, dry, physical test 3 @ 110 mm 273
J.7 Full pipe angle of repose, DEM $\mu_{pp,s} = 0.18$, $\mu_{pp,r} = 0.60$ 274
J.8 Full pipe angle of repose, DEM $\mu_{pp,s} = 0.30$, $\mu_{pp,r} = 0.30$ 274
J.9 Full pipe angle of repose, DEM $\mu_{pp,s} = 0.30$, $\mu_{pp,r} = 0.90$ 274
J.10 Full pipe angle of repose, DEM $\mu_{pp,s} = 0.60$, $\mu_{pp,r} = 0.18$ 275
J.11 Full pipe angle of repose, DEM $\mu_{pp,s} = 0.60$, $\mu_{pp,r} = 0.60$ 275
J.12 Full pipe angle of repose, DEM $\mu_{pp,s} = 0.60$, $\mu_{pp,r} = 1.00$ 275
J.13 Full pipe angle of repose, DEM $\mu_{pp,s} = 0.90$, $\mu_{pp,r} = 0.30$ 276
J.14 Full pipe angle of repose, DEM $\mu_{pp,s} = 0.90$, $\mu_{pp,r} = 0.90$ 276
J.15 Full pipe angle of repose, DEM $\mu_{pp,s} = 1.00$, $\mu_{pp,r} = 0.60$ 276
J.16 Full pipe angle of repose, DEM $\mu_{pp,s} = 0.73$, $\mu_{pp,r} = 0.28$ 277
J.17 Full pipe angle of repose sensitivity, DEM $\epsilon_{pp} = 0.10$ 277
J.18 Full pipe angle of repose sensitivity, DEM $\epsilon_{pp} = 1.00$ 277
J.19 Full pipe angle of repose sensitivity, DEM $\mu_{pw} = 0.10$ 278
J.20 Full pipe angle of repose sensitivity, DEM $\rho = 2000$ kg/m^3 . . . 278
J.21 Full pipe angle of repose sensitivity, DEM $\rho = 5000$ kg/m^3 . . . 278

K.1 Split pipe angle of repose, dry, physical test 1 279

K.2 Split pipe angle of repose, dry, physical test 2 279
K.3 Split pipe angle of repose, dry, physical test 3 279
K.4 Split pipe angle of repose, DEM $\mu_{pp,s} = 0.18$, $\mu_{pp,r} = 0.60$ 280
K.5 Split pipe angle of repose, DEM $\mu_{pp,s} = 0.30$, $\mu_{pp,r} = 0.30$ 280
K.6 Split pipe angle of repose, DEM $\mu_{pp,s} = 030$, $\mu_{pp,r} = 0.90$ 280
K.7 Split pipe angle of repose, DEM $\mu_{pp,s} = 0.60$, $\mu_{pp,r} = 0.18$ 281
K.8 Split pipe angle of repose, DEM $\mu_{pp,s} = 0.60$, $\mu_{pp,r} = 0.60$ 281
K.9 Split pipe angle of repose, DEM $\mu_{pp,s} = 0.60$, $\mu_{pp,r} = 1.00$ 281
K.10 Split pipe angle of repose, DEM $\mu_{pp,s} = 0.90$, $\mu_{pp,r} = 0.30$ 281
K.11 Split pipe angle of repose, DEM $\mu_{pp,s} = 0.90$, $\mu_{pp,r} = 0.90$ 282
K.12 Split pipe angle of repose, DEM $\mu_{pp,s} = 1.00$, $\mu_{pp,r} = 0.60$ 282
K.13 Split pipe angle of repose, DEM $\mu_{pp,s} = 0.73$, $\mu_{pp,r} = 0.28$ 283

L.1 Double cell angle of repose, dry, physical test 1 @ 50mm 284
L.2 Double cell angle of repose, dry, physical test 2 @ 50mm 285
L.3 Double cell angle of repose, dry, physical test 1 @ 130mm 285
L.4 Double cell angle of repose, dry, physical test 2 @ 130mm 286
L.5 Double cell angle of repose, DEM $\mu_{pp,s} = 0.73$, $\mu_{pp,r} = 0.28$ . . . 287
L.6 Double cell angle of repose sensitivity, DEM $\epsilon_{pp} = 0.10$ 287
L.7 Double cell angle of repose sensitivity, DEM $\epsilon_{pp} = 1.00$ 288
L.8 Double cell angle of repose sensitivity, DEM $\mu_{pw} = 0.10$ 288

M.1 Split pipe angle of repose, moist, physical test 1 289
M.2 Split pipe angle of repose, moist, physical test 2 289
M.3 Split pipe angle of repose, moist, physical test 3 289
M.4 Split pipe angle of repose, DEM cohesion density=75 kJ/m^3 . . 290
M.5 Split pipe angle of repose, DEM cohesion density=100 kJ/m^3 . . 290
M.6 Split pipe angle of repose, DEM cohesion density=125 kJ/m^3 . . 290
M.7 Split pipe angle of repose, DEM cohesion density=150 kJ/m^3 . . 290
M.8 Split pipe angle of repose, DEM cohesion density=175 kJ/m^3 . . 291
M.9 Split pipe angle of repose, DEM cohesion density=200 kJ/m^3 . . 291
M.10 Split pipe angle of repose, DEM cohesion density=225 kJ/m^3 . . 291

M.11 Split pipe angle of repose, DEM cohesion density=117 kJ/m^3 . . 291

N.1 Loadcell linearity check 294

O.1 Dry silo mass flow rate, loadcell measured, test 1 297
O.2 Dry silo mass flow rate, loadcell measured, test 2 298
O.3 Dry silo mass flow rate, loadcell measured, test 3 298
O.4 Moist silo mass flow rate, loadcell measured, test 1 299
O.5 Moist silo mass flow rate, loadcell measured, test 2 299

List of Tables

3.1 Input parameter settings, DEM bulk density tests 70
3.2 Input parameter settings, DEM wall friction tests 72
3.3 Input parameter settings, DEM pipe filling 75
3.4 CCD sample points 77
3.5 Input parameter settings, DEM full pipe repose tests 77
3.6 Input parameter settings, DEM split pipe repose tests 79
3.7 Input parameter settings, DEM double cell repose tests 82
3.8 Input parameter settings, DEM adhesion energy density tests . 84
3.9 Input parameter settings, DEM cohesion energy density tests . . 86
3.10 Input parameter settings, DEM silo and chute flow tests 95

4.1 Coefficients of restitution summary for iron ore 100
4.2 Input parameters update, coefficient of restitution tests 101
4.3 Sliding and rolling friction coefficients summary, particle to wall 102
4.4 Input parameters update, inclined plane tests 103
4.5 Particle size distribution 103
4.6 Bulk densities, large and small containers 105
4.7 Average limiting shear stress and normal stress, physical 106
4.8 Full pipe angles of repose, physical 108
4.9 Split pipe angles of repose, physical 109
4.10 Double cell angles of repose, physical 109
4.11 Moist particle sliding angle summary, physical 111
4.12 Moist split pipe angles of repose, physical 111
4.13 DEM bulk density variation with DEM particle density 114

4.14 Input parameters update, bulk density tests 116
4.15 DEM bulk density, particle density = 3609 kg/m^3 117
4.16 DEM bulk density sensitivity 118
4.17 DEM wall friction angles 119
4.18 Input parameters update, wall friction tests 121
4.19 Average limiting shear and normal stresses, $\mu_{pw,s} = 0.47$ 122
4.20 DEM wall friction angle as a function of rolling friction 124
4.21 DEM full pipe angles of repose, CCD points 125
4.22 DEM split pipe angles of repose, CCD points 128
4.23 Input parameters update, angle of repose tests 133
4.24 DEM angles of repose verification 134
4.25 Angles of repose sensitivity test, $\epsilon_{pp} = 0.1$ 135
4.26 Angles of repose sensitivity test, $\epsilon_{pp} = 1.0$ 135
4.27 Angles of repose sensitivity test, $\mu_{pw,s} = 0.1$ 135
4.28 Angles of repose sensitivity test, $\rho_p = 2000$ kg/m^3 136
4.29 Angles of repose sensitivity test, $\rho_p = 5000$ kg/m^3 136
4.30 Particle sliding as function of adhesion energy density 137
4.31 Input parameters update, adhesion energy density tests 139
4.32 Angle of repose as a function of cohesion energy density 139
4.33 Input parameters update, cohesion energy density tests 141
4.34 Dry silo mass flow rate summary, physical 143
4.35 Moist silo mass flow rate, physical 147
4.36 Dry remaining mass in the chute, physical 150
4.37 Moist remaining mass in the chute, physical 151
4.38 Comparison of DEM and physical flow rates, dry 154
4.39 Comparison of DEM and physical flow rates, adjusted parameters 161
4.40 Sensitivity of DEM silo mass flow rate 163
4.41 Comparison of DEM and physical flow rates, moist 164
4.42 Sensitivity of DEM mass of material remaining on chute 173

5.1 Minimum number of DEM calibration experiments 193

D.1 Existing moisture content 254

E.1 Coefficient of restitution, particle to particle 256
E.2 Coefficient of restitution, particle to wall surface 257

F.1 Coefficients of sliding and rolling friction, particle to wall 258
F.2 Moist particle sliding angle 259

G.1 Bulk density, small container 260
G.2 Bulk density, large container 260

H.1 Average limiting shear and normal stresses, $\mu_{pw,s} = 0.2$ 262
H.2 Average limiting shear and normal stresses, $\mu_{pw,s} = 0.4$ 263
H.3 Average limiting shear and normal stresses, $\mu_{pw,s} = 0.6$ 265
H.4 Average limiting shear and normal stresses, $\mu_{pw,s} = 0.9$ 267

I.1 CCD sample points 271

O.1 Silo mass flow rates, scale, dry 297
O.2 Silo mass flow rates, scale, moist 299

P.1 Minimum number of DEM calibration experiments 300

List of Symbols

α_i	Angular acceleration of a particle	rad/s^2
β	Critical damping ratio	
$\Delta\epsilon$	Change in normal strain	
$\Delta\sigma$	Change in normal stress	N
Δt	Time step	s
ϵ	Coefficient of restitution	
ϵ_{pp}	Particle to particle coefficient of restitution	
ϵ_{pw}	Particle to wall coefficient of restitution	
μ	Coefficient of friction	
μ_r	Coefficient of rolling friction	
μ_s	Coefficient of sliding friction	
$\mu_{pp,r}$	Particle to particle coefficient of rolling friction	
$\mu_{pp,s}$	Particle to particle coefficient of sliding friction	

$\mu_{pw,r}$	Particle to wall coefficient of rolling friction	
$\mu_{pw,s}$	Particle to wall coefficient of sliding friction	
ν	Poisson's ratio	
$\nu_{particle}$	Poisson's ratio of a bulk material particle	
ν_{wall}	Poisson's ratio of wall surface material	
ω_i	Angular velocity of a particle	rad/s
ϕ	Angle of friction	deg
ϕ_w	Wall friction angle	deg
ϕ_{FR}	Full pipe angle of repose	deg
ϕ_{SR}	Split pipe angle of repose	deg
ϕ_{WR}	Withdrawal angle of repose	deg
ρ	Density	kg/m^3
ρ_b	Bulk density	kg/m^3
ρ_p	Particle density	kg/m^3
σ	Normal stress	Pa
τ	Shear Stress	Pa
θ_i	Angular position of a particle	rad
$\vec{F}_b$	Resultant body force acting on a particle	N

$\vec{F_c}$	Resultant contact force acting on a particle	N
$\vec{F_i}$	Resultant force acting on a particle	N
$\vec{F_n}$	Resultant normal contact force acting on a particle	N
$\vec{F_s}$	Resultant shear contact force acting on a particle	N
$\vec{M_i}$	Resultant moment acting on a particle	Nm
$\vec{r}$	Distance from contact plane to particle centre of mass	m
a_i	Linear acceleration of a particle	N
c	Cohesive strength	Pa
E	Young's Modulus	Pa
E'	Confined Young's Modulus	Pa
e_v	Voids ratio	
$E_{particle}$	Young's Modulus of particle material	Pa
E_{wall}	Young's Modulus of wall surface material	Pa
ED_a	Adhesion energy density	J/m^3
ED_c	Cohesion energy density	J/m^3
G	Shear Modulus	MPa
m	Mass	kg
m_i	Mass of a particle	kg

V	Voltage	V
v_i	Linear velocity of a particle	m/s
x_i	Linear position of a particle	m

Acronyms

CAD	Computer Aided Design
CCD	Central Composite Design
DEM	Discrete Element Model
DMT	Derjagui-Muller-Topolov
DOE	Design of Experiments
JKR	Johnson-Kendall-Roberts
LAMMPS	Large-scale Atomic/Molecular Massively Parallel Simulator
LIGGGHTS	LAMMPS Improved for General Granular and Granular Heat Transfer Simulation
PSD	Particle Size Distribution
RSM	Response Surface Methodology
TBSA	TUNRA Bulk Solids Africa

1 Introduction

This chapter briefly gives an overview of the field of bulk materials handling equipment design, the Discrete Element Method (DEM), calibration of the DEM model and the need for an effective and efficient calibration procedure. The chapter is organised into four main sections, namely background, research motivation, research question and objectives.

1.1 Background

Bulk materials handling is an engineering field concerned with the design of equipment used for storage, transporting and processing of bulk materials such as mineral ores, agricultural products, heavy soils and construction materials. Examples of bulk materials handling equipment are: conveyor belts, transfer chutes, silos, hoppers, feeders, stackers, reclaimers and drag-line buckets. Traditionally, bulk materials handling equipment has been designed using analytical continuum methods which are derived from the equation of continuity, despite the fact that bulk materials are composed of discrete particles which make them discontinuous. These methods are also limited to two dimensional analyses making it impossible to visualise and understand how the bulk material flows in the third spatial direction (Grima and Wypych, 2011*b*). The other method widely used is that of trial and error where full scale prototypes are developed, tested and modified until a satisfactory design has been found. This approach requires a lot of experience and time, and is very costly.

Discrete Element Modelling (DEM) is a numerical technique that models the behaviour of individual particles to provide insights into the behaviour of the bulk material. The method accounts for particle interactions with other particles or wall surfaces, allowing three dimensional visualisation of the behaviour of bulk materials in relation to the handling equipment. This enables equipment designs to be developed and simulations thereof run on a computer in order to evaluate the suitability of the equipment for specific applications (Grima et al., 2011). According to Nordell (1997), the modelling of granular behaviour using DEM has the potential to be one of the most important scientific advancements to the mining industry. The method has also potential to address handling equipment design in industries such as pharmaceuticals, agriculture and foodstuffs (Johnstone, 2010), addressing limitations of continuum methods in equipment design (Grima et al., 2013). It is expected that as computer hardware and algorithms continue to improve, DEM results will be more rapidly obtained and more accurate. DEM can be used to fine tune the designs reached by using the analytical continuum methods or using past experience. This makes DEM a cost effective design validation tool before equipment is manufactured.

DEM models require parameter inputs that relate to material, geometric and interaction properties. These parameters comprise particle stiffness, Poisson's ratio, density, shape and size distributions, static and rolling coefficients of friction and an energy dissipation parameter, such as coefficient of restitution, or a damping coefficient. However, due to computational limitations and the need to obtain DEM results in a reasonable amount of time, some restrictions are imposed on the DEM model parameters. In particular, restrictions are put on the number, size and shape of particles that can be realistically modelled. These restrictions, when coupled with the inherent assumptions made in the contact models, result in a mismatch between the model and real bulk material flow behaviours. To compensate for the mismatch, parameter calibration is needed to ensure that the modelled bulk material behaviour is comparable to

the physical bulk material behaviour. The model input parameters are thus adjusted so that the simulated bulk material behaviour matches the real bulk material behaviour, but herein lies the main challenge with DEM, the question of the relevance of the calibrated model when predicting an unknown situation.

DEM calibration is carried out to assign appropriate input parameters that define particle to particle interactions and particle to boundary surface interactions, in order to achieve a mechanical response that matches the response observed in physical laboratory tests, or in an application. As such, the laboratory calibration experiments should be representative of the flow behaviour experienced by the bulk material in full scale operation (Hastie et al., 2012). Once calibration is done, calibrated parameters can be used in general bulk material flow problems using the tested bulk material and wall surfaces.

Bulk material flow behaviour can be characterised by the dominant flow regime. Two different types of flow behaviours encountered in bulk materials handling applications are the quasi-static and dynamic flow regimes, with an intermediate flow regime characterising the transition between the two extreme regimes (Savage et al., 1983). The quasi-static flow regime is characterised by enduring contacts between particles, high bulk densities, high confining pressures, slow shearing (low inertia) and energy dissipation through friction. Such flows are encountered in handling equipment such as silos, hoppers, and feeders where material is moving relatively slowly. The dynamic flow regime is characterised by low bulk densities, very low confining pressures, rapid shearing and dissipation of energy through inelastic collisions. Such flows are encountered in transfer chutes and ship loaders, for example. However, one of the drawbacks of DEM calibration experiments is that they are often selected without consideration of the flow regime prevailing in the application, whose parameters they are meant to calibrate.

The two dominant calibration approaches generally used, namely the random parameter value adjustment and the direct measurement approach, have been

shown to have limitations in modelling bulk material behaviour (Marigo and Stitt, 2015). In random parameter values adjustment, a single or a few bulk material responses are physically measured, and all the DEM input parameters adjusted randomly, until the DEM bulk material behaviour matches the observed physical behaviour. The random tuning is often done without regard as to whether the tuned input parameters have a significant effect on the bulk material behaviour. In the direct measurement approach, all the input parameters are directly measured using some physical experimental procedure.

The limitations of the first approach of random parameter value adjustments are: various combinations of parameter values give the same bulk response, the parameter values have no physical meaning, the process of parameter estimation is time consuming, it is impossible to know how many DEM simulations are required in advance (Hanley et al., 2011) and there is no guarantee that the parameters obtained will be valid when applied to a different geometry. The second approach of direct physical measurement of parameter values is limited by the difficulty of directly measuring the parameters and restrictions imposed on the particle number, size and shape by the computational resources (Grima and Wypych, 2011*b*). Also, not all of the physics of particle interactions can be modelled, so models can only take into account the main variables which must be adjusted to match the model and real bulk material behaviour.

The challenge of calibrating DEM models has been highlighted to be one of the major limitations for DEM use beyond the research community (Marigo and Stitt, 2015). If the method is to be broadly applied in industry as an equipment design or troubleshooting tool, then validated calibration methods which are simple, rapid and accurate need to be developed. Calibrated parameter values determine the overall response of the material. As such, it is critical that validation is carried out to ensure these parameters are representative of material behaviour.

1.2 Motivation

To date, the process of DEM calibration has not been structured and systematic, which has inhibited the use of DEM in solving practical problems in industry. Therefore, this research was motivated by the need to develop a structured framework within which DEM models could be effectively and efficiently calibrated in order to produce realistic simulations.

1.3 Research Questions

The following research questions were raised:

- Which combination of laboratory tests (physical and numerical) would enable the determination of unique DEM input parameter values?
- In the context of a structured framework, what order should the identified calibration experiments and simulations be conducted in so as to isolate the effects of specific input parameters at each step?

1.4 Objectives

The aim of the research was to develop a DEM input parameter calibration framework that is simple, effective and efficient, which takes into consideration the dominant flow regimes. The research was limited to calibrating the DEM input parameters assuming particles did not break during the simulation process. The specific objectives were to:

1. Develop a sequential DEM parameter calibration framework encompassing a series of experiments, that are ordered such that in each test, only the dominant input parameter is calibrated.

2. Identify specific laboratory experiments to isolate the effects of specific input parameters, and conduct physical experiments and DEM simulations thereof to derive a set of DEM model input parameters.

3. Execute the calibration framework with a sample bulk material and validate the results in laboratory-scale silo and chute flows.

1.5 Adopted Software

LIGGGHTS PUBLIC version 3.7.0 was adopted for the simulation work. The version implemented the following contact and bonding models:

- Hertz contact model
- Hooke contact model
- Johnson-Kendall-Roberts bonding model (SJKR)

2 Literature Review

This chapter briefly reviews the relevant literature on bulk materials flow regimes, DEM theory, DEM input parameters and calibration experiments. The chapter is organised into nine sections, with Section 2.1 covering bulk materials flow regimes, Section 2.2 to Section 2.6 covering the main aspects of the DEM method, Section 2.7 covering the DEM software, Section 2.8 covering the DEM input parameters and existing calibration approaches, and Section 2.9 covering the commonly used DEM calibration experiments.

2.1 Bulk Materials Flow Regimes

Savage et al. (1983) categorised the flow of granular materials as either quasi-static or inertial. He observed that within the quasi-static regime, the overwhelming effect of interaction between particles, and between particles and wall surfaces was mainly due to sliding and rolling friction. He also observed that in inertial flows, the interactions were mainly dominated by inelastic impacts which were modelled in DEM software using the coefficient of restitution. The same observations were made by Campbell (2006) who categorised bulk granular flow regimes as either quasi-static or rapid flow, and Zhou and Sun (2013) who categorised the same flow regimes as slow and rapid flow respectively. This clearly shows that the significance of individual input parameters differs depending on the prevailing flow regime, and calibration experiments should be chosen such that they accurately calibrate parameters relative to the expected dominant flow regime.

In the rapid flow regime, the bulk material possesses high kinetic energy and the material is less confined such that it freely flows in one or more dimensions without restriction. The dynamic flow regime is characterised by low bulk densities, very low confining pressures, rapid shearing and dissipation of energy through inelastic collisions. This type of flow is observed in transfer chutes where the bulk material has the freedom to increase velocity and kinetic energy in the direction of flow, as a function of the dimensions of the confining geometry. This type of flow regime is also encountered in the split pipe (Section 3.3.8) and double cell (Section 3.3.9) angle of repose tests. In this regime, because the particles have freedom to acquire high kinetic energy, energy dissipation at impact is significant enough to affect the bulk material behaviour. It is therefore important that DEM parameters that define energy dissipation due to impact be precisely calibrated in order to ensure conformity between the observed physical and numerical behaviours of the material (Savage et al., 1983; Campbell, 2006; Zhou and Sun, 2013). These input parameters are either the coefficient of restitution or the damping coefficient, depending on the DEM software used.

In the quasi-static flow regime, the bulk material possesses little kinetic energy and the flow of the material is regulated in all the dimensions of the confining geometry. The regime is characterised by enduring contacts between particles, high bulk densities, high confining pressures, slow shearing (low inertia) and energy dissipation through friction. This type of flow is encountered in silos where the material that exits the silo is regulated which results in downward movement of bulk material in the silo being very slow. The same flow regime can be seen in the traditional angle of repose tests in which the confining geometry, usually in the form of a cylindrical or conical shape, is slowly raised to minimise dynamic effects on the flow. In this regime, because the particles are regulated and confined, the bulk behaviour is affected by the relative movement between particles which is a function of frictional properties. As such, in applications where such flows are dominant, it is important to precisely cali-

brate parameters that affect the frictional properties of the particles (Savage et al., 1983; Gröger and Katterfield, 2006; Campbell, 2006; Brummer, 2010; Zhou and Sun, 2013).

Even though one flow regime may be dominant in a specific application, the other flow regime may still exist in certain regions of flow in the same application. In this situation, it is therefore imperative that all the parameters are precisely calibrated to capture the flow regimes in all the regions of flow.

2.2 DEM Process Overview

DEM is a numerical modelling technique for particle systems in which the interactions between particles, and between particles and wall surfaces are modelled as a dynamic process (Thornton, 2015). The time evolution of the particle system is advanced by applying a simple explicit finite difference integration scheme to obtain new particle velocities, displacements and positions at each time step within the bulk material and confining geometry.

At the start of the simulation, the body forces and contact forces acting on each particle in the system are computed. Body forces include gravity, electromagnetism or electrostatic forces. The most common body force in bulk materials handling applications is gravity. The contact forces are calculated by using the soft sphere approach where contacting particles and boundary surfaces are allowed to develop an overlap which represents local deformation of particles at contact points (O'Sullivan, 2011). Particles and boundary surfaces are considered to be connected by springs and dampers in the normal and tangential directions, whose stiffness and damping values together with the overlap distance are used to compute the contact forces. The total contact force acting on a single particle is given by Equation 2.1.

$$\vec{F_c} = \vec{F_n} + \vec{F_s} \tag{2.1}$$

where $\vec{F_c}$ is the resultant contact force acting on a particle, $\vec{F_n}$ is the resultant normal contact force acting on a particle, and $\vec{F_s}$ is the resultant tangential contact force acting on a particle.

The resultant force acting on each particle at a contact point is computed by vector summation of the body and contact forces as given by Equation 2.2.

$$\vec{F_i} = \vec{F_c} + \vec{F_b} \tag{2.2}$$

where $\vec{F_i}$ is the overall resultant force acting on a particle, and $\vec{F_b}$ is the resultant body force acting on a particle.

The moment acting on each particle is determined by multiplying the tangential force at a contact point by the perpendicular distance to the centre of mass as given by Equation 2.3.

$$\vec{M_i} = \vec{F_s} * \vec{r} \tag{2.3}$$

where $\vec{M_i}$ is the resultant moment acting on a particle at a contact, and $\vec{r}$ is the perpendicular distance from the contact plane to the particle's centre of mass.

The translational and angular accelerations of each particle are then determined by the application of Newton's second law of motion as given by Equation 2.4 and Equation 2.5 respectively.

$$\vec{a_i} = \frac{\sum \vec{F_i}}{m_i} \tag{2.4}$$

$$\vec{\alpha_i} = \frac{\sum \vec{M_i}}{I_i} \tag{2.5}$$

where $\vec{a_i}$ is the resultant translational acceleration of a particle, m_i is the mass of the particle, $\vec{\alpha_i}$ is the angular acceleration of the particle, and I_i is the mass moment of inertia of the particle.

By performing numerical integration of Equations 2.4 and 2.5, the translational and angular velocities of each particle after a time step of Δt are determined by Equations 2.6 and 2.7 respectively.

$$v_{i+1} = v_i + a_i \Delta t \tag{2.6}$$

$$\omega_{i+1} = \omega_i + \alpha_i \Delta t \tag{2.7}$$

The new translational and angular positions of each particle after a time step of Δt are given by Equations 2.8 and 2.9 respectively.

$$x_{i+1} = x_i + v_i \Delta t \tag{2.8}$$

$$\theta_{i+1} = \theta_i + \omega_i \Delta t \tag{2.9}$$

where, for Equations 2.6 to 2.9, v is the translational velocity of the particle, ω is the angular velocity of the particle, x is the linear position of the particle and θ is the orientation of the particle.

At the new positions, new contacts are detected and the resultant forces and moments are calculated. The process is advanced by another timestep Δt. This cycle is repeated until the required simulation time has elapsed.

2.3 DEM Contact Models

The DEM contact model describes how the particles behave when they interact with each other or with wall surfaces. Each particle to particle interaction or particle to wall surface interaction is described by a simple constitutive model. Existing contact models can be categorised into contact stiffness models and bonding models. The required DEM input parameters are dependent on the contact model being used.

2.3.1 Contact stiffness models

These models describe the elastic and elastic–plastic relationship between the contact forces and relative displacements in contacting particles. Three main stiffness contact models were identified by Renzo and Maio (2004) as the linear spring-dashpot contact model, the Hertz-Mindlin contact model and the Walton-Braun contact model.

Linear spring-dashpot contact model The linear spring-dashpot contact model also called the Hooke model (CFDEM, 2017), uses two pairs of linear spring-dashpot models based on the work of Cundall and Strack (CD-Adapco, 2014), as illustrated in Figure 2.1 (Renzo and Maio, 2004). The spring represents the repulsive force between the contacting particles while the dashpot accounts for energy dissipation due to imperfect elastic collisions. The spring stiffness values are either calibrated directly or are internally computed using the calibrated values of the Young's Modulus and the equivalent particle radius.

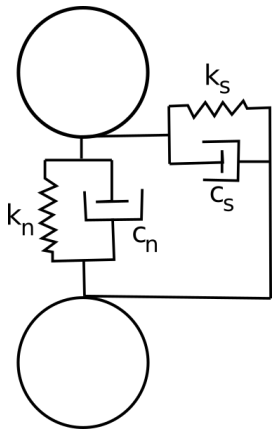


Figure 2.1: Spring dashpot model (CD-Adapco, 2014)

The normal and tangential contact forces for this model are computed as given by Equations 2.10 and 2.11 (O'Sullivan, 2011).

$$\vec{F_n} = -k_n \delta_n - c_n v_n \tag{2.10}$$

$$\vec{F_s} = \begin{cases} -k_s - c_s v_s, & \text{for } \|k_s \delta_s\| < \|\mu_s k_n \delta_n\| \\ \mu F_n, & \text{otherwise} \end{cases} \tag{2.11}$$

where

$$c_n = 2\beta\sqrt{m^* k_n} \tag{2.12}$$

$$c_s = 2\beta\sqrt{m^* k_s} \tag{2.13}$$

$$m^* = \frac{m_1 m_2}{m_1 + m_2} \tag{2.14}$$

$$\beta = \frac{\ln \epsilon}{\sqrt{\pi^2 + \ln^2 \epsilon}} \tag{2.15}$$

where, for Figure 2.1 and Equations 2.10 to 2.15, k_n is the normal spring stiffness, k_s is the tangential spring stiffness, c_n is the normal damping coefficient, c_s is the tangential damping coefficient, δ_n is the normal overlap distance, δ_s is the tangential overlap distance, v_n is the relative normal velocity, v_s is the relative tangential velocity, μ_s is the coefficient of sliding friction, m^* is the equivalent mass, m_i is the mass for particle i, β is the critical damping ratio and ϵ is the coefficient of restitution.

Thornton et al. (2011) showed that the chosen values of tangential and normal stiffness are constrained by Equation 2.16.

$$\frac{2}{3} \leq \frac{k_s}{k_n} \leq 1 \tag{2.16}$$

Hertz-Mindlin contact model The Hertz-Mindlin contact model was developed to overcome the non-physical nature of the linear spring stiffness model (Renzo and Maio, 2004). The model can also depicted by Figure 2.1 with the

spring stiffness values being non-linear, and related to the particle material properties by Equation 2.17 and Equation 2.18 (Renzo and Maio, 2004). The normal contact force is given by Equation 2.19 while the tangential contact force is given by Equation 2.11.

$$k_n = 2E^* \sqrt{R^* \delta_n} \tag{2.17}$$

$$k_s = 8G^* \sqrt{R^* \delta_n} \tag{2.18}$$

$$\vec{F_n} = -k_n \delta_n^{\frac{3}{2}} - c_n \nu_n \tag{2.19}$$

In Equations 2.17 and 2.18, the values of R^*, E^* and G^* are determined by Equations 2.20, 2.21 and 2.22 respectively.

$$R^* = \frac{R_1 R_2}{R_1 + R_2} \tag{2.20}$$

$$\frac{1}{E^*} = \frac{1 - \nu_1^2}{E_1} + \frac{1 - \nu_1^2}{E_2} \tag{2.21}$$

$$\frac{1}{G^*} = \frac{2(2 - \nu_1)(1 + \nu_1)}{E_1} + \frac{2(2 - \nu_2)(1 + \nu_2)}{E_2} \tag{2.22}$$

where R^* is the equivalent particle radius of the interacting bodies, R_i is the radius for particle i, E^* is the equivalent Young's Modulus of the interacting bodies, E_i is the Young's Modulus for particle i, G^* is the equivalent Shear Modulus of the interacting bodies and ν is the Poisson's ratio.

Walton-Braun contact model The Walton-Braun model is an elastic-plastic contact model used when collision between particles involves plastic deformation. This scenario results in differing stiffness values during loading and unloading processes as illustrated in Figure 2.2.

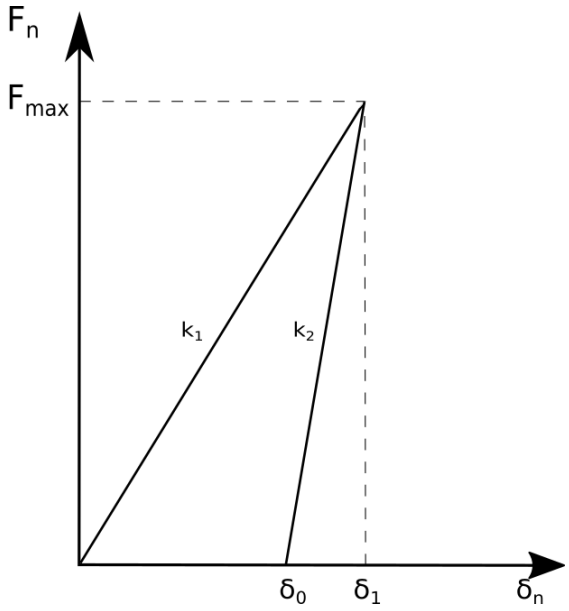


Figure 2.2: Walton-Braun model (CD-Adapco, 2014)

Figure 2.3 shows the overlapped DEM particles and the normal overlap distance, δ_n. The normal force during the loading and unloading is given by Equation 2.23. As in the linear spring model, the loading and unloading spring stiffness values are parameters to be calibrated. O'Sullivan (2011) established the relationship between the loading and unloading spring stiffness to be related to the normal coefficient of restitution by Equation 2.24.

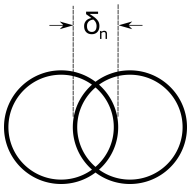


Figure 2.3: Contacting DEM particles with overlap

$$F_n = \begin{cases} -k_1\delta_1, & \text{for loading} \\ -k_2(\delta_1 - \delta_0), & \text{for unloading} \end{cases} \tag{2.23}$$

$$\frac{k_1}{k_2} = \epsilon_n^2 \tag{2.24}$$

where k_1 is the spring stiffness during loading, k_2 is the spring stiffness during unloading, δ_0 is the relative normal overlap when unloading curve reaches zero force, δ_1 is the maximum particle overlap and ϵ is the coefficient of restitution.

Other variations of the Walton-Braun contact model are the Luding and Edinburgh elasto-platic contact models. However, these models are not evaluated as they are beyond the scope of this research.

2.3.2 Bonding models

Bonding models work in tandem with stiffness models to take into account particle breakage, and place a limit on the total normal and shear forces that a contact can carry before rupture by enforcing bond strength limits. When particles adhere to each other, they form either strong or weak bonds. Strong bonds may be formed by solid, cemented or by viscous liquid bridges. Weaker bonds may be provided by pendular liquid bridges, Van der Waals forces, electrostatics or electromagnetism (O'Sullivan, 2011; Thornton, 2015). The type of the bond dictates the bonding contact model. Two such models reported in literature are the parallel bond model and the linear cohesion model (O'Sullivan, 2011; Thornton, 2015).

Parallel bond model The parallel bond model introduces strong attractive inter-particle bonds using a massless bar connecting a pair of particles as illustrated in Figure 2.4 (Mak et al., 2012). The bar can transmit force and torque between particles and is subject to cracking under sufficient loading. The tensile and shear strengths of the bonds are specified by the user. When the bond is subjected to a load exceeding the specified strength, it breaks and two particles are formed that will interact with each other using the stiffness bonding models. This model is used to form rigid bonded particles using irregular particles that break when subjected to loads above specified bond strengths. The model would typically be used in materials where degradation is an important consideration, such as mineral ore crushing and milling.

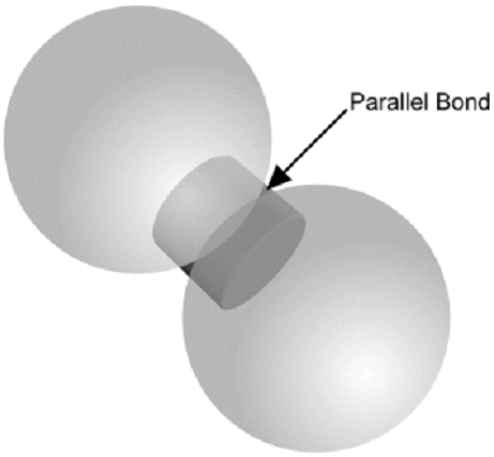


Figure 2.4: Parallel bond (CD-Adapco, 2014)

Linear cohesion model The linear cohesion model is used to simulate weak intermolecular forces between particles as found in systems of moist particles, or in particles with a size range of less than 50 μm such as powders. Two variants of the model are described in published literature (O'Sullivan, 2011), namely the Johnson-Kendall-Roberts (JKR) model and the Derjaguin-Muller-Toporov (DMT) model. The principal difference between the JKR and DMT model formulations is the surface area where the cohesion force is acting. In the JKR model, this area is limited to direct contact, while in the DMT model it also incorporates the neck area in immediate contact proximity (CD-Adapco, 2014).

2.4 DEM Particle Shape and Size Distribution

Most three dimensional DEM simulation codes make use of spherical particles because it is easy to identify contacts. If the particles are found to contact or almost contact (in the case of tensile force transmission), the geometry of the contact point, including the contact overlap or separation, can easily be accurately calculated. However a system of spherical particles has a lower internal friction than that of real materials due to the lack of particle interlocking. In real materials, particle irregularity and surface asperities inhibit

motion thereby resulting in a higher internal angle of friction. To compensate for this behaviour, two methods are used, either independently, or in combination, namely the multi-sphere method (Markauskas et al., 2015) and the rolling resistance method (Ai et al., 2011; Wensrich and Katterfield, 2012).

In the multi-sphere method, a number of spherical particles of varying sizes are rigidly clumped together to re-create the desired shape which exhibits the interlocking. In most cases these shapes are only crudely captured by using a limited number of spheres. To capture the shape of the real material precisely requires a very high number of spheres which has the penalty of significantly increased computational time, particularly because the computational timestep is dependent on the smallest particle radius present in the simulation. Favier et al. (2001) noted that this method required the simplest contact detection algorithm. Coetzee (2016) investigated the effect of particle shape accuracy on hopper discharge with single spheres, 2-clumped spheres, 4-clumped spheres and 8-clumped spheres, and concluded that any of the clumped spheres, if calibrated, could accurately model hopper discharge.

In the rolling resistance method, an additional torque is applied at contact points to resist the applied rolling motion (Ai et al., 2011; Wensrich and Katterfield, 2012). This process simulates the resistance to rotation that real materials with irregular shapes and finite surface roughness experience. However, Barrios et al. (2013) noted that if particles were described in a simplistic way as single spheres, then DEM simulation of their flow no longer matched the experimental results, requiring fitting some of the contact parameters in order to match the observed global flow, so that much of the physical meaning of the parameters was lost. Coetzee (2016) also noted that, while the clumped spheres produced reliable results, single spheres resulted in discrepancies between the DEM and physical bulk behaviours. As such, researchers combine the rolling resistance and multi-sphere approaches. In DEM codes, the rolling resistance is applied by prescribing a rolling friction coefficient (Zhou et al., 1999).

Other methods that are used to simulate particle irregularity include modelling particles using ellipsoids, polyhedral and superquadrics bodies (O'Sullivan, 2011). However, these modelling approaches require more computational resources, making them less attractive in cases where computational resources are limited. In Coetzee (2016) investigations, it was also shown that clumped spheres, that require less computational resources, can adequately model particle irregularity, hence ellipsoids, superquadrics and polyhedrons were not investigated further in this research.

2.5 DEM Energy Dissipation

Energy dissipation that occurs in physical systems of granular materials is captured in DEM codes by adding some numerical damping to the system of particles. This is achieved by specifying a damping coefficient which is used by the contact model equations. Depending on the software used, the damping coefficient can either be directly calibrated or it can be derived from the coefficient of restitution, using Equation 2.25 (O'Sullivan, 2011).

$$\beta = \frac{\ln \epsilon}{\sqrt{\pi^2 + (\ln \epsilon)^2}} \tag{2.25}$$

where β is the damping coefficient and ϵ is the coefficient of restitution.

The coefficient of restitution measures energy dissipation properties of bulk material particles at impact with other particles or a wall surface. It is computed as the ratio of relative velocity after impact to that before impact, as given by Equation 2.26, where ϵ is the coefficient of restitution and v is the particle velocity. For a particle that is released from rest at a height h_0 and rebounded from a surface to a height h_f, it may be shown by considering the conversion of potential to kinetic energy that the coefficient of restitution may be expressed in the form of Equation 2.27. This parameter is evidently critical in flows where the dynamic regime is dominant.

$$\epsilon = \left| \frac{v_{\text{after impact}}}{v_{\text{before impact}}} \right| \tag{2.26}$$

$$\epsilon = \sqrt{\frac{h_f}{h_0}} \tag{2.27}$$

The measurement of coefficient of restitution in a drop test requires the particle used to have a spherical or nearly spherical shape. However, it is difficult to grind a perfect sphere and so a large number of tests are required to get satisfactorily acceptable rebounds for use in computing the coefficient of restitution.

When using viscous damping, normal and shear dashpots are added to the contact, as illustrated in Figure 2.1. Viscous damping is characterised by a critical damping ratio in which the system transient behaviour decays at the quickest rate without oscillations. Tsuji et al. (1993) established the relationship between the critical damping ratio and the coefficient of restitution as given by Equation 2.25. The amount of dissipation in real impacts actually depends on the relative approach velocity of the particle, so that small amounts of dissipation corresponds to low velocity collisions (Maio and Renzo, 2005; Thornton, 2015). This effect is, however, neglected in DEM codes and constant restitution coefficients are assumed.

2.6 DEM Timestep and Simulation Time

DEM simulation involves tracking the positions, velocity, accelerations, forces etc. of particles, which are determined at discrete instants of time. The term 'timestep'in DEM refers to the time between successive iterations. If a bigger timestep is used, the simulation process will proceed faster as compared to when a small time step is used. However, two main factors limit the timestep that can be used in the simulation, namely stability and accurate resolution of particle interactions.

The explicit central difference integration scheme used in DEM simulations is conditionally stable, so small timesteps should be used to ensure system stability and meaningful results (Thornton, 2015). Individual particle movement is affected by collisions the particle makes with neighbouring particles, boundary surfaces and other particles far beyond its neighbourhood through the propagation of disturbance waves. For accurate resolution of particle interactions, the timestep used should be such that during a single timestep, disturbances can only propagate from one particle to its immediate neighbours (Thornton, 2015).

To simplify the model, the assumption is made that during disturbances all the energy is transferred by Rayleigh waves (Thornton, 2015). A Rayleigh wave is a wave along the surface of a solid, elastic body (Thornton et al., 2011). The timestep is based on the minimum particle size in the simulation which dictates the critical time step to be less than or equal to that given by Equation 2.28. In most simulations 20% of the critical time step has been found to result in good resolution and system stability (Thornton, 2015).

$$\Delta t_{step} = 0.2\Delta t_{critical} = \frac{0.2\pi R\sqrt{\frac{\rho}{G}}}{0.163\nu + 0.8766} \tag{2.28}$$

where R is the radius of the smallest particle in the simulation in metres, ρ is the particle density in kg/m^3, G is the Shear Modulus in Pascals, ν is the Poisson's ratio and the timestep is in seconds. The 20% factor is already accounted for in the equation.

The simulation time is affected by a number of factors including:

- The total number of particles in the system: the higher the number of particles, the higher the number of data points to be calculated, resulting in a higher computational cost.

- The minimum particle size in the system: the minimum particle size in

the simulation dictates the time step to be smaller thereby increasing the computational cost.

- Particle shape: in most DEM codes complex shapes are achieved by clumping of simple spherical shapes. This has an effect of increasing the number of data points to be computed hence increasing the computational cost.

- Material properties: as can be observed from Equation 2.28, density, Shear Modulus and Poisson's ratio all affect the time step and hence the simulation time.

By adjusting these identified factors, it has been found that the computational time can be reduced. Some of the strategies found in literature are:

- Coarse graining. This involves scaling up of particle size, thereby increasing the timestep (Grima and Wypych, 2011*a*).

- Reducing the Shear Modulus to 10^7 Pa increases the critical timestep without affecting the simulation results (Langston et al., 1995; Zhou et al., 2001; Xu et al., 2002; Camborros et al., 2013).

2.7 DEM Simulation Software

There are a number of DEM software codes. Some of these codes include Rocky, EDEM, StarCCM+, Newton and LIGGGHTS. All of the above mentioned codes are commercial except for LIGGGHTS, which is open source. However, LIGGGHTS does not have a graphical user interface and is difficult to set up, making it unattractive for general use. The major advantage of LIGGGHTS, on the other hand, is that it allows one to modify and extend its capabilities, which makes it an ideal code for researchers.

2.7.1 DEM simulation in LIGGGHTS

LIGGGHTS is an acronym for LAMMPS Improved for General Granular and Granular Heat Transfer Simulations (CFDEM, 2017). It is an open source code for particle simulation developed by Sandia National Laboratories. However, the software does not have a user interface of its own and relies on a third party visualisation software called Paraview. LIGGGHTS is downloaded as a directory of C++ source files onto a computer. The source files are then built into an executable file by the user. The process of building a LIGGGHTS executable file is difficult in the Windows operating system and relatively easy in the Linux operating system. As such, the developers of LIGGGHTS recommend that DEM simulations be performed in Linux. Appendix Q outlines the procedure for LIGGGHTS installation in the Linux environment.

A simulation in LIGGGHTS involves creating an input file in a text editor with the specifications of the simulation to be conducted. The specifications of the simulation include characteristics of the bulk material, input parameters, equipment geometry, the simulation domain and the required output files, together with parameters to be recorded in those files. The output files can be csv spreadsheet files which are opened by a spreadsheet program such as Microsoft Excel, or binary files that are opened by a visualisation software such as Paraview.

LIGGGHTS implements two main contact stiffness models namely, the Hertz and Hooke models described in Section 2.3.1. The choice of which model to use depends on the user. Maio and Renzo (2005) investigated the performance of the two contact models and concluded that the Hertz model was more accurate than the Hooke contact model. In this research, the Hertz model was chosen for the simulations in line with this finding.

2.8 Calibration of DEM Input Parameters

The purpose of DEM calibration is to assign appropriate values to input parameters that define particle to particle interactions and particle to wall surface interactions, in order to achieve a model bulk material response that matches the response observed in physical laboratory tests, or in an application.

2.8.1 DEM input parameters

DEM input parameters may differ slightly from one software package to another. In LIGGGHTS, the required input parameters are:

- Coefficient of sliding friction, which is split into two independent components of particle to particle ($\mu_{pp,s}$) and particle to wall surface ($\mu_{pw,s}$) coefficients. These parameters significantly affect the simulated flow behaviour, especially in the quasi-static flow regime, hence the need to accurately determine their values (Savage et al., 1983; Langston et al., 1995; Gröger and Katterfield, 2006).

- Coefficient of rolling friction, which is split into two independent components of particle to particle ($\mu_{pp,r}$) and particle to wall surface ($\mu_{pw,r}$) coefficients. These parameters are as equally important as the coefficients of sliding friction, especially under the quasi-static flow regime (Savage et al., 1983; Langston et al., 1995; Gröger and Katterfield, 2006).

- Coefficient of restitution, which is split into two independent components of particle to particle (ϵ_{pp}) and particle to wall (ϵ_{pw}) coefficients. These parameters have a significant impact on the simulated response in the dynamic flow regime, hence the need to accurately determine their values (Savage et al., 1983).

- Particle density (ρ_p) significantly affects the bulk density, hence the need to calibrate it with a reasonable degree of accuracy (Horn, 2012).

- Young's Modulus (E) of both the particles and walls have been shown to have an insignificant effect the DEM results over a wide range of values (Lommen et al., 2014). Hence, published values are often used.

- Poisson's ratio (ν) of both particles and walls have been shown to have an insignificant effect on the simulated bulk material flow behaviour, and are assigned literature obtained values (Horn, 2012).

- Particle shape has been shown to be important in reproducing the interlocking effect of real material. This is achieved in DEM by using clumped spheres or single spheres with a higher rolling resistance coefficient specified (Ai et al., 2011; Coetzee, 2016). However, the use of single spheres was concluded to give results that were less accurate as compared to clumped spheres (Barrios et al., 2013; Coetzee, 2016). As such, researchers use irregular shapes, which are not necessarily an accurate representation of the real particles, in conjunction with higher rolling resistance (Grima and Wypych, 2011*b*; Grima et al., 2013; Marigo and Stitt, 2015).

- Particle size significantly affects the simulation time. If the particle size is small, the timestep, as dictated by Equation 2.28, would be small, thereby resulting in longer simulation time. To reduce the simulation time, particle sizes are scaled up (Grima and Wypych, 2011*b*).

- Timestep. This parameter affects the stability of DEM simulation and is critical for detecting particle interaction. It is recommended to be set at a value lower than 20% of the Rayleigh timestep. The maximum recommended timestep may be computed using Equation 2.28 (O'Sullivan, 2011; Thornton, 2015).

- Cohesion Energy Density. This parameter measures the amount of energy required to separate bonded materials due to weak intermolecular forces, as found in moist materials or particles sizes less than 50 μm.

Bonding may either be particle to particle (ED_c) or particle to wall surface (ED_a) (O'Sullivan, 2011). Though in literature, both particle to particle and particle to wall surface bonding are referred to as 'cohesion energy density', in this research, the particle to wall surface bonding strength will be referred to as 'adhesion energy density'.

2.8.2 Approaches to DEM calibration

Marigo and Stitt (2015) identified two main approaches used to calibrate DEM input parameters as 'direct measurement' and 'random parameter search'. The same approaches were also identified by Rackl and Hanley (2016) as 'direct measurement' and 'trial-and-error' approaches respectively.

Direct measurement: The first approach involves the direct measurement of input parameters. Krügger (2009) used direct measurement to determine the input parameters of coal and validated them using the direct shear test (see Section 2.9.1). In his investigations, he alluded to the difficulties in directly measuring the particle to particle coefficient of sliding friction, and he had to assume it was equal to the particle to wall coefficient of sliding friction. He went on to model the DEM particles using single spherical particles. On validating his results using the measured input parameters in DEM, there was a disagreement between the physically measured and DEM direct shear results by between 66% and 71%.

Barrios et al. (2013) also used direct measurement for iron ore pellets DEM input parameters, and validated the results using a poured angle of repose test. They carried out two sets of DEM tests, all using the measured input parameters, while they varied the number of clumped spheres. In the first set, they used single spheres and there was an 88% difference in the angles of repose between the physical and DEM results. The difference in the angles of repose was only eliminated by randomly varying the friction coefficients. In the second set, they used four clumped spheres to model a DEM particle

and the difference in the physical and DEM angles of repose was reduced to 12%. They then concluded that, if input parameters are determined through direct measurement, then the model material has to perfectly match the real material in shape and size distribution. However, this is not possible due to limitations in the ability to produce every shape and size of the real material. Even if it was possible to correctly capture all the intricacies of the real material in the model material, computational resources would not allow any realistic simulations thereof.

These previous researchers showed that, while some input parameters were easy to measure, others such as the particle to particle coefficients of sliding and rolling friction were difficult to measure because of their dependence on particle shape and size. Even in the case where all input parameters could be measured, if these parameters were to be implemented directly in DEM code, the simulated and physical experiment responses would still differ due to the idealised contact laws used in the DEM codes, especially in cases where the flow regime was very sensitive to particular input parameters. This scenario therefore calls for further adjustments to the input parameters in order for the simulated response to be comparable to the physical experiment, or real application response. This process again introduces some randomness in final tuning to match the physical and numerical responses, and there is no procedure for how these adjustments may be made. Curry et al. (2009) observed that measuring individual micro parameters and applying them directly in DEM simulations did not guarantee accurate physical results. Grima and Wypych (2011*b*), and Rackl and Hanley (2016) also concluded that direct measurement of input parameters did not result in the correspondence between the DEM and physical results due to the scaling of particles in DEM. They went on to highlight that correct input parameters could only be obtained by calibration using appropriate bulk material responses.

Random parameter adjustment: The second approach involves determination of input parameters by randomly adjusting parameter values until the simulated and physical experiments' mechanical responses are comparable (Zhou and Sun, 2013). Mechanical responses are chosen such that they recreate the typical flow regime and bulk behaviour seen in an idealised application. Marigo and Stitt (2015) used this approach to calibrate input parameters for cylindrical pellets using the poured angle of repose as the bulk response. They calibrated six input parameters using only a single bulk response. They created 12 parameter sets, in which the six input parameters were randomly adjusted from one set to the other. For each set, they performed DEM angle of repose tests. They then compared the twelve DEM angles of repose to the physically measured angle of repose, and observed that three of the simulated angles of repose were comparable to the physically measured angle. One of the three sets was arbitrarily chosen to be a parameter set of calibrated values. The subsequent validation tests, using the calibrated parameters in a tumbling drum, resulted in discrepancies between the physically measured and DEM simulated results. They then concluded that the method of random parameter adjustment did not give optimal input parameters.

Rackl and Hanley (2016) calibrated seven input parameters of spherical glass beads using two bulk material responses and an optimisation algorithm. The bulk responses used were loose poured bulk density and poured angle of repose. They then verified their results using loose poured bulk density and angle of repose tests, and got satisfactory results. However, they never validated their results using a different geometry from the ones they used during calibration, hence the simulation may have failed if a different experimental set up was modelled.

Other researchers who used the random parameter calibration approach include Rojek et al. (2005), Asaf et al. (2006) and Wensrich and Katterfield (2012). These researchers showed that if the number of parameters (mathematical variables) to be calibrated was more than the number of mechanical

responses (simultaneous equations), the resulting system had multiple combinations of values that resulted in the same observed response. In this calibration approach, it was also observed that the input parameters were simply treated as adjustable parameters without any physical meaning despite the fact that the model was composed to give them distinct physical meaning (Barrios et al., 2013). However, in this approach, there was no guarantee that the obtained parameters would work in a different geometry, since their physical meaning would have been ignored during the calibration process.

The noted limitations of the two major calibration approaches therefore call for a structured framework, in which DEM calibration can be effectively executed. Such a framework should be developed on the strengths of each of the two previous approaches. This may be achieved by limiting direct measurement to input parameters that are easy to measure and do not significantly affect the bulk material behaviour. The rest of the input parameters would then be calibrated in a series of sequential calibration experiments. The calibration experiments are chosen to isolate the effects of specific input parameters at each stage. This will ensure that input parameters retain their physical meaning during the calibration process, hence should be application independent. This is the aim of this research.

2.9 DEM Calibration Experiments

DEM simulated bulk material behaviour is matched to the observed bulk flow behaviour through the process of input parameter calibration (Zhou and Sun, 2013). Various calibration experiments are reported in literature with the most common being the direct shear test, the angle of repose test, the volume test, the inclined plane test and the particle drop test. These will be discussed briefly.

2.9.1 Direct Shear Test

The Direct Shear Test (DST) employs a shear tester such as the Jenike Shear Tester, Shear Cell or Shear Box, and is widely used to characterise bulk material friction and cohesion properties. The DST consists of a bulk material sample that is contained in the shear box constructed of two halves (O'Sullivan et al., 2004). Figure 2.5 shows an illustration of the shear box setup to measure particle to particle bulk material friction properties. A sample of the bulk material is placed in the two halves of the cell, and is consolidated under the action of the normal load.

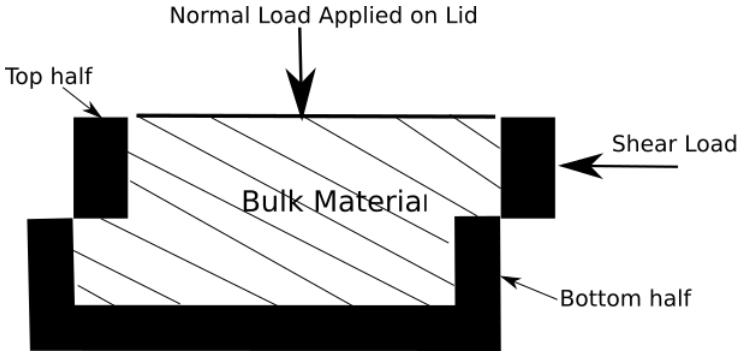


Figure 2.5: Direct shear test experiment

The sample is quasi-statically sheared laterally at a constant rate by moving the top half of the shear box relative to the fixed bottom, while simultaneously applying a normal load to the sample. The sample is sheared at various magnitudes of the normal load (stress) until a limiting shear stress (the shear stress at which strain increases at almost a constant value of shear stress) has been reached for each value of normal stress. Figure 2.6 shows the evolution of shear stress and limiting shear stress during shearing as a function of either time or displacement. The limiting shear stress is then plotted against normal stress, and a yield locus is determined, as illustrated in Figure 2.7. The bulk angle of internal friction, together with cohesion properties, are then inferred from the plotted line of best fit using Equation 2.29, which represents the locus of internal failure and incipient flow of the material. Equation 2.29 is known as the Mohr-Coulomb equation (Horn, 2012).

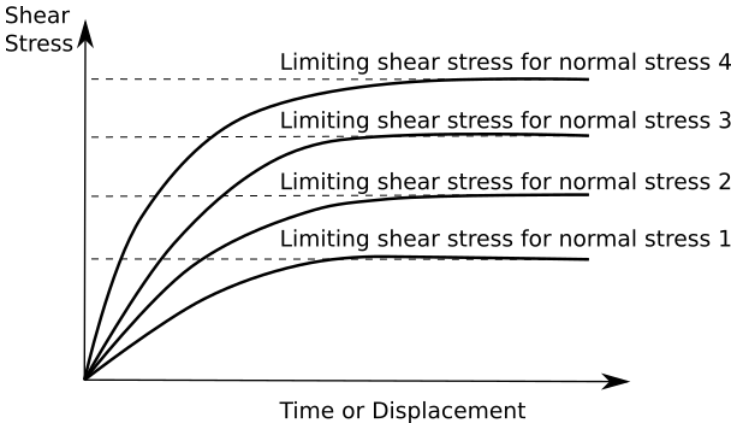


Figure 2.6: Shear stress evolution during shearing

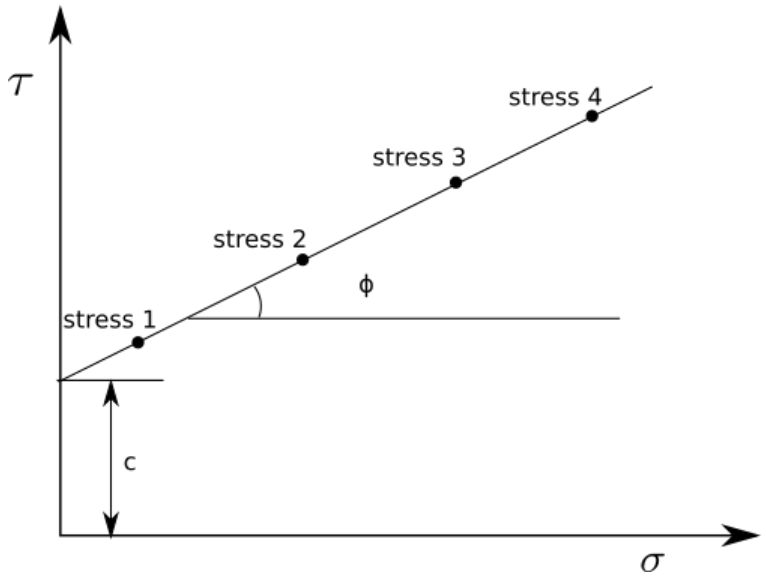


Figure 2.7: Bulk material failure envelope

$$\tau = \sigma \tan \phi + c \tag{2.29}$$

where τ is the average limiting shear stress, σ is the normal stress, c is cohesion and ϕ is the angle of internal friction.

If each term in Equation 2.29 is multiplied by the cell cross sectional area, divided by the coefficient of $\tan \phi$, and ϕ made the subject of formula, it reduces to Equation 2.30.

$$\phi = \arctan(\mu - K) \tag{2.30}$$

where ϕ is the angle of internal friction, μ is the coefficient of friction and K is a constant associated with cohesion. Figure 2.8 shows the plot of Equation 2.30, for $K = 0.0$ and $K = 0.05$ to show a non-linear relationship between the friction angle and the friction coefficient.

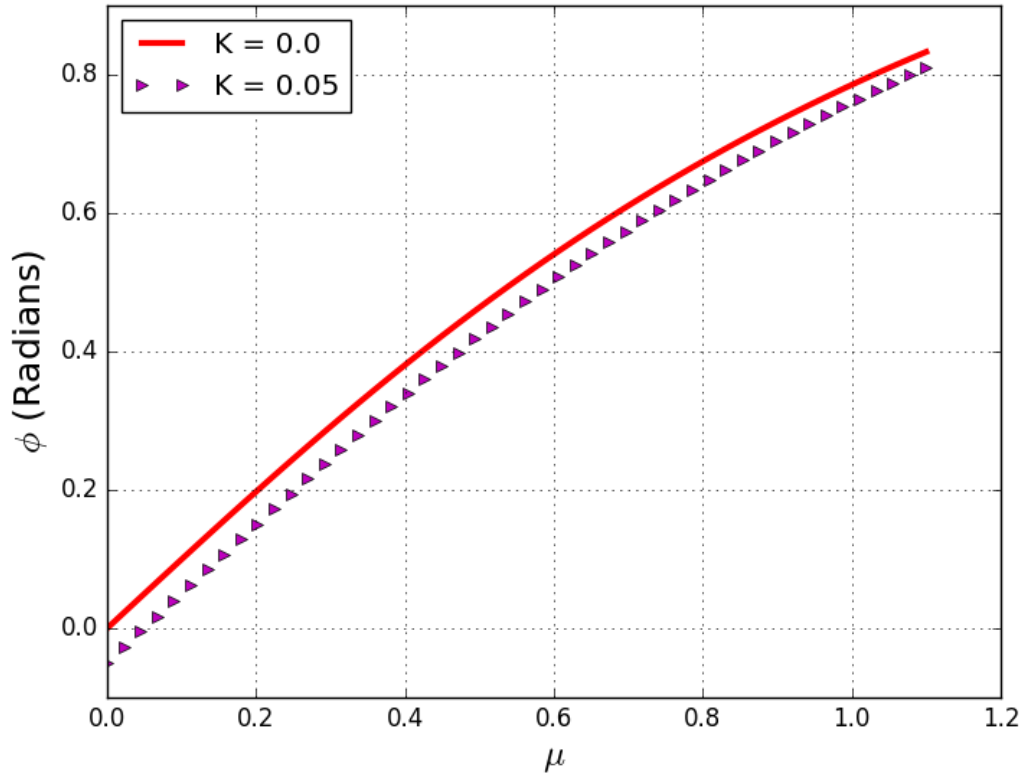


Figure 2.8: Variation of friction angle with coefficient of friction

By setting up the same experiment in the DEM code under the same loading conditions, DEM parameters are varied until the same value of angle of friction as in the physical set up is attained. The set of parameter values that result in the same value of angle of internal friction as in the physical test are then the calibrated parameters.

The angle of internal friction largely depends on the particle to particle coefficients of sliding and rolling friction, particle shape and size distribution, and to a small extent, on the particle density (Horn, 2012). As such, the angle of internal friction is an important bulk response in the calibration of DEM model parameters for bulk materials flow applications, because the parameters it depends on dictate the flow behaviour of bulk materials (Gröger and Katterfield, 2006).

Calibrating DEM parameters using this approach alone has the problem of there being several combinations of parameter values that may result in the same value of angle of internal friction. This potentially results in the calibrated parameters not being representative of reality, and may only be applicable to the geometry used for calibration.

If the bottom half of the shear cell in Figure 2.5 is replaced by a wall surface material, the angle of wall friction between the bulk material and wall surface is determined in a similar manner, where normal stress and shear stress are recorded. The resulting angle of wall friction can then be used to calibrate the particle to wall surface coefficient of sliding friction.

2.9.2 Angle of repose tests

The angle of repose for a bulk material sample is the measure of inclination of the free surface to the horizontal of a bulk solids pile (Ileleji and Zhou, 2008). The angle of repose is dependent on the method used for its determination. There are four angles of repose reported in the literature, which are dependent on their formation, and which do not necessarily yield similar angles. These include the poured angle of repose, the drained angle of repose, the split pipe angle of repose and the dynamic angle of repose.

Poured angle of repose: The poured angle of repose is measured from a heap formed by pouring material onto a flat surface (Merkus and Meesters, 2016), as illustrated in Figure 2.9. This angle of repose and the resultant flow regime (quasi-static or dynamic) depends on the pour height and/ or lifting speed of the container used in forming the heap. The pour height is the distance between the bottom of the material container and the top of the heap of the bulk material. When the pour height is relatively small, particle velocities are lower and consequently the bulk material flow regime is quasi-static, and the angle of repose is higher. As the pour height is increased, the kinetic energy of the particles at impact with the heap increases, the flow regime transitions to dynamic, and the angle of repose is reduced. This flow behaviour is typical of material being deposited on a stockpile from a conveyor belt. Li et al. (2017) investigated the dependence of angle of repose on particle velocity and concluded that the angle of repose reduced exponentially with impact velocity increase.

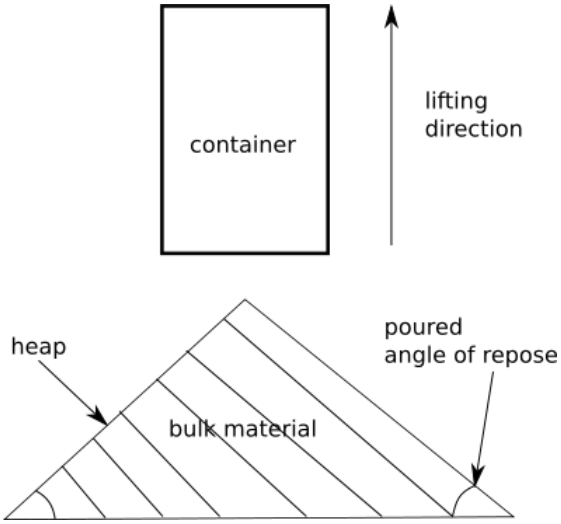


Figure 2.9: Poured angle of repose

Drained angle of repose: The drained angle of repose is measured on the internal conical face of a material which has been formed when drained from an orifice of a flat bottomed container, as illustrated in Figure 2.10 (Merkus and Meesters, 2016). The angle formed depends on the orifice size. If the

orifice at the bottom allows the material to flow freely without confinement, the particles will possess high levels of kinetic energy making the flow regime in the middle dynamic. This flow behaviour is typical of flow in chutes. However if there is an obstruction below the orifice in the form of a heap of bulk material that limits the kinetic energy, then the flow regime is quasi-static. This flow behaviour is typical of flow from a storage facility into a feeder. Zhou et al. (2002) found that dimensions of the container in which the angle of repose was formed affected the drained angle of repose. If the container dimensions were small, container walls significantly affected the angle of repose, resulting in steeper angles..

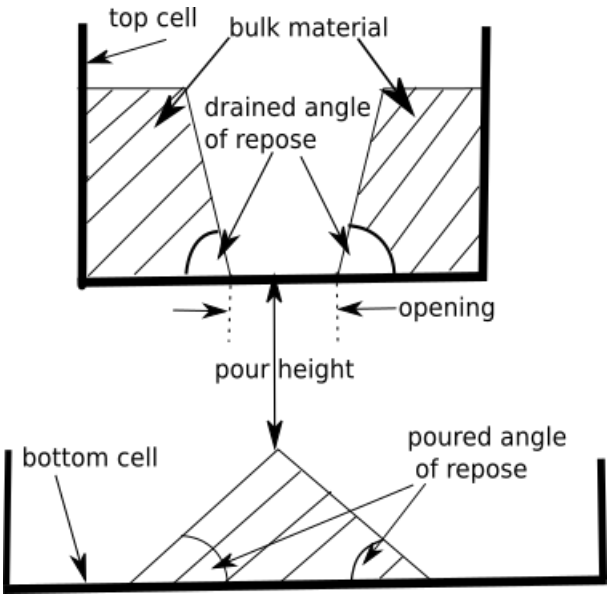


Figure 2.10: Drained angle of repose

Split pipe angle of repose: The split pipe angle of repose is a modification of the poured angle of repose in which the influence of the particle to wall friction effects are negligible. Figure 2.11 shows two half sections of a pipe which are positioned on a pedestal, the pipe is filled with material, and the two halves rapidly removed outwards. The pedestal on which the heap is formed has a finite diameter, which further reduces the wall friction effects. This setup for measuring angle of repose was conceptualised by Grima and Wypych (2011*b*)

at Wollongong University in Australia. The dominant flow regime in this test is dynamic since the material is unconfined from all the sides and falls freely.

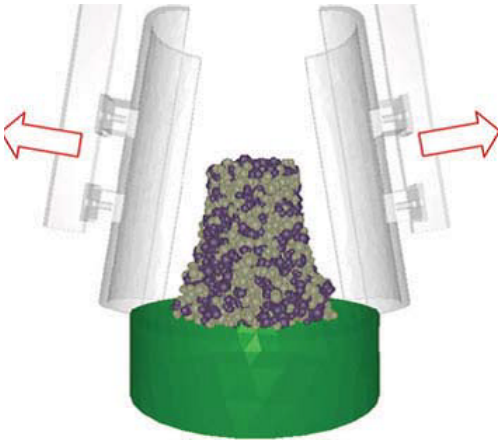


Figure 2.11: Split pipe angle of repose (Grima and Wypych, 2011*a*)

Dynamic angle of repose: The dynamic angle of repose is measured from the free surface of the material formed in a rotating drum, as illustrated in Figure 2.12 (Merkus and Meesters, 2016). The dominant flow regime in the rotating drum is dynamic depending on the rotational speed of the drum. This flow regime is typical of flow in a ball mill.

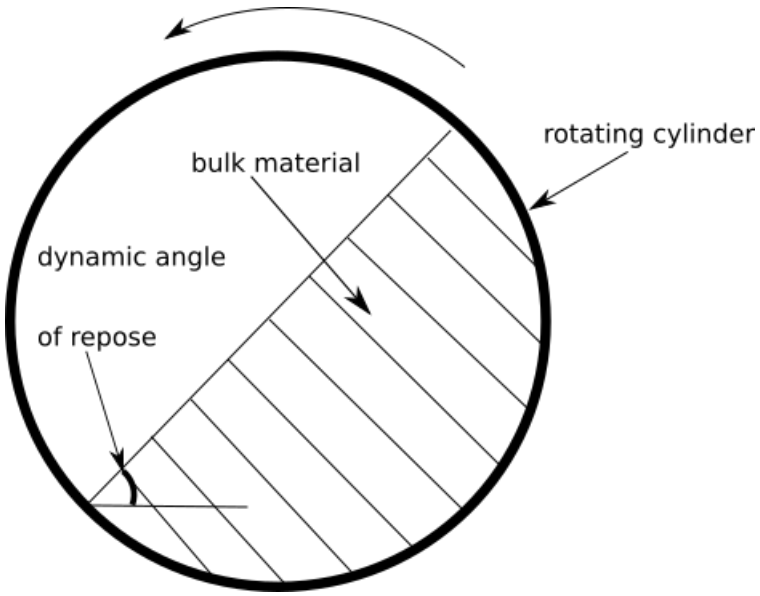


Figure 2.12: Dynamic angle of repose

The angle of repose is different for the same material depending on the test used; as such, the method of acquiring the angle should be relevant to a specific

application and flow regime. Together with the angle of internal friction, the angle of repose is an important bulk material response in characterising the frictional and cohesion properties of bulk materials.

If used as a DEM calibration experiment, the physical experiment is done and replicated in the DEM code, in which parameter values are varied until the angle of repose values of the physical experiments and simulation are comparable. However, this is an ill-posed problem if performed as the only calibration experiment, due to there being no unique combination of input values that result in a particular single angle of repose value.

The DEM input parameters that have been found to significantly influence the angle of repose are the particle to particle coefficients of sliding and rolling friction, cohesion, and particle shape and size distribution (Zhou et al., 2002; Brummer, 2010). With particle size and shape fixed, and the bulk material cohesionless, the angle of repose may therefore be used to calibrate the particle to particle coefficients of sliding and rolling friction. If the bulk material is cohesive, and the coefficients of sliding and rolling friction are known, the angle of repose may be used to calibrate cohesion energy density. The logic of calibrating cohesion energy density, after acquiring the frictions coefficients, is that an increase in the angle of repose is only a function of cohesion.

2.9.3 Bulk density test

The bulk density test uses the loose poured bulk density of dry bulk material to calibrate particle density. The bulk density of the real bulk material is determined by putting a mass of the bulk material into a container of known volume and calculating the bulk density by dividing the material mass by the container volume. The same test is repeated in the DEM code and the particle density is varied until the DEM and physical bulk densities are equal. The value of DEM particle density that results in the physical and DEM bulk

densities being equal is the calibrated particle density (Horn, 2012; Coetzee and Els, 2009).

Bulk density is related to the particle density through a third parameter called voids ratio, as shown by Equation 2.31 (Horn, 2012). Voids ratio, e_v, is the ratio of the volume of the air gaps between particles (voids) to the total volume of the bulk material. As such, for a given voids ratio and container volume, bulk density is a function of particle density, hence the use of bulk density to calibrate DEM particle density.

$$\rho_b = \frac{\rho_p}{1 + e_v} \tag{2.31}$$

where ρ_b is the bulk density in kg/m^3, ρ_p is the particle density in kg/m^3 and e_v is the voids ratio.

Brummer (2010) observed that the particle density obtained through calibration from the bulk density test was more accurate than the directly measured particle density. This observation is consistent with the fact that in DEM, the particle size distribution (PSD), shape and number of particles cannot be realistically modelled as they are in the real material. As such, this difference in the DEM and real materials results in different void ratios between the two materials for a given volume. Given the unavoidable differences in the voids ratio, the DEM particle density would have to be different from the real particle density in order for there to be equality of DEM and real material bulk densities, as can observed from Equation 2.31.

The bulk density test requires extreme care to ensure that the conditions under which the physical test is conducted are the same in the DEM test. This is important because as the container size gets larger, the material at the bottom become more consolidated due to the pressure exerted by a larger mass of overlying material. As such, any differences in the container size or conditions between the physical and DEM tests may distort the obtained results.

2.9.4 Inclined plane test

The inclined plane test is used to determine the coefficients of sliding and rolling friction between the particle and a wall surface material. For determination of the coefficient of sliding friction, a dry granule of the material is selected that has a flat facet. The granule is placed on a wall material sample with the flat facet in contact with the wall material, in order to inhibit rolling. This approach ensures that the particle will always slide before rolling so that only the sliding component can be measured. The plane is then gradually tilted until the particle starts sliding down the plane. The angle at which sliding begins is the angle associated with particle to wall friction friction, and is given by Equation 2.32.

$$\mu = \tan(\phi) \tag{2.32}$$

where μ is the coefficient of friction and ϕ is the angle at which sliding commences. The resulting value of the sliding friction coefficient, $\mu_{pw,s}$, is then the calibrated value (Barrios et al., 2013).

In order to determine the coefficient of rolling friction, $\mu_{pw,s}$, the same procedure is repeated with a spherical particle instead of a flat faced particle. This ensures that the particle rolls before sliding.

2.9.5 Coefficient of restitution test

The coefficient of restitution test is used to measure the particle coefficient of restitution, ϵ, as the ratio between the relative velocities of the particle after and before impact, by dropping a spherical granule of the bulk material onto a surface. Instead of using velocity ratio, the ratio of square root of the rebound and drop heights may be used to calculate the coefficient of restitution as this is easier to measure. The physically measured value of coefficient of restitution

is directly used in the DEM model (Barrios et al., 2013) so that the DEM particle possesses the same energy dissipation property as the real particle.

The accuracy of the method is limited by the difficulties in obtaining a perfectly spherical particle shape, and estimation of the original and rebound heights. Also, the coefficient of restitution has been found to be shape and impact velocity dependent; however, all the DEM codes assume a constant value of the coefficient of restitution (Thornton, 2015). Assuming a constant coefficient of restitution may work in the case of the quasi-static flow regime where energy dissipation is more a function of friction than impact. In the case where the flow regime is dynamic, where collision between particles significantly affects bulk material behaviour, it may be necessary to increase the accuracy of determining the coefficient of restitution. The accuracy can be increased by having a high number of repetitions and statistical analysis to reduce the uncertainty associated with the obtained average coefficient of restitution.

2.10 Response Surface Methodology

When a response variable or performance characteristic is a function of more than one independent variable, then there is a need for methods that efficiently relate the response variable to the independent variables. One such method is the Response Surface Methodology (RSM). Myers et al. (2009) described the RSM as a collection of statistical and mathematical techniques used in the design, development, improvement and optimisation of processes and products.

In DEM calibration, the methodology has potential to be used to calibrate the input parameters in cases where a single bulk response is affected by two input parameters. An application example would be in the calibration of the particle to particle coefficients of sliding and rolling friction, which both significantly affect the angles of repose and the internal angle of friction.

In the methodology, experiments are performed by systematically sampling and varying the independent variables within a defined range of feasible values while the response of interest is recorded. Using the data obtained during these experiments, an empirical model is fitted that best describes the relationship between the response and the independent variables. The empirical equation can then be used to maximise or minimise the response subject to the independent variables using simple calculus. The RSM process can therefore be split into three major activities (Myers et al., 2009) which are: experimental strategy, empirical statistical modelling and optimisation methods.

2.10.1 Experimental Strategy

Experimental strategy consists of methods to efficiently sample values from the feasible region of the independent variables, to be used in performing the experiments and obtaining corresponding response values. The obtained results should be representative of the variation of the measured response with change in independent variables in the range of the sampled independent variables. The best known approach to designing and conducting such experiments is a technique called Design of Experiments (DOE). This approach, when used in RSM, uses the Central Composite Design (CCD) method for establishing the relationship between the response and the independent variables (Myers et al., 2009; ReliaSoft, 2015).

CCD design is one of the most important designs for fitting second order polynomial response surface models, and is used extensively in selecting the sample points for RSM (Myers et al., 2009). These sample points are a function of the number of independent variables being investigated. In the case of a response which is a function of two independent variables, the minimum number of sample points should be nine which are chosen, as shown in Figure 2.13. In the figure, the reference sample point is first chosen to coincide with the (0,0) point. Then the other points are chosen as ratios of the reference point specific

to the values used in the experiment. Variables, x_1 and x_2, in the figure are independent variables, and the values in brackets are the relative positions of values to be used in the experiments. This combination of high/low values of the independent parameters are assessed in the results.

The output of the CCD is values of independent variables at sample points together with the corresponding response values. The response values are determined by carrying out either physical experiments or numerical simulations with the independent variables set at the sample points values.

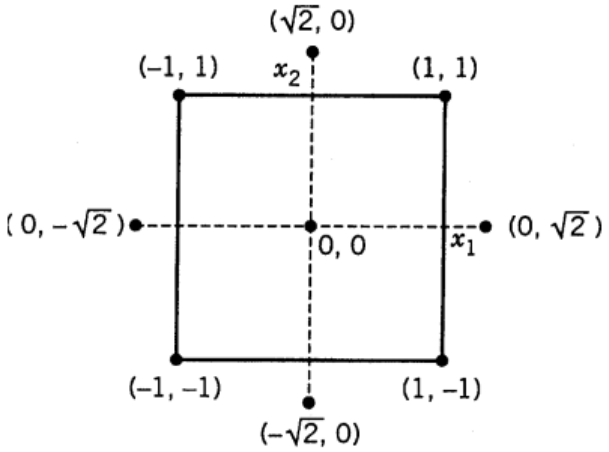


Figure 2.13: CCD sample points for 2 independent variables (Myers et al., 2009)

2.10.2 Empirical Statistical Modelling

Empirical modelling consists of activities to develop appropriate approximating relationships between the response or characteristic being measured, and the independent variables. These approximating equations are developed by fitting the data collected during the experimental strategy phase. Empirical models for RSM are mostly developed using multiple regression analysis methods. The models developed may be first, second or higher order depending on the number of independent variables involved, and the precision required in the estimation of the relationship between independent variables and the measured response. Equations 2.33, 2.34 and 2.35 show examples of two independent

variable multiple regression approximated empirical relations, for a first order model, first order model with interaction terms, and for a second order model with interaction terms, respectively.

$$y = \beta_0 + \beta_1 x_1 + \beta_2 x_2 + e \tag{2.33}$$

$$y = \beta_0 + \beta_1 x_1 + \beta_2 x_2 + \beta_{12} x_1 x_2 + e \tag{2.34}$$

$$y = \beta_0 + \beta_1 x_1 + \beta_2 x_2 + \beta_{11} x_1^2 + \beta_{22} x_2^2 + \beta_{12} x_1 x_2 + e \tag{2.35}$$

where y is the response, x_i are independent variables, β_i are regression coefficients and e is the error term, which is to be minimised during the optimisation process.

Higher order and interaction terms in empirical equations can be reduced to linear terms. Equation 2.36 shows an example of the reduced form of Equation 2.35 with second order and interaction terms.

$$y = \beta_0 + \beta_1 x_1 + \beta_2 x_2 + \beta_3 x_3 + \beta_4 x_4 + \beta_5 x_5 + e \tag{2.36}$$

where $\beta_3 = \beta_{11}$, $x_3 = x_1^2$, $\beta_4 = \beta_{22}$, $x_4 = x_2^2$, $\beta_5 = \beta_{12}$ and $x_5 = x_1 x_2$.

Given an experiment with n independent observations $y_1, y_2, \ldots, y_n$, of the response y, at n sample points, which is a function of k variables $x_1, x_2, ..., x_k$, let the value of variable x_j at the i^{th} sample point be denoted by x_{ij}. The observations at n sample points, y_1, y_2, ..., y_n, can be expressed as functions of the independent variables by a system of Equations 2.37.

$$
\begin{aligned}
y_1 &= \beta_0 + \beta_1 x_{11} + \beta_2 x_{12} + \ldots + \beta_k x_{1k} + e_1 \\
y_2 &= \beta_0 + \beta_2 x_{21} + \beta_2 x_{22} + \ldots + \beta_k x_{2k} + e_2 \\
&\vdots \\
y_n &= \beta_0 + \beta_1 x_{n1} + \beta_2 x_{n2} + \ldots + \beta_k x_{nk} + e_n
\end{aligned}
\tag{2.37}
$$

In the system of Equations 2.37, some of the variables of the x_k variables may be in reduced form as in Equation 2.35. The system of equations may be represented in matrix notation by Equation 2.38.

$$
\boldsymbol{y} = \boldsymbol{X}\boldsymbol{\beta} + \boldsymbol{e} \tag{2.38}
$$

where

$$
\boldsymbol{y} = \begin{Bmatrix} y_1 \\ y_2 \\ \vdots \\ y_n \end{Bmatrix}
$$

$$
\boldsymbol{X} = \begin{bmatrix} 1 & x_{11} & x_{12} & \ldots & x_{1k} \\ 1 & x_{21} & x_{22} & \ldots & x_{2k} \\ \vdots & \vdots & \vdots & & \vdots \\ 1 & x_{n1} & x_{n2} & \ldots & x_{nk} \end{bmatrix}
$$

$$\boldsymbol{\beta} = \begin{Bmatrix} \beta_0 \\ \beta_1 \\ \vdots \\ \beta_n \end{Bmatrix}$$

$$\boldsymbol{e} = \begin{Bmatrix} e_1 \\ e_2 \\ \vdots \\ e_n \end{Bmatrix}$$

where $\boldsymbol{y}$ is the vector of observations/responses, $\boldsymbol{X}$ is the coefficients matrix composed of independent variable settings and their interactions, $\boldsymbol{\beta}$ is the vector of regression coefficients, and $\boldsymbol{e}$ is the error vector.

The least squares method is typically used to estimate the regression coefficients $\boldsymbol{\beta}$ in the multiple regression model. The least squares estimators $\boldsymbol{b}$ of the coefficients $\beta_0, \beta_1, ..., \beta_k$ are then solved by Equation 2.39

$$\boldsymbol{b} = (\boldsymbol{X'X})^{-1}\boldsymbol{X'y} \tag{2.39}$$

where $\boldsymbol{X'}$ is the transpose of matrix $\boldsymbol{X}$.

The coefficient of multiple determination (R^2) which measures the amount of reduction in the variability of $\boldsymbol{y}$ by using independent variables $x_1, x_2, ..., x_k$ as regressor variables may then be used to measure the goodness of fit of the obtained empirical model. The value of R^2 varies between 0 and 1 with higher values indicating a good fit of the data. The coefficient of multiple determination is computed using Equation 2.40 (Myers et al., 2009).

$$R^2 = 1 - \frac{SS_E}{SS_T} \tag{2.40}$$

where

$$SS_E = \boldsymbol{y'y} - \boldsymbol{b'X'y} \text{ and } SS_T = \boldsymbol{y'y} - \frac{1}{n}\sum_{i=1}^{n} y_i$$

where $\boldsymbol{y'}$ is the transpose of vector $\boldsymbol{y}$ and $\boldsymbol{b'}$ is the transpose of vector $\boldsymbol{b}$.

In this research, the RSM was used to derive empirical equations relating the angle of repose to the particle to particle coefficients of sliding and rolling friction. Appendix A.8 shows the general implementations of the RSM equations in Python, for the calculation of regression coefficients and goodness of fit values.

2.10.3 Optimisation Methods and Numerical Computing

Optimisation methods are used to efficiently find the values of independent variables that produce desirable values of the response variable (ReliaSoft, 2015). These methods operate on the empirical models that are developed during the statistical modelling phase. Extensive use is made of computer algorithms for this purpose. In this research Python, Numpy, Scipy and Matplotlib were used for this purpose, with the algorithms presented in Appendix A.

3 Experimental Methods and Apparatus

This chapter covers the experimental methods and apparatus used in the execution of all the physical and DEM experiments using iron ore with size range of 2 mm to 4.75 mm from a South African iron ore Mine. The size range was chosen because it was large enough to be reasonably modelled in DEM, and small enough to exhibit cohesion with an increase in moisture content. Some larger particles were used for particular tests such as coefficient of restitution and the inclined plane tests. Iron ore was used because it was readily available in the TUNRA Bulk Solids Africa (TBSA) Laboratory, where the experimental procedures were conducted. Perspex was used as the wall surface material in all the experiments because it is transparent, hence it allows visualisation of material flow through its surfaces.

The chapter is organised into six main sections covering the categorisation of flow regimes in Section 3.1, DEM calibration framework in Section 3.2, methods for physical calibration experiments in Section 3.3, methods for DEM calibration experiments in Section 3.4, methods for physical validation experiments in Section 3.5 and methods for DEM validation experiments in Section 3.6.

3.1 Flow Regimes Categorisation

In this research, a qualitative approach was used to categorise the flow regimes encountered in the flow of bulk materials. Two major flow regimes that were adopted for categorising flows are the quasi-static flow regime encountered in an application such as silo flow, and the dynamic flow regime encountered in an application like chute flow (Savage et al., 1983; Campbell, 2006; Zhou and Sun, 2013). Subsequently all the flow regimes in this research were categorised as either of the two.

The nature of the flow confining conditions was used as the criterion for differentiating the two flow regimes. These conditions pertain to whether the bulk material has the freedom to flow without restriction, or not. If the bulk material possesses high kinetic energy and the material is less confined such that it freely flows in one or more dimensions without restriction, then the flow regime is dynamic. If the bulk material possesses little kinetic energy and the flow of the material is regulated in all the dimensions of the confining geometry, then the flow regime is quasi-static. This categorisation is very simple and any application can be easily put into either of the two categories. Other possible categorisation methods would be to use bulk material velocity or bulk density, however, these parameters tend to differ in different flow regions of the equipment, and would also require expensive instrumentation for use in real applications.

3.2 DEM Calibration Framework

Figure 3.1 shows the flow of DEM calibration experiments within a proposed structured framework. In the framework, DEM input parameters are split into three categories.

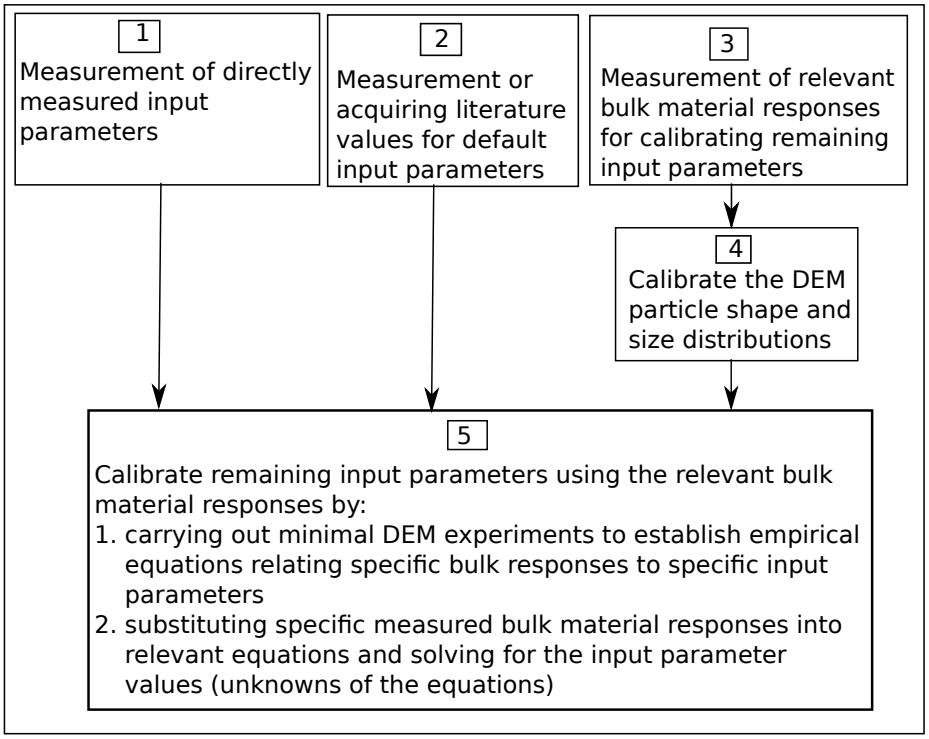


Figure 3.1: Calibration framework

The first category consists of input parameters that are determined by direct measurement (box 1 in the figure). For an input parameter to be considered for direct measurement, it should be easy to measure and it has meaning in the DEM model, or there is no known bulk material response for use in calibrating the parameter. These parameters are measured and recorded first, and used in the subsequent calibration experiments.

The second category consists of input parameters that are known not to significantly affect bulk material behaviour (box 2 in the figure). These values may be obtained from published literature or directly measured.

The third category consists of input parameters to be calibrated from observed bulk material responses (box 3 in the figure). For an input parameter to be considered for calibration from observed bulk responses, either it significantly affects the bulk material behaviour, such that direct measurements may be unreliable, or it is difficult to measure. Specific bulk material responses that are known to be significantly affected by input parameters in this category are then identified and directly measured.

Using the results of the physically measured particle shape and size distributions in box 2 of Figure 3.1, the DEM particle shape and size distributions are then modelled subject to the limitations imposed by simulation time (box 4 in the figure). Coetzee (2017) underscored the importance of particle shape and size models in DEM. He stressed that all the subsequent calibration results are a function of the model shape and size distributions. As such, any variations in shape should be accompanied by a re-calibration of the input parameters.

In box 5, the remaining input parameters in the third category are then calibrated from bulk material responses, identified in box 3, through the development and solution of model equations. The calibration experiments are executed sequentially such that the previously determined input parameter values are used in the subsequent calibration experiments.

3.3 Physical Calibration Experimental Methods

This section covers the physical experimental procedures conducted to either directly measure input parameter values (box 1 in Figure 3.1) or measure relevant bulk material responses (box 3 in Figure 3.1) for the calibration of specific input parameter values. The experimental methods for direct measurement (box 1) of input parameters are the coefficient of restitution test and the inclined plane test. The experimental methods for measurement of bulk material responses (box 3) are the particle size distribution test, particle shape characterisation test, bulk density test, wall friction test and angle of repose tests (double cell, full pipe and split pipe). In each test, the DEM input parameter measured or calibrated by the procedure is stated. Figure 3.2 shows the specific physical experimental methods covered in the context of the calibration framework of Figure 3.1.

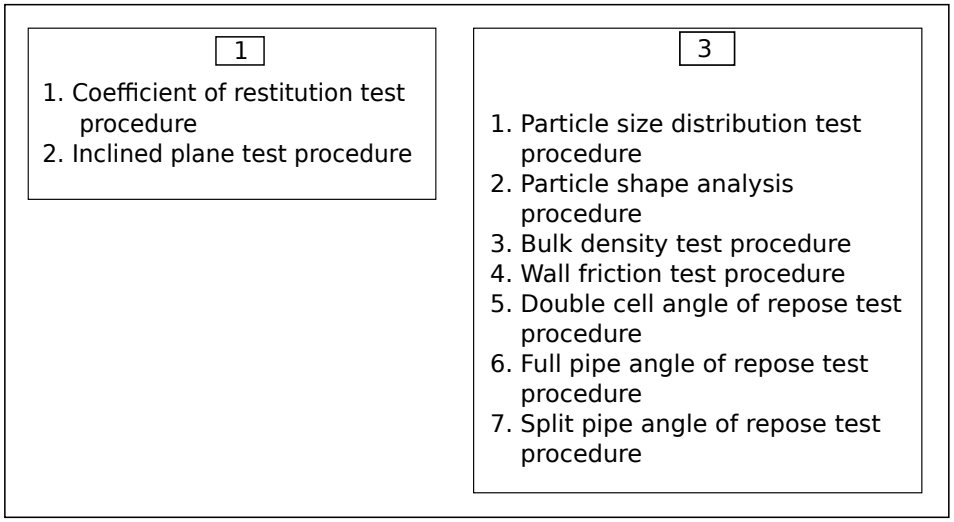


Figure 3.2: Calibration framework, physical experiments procedures

3.3.1 Coefficient of restitution test procedure

The coefficients of restitution for iron ore to iron ore impact and iron ore to perspex impact were determined using the particle drop test. This procedure was necessary especially for the dynamic flow regime where the energy dissipation due to collisions significantly affected the observed flow behaviour.

Before carrying out the procedure, two iron ore particles used in the procedure were prepared. The first particle was ground into an almost spherical shape with an approximate diameter of 10 mm. The second particle of approximate size 20 mm x 20 mm was ground flat on two opposite faces for use as an impact surface for the determination of iron ore to iron ore coefficient of restitution. A rectangular piece of perspex material was also prepared for use in determining the iron ore to perspex surface coefficient of restitution. The experimental procedure was carried out as follows:

1. The impact surface (perspex or iron ore) was rigidly clamped on top of a table with an even surface.

2. A white paper with distance graduations in millimetres was placed behind the clamped impact surface, in a vertical orientation.

3. A video camera was positioned in front of the clamped impact surface facing the graduated white paper. The camera used had a frame rate 30 frames per second.

4. With the aid of the graduated paper, the spherical particle was raised to a starting height of between 200 mm to 220 mm above the impact surface. The spherical particle was placed as close as possible to the graduated paper to minimise parallax error, as shown in Figure 3.3.

5. The video was started and the particle released onto the impact surface to rebound.

6. Steps (4) to (5) were repeated 100 times for each of the two impact surfaces (iron ore and perspex).

7. The videos were downloaded from the camera onto the computer. Videos in which the rebound direction was nearly vertical were accepted while those in which the rebound was irregular were rejected.

8. From the selected videos, the starting and rebound heights were recorded with the aid of the graduated scale.

9. For each picture the coefficient of restitution was determined using Equation 2.27.

10. The starting height, the rebound height and the coefficients of restitution were tabulated, and the average coefficient of restitution and the standard deviation calculated for each of the two impact surfaces (iron ore and perspex).

3.3.2 Inclined plane test procedure

The inclined plane test is carried out to measure the particle to wall coefficients of sliding and rolling friction. In addition, it is also used to determine the angle

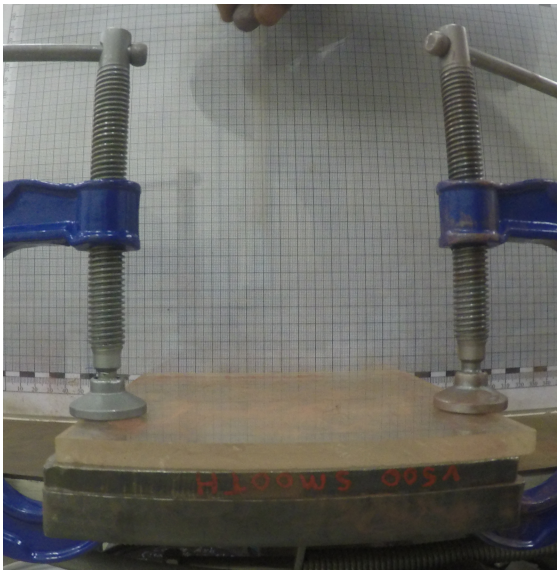


Figure 3.3: Particle drop test setup

at which a wet flat particle commences sliding for the purpose of calibrating the particle to wall surface adhesion energy density.

Prior to carrying out the procedure for sliding friction, an inclined plane was placed on top of a level surface, and a sample of five dry iron ore particles (approximately 25 mm in bounding diameter each) with flat faces was selected. Flat faces were used to ensure the particles slid before rolling occurred.

The experimental procedure was then carried out as follows:

1. A rectangular perspex sheet was placed in the tray of the inclined plane.

2. A single iron ore particle was selected from the sample of five flat faced particles and placed on top of the perspex sheet .

3. The inclined plane was slowly and carefully raised until the particle commenced sliding.

4. The inclined plane was stopped and locked in position, as shown in Figure 3.4. The angle of inclination was read from the inclined plane scale and recorded.

5. Steps (2) to (4) were conducted four times with each of the five flat faced particles.

6. The results were tabulated, and the coefficient of sliding friction corresponding to each of the twenty recorded angles calculated using Equation 2.32.

7. The average coefficient of sliding friction and the standard deviation were calculated and recorded.

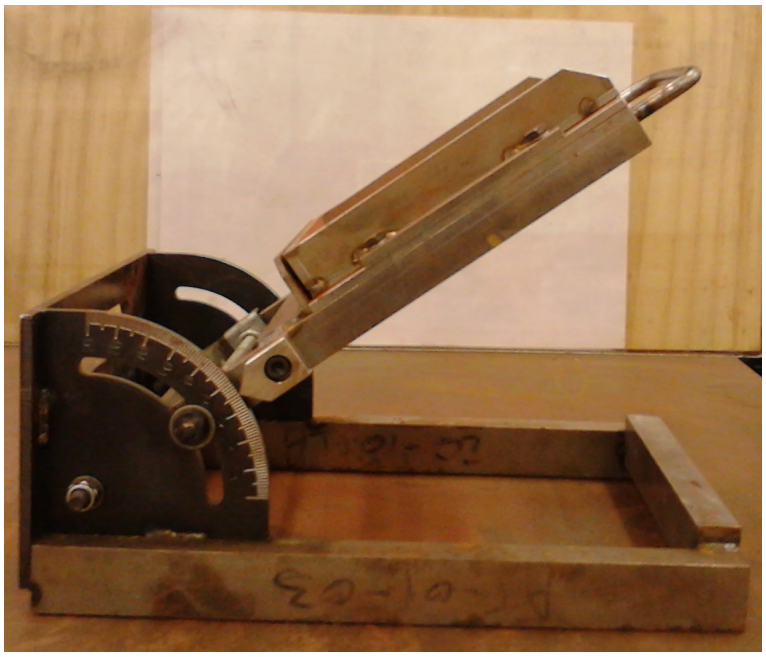


Figure 3.4: Inclinometer in raised position

In order to determine the coefficient of rolling friction, the same procedure was repeated using a spherical particle with an approximate diameter of 20 mm. Instead of carrying out the experiment with five particles by four tests, the spherical particle was tested twenty times. The resulting angle of inclination was the angle at which rolling commenced. The spherical particle was used to ensure that rolling preceded sliding.

In order to determine the inclination angle at which a moist particle commenced to slide, the same procedure was repeated from step (2) to step (5) with moist flat faced particles. The moist particles were seasoned in a bucket containing iron ore at a desired moisture content of 1.2%. This moisture state

was selected based on the flow property tests of the same material, which was determined to exhibit highest level of cohesion at 1.2%. The obtained inclination angles were used to calibrate iron ore to perspex adhesion energy density.

3.3.3 Particle size distribution test procedure

The Particle Size Distribution (PSD) procedure is carried out to determine the percentage contribution of different particle sizes in the bulk material. This procedure is necessary so that the DEM PSD may be modelled such that it is closer to the real physical material PSD. Bulk material PSD affects the cohesive behaviour of the material in that, as the particle size reduces, attractive forces between particles become dominant, resulting in the bulk material exhibiting higher levels of cohesion.

A sieved size range between 2 mm to 4.75 mm was selected for use in the experimental work. This size range was small enough to exhibit cohesion with an increase in moisture content and large enough to be fairly modelled in DEM at reasonable computational cost. The sizes were sieved from an iron ore sample with a known top size of 4.75 mm.

In order to obtain the PSD, three standard sieve sizes available at TUNRA Bulk Solids Africa (TBSA) laboratory were used. The sieve sizes were 4.0 mm, 2.8 mm and 2.0 mm. The following procedure was then used to obtain the PSD:

1. The mass of each of the three sieves was measured on a scale with a resolution of 0.1 g and recorded.

2. The three sieves were stacked on top of a base pan with the smallest sieve size at the bottom, in order of increasing aperture size.

3. A bulk material sample of approximately 800 g was placed into the top sieve.

4. The sieve shaker was started and left to run for 20 minutes.

5. The sieves stack was removed from the sieve shaker.

6. For each sieve (excluding the pan), the mass of the bulk material and the sieve was measured on a scale and recorded.

7. The mass of the remaining bulk material in each sieve was calculated by subtracting mass obtained in (1) from mass obtained in (6) and recorded.

8. The total mass of the bulk material sample was determined by adding total masses of each of the three sieve sizes.

9. The percentage contribution of each of the three sieve sizes was determined using masses determined in steps (7) and (8).

3.3.4 Particle shape analysis procedure

Particle shape analysis is carried out to determine the dominant particle shapes in the bulk material. The degree of irregularity and surface asperities of a bulk material influences its rolling resistance characteristics. A highly irregular shaped particle has a higher rolling resistance than a more regular shaped particle. This procedure is therefore necessary so that the DEM particle shape may be modelled such that it estimates the real material particle shape (Coetzee, 2016) within the limits of the available computational resources and time.

In this research, a simple visual inspection of particle shape was used. The approach was adopted because it has been shown that when a calibrated approach is taken, as opposed to direct measurement, the DEM particle shape may be crudely captured without distorting the results (Coetzee, 2016). The important aspect is to ensure some degree of irregularity in the shape. However, if an approach was adopted in which all the input parameters were directly

measured, then it would be imperative to capture as muany particle shapes, and as accurately as possible (Barrios et al., 2013). In such cases, there would be a need to quantitatively evaluate the particle shape using such parameters as the aspect ratio and sphericity.

A simple visual analysis procedure was used as follows:

1. Five particles were randomly selected from the bulk material.

2. The particles were placed on a flat surface and the dominant particle shape inferred by a simple visual inspection.

3.3.5 Bulk density measurement procedure

The bulk density test procedure is used to determine the loose poured bulk density (Brummer, 2010; Horn, 2012). The loose poured bulk density is then used to calibrate the DEM particle density.

Two cylindrical containers with different volumes and height were used to carry out the bulk density test. The smaller volume container with an internal diameter of 95 mm and a height of 12 mm, was used to determine the bulk density for use in calibrating the particle density. The larger volume container with an internal diameter of 94 mm and a height of 140 mm, was used to verify the ability of the calibrated particle density to correctly predict the bulk density measured with a different sized container. Verification of the bulk density was done using a different sized container because a container with a larger depth results in higher consolidation pressure at the bottom, hence a higher bulk density in comparison to a smaller depth container.

The experimental procedure used to determine the bulk density for each of the two containers was as follows:

1. The dimensions of cylindrical container were measured, and the volume computed.

2. The mass of the empty container was measured on a scale with a resolution of 0.1 g and recorded.

3. The container was placed on a flat surface and a sample of bulk material was poured into it in one steady pour until the container was overfilled.

4. Excess material was carefully scraped off using a scraper until the bulk material was level with the top of the container.

5. The mass of the bulk material and container was measured on the scale and recorded.

6. The recorded mass of the container was subtracted from the recorded mass of the bulk material and container to obtain the net mass of the bulk material.

7. The bulk density of the material was calculated by dividing the net mass of the bulk material by the volume of the container and recorded.

8. Steps (3) to (7) were conducted six times.

9. The average bulk density and the standard deviation were calculated and recorded.

3.3.6 Wall friction test procedure

The wall shear test procedure is carried out in order to measure the bulk material angle of wall friction. The angle of wall friction is then be used to calibrate the particle to wall coefficient of sliding friction. Although the test method used in DEM calibration uses the same apparatus as in wall friction tests conducted during flow properties tests, the procedure and objective are slightly different from the standard flow property test, in order to facilitate comparison in DEM.

The Jenike Shear Tester in the TBSA Laboratory, with a shear speed of 2.5 mm/minute, was used for this purpose. As was mentioned Section 2.9.1, the wall shear test procedure was performed by replacing the bottom half of the direct shear test illustrated in Figure 2.5 with the wall surface material. The experimental procedure used to determine wall friction angle was as follows:

1. The wall material sample was attached to the shear test equipment.

2. The shear ring, with internal diameter of 95 mm and 15 mm depth was placed on the wall surface material resting firmly against support screws on the shear tester.

3. A sample of the bulk material was placed into the shear ring and scraped level with surface of the ring. The shear ring was covered with the shear lid. The drive bracket attached to the shear lid was made to be in line with the shearing pin. Figure 3.5 shows the setup of the wall friction tester.

4. The weight carrier with a mass of 0.5 kg was hung on top of the shear lid and a mass of 1.5 kg placed on the carrier.

5. The data acquisition system on the computer was opened and a new worksheet opened in the data acquisition system for logging the data.

6. The shear tester was started and the shear force monitored on the data acquisition. When the shear force reached an almost constant value, data collection was started.

7. After every 0.2 minutes, an additional 2 kg mass was added on the hanger bringing the hanger masses to 3.5 kg, 5.5 kg and 7.5 kg. The data collection and shear tester were stopped after approximately 0.8 minutes of data collection.

8. The data collection worksheet was saved as a csv spreadsheet file. The data was made up of two columns, with one column being time and the other being shear force.

9. The wall surface material together with the shear ring, shear lid and bulk material were removed from the pedestal and weighed on the scale with a resolution of 0.1 g. The mass was recorded.

10. The mass of the wall surface material and shear ring was weighed and recorded.

11. The mass of the material above the shear plane was calculated by subtracting the mass obtained in step (10) from that obtained in step (9) and recorded.

12. The normal force acting on the bulk material for each of the masses used was calculated by adding the weight above the shear plane obtained in step (11) and mass of the weight carrier (0.5 kg) to each of the four masses to obtain total normal mass on the bulk material sample, and multiplying each normal mass by the acceleration due to gravity (9.81 m/s^2).

13. For each shear force data point in the saved csv file, the shear stress was calculated by dividing the shear force by the cross sectional area of the shear ring.

14. A graph of the shear stress against time was plotted. The plotted graph had four steps, with each step corresponding to one of the four masses on the weight carrier. The average shear stress for each step was calculated by averaging the shear stress data points at the step.

15. The normal stresses acting on the bulk material for each of the four normal forces was calculated by dividing the normal force in step (12) by the cross sectional area of the shear ring.

16. A graph of the shear stress against the normal stress was plotted and a linear best fit curve fitted on the data points using linear regression.

17. The gradient of the best fit curve was determined.

18. The angle of wall friction was determined as the arctangent of the gradient of the best fit curve. The gradient of a shear stress versus normal stress graph is equivalent to $\tan\phi$ as given by Equation 2.29.

19. Steps (2) to (18) were conducted a second time.

20. The average angle of wall friction was calculated from the two results.



Figure 3.5: Jenike wall shear tester

3.3.7 Full pipe angle of repose test procedure

The full pipe angle of repose test is carried out to determine the poured angle of repose. The obtained angle of repose with dry material is then used in the calibration of the particle to particle coefficients of sliding and rolling friction.

The method was chosen to calibrate iron ore to iron ore coefficients of sliding and rolling friction because it has been shown that the angle of repose of dry bulk material depends on these two parameters (Gröger and Katterfield, 2006).

A perspex cylindrical pipe with an internal diameter of 94 mm and a height of 140 mm was used to measure the angle of repose. The same test was repeated with a pipe with an internal diameter of 110 mm and a height of 140 mm in order to check if pipe dimensions had an effect on the obtained angle of repose. The following experimental procedure was used to determine the full pipe poured angle of repose:

1. The cylindrical pipe was placed on a pedestal with a circular base of diameter 230 mm.

2. A bulk material sample was poured into the pipe until it was full, and scraped level.

3. The pipe was lifted slowly (approximately 5 mm/s) allowing the bulk material to flow from underneath and form a heap. The pipe was removed when it was no longer in contact with the bulk material.

4. When the bulk material came to rest, a photograph of the heap was captured.

5. Steps (1) to (4) were conducted three times for each of the two pipe diameters.

6. The pictures were downloaded onto the computer and imported into CAD software for measuring the full pipe poured angle of repose.

7. The average full pipe poured angle of repose was calculated for the three tests.

3.3.8 Split pipe angle of repose test procedure

The split pipe angle of repose test is carried out to determine the split pipe poured angle of repose. The obtained angle of repose from dry bulk material is then used in the calibration of the particle to particle coefficients of sliding and rolling friction. The split pipe angle of repose obtained from moist bulk material is used to calibrate the particle to particle cohesion energy density. The use of angle of repose to calibrate cohesion energy density was based on the logic that all the frictional effects were factored into the model using dry material, and the increase in angle of repose when using moist material would be a function of cohesion only.

A perspex cylindrical pipe with an internal diameter of 94 mm and a height of 140 mm, was split into two halves for the purposes of measuring the split pipe angle of repose. The equipment used was similar in principle to the Grima and Wypych (2011*b*) slumped repose equipment in that it quickly loses contact with the material thereby minimising wall frictional effects. The following experimental procedure was used to determine the full pipe poured angle of repose:

1. The split pipe halves were placed on a pedestal with a circular base of 230 mm, diameter as shown in Figure 3.6.

2. A bulk material sample was poured into the split pipe while holding the two halves together until it was full, and scraped level.

3. Rapidly, the two split pipe halves were separated outwards using the handles, allowing the bulk material to flow unrestricted and form a heap on the pedestal.

4. When the bulk material had come to rest, a photograph of the heap was captured.

5. Steps (1) to (4) were conducted three times.

6. The pictures were downloaded onto a computer and imported into CAD software to measure the split pipe poured angle of repose. The obtained angles of repose were recorded.

7. The average split pipe poured angle of repose was calculated for the three tests.

3.3.9 Double cell angle of repose test procedure

The double cell angle of repose test is carried out to measure the angle of repose of the bulk material. The obtained angles of repose with dry material

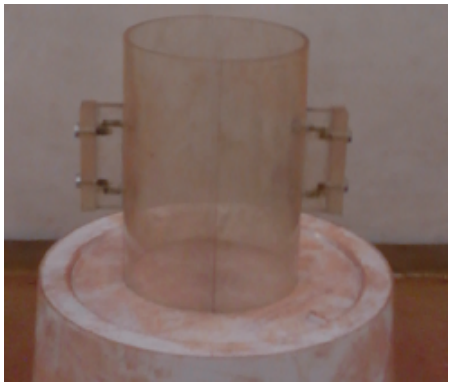


Figure 3.6: Split pipe angle of repose equipment setup

are then used to verify the calibrated values of particle to particle coefficients of sliding and rolling friction. The tester has two chambers with one directly above the other, the top chamber forms the drained angle of repose while the bottom chamber forms the poured angle of repose.

The double cell used had rectangular chambers with dimensions of 500 mm x 396 mm x 100 mm for the top chamber and 700 mm x 396 mm x 100 mm for the bottom chamber. Appendix C shows the detailed layout and dimensions of the double cell tester made of perspex wall material. The experimental procedure was carried out with two different depths of bulk material in the top cell. A depth of 50 mm was used for calibration purposes and another depth of 130 mm was used to observe how the obtained angles of repose vary with bed depth. The following experimental procedure was used to determine the double cell angles of repose:

1. The double cell tester was mounted on a flat surface.

2. The gate between the top and bottom cells of the double cell tester was closed.

3. A sample of the bulk material was placed into the top cell until an estimate of required depth was reached. A ruler was used to measure the depth of the material.

4. The bulk material was emptied into a bucket for use in subsequent tests.

This volume of material corresponded to the desired bulk material depth in the top cell.

5. The measured volume of bulk material from the bucket was poured into the top cell in one steady pour.

6. The bulk material in the top cell was carefully levelled.

7. The gate separating the top and bottom cells was rapidly opened allowing the bulk material to flow from the top cell to the bottom cell until it came to rest.

8. A photograph of the bulk material at rest recorded the drained angle of repose in the top cell, and the poured angle of repose in the bottom cell.

9. Steps (4) to (8) were conducted twice for each of the two upper cell depths of 50 mm and 130 mm.

10. The photos were downloaded onto a computer and imported into CAD software for measuring the angles of repose.

11. The average drained and poured angles of repose were calculated for the two repeat tests, for each of the two upper cell material depths (50 mm and 130 mm).

3.4 DEM Calibration Experimental Methods

This section covers the default DEM input parameters (box 3 in Figure 3.1), DEM particle shape and size distribution characterisation (box 4 in Figure 3.1), and the DEM experimental procedures conducted in LIGGGHTS to calibrate specific input parameters (box 5 in Figure 3.1). The calibration procedures covered are:

- bulk density tests to calibrate particle density,

- wall friction tests to calibrate particle to wall coefficient of sliding friction,
- full pipe and split pipe angle of repose tests to model equations relating the angles of repose to particle to particle friction coefficients,
- determination of the particle to particle friction coefficients from the model equations.
- double cell angle of repose tests to verify the obtained particle to particle friction coefficients,
- cohesion energy density calibration using the split pipe angle of repose, and
- adhesion energy density calibration using the inclined plane test to calibrate adhesion energy density.

The experimental procedures are arranged in a sequence which is such that the previously calibrated input parameters are used in the subsequent calibration tests. Figure 3.7 shows the specific DEM experimental methods covered in the context of the calibration framework of Figure 3.1.

3.4.1 DEM default input parameters

In the DEM simulations, the Young's Modulus and the Poisson's ratio were assigned default and literature solicited values respectively. The Young's Modulus value for the bulk material and wall surface material was set at a default value of 10^7 Pa in all the simulations. The value of this parameter affects the overall simulation time due to its relationship to the timestep; the lower the value, the shorter the simulation time. Lommen et al. (2014); Camborros et al. (2013); Zhou et al. (2001); Langston et al. (1995); Xu et al. (2002) in their investigations showed that the value could be reduced to 10^7 Pa without affecting the simulation results.

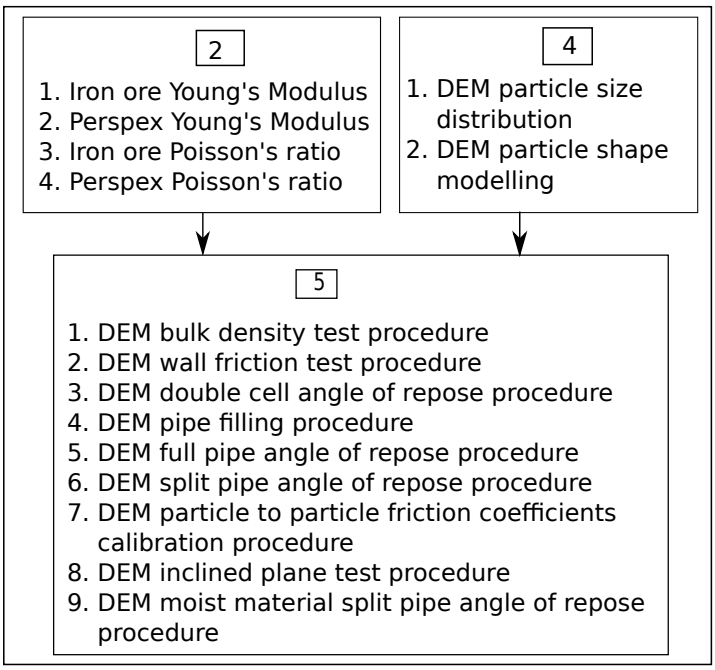


Figure 3.7: Calibration framework, DEM experimental procedures

Poisson's ratio for iron ore particles was set at 0.24 which was obtained from experimental tests by Asada and Omori (1983). The perspex Poisson's ratio was set at 0.37 which was obtained from the manufacturer's data sheet (Evonik-Industries, 2017). Based on Equation 2.28, and the values of Young's Modulus and Poisson's ratio given above, a timestep of 10^{-5} s was used in all the simulations. The timestep was monitored during simulations to ensure that its value was less than the maximum recommended value given by Equation 2.28. If the timestep exceeded the recommended value a warning message would be printed on the computer screen and the simulation stopped.

The Hertz contact model (Section 2.3.1) was used in all the simulations following the investigation of contact models performance carried out by Renzo and Maio (2004) where they found that the Hertz model gave results that were more realistic in comparison to the Hooke model. Being the only bonding model implemented LIGGGHTS, the JKR model was used to model cohesion and adhesion effects. Experiments used to calibrate frictional effects using dry material, were also used to calibrate cohesion and adhesion effects using cohesive material, based on the assumption that any increase in the response value of the material when using cohesive material was a function of cohesion alone.

3.4.2 DEM particle shape and size distribution

DEM bulk material particles are modelled to be as close as possible to physical bulk material particles. However, the accuracy of representation of DEM particle number, size and shape is limited by the available computational resources. As such, the number, size and shape of DEM particles differ from the actual physical bulk material particles so that simulations can be carried out within reasonable time frames. In LIGGGHTS, particles can either modelled as single spheres or clumped spheres. Clumped spheres, also known as multi-spheres, are single spheres combined to estimate the irregularity of real particles, hence they are more accurate than single spheres.

Based on Coetzee's findings Coetzee (2016), as reported earlier, a two clumped sphere was used in the DEM simulation. It consisted of a 3 mm diameter particle and a 1 mm diameter particle such that the combined particle had a bounding diameter of 4 mm. This was large enough to be simulated in a reasonable time frame, and is also within the range of 2 mm to 4.75 mm particle sizes of the real material. The reason for using only one clumped particle geometry was to facilitate the correct calculation of bulk density in Section 3.4.3. This choice was necessitated by the limitations of the simulation software used to correctly extract the number of each particle type in a container. As such, when using a different software package, it may be possible to accurately measure the bulk density with more than one clumped sphere.

Grima and Wypych (2011*b*) carried out a comprehensive investigation of DEM particle diameter scale up by approximate factors of two and three times the diameter of the physical particle, and concluded that the bulk material responses were comparable. Brummer (2010) investigated the effect of particle diameter scale up by factors of up to four times, and concluded that the resulting angles of repose remained constant. Based on these previous research results of particle diameter scale up, the use of 4 mm diameter to approximate all the size ranges in the physical material was considered to be adequate. See Section 4.2.1 and Figure 4.6 for more details.

3.4.3 DEM bulk density test procedure

The bulk density experimental procedure was carried out in DEM in order to calibrate the particle density, by enforcing equality between the DEM bulk density and the physically measured bulk density. Previous research showed that only particle density had a significant effect on the bulk density (Brummer, 2010; Horn, 2012) for a given particle size distribution. Since the PSD was fixed in Section 3.4.2, the use of bulk density to calibrate particle density was justified.

The DEM experimental procedure was performed at four different values of particle density while all the other input parameters were maintained constant. The four values of particle density used in the simulations were 2000 kg/m^3, 3000 kg/m^3, 4000 kg/m^3 and 5000 kg/m^3 respectively, where the particle density was expected to fall within this limiting range. These values were obtained by doing some preliminary test simulations. At each of the four values of particle density, the corresponding bulk density was obtained and recorded. An empirical equation was then developed that related DEM bulk density to DEM particle density using linear regression. In the empirical equation, the value of bulk density obtained in the physical experiment was inserted and the particle density solved for. The value of the obtained particle density became the calibrated particle density, because it enforced equality of the DEM and physical bulk densities.

Table 3.1 shows the input parameter settings used in the DEM bulk density tests, together with the approach used in their determination, the section outlining how they were determined, and the material state.

In the experiments, the particle to particle friction coefficients were assumed to have negligible effect on bulk density, hence were given default values of 0.5 each. The default value of 0.5 was chosen on the basis of being a mid-range value; this enables error minimisation in both directions in case the

Table 3.1: Input parameter settings, DEM bulk density tests

Input Parameter	**Value**	**Section**	**Material State**
$E_{particle}$ (MPa)	Literature	3.4.1	Dry
E_{wall} (MPa)	Literature	3.4.1	Dry
$\nu_{particle}$	Literature	3.4.1	Dry
ν_{wall}	Literature	3.4.1	Dry
ϵ_{pp}	Measured	3.3.1	Dry
ϵ_{pw}	Measured	3.3.1	Dry
$\mu_{pw,r}$	Measured	3.3.2	Dry
$\mu_{pw,s}$	Measured (Preliminary)	3.3.2	Dry
ρ_p (kg/m^3)	Being calibrated	-	Dry
$\mu_{pp,s}$	0.5	-	Dry
$\mu_{pp,r}$	0.5	-	Dry
ED_a (kJ/m^3)	0	-	Moist
ED_c (kJ/m^3)	0	-	Moist
Timestep (s)	10^{-5}	3.4.1	-

parameters do affect the bulk density. The validity of this assumption would later be checked in the sensitivity experiments. Adhesion and cohesion energy density were set at zero each since the material was dry.

As was highlighted in Section 2.7.1, a LIGGGHTS simulation was specified in an input file, which was read and executed by the software. In this DEM procedure, the following steps were followed:

1. The simulation domain was defined. This is the area in which the geometry is imported and particles are visible.

2. CAD geometry of the cylindrical container with a diameter of 95 mm and a height of 12 mm was imported as an stl file into the simulation domain. This container was the same as used in the physical experimental procedure in Section 3.3.5.

3. Bulk material particles were generated 5 mm above the container until the container was full to overflowing.

4. Excess material above the container rim was scraped off.

5. The simulation log file was opened, and the mass of a single clumped particle and the number of particles remaining in the container were recorded. The log file is automatically created and saved in the same directory as the input file every time a LIGGGHTS simulation is executed.

6. The total mass of the particles in the container was calculated by multiplying the number of particles and mass of a single particle read from the log file in step (5).

7. Bulk density of the DEM model material was calculated by dividing the total mass obtained in step (6) by volume of the cylindrical container in step (2), and recorded.

8. Steps (1) to (7) were conducted for each of the four values of particle density.

9. A graph was plotted of bulk density values obtained in step (7) against particle density values.

10. A linear best fit curve was fitted to the plotted data points and the linear equation relating bulk density to particle density computed.

11. The average bulk density obtained in the corresponding physical experiment was substituted into the equation obtained in step (10) and particle density solved for. The obtained particle density was then the calibrated particle density since it enforced equality between the simulated and physically measured bulk densities.

3.4.4 DEM wall friction test procedure

The DEM wall friction test experimental procedure was carried out in order to calibrate the particle to wall coefficient of sliding friction, by enforcing equality between the DEM angle of wall friction and the physically measured angle of wall friction.

Table 3.2 shows the parameter settings used in the DEM wall friction tests, together with the approach used in their determination, the section outlining how they were determined, and the material state.

Table 3.2: Input parameter settings, DEM wall friction tests

Input Parameter	**Value**	**Section**	**Material State**
$E_{particle}$ (MPa)	Literature	3.4.1	Dry
E_{wall} (MPa)	Literature	3.4.1	Dry
$\nu_{particle}$	Literature	3.4.1	Dry
ν_{wall}	Literature	3.4.1	Dry
ϵ_{pp}	Measured	3.3.1	Dry
ϵ_{pw}	Measured	3.3.1	Dry
$\mu_{pw,r}$	Measured	3.3.2	Dry
$\mu_{pw,s}$	Being calibrated	-	Dry
ρ_p (kg/m^3)	Calibrated	3.4.3	Dry
$\mu_{pp,s}$	0.5	-	Dry
$\mu_{pp,r}$	0.5	-	Dry
ED_a (kJ/m^3)	0	-	Moist
ED_c (kJ/m^3)	0	-	Moist
Timestep (s)	10^{-5}	3.4.1	-

The experimental procedure was performed at four different values of particle to wall coefficient of sliding friction. These values were 0.2, 0.4, 0.6 and 0.9. At each of the four values, the angle of DEM wall friction was obtained from the simulation. Linear regression was then used to develop an empirical equation (polynomial) relating the DEM angle of wall friction to the particle to particle coefficient of sliding friction. From the empirical equation, the value of particle to wall coefficient of sliding friction corresponding to a desired angle of wall friction could then be easily calculated. Therefore, by inserting the physically measured angle of wall friction into the empirical equation, the particle to wall coefficient of sliding friction that would enforce equality of DEM and physical angles of wall friction was determined. That value of particle to wall coefficient of sliding friction became the calibrated parameter value.

The detailed experimental procedure as specified in the LIGGGHTS input file was as follows:

1. The simulation domain was defined.

2. The shear ring and wall surface material CAD geometries were imported into the simulation domain. The dimensions of the shear ring and wall surface material were the same as used in the corresponding physical experiment in Section 3.3.6.

3. Bulk material particles were generated 5 mm above the shear ring until the ring was full to overflowing.

4. Excess bulk material above the shear ring rim was scraped off.

5. The lid CAD geometry was imported into the domain, and the shear ring covered with the lid.

6. The wall liner material was moved relative to the shear ring by specifying a velocity of 25 mm/minute. This value was ten times the shearing velocity used in the physical experiment. The scale up was done to speed up the simulation. Grima et al. (2011) scaled up the shearing rate by 100 and then by 1000 and concluded that the reduction in wall friction angle was insignificant.

7. The cumulative simulation time, normal force acting on the lid and the shear force acting on the wall surface material were saved into a csv spreadsheet file at each timestep.

8. The simulation was executed until the shear force reached a steady value.

9. Using the saved csv file in step (7), the normal and shear stresses were calculated at each timestep. Stresses were calculated by dividing the forces by the cross sectional area of the shear ring.

10. A graph of shear stress as a function of displacement was plotted. Displacement was calculated by multiplying the saved cumulative time by shear speed.

11. With the aid of the plotted graph of shear stress against displacement, the average shear stress for data points in the region of almost constant shear stress (limiting shear stress) was calculated and recorded.

12. The average normal stress of the data points corresponding to the chosen region of constant shear stress was calculated and recorded. The value of normal stress was higher than the applied stress because it included weight of the material above the shear plane.

13. Steps (1) to (11) were conducted for each of the applied normal forces (Step 5) of 14.72 N, 34.34 N, 54.96 N and 73.58 N. These normal forces corresponded to masses in kilograms of 1.5, 3.5, 5.5 and 7.5 respectively, that were used in the corresponding physical experiment.

14. A graph of the average shear stress obtained in step (11) was plotted against average normal stress obtained in step (12) for each of the four applied normal force cases.

15. Using the linear regression method, a linear curve was fitted to the plotted graph.

16. The gradient of the above fitted curve was calculated. The obtained gradient was the tangent of the angle of wall friction as given by Equation 2.29. The angle of wall friction was recorded.

17. Steps (1) to (16) were conducted for each of the four particle to wall coefficient of sliding friction values.

18. A graph of the angle of wall friction in step (16) was plotted against the particle to wall coefficient of sliding friction. Using the linear regression method, empirical equations relating the angle of wall friction to the particle to wall coefficient of sliding friction were developed by fitting first and second order polynomial equations. The goodness of fit parameter for each of the two equations was evaluated and the best fit equation selected for use in the DEM calibration.

19. The calibrated value of the particle to wall coefficient of sliding friction was determined by inserting the physically measured value of the angle wall friction into the empirical equation and solving for the particle to wall coefficient of sliding friction.

3.4.5 DEM pipe filling procedure

The DEM pipe filling procedure was carried out to fill a pipe with an internal diameter of 94 mm and a height of 140 mm with the DEM bulk particles. The output file from the simulation was then saved as a binary restart file for use in the full pipe and split pipe angle of repose DEM calibration experiments. This approach was taken because it eliminated the pipe filling time in the subsequent pipe repose experiments.

Table 3.3 shows the input parameter settings used in the DEM pipe filling procedure, together with the approach used in their determination, the section outlining how they were determined, and the material state.

Table 3.3: Input parameter settings, DEM pipe filling

Input Parameter	**Value**	**Section**	**Material State**
$E_{particle}$ (MPa)	Literature	3.4.1	Dry
E_{wall} (MPa)	Literature	3.4.1	Dry
$\nu_{particle}$	Literature	3.4.1	Dry
ν_{wall}	Literature	3.4.1	Dry
ϵ_{pp}	Measured	3.3.1	Dry
ϵ_{pw}	Measured	3.3.1	Dry
$\mu_{pw,r}$	Measured	3.3.2	Dry
$\mu_{pw,s}$	Calibrated	3.4.4	Dry
ρ_p (kg/m^3)	Calibrated	3.4.3	Dry
$\mu_{pp,s}$	Being calibrated	-	Dry
$\mu_{pp,r}$	Being calibrated	-	Dry
ED_a (kJ/m^3)	0	-	Moist
ED_c (kJ/m^3)	0	-	Moist
Timestep (s)	10^{-5}	3.4.1	-

Adhesion and cohesion energy density were set at zero because the material was dry. The detailed procedure as specified in the LIGGGHTS input file was as follows:

1. The simulation domain.

2. The three dimensional CAD geometries of the pipe and pedestal were imported into the simulation domain.

3. Bulk material particles were generated 5 mm above the pipe and allowed to fill the pipe to overflow. The material was scraped level with the pipe rim.

4. The state of the simulation at the end of step (3) was saved as a binary LIGGGHTS restart file.

3.4.6 DEM full pipe angle of repose procedure

The DEM full pipe experimental procedure was carried out to simulate and measure the angles of repose at CCD sampled points in Table 3.4, and establish empirical equations relating the full pipe poured angle of repose to the particle to particle coefficients of sliding and rolling friction. See Appendix I.1 for the CCD sampling procedure.

Table 3.5 shows the input parameter settings used in the DEM full pipe angle of repose procedure, together with the approach used in their determination, the section outlining how they were determined, and the material state.

Adhesion and cohesion energy density were set at zero each since the material was dry. The detailed procedure as specified in the LIGGGHTS input file was as follows:

1. The saved binary restart file (Section 3.4.5) with the full pipe filled with DEM particles was imported.

2. The pipe was slowly lifted allowing the DEM bulk material to flow from

Table 3.4: CCD sample points

Sample Point Number	$\mu_{pp,s}$	$\mu_{pp,r}$
1	0.18	0.60
2	0.30	0.30
3	0.30	0.90
4	0.60	0.18
5	0.60	0.60
6	0.60	1.00
7	0.90	0.30
8	0.90	0.90
9	1.00	0.60

Table 3.5: Input parameter settings, DEM full pipe repose tests

Input Parameter	**Value**	**Section**	**Material State**
$E_{particle}$ (MPa)	Literature	3.4.1	Dry
E_{wall} (MPa)	Literature	3.4.1	Dry
$\nu_{particle}$	Literature	3.4.1	Dry
ν_{wall}	Literature	3.4.1	Dry
ϵ_{pp}	Measured	3.3.1	Dry
ϵ_{pw}	Measured	3.3.1	Dry
$\mu_{pw,r}$	Measured	3.3.2	Dry
$\mu_{pw,s}$	Calibrated	3.4.4	Dry
ρ_p (kg/m^3)	Calibrated	3.4.3	Dry
$\mu_{pp,s}$	Being calibrated	-	Dry
$\mu_{pp,r}$	Being calibrated	-	Dry
ED_a (kJ/m^3)	0	-	Moist
ED_c (kJ/m^3)	0	-	Moist
Timestep (s)	10^{-5}	3.4.1	-

underneath, until the pipe was clear of the bulk material. The step was achieved by specifying a linear velocity on the pipe of 5 mm/s in the vertical direction. A velocity of 5 mm/s was a rough estimate obtained from timing the lifting of the real pipe and was low enough not to induce vertically upwards velocity of particles in contact with the pipe.

3. The simulation was executed until the total kinetic energy of the particles had fallen below 10^{-8} J.

4. The simulation state was saved and opened in Paraview. The simulation snapshot in Paraview was saved as a png picture file.

5. The png file was imported into CAD software and the poured angles of repose measured. Two poured angles of repose were measured on the opposite sides of the heap.

6. The average full pipe poured angle of repose was calculated and recorded.

7. Steps (1) to (6) were conducted for all the nine parameter combinations in the CCD table.

8. A three dimensional graph of the angle of repose against the particle to particle coefficients of sliding and rolling friction was plotted.

9. First and second order response surface equations were fitted to the data points, using the response surface methodology described in Section 2.10 and implemented in Python as documented in Appendix A.5. The goodness of fit of each equation was evaluated.

10. The response surface equation that best fitted the data was selected and documented for use in the calibration of the particle to particle coefficients of sliding and rolling friction.

3.4.7 DEM split pipe angle of repose procedure, dry

The DEM split pipe experimental procedure was carried out to simulate and measure the split pipe angles of repose at CCD sampled points in Table 3.4. The data obtained from the simulations was then used to establish empirical equations relating the split pipe poured angle of repose to the particle to particle coefficients of sliding and rolling friction. Table 3.6 shows the input

parameter settings used in the DEM split pipe angle of repose procedure, together with the approach used in their determination, the section outlining how they were determined, and the material state.

Table 3.6: Input parameter settings, DEM split pipe repose tests

Input Parameter	**Value**	**Section**	**Material State**
$E_{particle}$ (MPa)	Literature	3.4.1	Dry
E_{wall} (MPa)	Literature	3.4.1	Dry
$\nu_{particle}$	Literature	3.4.1	Dry
ν_{wall}	Literature	3.4.1	Dry
ϵ_{pp}	Measured	3.3.1	Dry
ϵ_{pw}	Measured	3.3.1	Dry
$\mu_{pw,r}$	Measured	3.3.2	Dry
$\mu_{pw,s}$	Calibrated	3.4.4	Dry
ρ_p (kg/m^3)	Calibrated	3.4.3	Dry
$\mu_{pp,s}$	Being calibrated	-	Dry
$\mu_{pp,r}$	Being calibrated	-	Dry
ED_a (kJ/m^3)	0	-	Moist
ED_c (kJ/m^3)	0	-	Moist
Timestep (s)	10^{-5}	3.4.1	-

Adhesion and cohesion energy density were set at zero each since the material was dry. The detailed procedure as specified in the LIGGGHTS input file was as follows:

1. The saved binary restart file with the full pipe filled with DEM particles was imported.

2. The pipe was deleted from the simulation, allowing the bulk material to slump and form a heap.

3. The simulation was executed until the total kinetic energy of the particles had fallen below 10^{-8} J.

4. The simulation state was saved and opened in Paraview. The simulation snapshot in Paraview was saved as a png picture file.

5. The png file was imported into CAD software and the poured angles of repose measured. Two poured angles of repose were measured on the opposite sides of the heap.

6. The average split pipe poured angle of repose was calculated and recorded.

7. Steps (1) to (6) were conducted for all the nine parameter combinations in the CCD table.

8. A three dimensional graph of the angle of repose against the particle to particle coefficients of sliding and rolling friction was plotted.

9. First and second order response surface equations were fitted to the data points, using the response surface methodology described in Section 2.10 and implemented in Python as documented in Appendix A.6. The goodness of fit of each equation was evaluated.

10. The response surface equation that best fitted the data was selected and documented for use in the calibration of the particle to particle coefficients of sliding and rolling friction.

3.4.8 DEM particle to particle friction coefficients calibration procedure

The DEM particle to particle friction calibration procedure was carried out to calibrate the particle to particle coefficients of sliding and rolling friction. This was achieved by solving simultaneously the two empirical equations obtained in the methods of Section 3.4.6 and Section 3.4.7.

The empirical equations obtained for the calibration of the particle to particle coefficients of sliding and rolling friction were functions of two independent variables. Therefore in order to solve for the independent variables, two equations were needed to be simultaneously solved. The values of the particle to

particle coefficients of sliding and rolling friction obtained from solving the equations were the calibrated parameter values. The following detailed procedure was used:

1. The angles of repose in the equations were substituted by angle of repose values obtained in the equivalent physical angle of repose experiments. This enforced equality between the DEM angle of repose and the physically measured angle of repose.

2. The equations were solved simultaneously to obtain the values of particle to particle coefficients of sliding and rolling friction that would result in the DEM and physical angles of repose being equal. The obtained values were the calibrated parameter values.

3.4.9 DEM double cell angle of repose procedure

The DEM double cell experimental procedure was carried out to verify the calibrated values of particle to particle coefficients of sliding and rolling friction obtained in Section 3.4.8. The double cell experiment was set up in DEM using equipment with the same dimensions as the one used in the equivalent physical experiment. Table 3.7 shows the input parameter settings used in the DEM double cell angle of repose procedure, together with the approach used in their determination, the section outlining how they were determined, and the material state.

Adhesion and cohesion energy density were set at zero each since the material was dry. The detailed procedure as specified in the LIGGGHTS input file was as follows:

1. The simulation domain was defined.

2. The three dimensional CAD geometries of the double cell equipment were imported into the simulation domain.

Table 3.7: Input parameter settings, DEM double cell repose tests

Input Parameter	**Value**	**Section**	**Material State**
$E_{particle}$ (MPa)	Literature	3.4.1	Dry
E_{wall} (MPa)	Literature	3.4.1	Dry
$\nu_{particle}$	Literature	3.4.1	Dry
ν_{wall}	Literature	3.4.1	Dry
ϵ_{pp}	Measured	3.3.1	Dry
ϵ_{pw}	Measured	3.3.1	Dry
$\mu_{pw,r}$	Measured	3.3.2	Dry
$\mu_{pw,s}$	Calibrated	3.4.4	Dry
ρ_p (kg/m^3)	Calibrated	3.4.3	Dry
$\mu_{pp,s}$	Calibrated	3.4.6	Dry
$\mu_{pp,r}$	Calibrated	3.4.7	Dry
ED_a (kJ/m^3)	0	-	Moist
ED_c (kJ/m^3)	0	-	Moist
Timestep (s)	10^{-5}	3.4.1	-

3. Bulk material particles were generated 5 mm above the top cell of the double cell, and the material scraped level at a depth of 50 mm.

4. The state of the simulation at the end of step (3) was saved as a binary LIGGGHTS restart file. A restart file is used in LIGGGHTS to save the state of a simulation, and reuse it as input into another simulation or use it to continue the same simulation.

5. The restart file was imported into another LIGGGHTS simulation.

6. The gate separating the top and double cells was instantaneously opened by deleting it from the simulation domain.

7. The simulation was executed until the total kinetic energy of the particles had fallen below 10^{-8} J.

8. The simulation state was saved and opened in Paraview. The simulation snapshot in Paraview was saved as a png picture file.

9. The png file was imported into CAD software and the drained angles of repose in the top cell and the poured angles of repose in the bottom cell measured. There were two drained angles of repose, one on each side of the gate. Two poured angles of repose were also measured on the opposite sides of the heap in the bottom cell.

10. The average drained angle of repose and average poured angle of repose were calculated and recorded.

11. The average drained and poured angles of repose were compared to the physically measured values in Section 3.3.9.

3.4.10 DEM inclined plane test procedure, moist

The DEM inclined plane test was carried out with moist material to calibrate adhesion energy density. Adhesion energy density measures the strength of the bond between the bulk material and the wall surface. This was achieved by simulating the angle at which a single particle began to slide on the inclined plane with perspex wall surface, at seven values of the adhesion energy density of 0 kJ/m^3, 5 kJ/m^3, 10 kJ/m^3, 15 kJ/m^3, 20 kJ/m^3, 25 kJ/m^3 and 30 kJ/m^3. The range was determined by conducting some preliminary tests. An empirical relationship was developed relating the angle at which the moist particle began to slide and the adhesion energy density. The empirical equation was then used to calculate the adhesion energy when the angle at which sliding commenced was equal to that measured physically. The obtained adhesion energy density is the calibrated value because it enforced equality between the DEM and physically measured angle at which a moist particle begins to slide.

This procedure must only be used after the particle to wall coefficient of sliding friction has been calibrated. This means, any difference between the angle at which a wet particle commences to slide and the angle at which a dry particle begins to slide is a function of adhesion.

Table 3.8 shows the input parameter settings used in the DEM inclined plane test procedure, together with the approach used in their determination, the section outlining how they were determined, and the material state.

Table 3.8: Input parameter settings, DEM adhesion energy density tests

Input Parameter	**Value**	**Section**	**Material State**
$E_{particle}$ (MPa)	Literature	3.4.1	Dry
E_{wall} (MPa)	Literature	3.4.1	Dry
$\nu_{particle}$	Literature	3.4.1	Dry
ν_{wall}	Literature	3.4.1	Dry
ϵ_{pp}	Measured	3.3.1	Dry
ϵ_{pw}	Measured	3.3.1	Dry
$\mu_{pw,r}$	Measured	3.3.2	Dry
$\mu_{pw,s}$	Calibrated	3.4.4	Dry
ρ_p (kg/m^3)	Calibrated	3.4.3	Dry
$\mu_{pp,s}$	Calibrated	3.4.8	Dry
$\mu_{pp,r}$	Calibrated	3.4.8	Dry
ED_a (kJ/m^3)	Being calibrated	-	Moist
ED_c (kJ/m^3)	0	-	Moist
Timestep (s)	10^{-5}	3.4.1	-

Cohesion energy density was set to zero since only one moist particle was used. The detailed procedure as specified in the LIGGGHTS input file was as follows:

1. The simulation domain was defined.

2. The three dimensional geometry of the inclinometer was imported into the simulation domain. The surface of the inclinometer was normal to the vertical direction.

3. A single DEM particle was generated above the inclinometer and let to drop and come to rest on the inclinometer surface

4. The inclinometer was rotated about an axis parallel to its surface at a rotation period of 300 s until the particle slid off the inclinometer. The rotation period was approximated by timing the rotation rate of the physical inclinometer test so as to minimise any inertial effects.

5. As the rotation proceeded, the rotation angle and kinetic energy of the particle were logged in a csv spreadsheet file.

6. At the end of the simulation, the csv file was opened and a graph of kinetic energy against inclination angle plotted.

7. The angle at which sliding commenced was determined. The angle corresponded to the point at which the kinetic energy rapidly increased as the particle started sliding.

8. Steps (1) to (7) were conducted for each value of the six values of adhesion density. These values were reached at by conducting trial runs, so that the actual adhesion energy density is bracketed by the minimum and maximum values.

9. A graph of the angle at which sliding commenced was plotted against the adhesion energy density.

10. First order and a second order polynomial equations were fitted to the plotted data using linear regression and the goodness of fit evaluated.

11. The empirical equation that best fitted the data was selected.

12. The adhesion energy density was determined by substituting the physically measured angle of inclination of a moist particle into the equation. The value of adhesion energy density obtained was the calibrated parameter value.

3.4.11 DEM split pipe angle of repose procedure, moist

The DEM split pipe experimental procedure was carried out for moist material to simulate and measure the split pipe angles of repose at seven values of cohesion energy density of 75 kJ/m^3, 100 kJ/m^3, 125 kJ/m^3, 150 kJ/m^3, 175 kJ/m^3, 200 kJ/m^3 and 225 kJ/m^3. The range was determined by carrying out

preliminary tests. The data obtained from the simulations was then used to establish empirical equations relating the split pipe poured angle of repose of moist material to the cohesion energy density, and calibrate cohesion energy density.

It should be noted that this procedure requires the particle to particle coefficients of sliding and rolling friction to have been calibrated with dry bulk material. It would therefore mean any changes in the angle of repose between the dry and moist material is a result of cohesion. Gröger and Katterfield (2006) established that the angle of repose is a function of inter-particle friction and cohesion.

Table 3.9 shows the input parameter settings used in the DEM split pipe angle of repose procedure, together with the approach used in their determination, the section outlining how they were determined, and the material state.

Table 3.9: Input parameter settings, DEM cohesion energy density tests

Input Parameter	**Value**	**Section**	**Material State**
$E_{particle}$ (MPa)	Literature	3.4.1	Dry
E_{wall} (MPa)	Literature	3.4.1	Dry
$\nu_{particle}$	Literature	3.4.1	Dry
ν_{wall}	Literature	3.4.1	Dry
ϵ_{pp}	Measured	3.3.1	Dry
ϵ_{pw}	Measured	3.3.1	Dry
$\mu_{pw,r}$	Measured	3.3.2	Dry
$\mu_{pw,s}$	Calibrated	3.4.4	Dry
ρ_p (kg/m^3)	Calibrated	3.4.3	Dry
$\mu_{pp,s}$	Calibrated	3.4.8	Dry
$\mu_{pp,r}$	Calibrated	3.4.8	Dry
ED_a (kJ/m^3)	Calibrated	3.4.10	Moist
ED_c (kJ/m^3)	Being calibrated	-	Moist
Timestep (s)	10^{-5}	3.4.1	-

The detailed procedure as specified in the LIGGGHTS input file was as follows:

1. The saved binary restart file with the full pipe filled with DEM particles was imported.

2. The pipe from the simulation was deleted allowing the bulk material to slump and form a heap.

3. The simulation was executed until the total kinetic energy of the particles had fallen below 10^{-8} J.

4. The simulation state was saved and opened in Paraview. The simulation snapshot in Paraview was saved as a png picture file.

5. The png file was imported into CAD software measure the poured angles of repose measured. Two poured angles of repose were measured on the opposite sides of the heap.

6. The average split pipe poured angle of repose was calculated and recorded.

7. Steps (1) to (7) were repeated for each value of the six values of cohesion density.

8. A graph of the average split pipe angle of repose against cohesion energy density was plotted.

9. First order and a second order polynomial equations were fitted to the plotted data using linear regression and the goodness of fit evaluated.

10. The empirical equation that best fitted the data was selected.

11. The cohesion energy density was determined by substituting the physically measured split pipe angle of repose of moist material into the equation. The value of cohesion energy density obtained was the calibrated parameter value.

3.5 Physical Validation Experimental Methods

This section covers the physical experimental methods for validating the calibrated DEM input parameters. Validation experiments were conducted in order to verify the capability of the calibrated DEM input parameters to predict the behaviour of bulk material under the quasi-static and dynamic flow regimes for dry and moist iron ore. Experiments were conducted in geometries that were different from the ones used during the calibration process.

The experimental procedures carried out were silo flow to simulate the quasi-static flow regime, and chute flow to simulate the dynamic flow regime. Experimental work on the silo involved measuring the dry and moist bulk material mass flow rates and flow profiles. Work on the chute involved measuring the chute flow profiles, and the mass of dry and moist bulk material that remained on the chute after flow had ceased. To aid the entrapment of material in the chute, two ledges with 8 mm protrusions were installed at bottom of the chute as shown in Appendix C.

3.5.1 Validation test equipment

A test frame was designed and fabricated for the purpose of suspending a silo in the upper section and a chute in the lower section. The silo was suspended in the upper section of the frame from a 100 kg rated loadcell. The loadcell was attached to the top middle cross member of the frame through a bolt. Figure 3.8 shows the schematic of the assembled test equipment. The layout and dimensions of the frame are shown in Appendix C. The specifications of the loadcell are given in Appendix N.3.

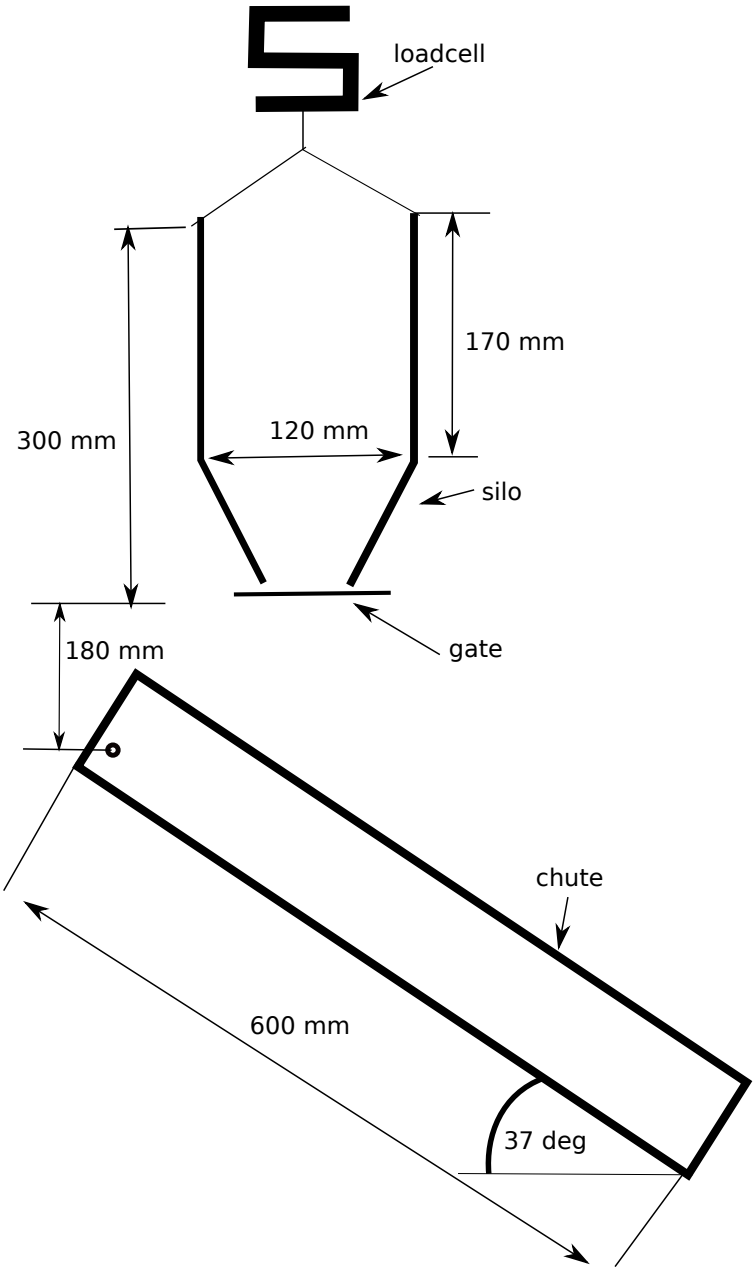


Figure 3.8: Silo and chute setup

3.5.2 Physical silo flow test procedure

The silo flow experimental procedure was carried out in order to measure the mass flow rate of the bulk material discharging from a silo, and to observe the flow profiles. The results were then compared to an equivalent DEM experiment, in order verify the capability of the calibrated DEM parameters to predict the behaviour of the bulk material under the quasi-static flow regime. The procedure was used with dry bulk material in which cohesion and adhesion were negligible, and was also carried out on moist material where cohesion and adhesion have a significant effect.

The silo used had the rectangular section having cross sectional dimensions of 120 mm x 184 mm and a height of 170 mm while the lower inverted truncated triangular prism had an opening with dimensions of 20 mm x 120 mm and a height of 130 mm. The detailed layout and dimensions of the silo are given in Appendix C. The detailed experimental procedure was as follows:

1. The loadcell was attached to the steel frame.

2. The loadcell output was connected to the amplifier, and the amplifier output connected to the data acquisition system.

3. A hook was attached on the lower end of the loadcell.

4. The empty silo together with the bottom opening gate were placed on the scale and their mass recorded. The scale had a resolution of ± 0.1 g.

5. The silo gate was closed before the bulk material sample was filled to a depth of 75 mm for dry material, and 60 mm for moist bulk material, measured from the hopper/silo transition. The bulk material was levelled. 60 mm depth for moist material was equivalent to all the available moist material.

6. The silo with bulk material was placed on the scale and the mass of the bulk material and silo recorded.

7. The mass of iron ore in the silo was determined by subtracting the mass obtained in step (4) from the mass obtained in (6).

8. The silo with iron ore was suspended from the loadcell, while the bottom opening was closed by an externally supported gate.

9. A video camera was set focusing on the silo.

10. The data acquisition system and the video camera were started. The gate at the silo bottom was rapidly pulled away allowing the bulk material to exit the silo.

11. When the silo was empty, the data acquisition system and the video camera were stopped.

12. The data acquisition file made up of time and voltage columns was saved as a csv spreadsheet file. The voltage readings were converted into mass values by using Equation N.1, obtained during loadcell linearity calibration. The mass values represented the instantaneous mass of the bulk material remaining in the silo.

13. A graph of mass against time was plotted. A line of best fit was fitted in the region where the rate of mass decrease was linear.

14. The loadcell measured mass flow rate (instantaneous) was determined as being equal to the magnitude of the gradient of the best fit line.

15. The video from the camera was downloaded into a computer and opened in an editing software. The video was run in the editing software frame to frame using the forward control button. The times at which the silo started discharging and the time at which it stopped discharging were recorded.

16. The total discharge time was determined by subtracting the time at which the silo started discharging from the time at which it stopped

discharging. The total silo discharge time was also estimated from the graph plotted in step (13), as the time at which the mass recorded by the loadcell remained constant.

17. The average mass flow rate from scale and video measurements was determined by dividing the total mass of bulk material in step (7) by the discharge time in step (16).

18. The flow profiles of the bulk material in the silo were captured by taking snapshots of the simulation state when the silo was full, three quarter full, half full, one quarter full and one eighth full.

19. Steps (5) to (18) were conducted three times.

20. The average mass flow rate from the three tests was calculated.

3.5.3 Physical chute flow test procedure

The chute flow experimental procedure was carried out to determine the flow profiles in the chute, and the mass of material that remained in the chute after flow had stopped. The experiment was conducted twice, with dry bulk material and then with moist bulk material. The results were then compared to an equivalent DEM experiment, in order verify the capability of the calibrated DEM parameters to predict the behaviour of the bulk material in a dynamic flow regime.

The layout and dimensions of the chute are shown in Appendix C. An angle of inclination of 37 ^{o} to the horizontal was maintained in all the chute flow experiments. The angle was reached after preliminary tests to the minimum angle that allowed rapid flow in the chute, while retaining some material trapped by the ledges after flow had stopped.

The detailed experimental procedure used was as follows:

1. The chute was placed on the scale and the mass recorded. The scale had a resolution of ±0.1 g

2. The chute was attached to the steel frame using a pin that allowed it to rotate and be preset at different inclinations. It was inclined at 37 ° to the horizontal.

3. The silo discharge point was located directly above the top end of the chute.

4. Iron ore sample was placed into the silo while the outlet was closed by an externally supported gate.

5. A video camera was set focused on the chute, and started.

6. The silo gate was opened allowing the bulk material to flow into the chute, and out of the chute at the bottom end.

7. When the silo was empty and the bulk material in the chute was stationary, the video camera was stopped, and the chute carefully removed from the test frame. The chute with bulk material was placed on the scale to measure the mass of the bulk material and the chute.

8. The mass of the bulk material remaining in the chute was determined by subtracting the mass recorded in step (1) from mass recorded in step (7).

9. The flow profiles of the bulk material in the chute during steady state flow and after flow had stopped were captured by taking flow snapshots during steady state flow and when flow has ceased.

10. Steps (2) to (9) were conducted twice.

11. The average remaining mass in the chute from the two tests was calculated and recorded.

3.6 DEM Validation Experimental Methods

This section outlines the DEM experimental procedures used to validate the capability of the calibrated input parameters to predict the flow of bulk materials. The procedures discussed include bulk material flow in the silo and chute. Mass flow rate and flow profiles were measured in the case of silo flow, while flow profiles and the mass of material remaining in the chute were measured for chute flow.

3.6.1 DEM silo flow test procedure

The DEM silo flow procedure was carried out to determine the mass flow rate and flow profiles of the DEM bulk material sample in a silo. The obtained flow rate and flow profiles were then compared to the equivalent physical experiments. This procedure served to verify if the method used for calibration of DEM input parameters yielded values that could correctly predict bulk material flow under quasi-static flow regime. The experimental procedure was conducted with both dry and moist iron ore.

Table 3.10 shows the sources of input parameter settings used in the DEM silo flow validation procedure, together with the approach used in their determination, the section outlining how they were determined, and the material state.

The calibrated adhesion and cohesion energy density were only used when simulating moist material: in the simulations of dry material, the parameters were set to zero. The detailed procedure as specified in the LIGGGHTS input file was as follows:

1. The simulation domain was defined.

2. The silo and gate CAD geometries were imported into the simulation domain. The dimensions of the silo were the same as used in the equivalent physical experiment.

Table 3.10: Input parameter settings, DEM silo and chute flow tests

Input Parameter	**Value**	**Section**	**Material State**
$E_{particle}$ (MPa)	Literature	3.4.1	Dry
E_{wall} (MPa)	Literature	3.4.1	Dry
$\nu_{particle}$	Literature	3.4.1	Dry
ν_{wall}	Literature	3.4.1	Dry
ϵ_{pp}	Measured	3.3.1	Dry
ϵ_{pw}	Measured	3.3.1	Dry
$\mu_{pw,r}$	Measured	3.3.2	Dry
$\mu_{pw,s}$	Calibrated	3.4.4	Dry
ρ_p (kg/m^3)	Calibrated	3.4.3	Dry
$\mu_{pp,s}$	Calibrated	3.4.8	Dry
$\mu_{pp,r}$	Calibrated	3.4.8	Dry
ED_a (kJ/m^3)	Calibrated	3.4.10	Moist
ED_c (kJ/m^3)	Calibrated	3.4.11	Moist
Timestep (s)	10^{-5}	3.4.1	-

3. Bulk material particles were generated at 5 mm above the silo and scraped level to a depth of 75 mm for dry bulk material and 60 mm for moist bulk material, to match the physical experiment.

4. The gate was instantaneously deleted from the simulation to allow the DEM bulk material to be discharged from the silo.

5. The state of the simulation was saved in a binary file while the number of particles remaining in the silo with time was saved in a csv spreadsheet file.

6. The simulation was executed until the silo was empty.

7. The saved csv spreadsheet file was opened and the mass remaining in the silo at each time instance calculated by multiplying the number of particles by the mass of a single particle. The mass of a single particle was found in the log file that automatically gets created when a LIGGGHTS simulation executes.

8. A graph of the mass remaining in the silo against time was plotted. A line of best fit was fitted in the middle of the plot.

9. The mass flow rate of the bulk material as being equal to the magnitude of the gradient of the best fit line.

10. The binary file saved in step (5) was opened in Paraview for simulation visualisation.

11. The visualisation was run one step at a time using the forward control button. The snapshots of the simulation were saved as png picture files when the silo was full, three quarter full, half full, one quarter full and one eighth full.

12. The obtained mass flow rate was compared to that obtained in the equivalent physical experiment.

13. The flow profiles were compared to those at obtained in the equivalent physical experiment.

3.6.2 DEM chute flow test procedure

The DEM chute flow procedure was carried out to determine the flow profiles and remaining mass of the DEM bulk material after flow had stopped in a chute with two ledges. The obtained flow profiles and remaining mass of the DEM bulk material were then compared to the equivalent physical experiments. This procedure served to verify if the method used for calibration of DEM input parameters yielded values that could correctly predict bulk material flow under the dynamic flow regime.

The experimental procedure was used with both dry and moist material. Table 3.10 shows the procedures used to obtain input parameter values used in the DEM chute flow validation test. The calibrated adhesion and cohesion energy density were only used when simulating moist material, in simulations of dry material, the parameters were set to zero.

The detailed procedure as specified in the LIGGGHTS input file was as follows:

1. The simulation domain was defined.

2. The chute, silo and stopper CAD geometries were imported into the simulation domain. The dimensions of the chute and silo were the same as used in the equivalent physical experiment.

3. Bulk material particles were generated 5 mm above the silo and scraped level to a depth of 75 mm for dry bulk material and 60 mm for moist bulk material.

4. The gate was instantaneously deleted from the simulation allowing the DEM bulk material to be discharged from the silo into the chute, and out of the chute.

5. The state of the simulation was saved in a binary file while the number of particles remaining in the simulation with time was saved in a csv spreadsheet file.

6. The simulation was executed until the silo was empty, and the total kinetic energy of particles on the chute have gone below 10^{-8} J.

7. The saved csv file was opened and the mass remaining in the chute at each time instance determined by multiplying the number of particles by the mass of a single particle. The mass of a single particle was found in the log file that automatically gets created when a LIGGGHTS simulation executes.

8. The mass of the bulk material remaining in the chute after flow had stopped was determined as being equal to the computed mass at the end of the csv file in step (7)

9. The binary file saved in step (5) was opened in Paraview to visualise the simulation.

10. The visualisation was run one step at a time using the forward control button. The snapshots of the simulation were saved as png picture files during steady state flow, and when the flow had stopped.

11. The obtained mass of the remaining bulk material on the chute was compared to that obtained in the equivalent physical experiment.

12. The flow profiles were compared to those obtained in the equivalent physical experiment.

4 Data Processing and Results

This chapter covers data processing and results of the physical and DEM experiments carried out using the methods described in Chapter 3. The results are organised into four main sections, namely the physical calibration experimental results in Section 4.1, the DEM calibration experimental results in Section 4.2, the physical validation experimental results in Section 4.3 and the DEM validation experimental results in Section 4.4.

4.1 Physical Calibration Experimental Results

This section presents data processing and results of the physical calibration experiments. Results are presented starting with experiments that directly measure the input parameter values (box 1 in Figure 3.1), ending with the results of experiments that calibrate input parameters through specific bulk material responses (box 3 in Figure 3.1). Figure 4.1 shows the covered experimental results in the context of the calibration framework of Figure 3.1.

4.1.1 Coefficient of restitution test results

The coefficient of restitution tests were carried out to measure the particle to particle coefficient of restitution and particle to wall surface coefficient of restitution, using the procedure described in Section 3.3.1. The recorded number of valid tests were 43 and 27 for particle to wall surface and particle to particle

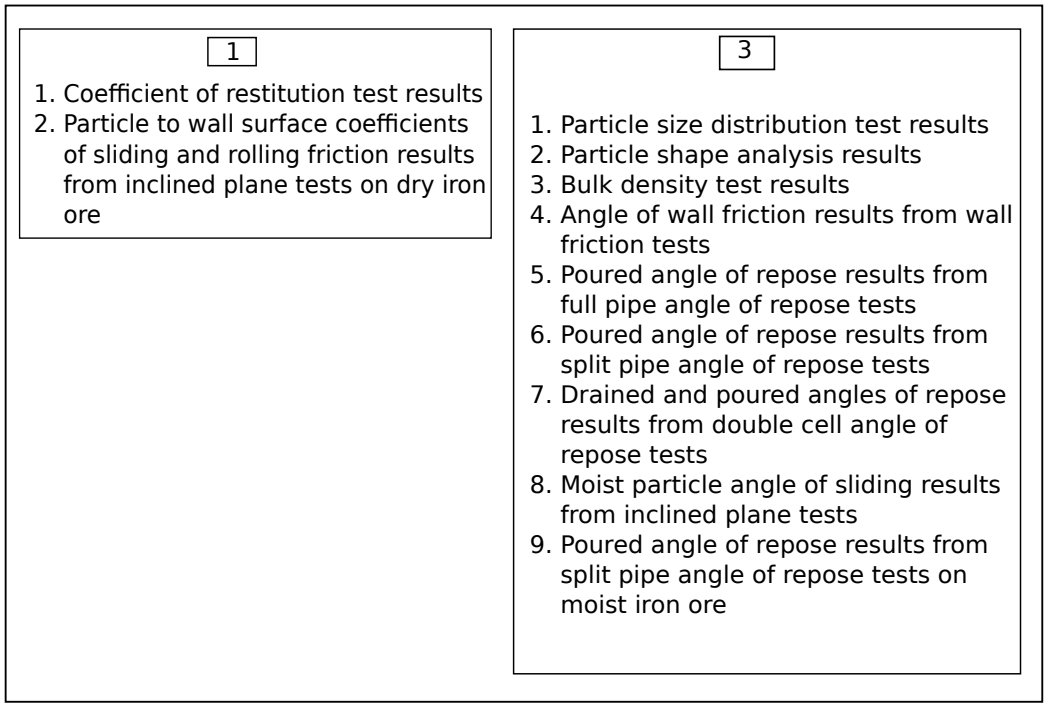


Figure 4.1: Calibration framework, physical experimental results

tests respectively. Table 4.1 shows the test results summary, while Tables E.1 and E.2 in Appendix E show the detailed observations and test results.

Table 4.1: Coefficients of restitution summary for iron ore

Parameter	**Particle to Particle Coefficient of Restitution**	**Particle to Wall Surface Coefficient of Restitution**
Minimum	0.46	0.39
Maximum	0.74	0.67
Average	0.61	0.56
Standard Deviation	0.08	0.06

The measured values of coefficient of restitution showed a high degree of dispersion as observed in the relatively high values of the standard deviation, which were 13.1% of the average value for particle to particle and 10.7% of

the average value for particle to wall surface interactions. The high values of dispersion were due to the imperfect impacts as a result of using an imperfect sphere. This imperfection introduced variability in the obtained values from one test to another. The measured average values of the coefficients of restitution in Table 4.1 were used in subsequent DEM simulations as the calibrated parameter values.

Table 4.2 shows an update of the DEM input parameter values after the coefficient of restitution values were obtained.

Table 4.2: Input parameters update, coefficient of restitution tests

Input Parameter	**Value**	**Material State**
$E_{particle}$ (MPa)	10	Dry
E_{wall} (MPa)	10	Dry
$\nu_{particle}$	0.24	Dry
ν_{wall}	0.37	Dry
ϵ_{pp}	0.61	Dry
ϵ_{pw}	0.56	Dry
$\mu_{pw,r}$	Not yet determined	Dry
$\mu_{pw,s}$	Not yet determined	Dry
ρ_p (kg/m^3)	Not yet determined	Dry
$\mu_{pp,s}$	Not yet determined	Dry
$\mu_{pp,r}$	Not yet determined	Dry
ED_a (kJ/m^3)	Not yet determined	Moist
ED_c (kJ/m^3)	Not yet determined	Moist
Timestep (s)	10^{-5}	-

4.1.2 Inclined plane test results, dry

Inclined plane tests were carried out to measure the particle to wall surface coefficients of sliding and rolling friction, using the procedure described in Section 3.3.2. A total of 20 tests were conducted for each of the two parameters. Table 4.3 shows the test results summary, while Table F.1 in Appendix F.1 shows the detailed test observations and results.

Table 4.3: Sliding and rolling friction coefficients summary, particle to wall

Parameter	**Iron Ore to Perspex Coefficient of Sliding Friction**	**Iron Ore to Perspex Coefficient of Rolling Friction**
Minimum	0.45	0.07
Maximum	0.51	0.16
Average	0.47	0.10
Standard Deviation	0.02	0.03

The degree of dispersion of the particle to wall surface coefficients of sliding friction values was fairly small as shown by a standard deviation which is 4.3% of the average value, however, the coefficient of rolling friction values showed a high degree of dispersion as shown by the standard deviation value which is 30% of the average value. Large variations in the coefficient of rolling friction from test to test were a result of the imperfect sphere used, generally very small angles at which rolling commenced, and the uncertainty in the experimental equipment, where the tray is raised and locked manually once the particle moved. The accuracy of the obtained average values can be increased by conducting a sufficiently high number of tests, which are not less than 20, in order to obtain statistically relevant results (Montgomery and Runger, 2014). Furthermore,the accuracy of the obtained average value of the rolling friction coefficient can be increased by increasing the accuracy of the spherical shape, and using a mechanical mechanism to rotate the inclined plane to reduce dynamic effects from manual rotation.

The measured average values of the two particle to wall surface friction coefficients in Table 4.3 were used in subsequent DEM simulations as the calibrated parameter values.

Table 4.4 shows an update of the DEM input parameter values after the measurement of the particle to wall coefficients of sliding and rolling friction.

Table 4.4: Input parameters update, inclined plane tests

Input Parameter	Value	Material State
$E_{particle}$ (MPa)	10	Dry
E_{wall} (MPa)	10	Dry
$\nu_{particle}$	0.24	Dry
ν_{wall}	0.37	Dry
ϵ_{pp}	0.61	Dry
ϵ_{pw}	0.56	Dry
$\mu_{pw,r}$	0.10	Dry
$\mu_{pw,s}$	0.47	Dry
ρ_p (kg/m^3)	Not yet determined	Dry
$\mu_{pp,s}$	Not yet determined	Dry
$\mu_{pp,r}$	Not yet determined	Dry
ED_a (kJ/m^3)	Not yet determined	Moist
ED_c (kJ/m^3)	Not yet determined	Moist
Timestep (s)	10^{-5}	-

4.1.3 Particle size distribution test results

A PSD test was carried out on iron ore, using the procedure outlined in Section 3.3.3. Table 4.5 shows the iron ore PSD analysis results. The purpose of these results was for approximating the PSD of the DEM material, subject to limitations on simulation time.

Table 4.5: Particle size distribution

Size Range (mm)	Mass of Sieve + Material (kg)	Mass of Sieve (kg)	Mass of Material (kg)	Contribution (%)
2.0 - 2.80	2.05	1.86	0.189	15.8
2.8 - 4.00	2.35	1.89	0.466	39.1
4.0 - 4.75	1.90	1.37	0.537	45.1
Total			**1.19**	**100**

4.1.4 Particle shape analysis results

Five iron ore particles were randomly selected as per the procedure outlined in Section 3.3.4. Figure 4.2 shows the shapes of the selected particles, whose sieve size range is between +2 mm and −4.75 mm. The purpose of these particle shapes was for approximating the shape of DEM particles, as shown in Figure 4.6.



Figure 4.2: Iron particle shapes

4.1.5 Bulk density test results

The bulk density test was carried out in order to determine the loose poured bulk density of iron ore using the procedure outlined in Section 3.3.5. Bulk density tests were carried out using two containers of different sizes, with each conducted six times. The average small container bulk density was later used to calibrate the DEM particle density, while the large container bulk density was used in verifying the obtained DEM particle density. Table 4.6 shows the summary of bulk density test results, while Appendix G shows the detailed observations and results.

Table 4.6 shows the physical maximum, minimum, average and standard deviation of the bulk density tests carried out in a small and a large container. The average bulk density obtained using the small container was used in the calibration of the DEM particle density. The small container was used because it minimises the required simulation time. A comparison of the iron ore bulk density values obtained from different container sizes, shows an increase in bulk

Table 4.6: Bulk densities, large and small containers

Statistic	**Bulk Density in Small Container (kg/m^3)**	**Bulk Density in Large Container (kg/m^3)**
Minimum	1800	1899
Maximum	1865	1930
Average	1833	1908
Standard Deviation	24	16

density with container size. This observation is attributable to the fact that, as volume increases, variations in excess mass of material scraped off when levelling are negligible. Added to that, increasing the height of the container causes material at the bottom of the container to be more compacted, hence causing an increase in the bulk density.

4.1.6 Wall friction test results

The wall friction test was carried out in order to determine the angle of wall friction between iron ore particles and a perspex surface. The angle of wall friction would be used to calibrate the particle to wall coefficient of sliding friction. The experiment was carried out according to the procedure outlined in Section 3.3.6. Because of the large amount of the generated data, a Python program (Appendix A.2) was developed to import the csv file generated in step (8) of the procedure, and perform all the relevant intermediate calculations stipulated in the procedure, plotting of the graphs and calculating the angle of wall friction.

Figure 4.3 shows the plots of stepped shear stress as a function of time for the two tests conducted.

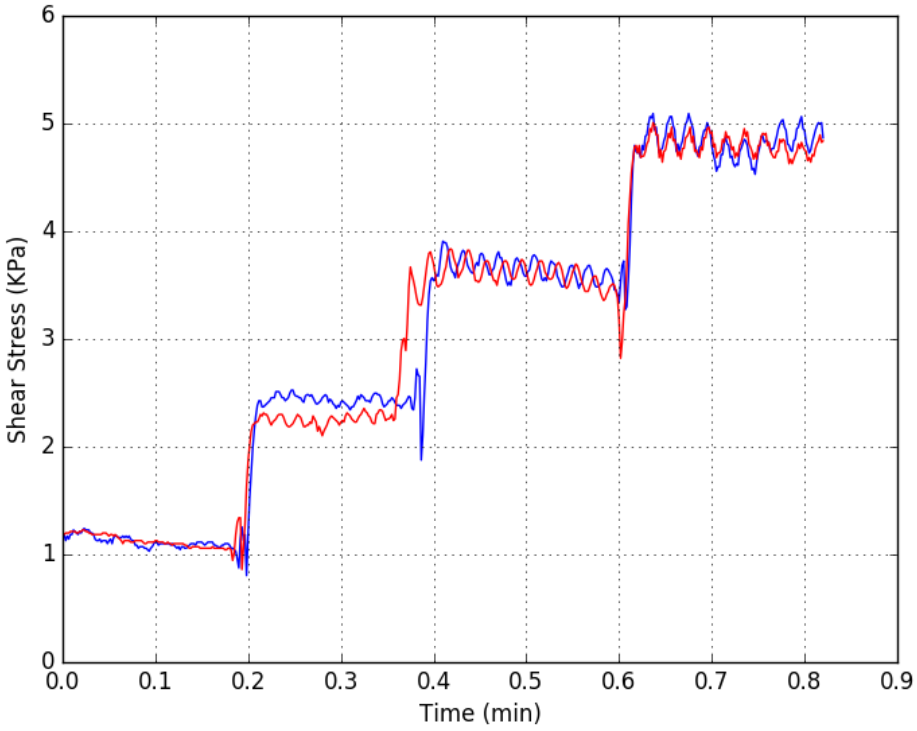


Figure 4.3: Shear stress evolution with time, physical tests

Table 4.7 shows the average limiting shear stresses and corresponding normal stresses for the two experiments conducted.

Table 4.7: Average limiting shear stress and normal stress, physical

	Normal Load (kg)			
	1.5	**3.5**	**5.5**	**7.5**
Experiment 1 Average Shear Stress (kPa)	1.13	2.18	3.45	4.72
Experiment 2 Average Shear Stress (kPa)	1.13	2.38	3.61	4.80
Normal Shear Stress (kPa)	3.18	5.95	8.72	11.49

The graph of shear stress as a function of normal stress for each of the two experiments was plotted, as shown in Figure 4.4. The gradients of the two plots were computed to be 0.435 and 0.442 respectively for the first and second

experiments, from which the respective angles of wall friction were calculated to be 23.5 ° and 23.8 °.

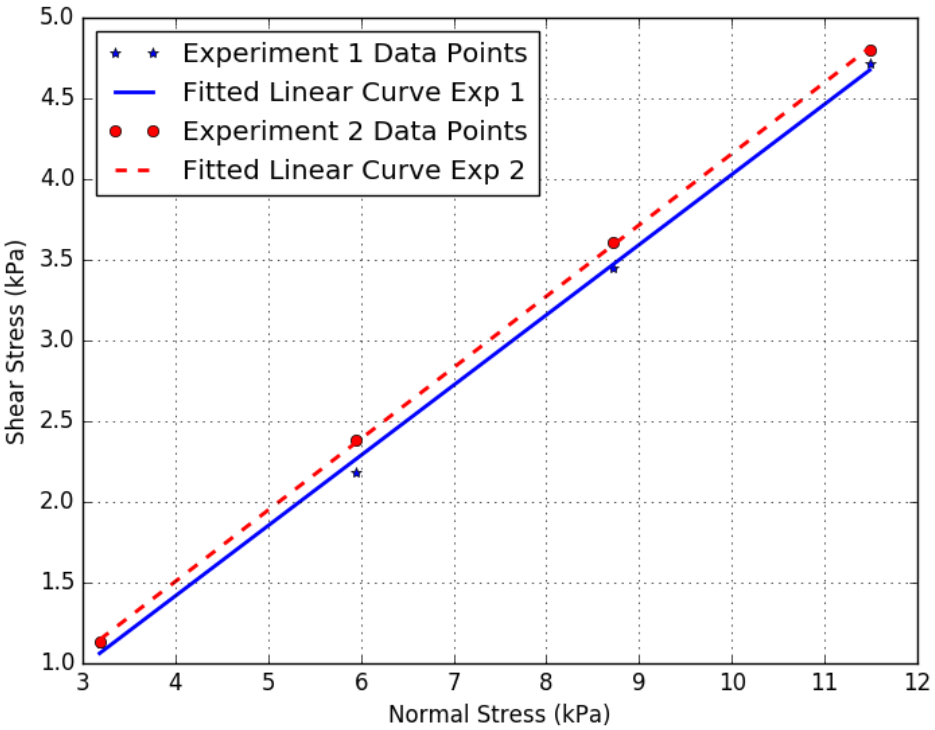


Figure 4.4: Angle of wall friction, physical tests

From the two conducted experiments, the average angle of wall friction was calculated to be 23.7°. The obtained average angle of wall friction would be used to calibrate the particle to wall surface coefficient of sliding friction.

4.1.7 Full pipe angle of repose test results

Three full pipe angle of repose tests were carried out to determine the full pipe poured angle of repose of iron ore for two different pipe diameters using the procedure outlined in Section 3.3.7. Table 4.8 shows a summary of the poured angles of repose for the two 94 mm and 110 mm pipe diameters, while the detailed pictures of the results are shown in Appendix J.1. The visual inspection method used to determine the angle of repose was estimated to result in an error of ±1°.

Table 4.8: Full pipe angles of repose, physical

Statistic	**Poured Angle of Repose @94 mm Pipe Diameter (±1°)**	**Poured Angle of Repose @110 mm Pipe Diameter (±1°)**
Minimum	34	35
Maximum	40	39
Average	36	37

The angle of repose obtained from the 94 mm pipe diameter was used in the calibration of the particle to particle coefficients of sliding and rolling friction, while 110 mm pipe diameter was used to observe the effect of pipe size on the angle of repose. A comparison of the two angles of repose from the different pipe diameters show that the full pipe poured angle of repose is relatively insensitive to pipe diameter. However, a large diameter pipe results in a reduced dispersion of obtained angles of repose from repeat experiments. This observation is shown by a standard deviation of large pipe diameter which is 4.1% of the average poured angle of repose, while that of the small pipe diameter is 6.4% of the average poured angle of repose. Therefore, it would be favourable to use as large a pipe diameter for calibration experiments as can be allowed by the budgeted simulation time.

4.1.8 Split pipe angle of repose test results

Three split pipe angle of repose tests were carried out to determine the split pipe poured angle of repose of dry iron ore using the procedure outlined in Section 3.3.8. Table 4.9 shows a summary of the poured angles of repose for dry iron ore, while the detailed pictures of the results are shown in Appendix K.1. The visual inspection method used to determine the angle of repose was estimated to result in an error of ±1°.

The average split pipe angle of repose was used to calibrate the particle to particle coefficients of sliding and rolling friction. The degree of dispersion of

Table 4.9: Split pipe angles of repose, physical

Statistic	**Poured Angle of Repose @94 mm Pipe Diameter (±1°)**
Minimum	20
Maximum	23
Average	21

the measured angles of repose is relatively low with a standard deviation that is 4.8% of the average split pipe poured angle of repose. Accuracy of the obtained average value can be improved by increasing the number of experimental tests.

4.1.9 Double cell angle of repose test results

Two double cell angle of repose tests were carried out to determine the drained and poured angles of repose of iron ore using the procedure outlined in Section 3.3.9. Table 4.10 shows the summary of the drained and poured angles of repose for the 50 mm and 130 mm depths of iron in the top cell of the double cell, while the detailed pictures of the results are shown in Appendix L.1. The visual inspection method used to determine the angle of repose was estimated to result in an error of ±1°.

Table 4.10: Double cell angles of repose, physical

Statistic	**Drained Angle of Repose @50 mm Depth (±1°)**	**Poured Angle of Repose @50 mm Depth (±1°)**	**Drained Angle of Repose @130 mm Depth (±1°)**	**Poured Angle of Repose @130 mm Depth (±1°)**
Minimum	38	27	39	36
Maximum	45	29	42	37
Average	41	28	40	37

The average angles of repose for the upper cell depth of 50 mm was used to verify the particle to particle coefficient of sliding and rolling friction calibrated using the full pipe and split pipe angles of repose.

Table 4.10 shows the maximum, minimum and average drained and poured angles of repose obtained with two different depths of iron ore in the upper cell. A comparison of the angles of repose at different upper cell depths showed that the drained angle of repose was relatively insensitive to variations in depth, while the poured angle of repose significantly changed with depth as seen by an increase of 32% in angle of repose when the depth in the upper cell was increased from 50 mm to 130 mm. This difference was attributed to the change in flow regimes from quasi-static to dynamic with depth of material. A smaller depth in the upper cell results in a smaller heap in the bottom cell. This causes material to travel longer in between the cells, accumulate more kinetic energy and disperse more on impact, resulting in a shallow angle of repose. On the other hand, a larger depth in the top cell results in a larger heap in the bottom cell. This causes material to travel a shorter distance in between the cells, resulting in less kinetic energy and a relatively steeper poured angle of repose.

4.1.10 Inclined plane test results, moist

Twenty inclined plane tests were carried out to measure the angle at which a moist iron ore particle commences to slide on perspex, using the procedure described in Section 3.3.2. Table 4.11 shows the test results summary, while Table F.2 in Appendix F.2 shows the detailed test results.

The average sliding angle was used to calibrate the adhesion energy density between the perspex wall material and iron ore particles in DEM. Since the sliding angle of a moist particle is a function of both friction and adhesion, calibration using the obtained value of sliding angle was conducted only after

Table 4.11: Moist particle sliding angle summary, physical

Statistic	**Sliding Angle (°)**
Minimum	32
Maximum	40
Average	37
Standard Deviation	2.5

the particle to wall coefficient of sliding friction has been calibrated with dry material. This ensured that frictional effects are factored into the results. A comparison of the average sliding angles of dry and moist particles showed a difference of 12°. This difference represented the effect of adhesion.

4.1.11 Split pipe angle of repose test results, moist

Three split pipe angle of repose tests were carried out to determine the split pipe poured angle of repose of moist iron ore using the procedure outlined in Section 3.3.8. Table 4.12 shows the summary of the poured angles of repose for moist iron ore, while the detailed pictures of the results are shown in Appendix M.1. The visual inspection method used to determine the angle of repose was estimated to result in an error of ±1°.

Table 4.12: Moist split pipe angles of repose, physical

Statistic	**Poured Angle of Repose @94 mm Pipe Diameter (±1°)**
Minimum	23
Maximum	27
Average	25

The average angle was used to calibrate the iron ore particles cohesion energy density. Gröger and Katterfield (2006) identified cohesion and friction as the parameters that significantly affected the angle of repose. As such, the obtained angle of repose was only used to calibrate cohesion energy density after the particle to particle friction coefficients were calibrated using dry material. This ensured that frictional effects were factored into the results. A difference of 4° between the dry (Table 4.9) and moist split pipe angles of repose was due to cohesion effects.

4.2 DEM Calibration Experimental Results

This section outlines the processing of data and results of the DEM calibration experiments. These experiments made use of observed bulk responses to tune specific input parameters so that the DEM bulk response matched the physically observed bulk response (boxes 4 and 5 in Figure 3.1). Figure 4.5 shows the position of the presented results in the general framework of Figure 3.1. The DEM experimental results are presented in an order that allows the previously calibrated input parameters to be used in subsequent calibration experiments.

4.2.1 DEM particle size and shape model

Only a single DEM particle size and shape was used in all the DEM simulations. Figure 4.6 shows the particle shape and size made of two clumped spheres, side by side with a real iron ore sample particle. The particles were chosen to approximate triangular shape of the real particles, hence a big and small sphere. The DEM particle shape was a compromise between the need to capture the irregularities of the real particle shape and to minimise computational time.

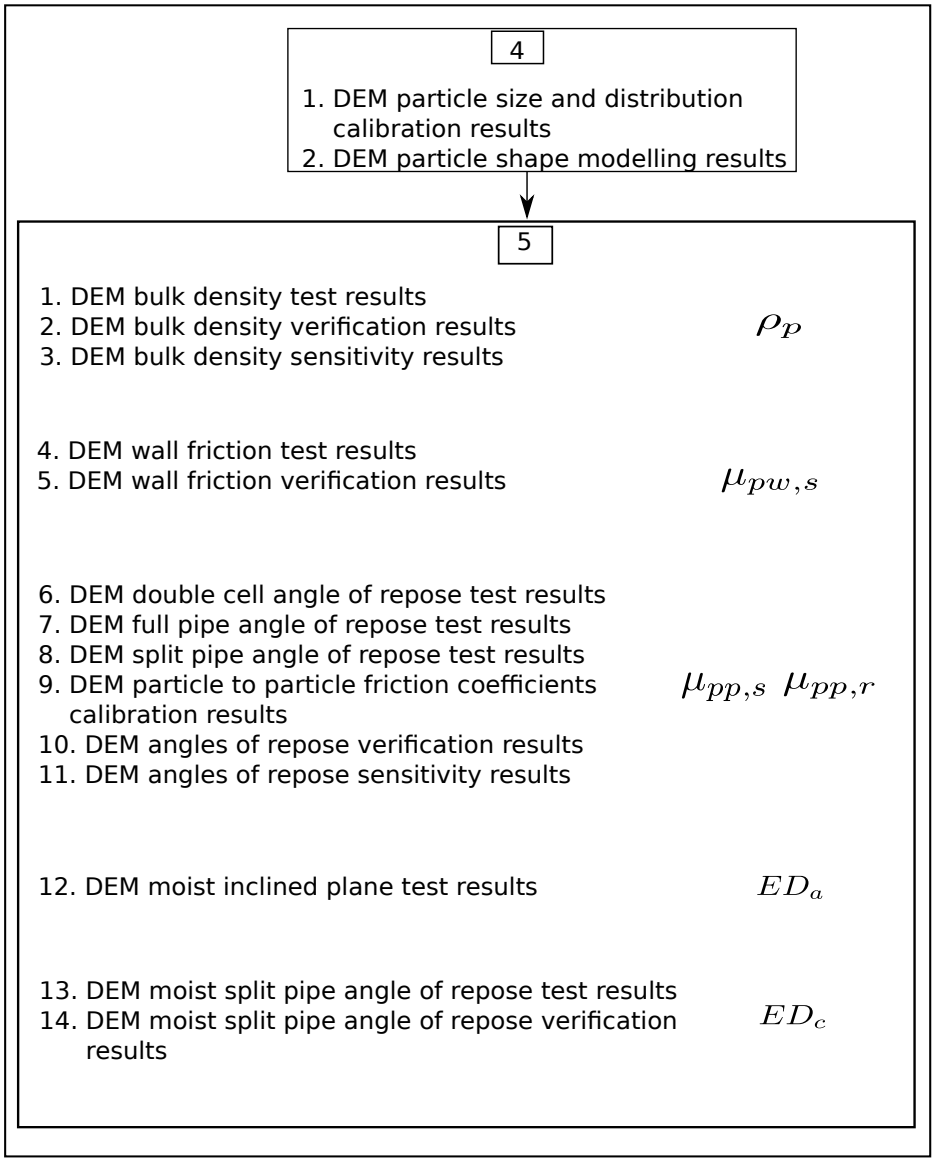


Figure 4.5: Calibration framework, DEM experimental results

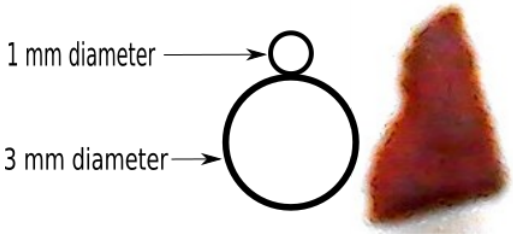


Figure 4.6: Clumped spheres particle

4.2.2 DEM bulk density test results

The DEM bulk density test was carried out to calibrate the iron ore DEM particle density in accordance with the procedure outlined in Section 3.4.3. The particle shape was modelled as shown in Figure 4.6, while the input parameters were set at values stated in the procedure. Table 4.13 shows the values of DEM bulk density obtained for each of the four simulated values of particle density.

Table 4.13: DEM bulk density variation with DEM particle density

Particle Density (kg/m^3)	**Particle Mass (kg)**	**Number of Particles**	**Total Mass (kg)**	**Bulk Density (kg/m^3)**
2000	2.93×10^{-5}	2050	0.0602	1000
3000	4.40×10^{-5}	2103	0.0926	1538
4000	5.87×10^{-5}	2083	0.1222	2032
5000	7.34×10^{-5}	2082	0.1527	2538

A plot of bulk density against particle density was made yielding a linear correlation. A best fit linear curve was fitted, as shown in Figure 4.7. The coefficients of the linear equation defining the curve were calculated using a linear regression solver . Equation 4.1 defines the relationship between the DEM bulk density and DEM particle density with $R^2 = 1.00$, where ρ_b is the bulk density in kg/m^3 and ρ_p is the particle density in kg/m^3.

$$\rho_b = 0.5\rho_p - 11.2 \tag{4.1}$$

The physical average iron ore bulk density of 1833 kg/m^3, measured using a small container in Section 4.1.5, was substituted into the equation and the DEM particle density determined to be 3609 kg/m^3. This particle density became the DEM calibrated particle density, since it was obtained by enforcing

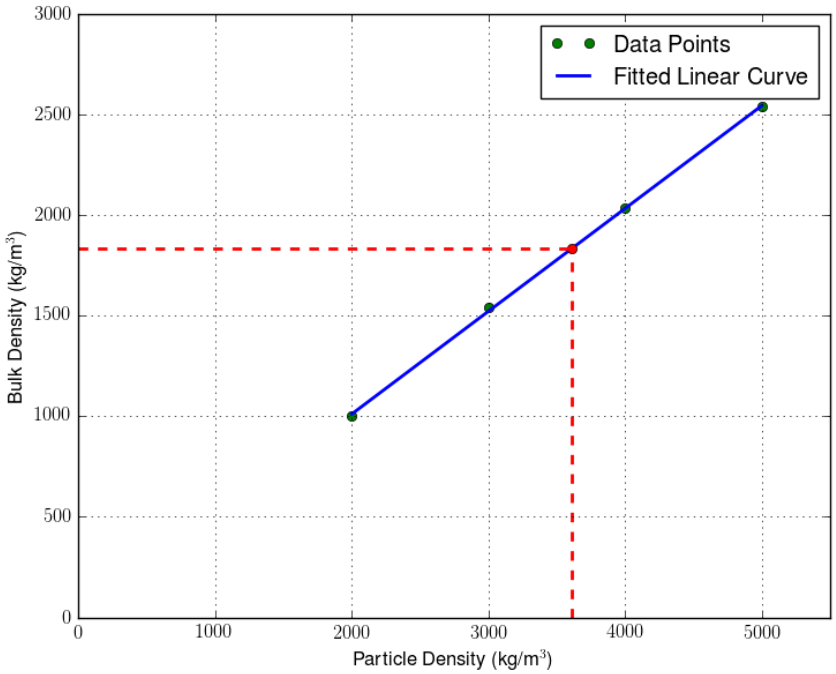


Figure 4.7: DEM bulk density as a function of DEM particle density

an equality between the physical and DEM bulk densities.

Plotting of the graph, conducting linear regression and solving of the equation for particle density were all automatically performed by the Python program in Appendix A.1. The inputs to the program were the physically measured average bulk density and the bulk densities at the four values of particle densities used in the procedure. The output of the program was the graph showing DEM bulk density as a function of particle density, the goodness of fit value of the fitted equation and the calibrated particle density.

The results show that the relationship between DEM bulk density and particle density can be quantitatively modelled with a linear equation, within a reasonable error band. Equation 4.1 implies that a particle density of zero yields a bulk density of -11.2 kg/m^3, which is not practical. The reason for that error is that empirical equations are only good at modelling the relationship between variables in a region bounded by the extreme values of the tested points. As such, Equation 4.1 is valid between 2000 kg/m^3 and 5000

kg/m^3. This implies that the test points used to construct the equation should be be chosen such that the solution being sought lies somewhere between the extreme test points. This can be done by either having a knowledge of the real particle density, which would then be used as a benchmark to choose extreme points lying on the lower and upper sides of the value, or by conducting some preliminary tests.

Table 4.14 shows an update of the DEM input parameter values after the calibration of particle density.

Table 4.14: Input parameters update, bulk density tests

Input Parameter	**Value**	**Material State**
$E_{particle}$ (MPa)	10	Dry
E_{wall} (MPa)	10	Dry
$\nu_{particle}$	0.24	Dry
ν_{wall}	0.37	Dry
ϵ_{pp}	0.61	Dry
ϵ_{pw}	0.56	Dry
$\mu_{pw,r}$	0.10	Dry
$\mu_{pw,s}$	0.47	Dry
ρ_p (kg/m^3)	3609	Dry
$\mu_{pp,s}$	Not yet determined	Dry
$\mu_{pp,r}$	Not yet determined	Dry
ED_a (kJ/m^3)	Not yet determined	Moist
ED_c (kJ/m^3)	Not yet determined	Moist
Timestep (s)	10^{-5}	-

4.2.3 DEM bulk density verification results

The obtained value of iron ore DEM particle density of 3609 kg/m^3 was used in a simulation in accordance with the procedure described in Section 3.4.3,

steps (1) to (7). The purpose of the simulation was to verify if the use of the calibrated particle density in a DEM simulation would predict the correct physically measured bulk density. Two container sizes were used together with the procedure. Table 4.15 shows the simulated values of bulk density and their percentage deviation from the physically measured values (Section 4.1.5). Each DEM particle had a mass of 5.29×10^{-5} kg.

Table 4.15: DEM bulk density, particle density = 3609 kg/m^3

Container Size	**Number of Particles**	**Total Mass (kg)**	**DEM Bulk Density (kg/m^3)**	**Actual Bulk Density (kg/m^3**	**Difference from Physical (%)**
Small	2094	0.111	1843	1833	0.5
Large	35400	1.881	1929	1908	1.1

The verification results show that the calibrated particle density was able to reproduce the physically measured bulk densities with small error margins of 0.5% for the small volume and 1.1% for the larger volume. The error arose due to random variabilities of material that remained in the containers after scraping. This shows that the method used in calibrating particle density is at the least able to correctly predict bulk density in a geometry similar to the one used during calibration.

4.2.4 DEM bulk density sensitivity results

Sensitivity experiments were performed to determine the effect of input parameters that were maintained constant during particle density calibration, on the DEM bulk density. The procedure described in Section 3.4.3, steps (1) to (7), was used with a high and a low value for each input parameter. Table 4.16 shows the bulk densities obtained by varying each input parameter and the deviation from the DEM bulk density of 1843 kg/m^3.

Table 4.16: DEM bulk density sensitivity

Adjusted Input Parameter	**Total Mass of Particles (kg)**	**Bulk Density (kg/m^3)**	**Deviation (%)**
$\mu_{pp,s} = 0.1$	0.125	2079	11.4
$\mu_{pp,s} = 1.0$	0.106	1762	4.39
$\mu_{pp,r} = 0.1$	0.116	1932	4.60
$\mu_{pp,r} = 1.0$	0.108	1794	2.63
$\mu_{pw,s} = 0.1$	0.115	1913	3.68
$\mu_{pw,s} = 1.0$	0.110	1829	0.76
$\mu_{pw,r} = 0.1$	0.111	1843	0.00
$\mu_{pw,r} = 1.0$	0.110	1831	0.62
$\epsilon_{pp} = 0.1$	0.109	1805	2.05
$\epsilon_{pp} = 1.0$	0.117	1939	4.99
$\epsilon_{pw} = 0.1$	0.111	1849	0.33
$\epsilon_{pw} = 1.0$	0.110	1836	0.38

where $\mu_{pp,s}$ is the particle to particle coefficient of sliding friction, $\mu_{pp,r}$ is the particle to particle coefficient of rolling friction, $\mu_{pw,s}$ is the particle to wall coefficient of sliding friction, $\mu_{pw,r}$ is the particle to wall coefficient of rolling friction, ϵ_{pp} is the particle to particle coefficient of restitution and ϵ_{pw} is the particle to wall coefficient of restitution.

It can be observed from Table 4.16 that as the coefficients of friction are reduced, more particles enter the container resulting in a larger mass than for higher values of friction coefficients. This is consistent with the fact that higher friction coefficients inhibit movement while lower values allow more relative movement.

The particle to particle coefficient of static friction shows a significant variation of approximately 11% from the calibrated bulk density as the value was reduced to 0.1. On increasing this parameter to 1.0 a variation of 4% was recorded. This shows that the coefficient of static friction has some effect on the bulk

density test, however a good choice based on experience during the test will yield results that are less sensitive to its variation. For high friction materials, a mid range value of 0.5 will minimise any variations due to changes of this parameter. This can be observed from small variations in bulk density when the particle to particle coefficient of sliding friction is increased to 1.0.

Particle to particle coefficient of restitution also has a slight effect on bulk density as seen by a variation of 5% when it was increased to 1.0. However this parameter is measured before the bulk density test so it does not alter the results. All the other parameters introduced variations that were below 5% and can be safely ignored during the bulk density test.

4.2.5 DEM wall friction test results

The DEM wall friction test was carried out in order to calibrate the dry iron ore to perspex coefficient of sliding friction using the procedure described in Section 3.4.4. This was achieved by enforcing the equality of the DEM angle of wall friction and the physically measured angle of wall friction.

Table 4.17 shows a summary of the angles of wall friction obtained at each of the four simulated values of iron ore to perspex coefficient of sliding friction, while Appendix H has the detailed observations and results.

Table 4.17: DEM wall friction angles

Coefficient of Sliding Friction	0.2	0.4	0.6	0.9
Gradient of the fitted linear curve	0.197	0.383	0.524	0.595
DEM Angle of Wall Friction (°)	11.2	21.0	27.7	30.8

Figure 4.8 shows the DEM angle of wall friction as a function of coefficient of sliding friction, fitted with a second order polynomial. Equation 4.2 defines the the relationship between the angle of wall friction and the iron ore to perspex coefficient of sliding friction, with $R^2 = 1.00$.

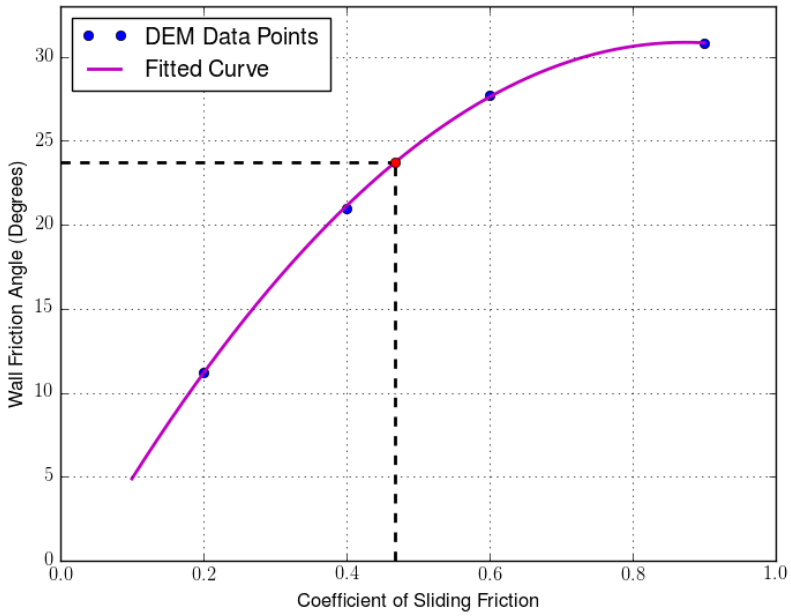


Figure 4.8: DEM wall friction angle as a function of sliding friction, second order

$$\phi_w = -43.4\mu_{pw,s}^2 + 75.8\mu_{pw,s} - 2.3 \tag{4.2}$$

where ϕ_w is the angle of wall friction in degrees and $\mu_{pw,s}$ is the coefficient of sliding friction.

Substituting the physically measured wall friction angle of $\phi_w = 23.7^{\circ}$ into the equation yields $\mu_{pw,s} = 0.47$

The same results in Table 4.17 were fitted with a first order polynomial, and its goodness of fit value determined to be $R^2 = 0.90$. Based on the goodness of fit values, the second order polynomial fitted the data better than the first order, hence the value of iron ore to perspex obtained from second order equation of $\mu_{pw,s} = 0.47$ became the calibrated value.

The results show that a second order polynomial models the relationship between the angle of wall friction and the particle to wall surface coefficient of sliding friction with a high degree of accuracy, as indicated by the goodness of

fit value. The constant term of -2.3 in Equation 4.2 implies a negative value of wall friction angle when the the particle to particle coefficient of sliding friction is zero, which practically is not possible. Empirical equations are only valid within the region bounded by the extreme values used in their construction (Myers et al., 2009), hence the constructed equation is valid between 0.2 and 0.9. As such, when modelling the equation, the extreme points used in constructing the equation must bound the area in which the sought solution lies.

Table 4.18 shows an update of the DEM input parameter values after the calibration of particle wall coefficient of sliding friction.

Table 4.18: Input parameters update, wall friction tests

Input Parameter	**Value**	**Material State**
$E_{particle}$ (MPa)	10	Dry
E_{wall} (MPa)	10	Dry
$\nu_{particle}$	0.24	Dry
ν_{wall}	0.37	Dry
ϵ_{pp}	0.61	Dry
ϵ_{pw}	0.56	Dry
$\mu_{pw,r}$	0.10	Dry
$\mu_{pw,s}$	0.47	Dry
ρ_p (kg/m^3)	3609	Dry
$\mu_{pp,s}$	Not yet determined	Dry
$\mu_{pp,r}$	Not yet determined	Dry
ED_a (kJ/m^3)	Not yet determined	Moist
ED_c (kJ/m^3)	Not yet determined	Moist
Timestep (s)	10^{-5}	-

4.2.6 DEM wall friction results verification

A verification wall friction test was executed in DEM using the calibrated value of iron ore to perspex coefficient of sliding friction, $\mu_{pw,s} = 0.47$. The

Table 4.19: Average limiting shear and normal stresses, $\mu_{pw,s} = 0.47$

	Normal Load (N)			
	14.7	**34.3**	**54.0**	**73.5**
Average Shear Stress @ 3mm - 4mm Displacement (kPa)	1.00	2.25	3.47	4.71
Average Normal Stress @ 3mm - 4mm Displacement (kPa)	2.25	5.07	7.90	10.9

procedure described in Section 3.4.4 was used up to step (16).

The input parameters were set at values given in Table 4.18. Particle to particle coefficients of friction, adhesion and cohesion energy density were set at values stipulated in the procedure.

Figure 4.9 shows the plot of shear stress as a function of time for the four normal loads applied. Shear stress and normal stress data points in the region between 3 mm and 4mm of the plot were averaged for each normal load case, and recorded in Table 4.19.

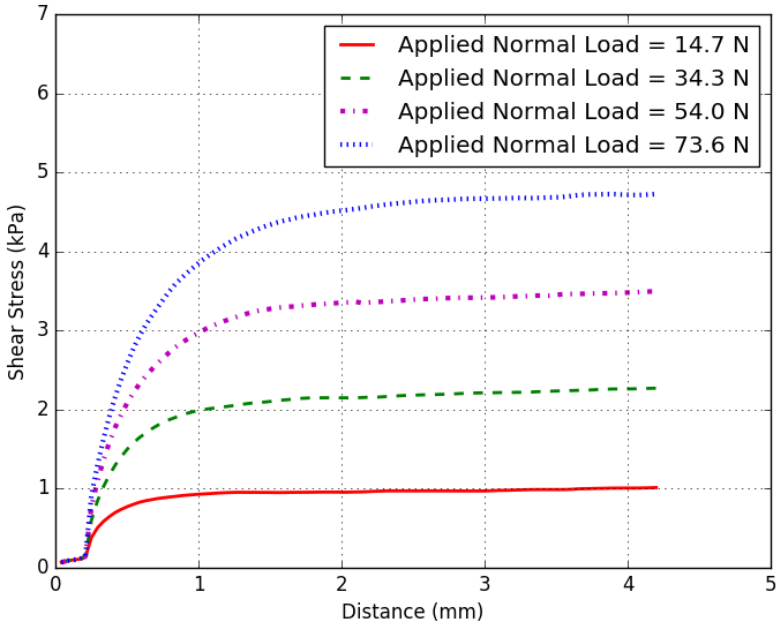


Figure 4.9: Shear stress evolution with displacement, $\mu_{pw,s} = 0.47$

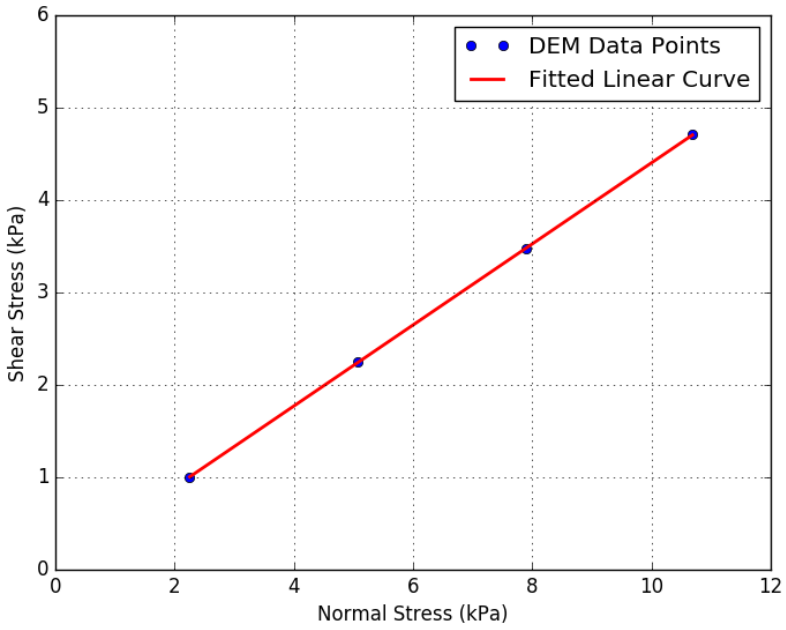


Figure 4.10: Angle of wall friction, $\mu_{pw,s} = 0.47$

The shear stress in Table 4.19 was plotted against the normal stress and a linear curve was fitted as shown in Figure 4.10. The gradient of the best fit line was computed to be 0.44. The corresponding angle of wall friction is therefore the arctangent of the gradient which is equal to 23.7°.

The verification results show that the calibrated particle to wall surface coefficient of sliding friction was able to reproduce the physically measured angle of wall friction of 23.7° in DEM. This shows the method used in calibrating the particle to wall coefficient of sliding friction is able to predict the correct angle of wall friction of a bulk material.

4.2.7 DEM wall friction sensitivity results

The DEM wall friction test was carried out to observe the sensitivity of particle to wall surface coefficient of rolling friction using the method described in Section 3.4.4. The only change made to the procedure was maintaining the particle to wall coefficient of sliding friction at its calibrated value in Table 4.18, while the particle to wall coefficient of rolling friction was varied.

Table 4.20 shows the DEM angle of wall friction at each of the four tests points.

Table 4.20: DEM wall friction angle as a function of rolling friction

Coefficient of Rolling Friction	0.2	0.4	0.6	0.9
DEM Angle of Wall Friction (°)	24.6	23.0	25.2	23.1

The results show that there was little change in the angle of wall friction when the particle to wall surface coefficient of rolling friction was varied from 0.2 to 0.9. The differences in the angle of wall friction from one point to the other were due to random variations in particle arrangements in the shear zone. This shows that the only significant factor affecting the angle of wall friction is the particle to wall surface coefficient of sliding.

4.2.8 DEM full pipe angle of repose results

The DEM full pipe angle of repose tests were performed at the CCD sampled points in Table I.1. The resulting data were then used to develop an empirical equation that relates the full pipe poured angle of repose to the particle to particle coefficients of sliding and rolling friction. The rest of the input parameters were set at values stated in the procedure (Section 3.4.6). Table 4.21 shows the obtained DEM angles of repose at each sample point, while Appendix J.2 shows the detailed simulation results.

A second order polynomial was fitted to the average full pipe poured angle of repose data in Table 4.21. The resulting response surface is shown in Figure 4.11 and the corresponding empirical equation given by Equation 4.3.

$$\phi_{FR} = 14.0 + 38.8\mu_{pp,s} + 17.1\mu_{pp,r} - 22.8\mu_{pp,s}^2 - 14.3\mu_{pp,r}^2 + 11.1\mu_{pp,s}\mu_{pp,r} \quad (4.3)$$

Table 4.21: DEM full pipe angles of repose, CCD points

$\mu_{pp,s}$	$\mu_{pp,r}$	**Average Poured Angle of Repose ($\pm 1^o$)**
0.18	0.60	25.0
0.30	0.30	30.0
0.30	0.90	31.0
0.60	0.18	31.5
0.60	0.60	38.0
0.60	1.00	39.0
0.90	0.30	36.5
0.90	0.90	41.5
1.00	0.60	42.5

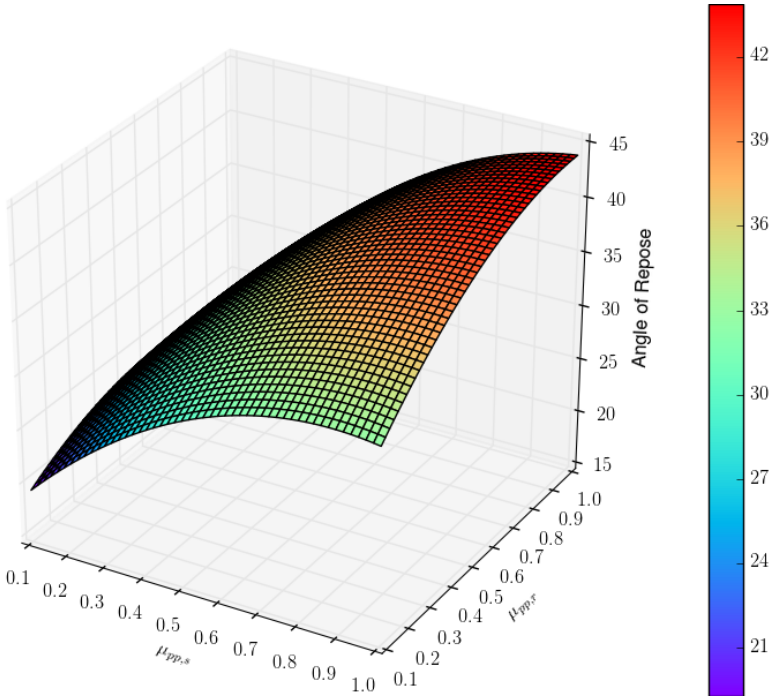


Figure 4.11: Full pipe angle of repose, second order response surface

where ϕ_{FR} is the full pipe poured angle of repose in degrees. The coefficient of multiple determination of the second order equation was determined to be $R^2 = 0.97$.

In order to aid the visualisation of data points location with respect to the fitted equation, respective values of $\mu_{pp,s}$ and $\mu_{pp,r}$ were substituted into Equation 4.3, thereby reducing the equation into a second order polynomial in one variable for each value of $\mu_{pp,s}$ or $\mu_{pp,r}$. Each of the obtained equations were then plotted together with the data in Table 4.21. Figures 4.12 and 4.13 show the plotted full pipe angles of repose as functions of the sliding and rolling coefficients of friction respectively.

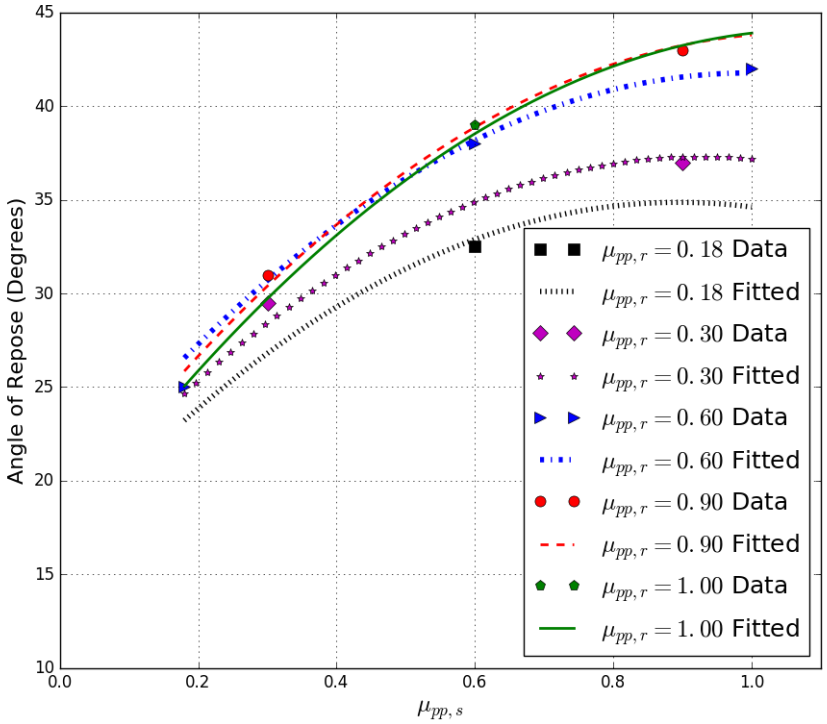


Figure 4.12: Variation of full pipe angle of repose with particle to particle sliding friction

A first order response surface was also fitted to the data, and its coefficient of multiple determination was determined to be $R^2 = 0.92$

Based on the R^2 values of the two response surface equations, the second order response equation was selected as the empirical equation that best defined the relationship between the angle of repose and the particle to particle coefficients of sliding and rolling friction.

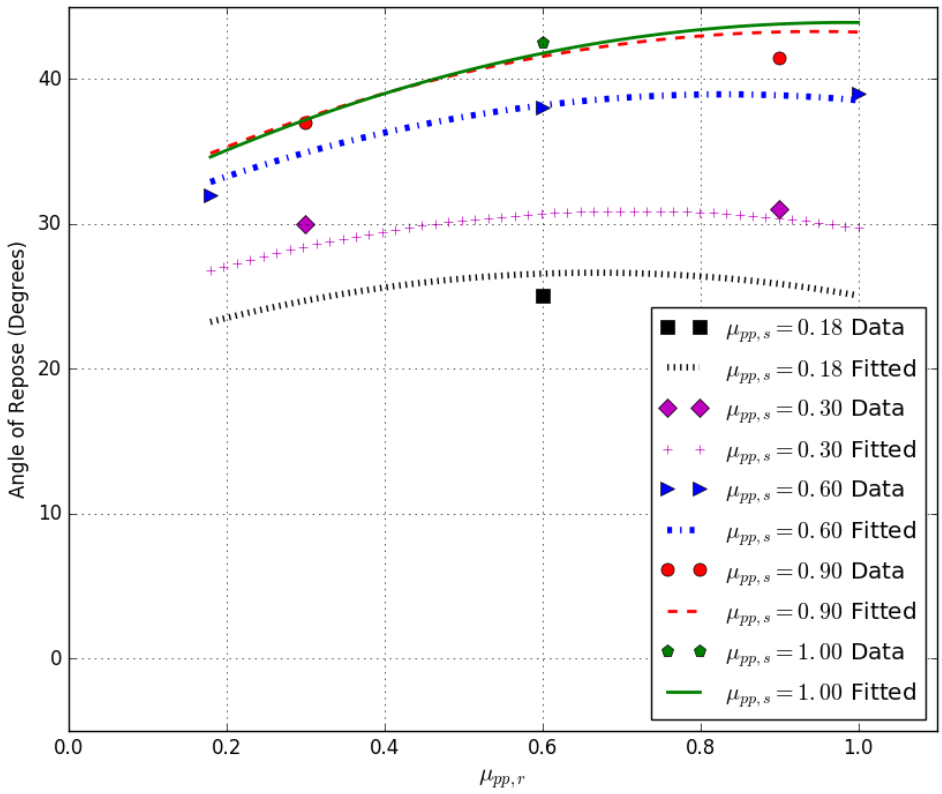


Figure 4.13: Variation of full pipe angle of repose with particle to particle rolling friction

A sensitivity test was conducted to determine variations in the equation coefficients by varying the two extreme angles in Table 4.21 by $\pm 1^{o}$. The change in equation coefficients was of the order of 0.01, and hence considered to be negligible.

Equation 4.3 would be simultaneously solved together with a second equation for the particle to particle coefficients of sliding and rolling friction. The equation is only valid within a region defined by the extreme values of the sampled data points (0.18 and 1.00) of Table 4.21.

4.2.9 DEM split pipe angle of repose results

The DEM split pipe angle of repose tests were carried out at the CCD sampled points in Table I.1. The obtained data was used to develop an empirical equation that relates the split pipe poured angle of repose to the particle to particle coefficients of sliding and rolling friction. The rest of the input parameters were set at values stated in the procedure (Section 3.4.7). Table 4.22 shows the obtained split pipe angles of repose at each sample point while Appendix K.2 shows the detailed simulation results in the form of pictures.

Table 4.22: DEM split pipe angles of repose, CCD points

$\mu_{\mathbf{pp,s}}$	$\mu_{\mathbf{pp,r}}$	**Average Poured Angle of Repose ($\pm 1^{o}$)**
0.18	0.60	17.0
0.30	0.30	19.0
0.30	0.90	20.5
0.60	0.18	19.5
0.60	0.60	22.0
0.60	1.00	23.0
0.90	0.30	21.0
0.90	0.90	23.0
1.00	0.60	23.0

Using the average split pipe angles of of repose from Table 4.22, the Python program in Appendix A.6 was used to fit a second order polynomial to the data.

Figure 4.14 shows the response surface plot, while the corresponding relationship between the split pipe angle of repose and the particle to particle coefficients of sliding and rolling friction is given by Equation 4.4 where ϕ_{SR} is in degrees.

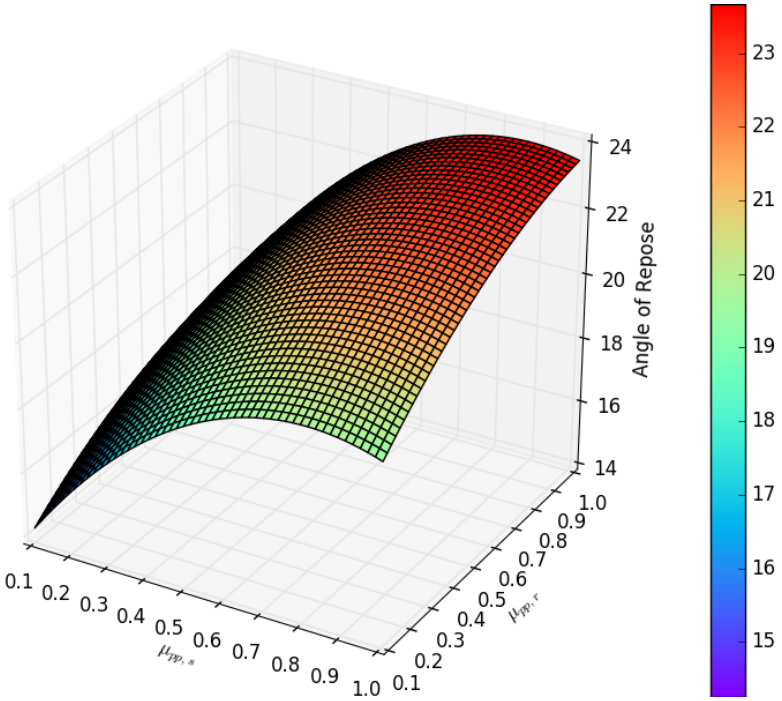


Figure 4.14: Split pipe angle of repose, second order response surface

$$\phi_{SR} = 11.9 + 17.9\mu_{pp,s} + 7.1\mu_{pp,r} - 11.1\mu_{pp,s}^2 - 3.7\mu_{pp,r}^2 + 1.4\mu_{pp,s}\mu_{pp,r} \quad (4.4)$$

The coefficient of multiple determination of the second order equation was determined to be $R^2 = 0.93$.

In order to aid the visualisation of data points location with respect to the fitted equation, respective values of $\mu_{pp,s}$ and $\mu_{pp,r}$ were substituted into Equation 4.4, thereby reducing the equation into a second order polynomial in one variable for each value of $\mu_{pp,s}$ or $\mu_{pp,r}$. Each of the obtained equations were then plotted together with the data in Table 4.22. Figures 4.15 and 4.16 show the plotted split pipe angles of repose as functions of the sliding and rolling coefficients of friction respectively.

A first order response surface was also fitted to the data, and its coefficient of multiple determination was determined to be $R^2 = 0.84$

Based on the R^2 values of the two equations, the second order equation was selected as the empirical equation that best defined the relationship between

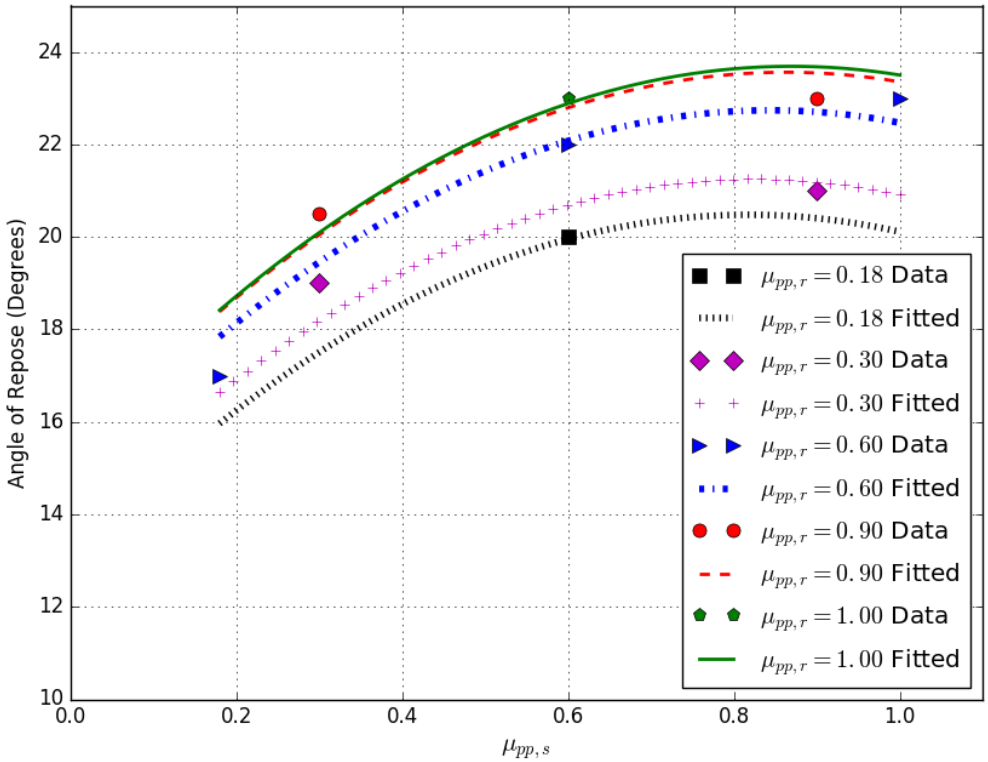


Figure 4.15: Variation of split pipe angle of repose with particle to particle sliding friction

the angle of repose and the particle to particle coefficients of sliding and rolling friction.

A sensitivity test was conducted to determine variations in the equation coefficients by varying the extreme angles in Table 4.21 by $\pm 1^{o}$. The change in equation coefficients was of the order of 0.01, and hence considered to be negligible.

Equation 4.4 would be simultaneously solved together with Equation 4.3 for the particle to particle coefficients of sliding and rolling friction. The equation is only valid within a region defined by the extreme values of the sampled data points (0.18 and 1.00) of Table 4.21.

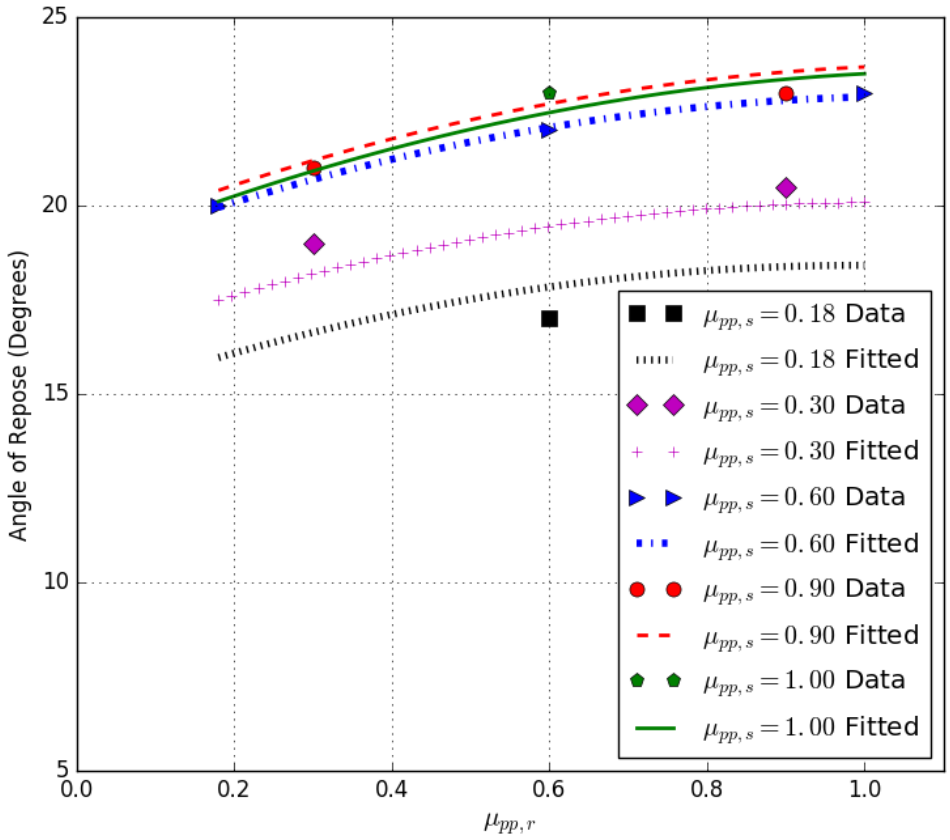


Figure 4.16: Variation of split pipe angle of repose with particle to particle rolling friction

4.2.10 DEM particle to particle friction calibration results

The DEM particle to particle friction calibration procedure outlined in Section 3.4.8 was used to calibrate the particle to particle coefficients of sliding and rolling friction for iron ore.

The two empirical equations in Sections 4.2.8 and 4.2.9, defining the relationship between the angles of repose and the particle to particle friction coefficients were equated to their corresponding physically measured angles of repose. Equation 4.3 was equated to the average full pipe poured angle of repose, $\phi_{FR} = 36^{o}$ (Section 4.1.7) to give Equation 4.5. Equation 4.4 was equated to the average split pipe poured angle of repose, $\phi_{SR} = 21^{o}$ (Section 4.1.8) to give Equation 4.6.

$$-22.8\mu_{pp,s}^2 - 4.3\mu_{pp,r}^2 + 11.1\mu_{pp,s}\mu_{pp,r} + 38.8\mu_{pp,s} + 17.1\mu_{pp,r} - 22.0 = 0 \quad (4.5)$$

$$-11.1\mu_{pp,s}^2 - 3.7\mu_{pp,r}^2 + 1.4\mu_{pp,s}\mu_{pp,r} + 17.9\mu_{pp,s} + 7.1\mu_{pp,r} - 9.1 = 0 \quad (4.6)$$

The Python program in Appendix A.7 was developed to solve the simultaneous equations. The obtained values of the particle to particle friction coefficients were $\mu_{s,pp} = 0.73$ and $\mu_{r,pp} = 0.28$. These values became the calibrated parameter values of the particle to particle friction coefficients because the enforced equality between the DEM and physical angles of repose.

A sensitivity test was done by varying the coefficients of Equations 4.3 and 4.4 to the nearest 0.01 (see Section 4.2.8 and 4.2.9), and the solution point remained changed by an order of 0.001. This means that measurement errors of $\pm 1^{\circ}$ do not significantly affect the obtained particle to particle coefficient of friction values.

An inspection of the Equations 4.3 and 4.4 relating the angles of repose to particle to particle friction coefficients, showed that they predicted angles of repose of 11.1° and 11.9° respectively, when the two friction coefficients assume zero values, which is not feasible in practice. This simply shows that the fitted equations are only good at predicting values within the boundaries defined by parameter values used in their construction, which in this case is 0.18 to 1.00 as given in Table 3.4 (Myers et al., 2009). Therefore, it follows that sample points should be selected such that the desired solution point is within the boundaries defined by the extreme points.

Table 4.23 shows an update of the DEM input parameter values after the calibration of particle to particle friction coefficients.

Table 4.23: Input parameters update, angle of repose tests

Input Parameter	**Value**	**Material State**
$E_{particle}$ (MPa)	10	Dry
E_{wall} (MPa)	10	Dry
$\nu_{particle}$	0.24	Dry
ν_{wall}	0.37	Dry
ϵ_{pp}	0.61	Dry
ϵ_{pw}	0.56	Dry
$\mu_{pw,r}$	0.10	Dry
$\mu_{pw,s}$	0.47	Dry
ρ_p (kg/m^3)	3609	Dry
$\mu_{pp,s}$	0.73	Dry
$\mu_{pp,r}$	0.28	Dry
ED_a (kJ/m^3)	Not yet determined	Moist
ED_c (kJ/m^3)	Not yet determined	Moist
Timestep (s)	10^{-5}	-

4.2.11 DEM angles of repose results verification

The DEM calibrated particle to particle coefficients of sliding and rolling friction values, which are $\mu_{s,pp} = 0.73$ and $\mu_{r,pp} = 0.28$, were used in verification simulations of the double cell, the full pipe and the split pipe experiments. The purpose of the verification was to observe if the calibrated values could correctly predict the physical angles of repose, when used in a simulation.

The double cell simulation was carried out using the procedure described in Section 3.4.9. The full pipe simulation was carried out using the procedure described in Section 3.4.6 starting from step (1) to step (6), while the split pipe simulation was carried out using the procedure described in Section 3.4.7 starting from step (1) to step (6).

In all the simulations, the input parameters were set at values given in Table 4.23. Adhesion and cohesion energy density were set at zero since the material was dry.

A summary of the verification simulation results compared against the physically measured values are shown in Table 4.24. The detailed results of the simulations in the form of pictures are documented in Appendix L.2 for the double cell, Appendix J.3 for the full pipe and Appendix K.3 for the split pipe.

Table 4.24: DEM angles of repose verification

Angle of Repose	**DEM Measured Value ($\pm 1^o$)**	**Physically Measured Value ($\pm 1^o$)**
Double Cell Drained	41	41
Double Cell Poured	27	28
Full Pipe Poured	36	36
Split Pipe Poured	21	21

The verification results show that the calibrated parameter values were able to predict the physically measured angles of repose within an error band of 1^o.

4.2.12 DEM angles of repose sensitivities

The purpose of the sensitivity tests was to observe how variations in the coefficient of restitution, particle to wall surface coefficient of sliding friction, and particle density affect the angles of repose. The procedure used was the same as the one used in Section 4.2.11. During the tests, only the input parameter being investigated was adjusted, while the rest of the input parameters were set at values given in Table 4.23, with adhesion and cohesion energy density, each assigned a value of zero (dry material).

Table 4.25 shows the effect of varying the particle to particle coefficient of restitution from its measured value (0.61) to 0.10 on the double cell and full pipe angles of repose.

Table 4.25: Angles of repose sensitivity test, $\epsilon_{pp} = 0.1$

Angle of Repose	**DEM Value** ($\pm 1^o$)	**Physically Measured Value** ($\pm 1^o$)
Double Cell Drained	41	41
Double Cell Poured	28	28
Full Pipe Poured	36	36

Table 4.26 shows the effect of varying the particle to particle coefficient of restitution from its measured value (0.61) to 1.0 on the double cell and full pipe angles of repose.

Table 4.26: Angles of repose sensitivity test, $\epsilon_{pp} = 1.0$

Angle of Repose	**DEM Value** ($\pm 1^o$)	**Physically Measured Value** ($\pm 1^o$)
Double Cell Drained	41	41
Double Cell Poured	**20**	28
Full Pipe Poured	36	36

Table 4.27 shows the effect of varying the particle to wall coefficient of sliding friction from its calibrated value (0.47) to 0.1 on the double cell and full pipe angles of repose.

Table 4.27: Angles of repose sensitivity test, $\mu_{pw,s} = 0.1$

Angle of Repose	**DEM Value** ($\pm 1^o$)	**Physically Measured Value** ($\pm 1^o$)
Double Cell Drained	**23**	41
Double Cell Poured	**21**	28
Full Pipe Poured	36	36

Table 4.28 shows the effect of varying the particle density from its calibrated value (3609 kg/m^3) to 2000 kg/m^3 on the full pipe angle of repose.

Table 4.28: Angles of repose sensitivity test, $\rho_p = 2000$ kg/m^3

Angle of Repose	**DEM Value ($\pm 1^o$)**	**Physically Measured Value ($\pm 1^o$)**
Full Pipe Poured	36	36

Table 4.28 shows the effect of varying the particle density from its calibrated value (3609 kg/m^3) to 5000 kg/m^3 on the full pipe angle of repose.

Table 4.29: Angles of repose sensitivity test, $\rho_p = 5000$ kg/m^3

Angle of Repose	**DEM Value ($\pm 1^o$)**	**Physically Measured Value ($\pm 1^o$)**
Full Pipe Poured	36	36

The detailed snapshots of the DEM sensitivity tests are documented in Appendix L.3 for the double cell and Appendix J.4 for the full pipe.

The angle of repose sensitivity results show that particle density has an insignificant effect on the angle of repose. Variations in the particle to particle coefficient of restitution show that the parameter affects the double cell poured angle of repose in which the flow regime is dynamic, while the other angles in which the flow is quasi-static are unaffected. The particle to wall surface coefficient of sliding friction has shown to have a significant effect on both double cell angles of repose, while it has no effect on the full pipe angle of repose. This means that the particle to wall surface coefficient of sliding friction should be calibrated before using the double cell experiment.

4.2.13 DEM inclined plane test results, moist

The DEM inclined plane test was carried out with a single DEM particle to calibrate the adhesion energy density. The procedure described in Section 3.4.10 was used.

Figure 4.17 shows the variation of kinetic energy of the particle as the inclinometer was rotated for seven values of adhesion energy density specified in the procedure. The point at which the kinetic energy started to rapidly increase marked the angle at which sliding of the particle commenced. Table 4.30 shows the particle sliding angle for each of the six values of adhesion energy density.

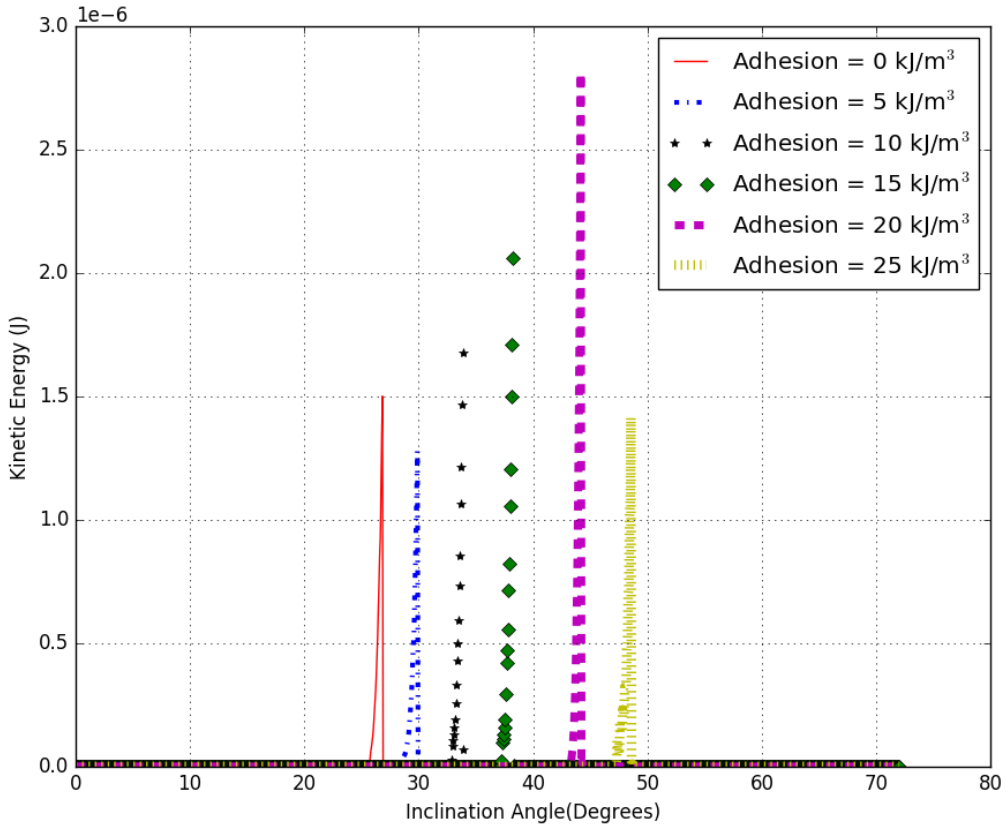


Figure 4.17: Kinetic energy of particles as a function of inclination angle

Table 4.30: Particle sliding as function of adhesion energy density

Adhesion Energy (kJ/m^3)	0	5	10	15	20	25	30
Sliding Angle (°)	24.6	25.7	28.6	32.8	37.2	43.3	47.4

By using the Python program in Appendix A.10, the data in the table was plotted and a first order polynomial equation fitted as shown in Figure 4.18, with $R^2 = 0.99$. The first order relationship is given by Equation 4.7, where ϕ_a is the particle sliding angle (in degrees) associated with adhesion and ED_a is the adhesion energy density in kJ/m^3.

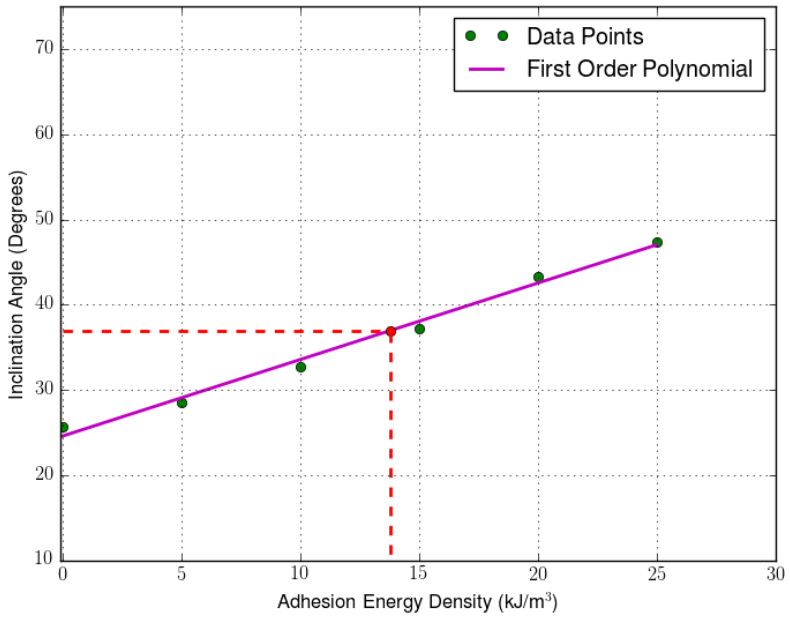


Figure 4.18: Adhesion energy density, first order polynomial

$$\phi_a = 0.87ED_a + 24.6 \tag{4.7}$$

Substituting the physically obtained value of $\phi_a = 37^o$ (Section 4.1.10) into Equation 4.7 yielded a calibrated value of adhesion energy density of 14 kJ/m^3.

The results show that the relationship between the moist particle sliding angle and adhesion energy density can be modelled using a first order polynomial equation, with a high degree of accuracy. The implications are that, the minimum number of DEM experiments required to calibrate adhesion energy density is two. The polynomial equation also shows that the angle of sliding at zero adhesion energy density is approximately 25°. This agrees with sliding angle of a dry particle measured in Table F.1.

Table 4.31 shows an update of the DEM input parameter values after the calibration of adhesion energy density.

Table 4.31: Input parameters update, adhesion energy density tests

Input Parameter	**Value**	**Material State**
$E_{particle}$ (MPa)	10	Dry
E_{wall} (MPa)	10	Dry
$\nu_{particle}$	0.24	Dry
ν_{wall}	0.37	Dry
ϵ_{pp}	0.61	Dry
ϵ_{pw}	0.56	Dry
$\mu_{pw,r}$	0.10	Dry
$\mu_{pw,s}$	0.47	Dry
ρ_p (kg/m^3)	3609	Dry
$\mu_{pp,s}$	0.73	Dry
$\mu_{pp,r}$	0.28	Dry
ED_a (kJ/m^3)	14	Moist
ED_c (kJ/m^3)	Not yet determined	Moist
Timestep (s)	10^{-5}	-

4.2.14 DEM split pipe angle of repose test results, moist

The DEM split pipe angle of repose experiment was carried out to calibrate cohesion energy density using the procedure outlined in Section 3.4.11. Table 4.32 shows a summary of the DEM angles of repose for the seven values of cohesion energy density tested, while Appendix M.2 shows the detailed angle of repose results.

Table 4.32: Angle of repose as a function of cohesion energy density

Cohesion Energy (kJ/m^3)	75	100	125	150	175	200	225
Angle of Repose (^{o})	22.0	23.5	25.5	27.5	29.0	30.5	32.0

The Python program in Appendix A.12 was developed to plot the data in the table, and fit a first order polynomial. Figure 4.19 shows the first order polynomial fit, while Equation 4.8 gives the first order relationship between

the angle of repose and cohesion energy density, where ϕ_{SR} is the split pipe angle of repose in degrees and ED_c is the cohesion energy density in kJ/m^3.

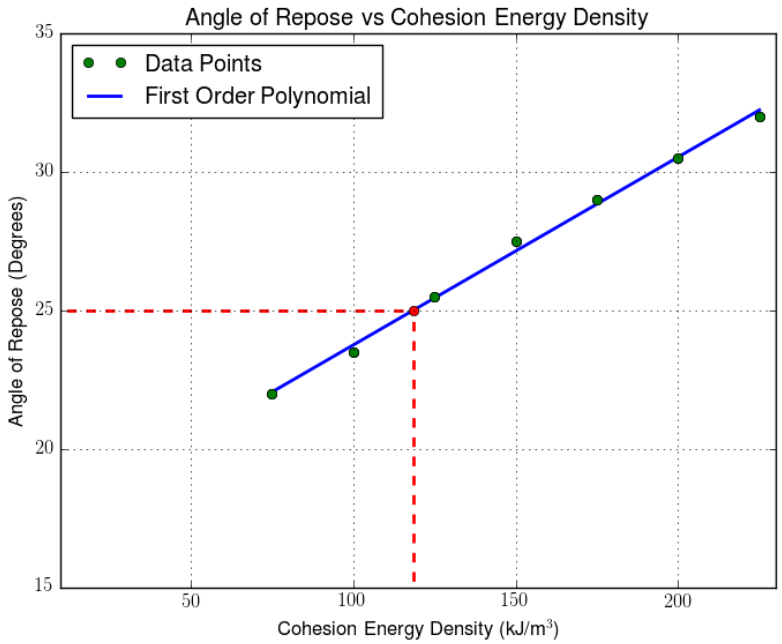


Figure 4.19: Cohesion energy density, first order polynomial

$$\phi_{SR} = 0.0679 ED_c + 17.0 \tag{4.8}$$

The goodness of fit of the first order polynomial is, $R^2 = 1.00$.

Substituting the physically obtained value of $\phi_{SR} = 25^o$ (Section 4.1.11) into Equation 4.8 yielded a calibrated value of cohesion energy density of 118 kJ/m^3.

The results show that the relationship between the moist iron ore split pipe angle of repose and cohesion energy density can be modelled using a first order polynomial equation with a high degree of accuracy. The implications are that, the minimum number of experiments to calibrate DEM cohesion energy density using the angle of repose is two.

Table 4.33 shows an update of the DEM input parameter values after the calibration of cohesion energy density.

Table 4.33: Input parameters update, cohesion energy density tests

Input Parameter	**Value**	**Material State**
$E_{particle}$ (MPa)	10	Dry
E_{wall} (MPa)	10	Dry
$\nu_{particle}$	0.24	Dry
ν_{wall}	0.37	Dry
ϵ_{pp}	0.61	Dry
ϵ_{pw}	0.56	Dry
$\mu_{pw,r}$	0.10	Dry
$\mu_{pw,s}$	0.47	Dry
ρ_p (kg/m^3)	3609	Dry
$\mu_{pp,s}$	0.73	Dry
$\mu_{pp,r}$	0.28	Dry
ED_a (kJ/m^3)	14	Moist
ED_c (kJ/m^3)	118	Moist
Timestep (s)	10^{-5}	-

4.2.15 DEM moist split pipe angle of repose verification

The DEM calibrated cohesion energy density of 118 kJ/m^3 was used in verification simulation of the split pipe angle of repose experiment using the procedure of Section 3.4.11 from step (1) to step (6). The purpose of the verification was to observe if the calibrated value could correctly predict the physical split pipe angle of repose, when used in a simulation.

During the test, the input parameters were set at the values given in Table 4.33.

A simulated split pipe poured angle of repose of was 25^o was obtained as shown in Appendix M.3. This angle is equal to the physically measured angle. This shows that the calibration method yields acceptable results.

4.3 Physical Validation Experimental Results

This section covers the results of physical validation experiments carried out to validate the input parameters obtained during calibration experiments executed in Sections 4.1 and 4.2. The experimental results included mass flow rate and flow profiles of iron ore in the silo, and iron ore flow profile and mass remaining in the chute.

4.3.1 Silo flow, dry material

The silo flow experimental procedure as described in Section 3.5.2 was carried out with dry iron ore in order to measure the iron ore mass flow rate and the flow profiles during silo emptying. The results were needed to compare with an equivalent DEM experiment in order to determine whether the previously calibrated input parameters without cohesion effects could correctly predict the quasi-static flow in the silo.

The experiment was conducted three times. Table 4.34 shows a summary of the average and instantaneous mass flow rates based on the scale and loadcell measurements of dry iron ore respectively. The measurements from the scale were only used to verify the loadcell measurements, while the loadcell average value would be used for comparison with the equivalent DEM experiment. The loadcell mass flow rates were obtained as the magnitudes of the gradients, of the graphs of mass variation with time.

Figure 4.20 shows the loadcell measured variation of mass in the silo. The detailed results of the measured flow rates are documented in Appendix O.1.

Figures 4.21 to 4.25 show the flow profiles captured at different levels of the silo during discharge.

A comparison of the results in Tables 4.34 shows that the loadcell and scale measured mass flow rates were in agreement. This means the obtained load

Table 4.34: Dry silo mass flow rate summary, physical

Statistic	**Scale Based Mass Flow Rate (kg/s)**	**Loadcell Based Mass Flow Rate (kg/s)**
Minimum	1.01	1.02
Maximum	1.02	1.06
Average	1.02	1.03

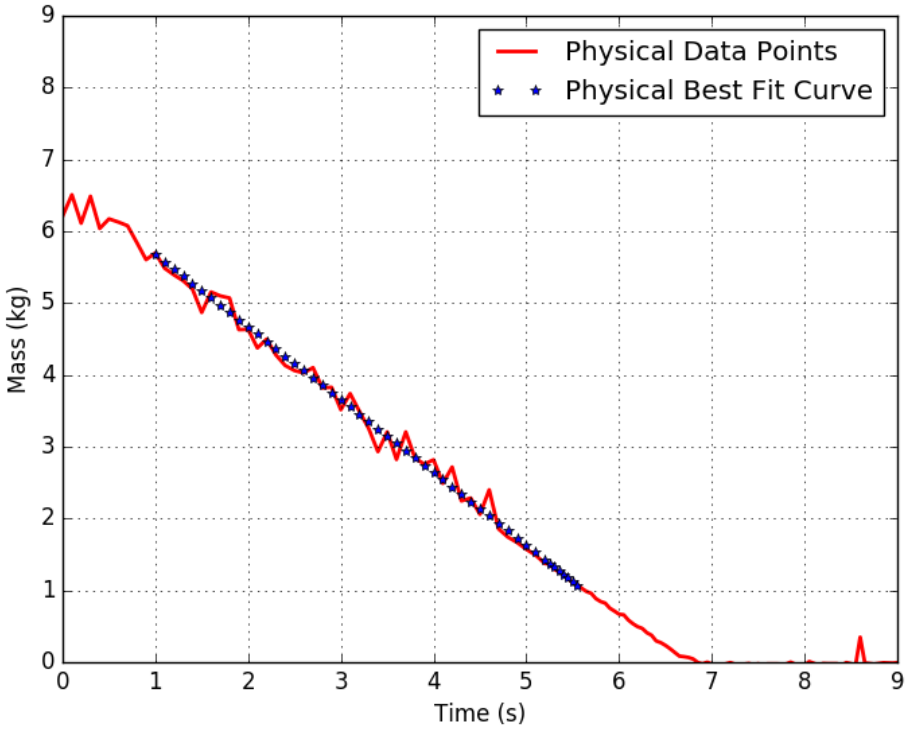


Figure 4.20: Mass variation with time, dry iron ore silo flow

cell average value is reliable. Figure 4.20 shows that the rate of mass reduction in the silo remained constant throughout the discharge process. This means the bulk material was flowing out without sticking on the wall surfaces.



Figure 4.21: Profile of physical silo full of dry iron ore



Figure 4.22: Profile of physical silo three quarters full of dry iron ore



Figure 4.23: Profile of physical silo half full of dry iron ore



Figure 4.24: Profile of physical silo one quarter full of dry iron ore



Figure 4.25: Profile of physical silo one eighth full of dry iron ore

4.3.2 Silo flow, moist material

The silo flow procedure as described in Section 3.5.2 was also carried out with moist iron ore in order to measure the mass flow rate and flow profiles. These would be compared with an equivalent DEM simulation to observe how the calibrated input parameters including cohesion effects, accurately model the real flow.

The experiment was conducted three times. Table 4.35 shows a summary of the scale and loadcell measured mass flow rates of dry iron ore in the silo.

Figure 4.26 shows the loadcell measured variation of mass in the silo. The detailed results of the measured flow rates are documented in Appendix O.2.

Figure 4.27 to Figure 4.30 show the flow profiles captured at different levels of the silo during discharge.

As was the case with dry material, comparison of the results in Tables 4.35

Table 4.35: Moist silo mass flow rate, physical

Statistic	**Scale Measured Mass Flow Rate (kg/s)**	**Loadcell Measured Mass Flow Rate (kg/s)**
Minimum	0.87	0.84
Maximum	0.88	0.88
Average	0.88	0.86

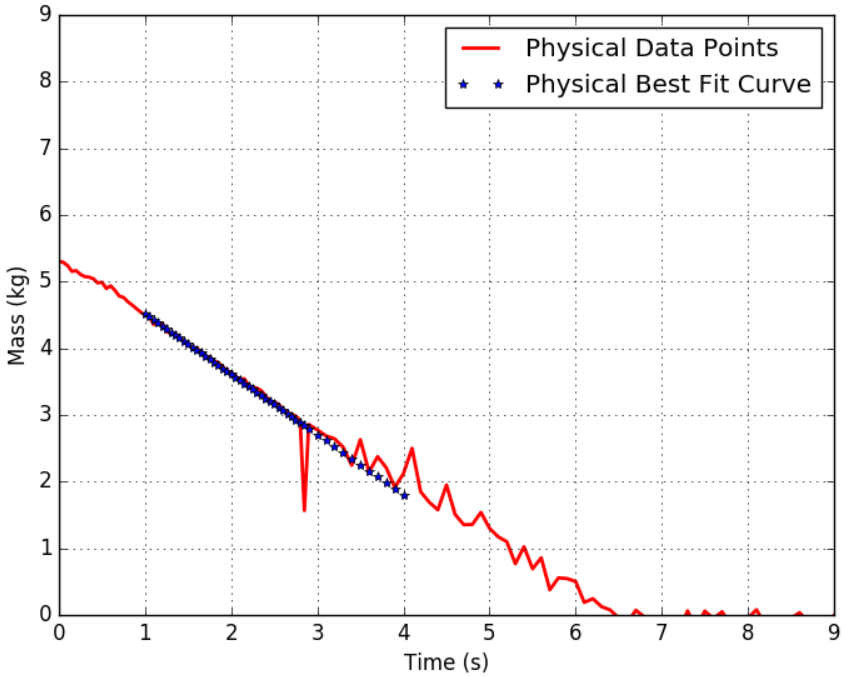


Figure 4.26: Mass variation with time, moist iron ore silo flow

shows that the loadcell and scale measured mass flow rates were in agreement. This means the obtained load cell average value is reliable. Figure 4.26 also shows that the rate of mass reduction in the silo had some oscillations, meaning the bulk material was sticking and slipping on the wall surfaces.



Figure 4.27: Profile of physical silo full of moist iron ore



Figure 4.28: Profile of physical silo half full of moist iron ore



Figure 4.29: Profile of physical silo one quarter full of moist iron ore



Figure 4.30: Profile of physical silo one eighth full of moist iron ore

4.3.3 Chute flow, dry material

The chute flow experiment was carried out with dry iron ore in order to measure the mass of material that remained in the chute after flow had stopped, and the flow profiles using the procedure outlined in Section 3.5.3. The results would then be compared to an equivalent DEM simulation to validate the capability of the calibrated input parameters to correctly model flow under dynamic conditions.

Table 4.36 shows the mass of dry iron ore remaining in the chute after flow stopped, while Figure 4.31 and Figure 4.32 show the flow profiles of dry iron ore in the chute during steady flow and after had flow ceased respectively.

Table 4.36: Dry remaining mass in the chute, physical

Test Number	**Mass Remaining in Chute (kg)**
1	0.85
2	0.80
Average	0.83

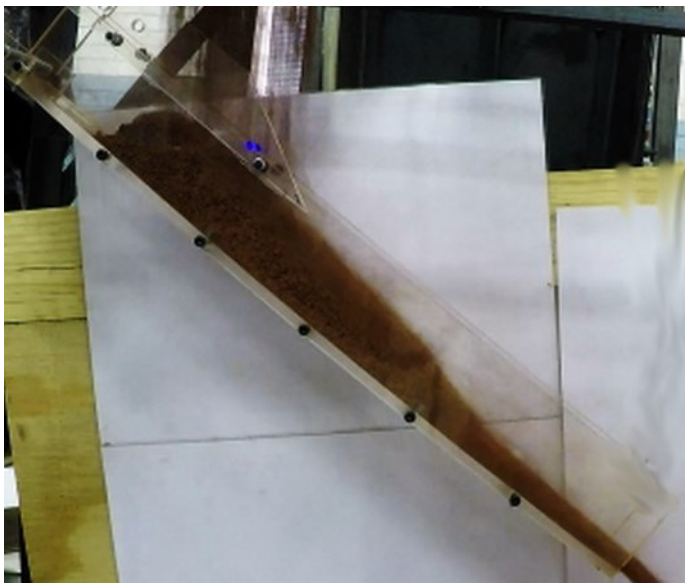


Figure 4.31: Profile of physical dry iron ore, chute steady flow

The results of mass remaining in the chute shows a small variation between the two tests conducted. The profile of the material remaining in the chute

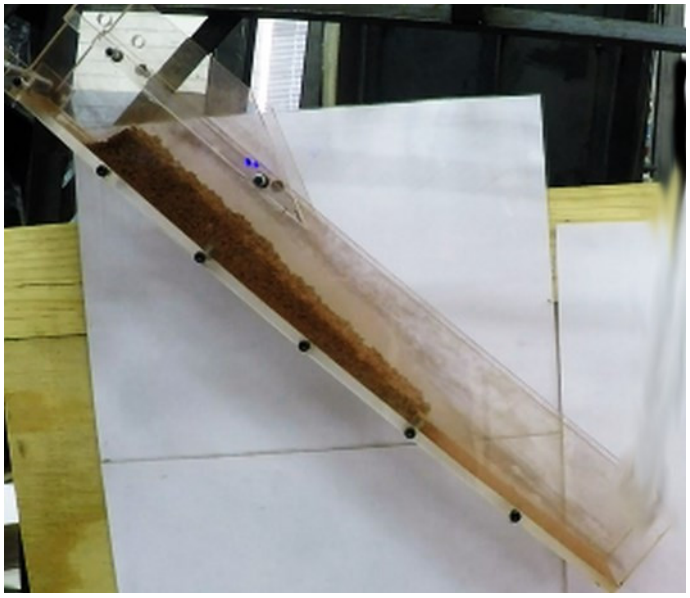


Figure 4.32: Profile of physical dry iron ore remaining in chute

shows that material stagnation was due to entrapment by the ledges at the bottom surface of the chute, as opposed to wall friction effect.

4.3.4 Chute flow, moist material

The same experimental procedure as carried out in Section 4.3.3 was performed with moist iron ore in chute. Table 4.37 shows the mass of moist iron ore remaining in the chute after flow stopped, while Figure 4.33 and Figure 4.34 show the flow profiles of moist iron ore in the chute during steady flow and after flow ceased respectively.

Table 4.37: Moist remaining mass in the chute, physical

Test Number	**Mass Remaining in Chute (kg)**
1	1.08
2	1.13
Average	1.11

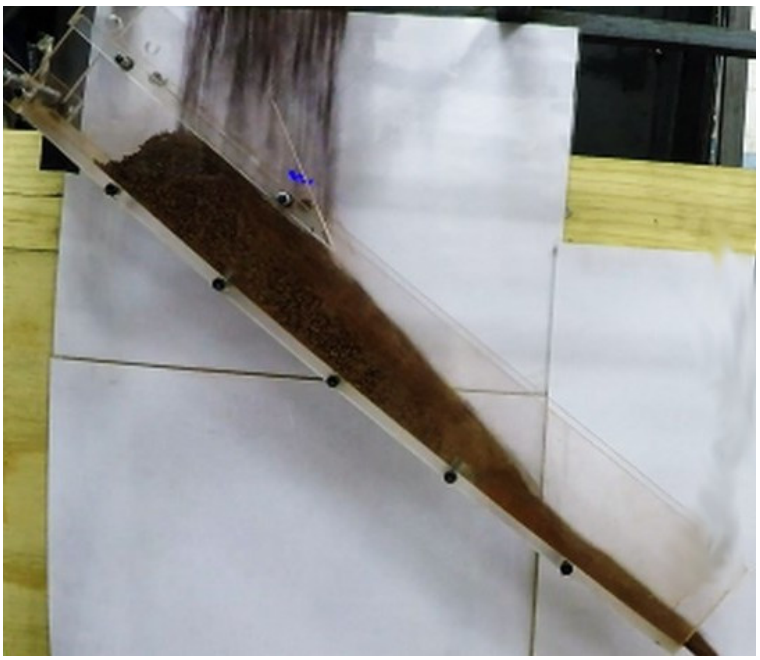


Figure 4.33: Profile of physical moist iron ore, chute steady flow

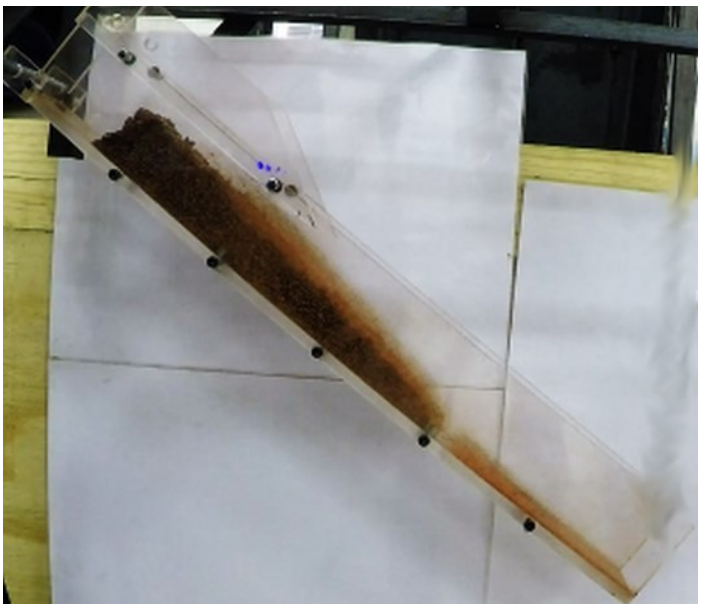


Figure 4.34: Profile of physical moist iron ore remaining in chute

The results of mass remaining in the chute shows a small variation between the two tests. The profile of the material remaining in the chute shows that material stagnation was due to entrapment by the ledges at the bottom surface of the chute.

4.4 DEM Validation Experimental Results

This section covers the results of DEM simulations for silo flow and chute flow using the calibrated input parameter values given in Table 4.33. The simulation results were compared to the results of the corresponding physical tests carried out in Section 4.3. Input parameters were also systematically varied from the calibrated values, and DEM experiments executed to observe the effect of input parameters on the quasi-static and dynamic flow regimes.

4.4.1 DEM silo flow test results, dry material

The procedure outlined in Section 3.6.1 was used with dry iron ore. Figure 4.35 shows the plot of mass remaining in the silo during the simulated discharge of material when using the calibrated parameter values, together with the loadcell measured discharge. The magnitude of the gradient of the plot during silo discharge was determined to be 1.33 kg/s. This value represented the magnitude of the mass flow rate for DEM simulated dry iron ore in the silo.

Table 4.38 shows a comparison of the DEM measured mass flow rate and the physically measured mass flow rates for dry iron ore.

Figures 4.36 to 4.40 show comparisons of the DEM and physical dry iron ore flow profiles at specific corresponding positions during silo discharge.

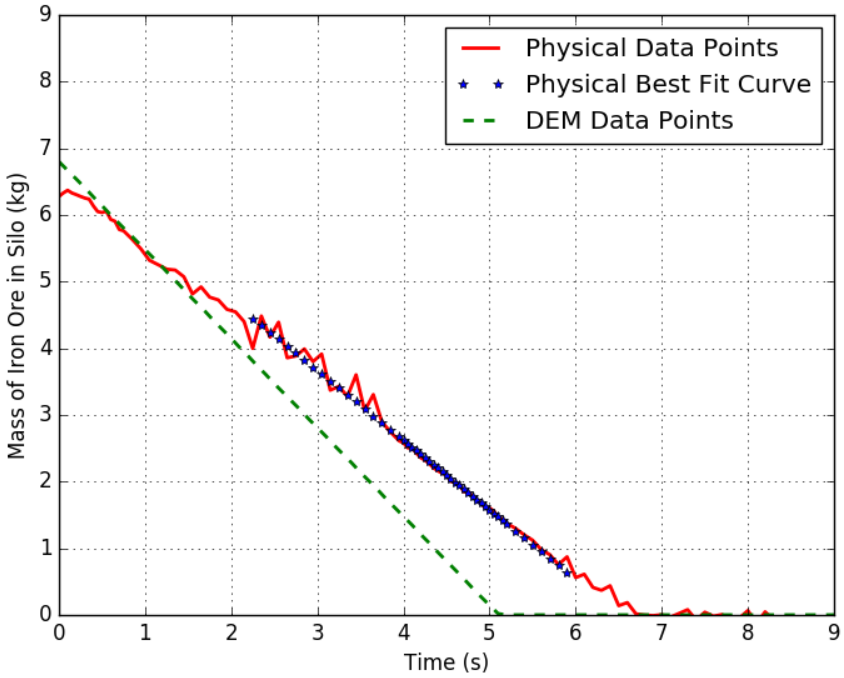


Figure 4.35: Silo flow mass variation with time, DEM dry

Table 4.38: Comparison of DEM and physical flow rates, dry

DEM Measured Mass Flow Rate (kg/s)	**Load Cell Measured Mass Flow Rate (kg/s)**
1.33	1.03

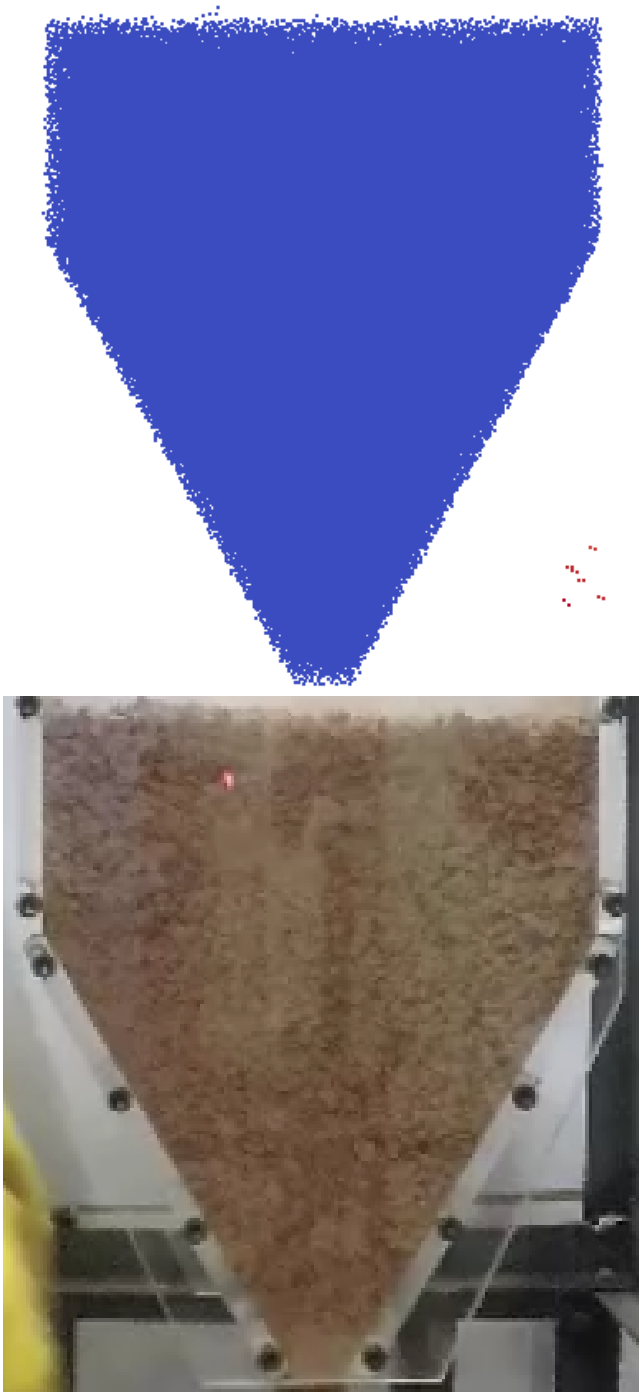


Figure 4.36: Flow profiles comparison, full silo, dry

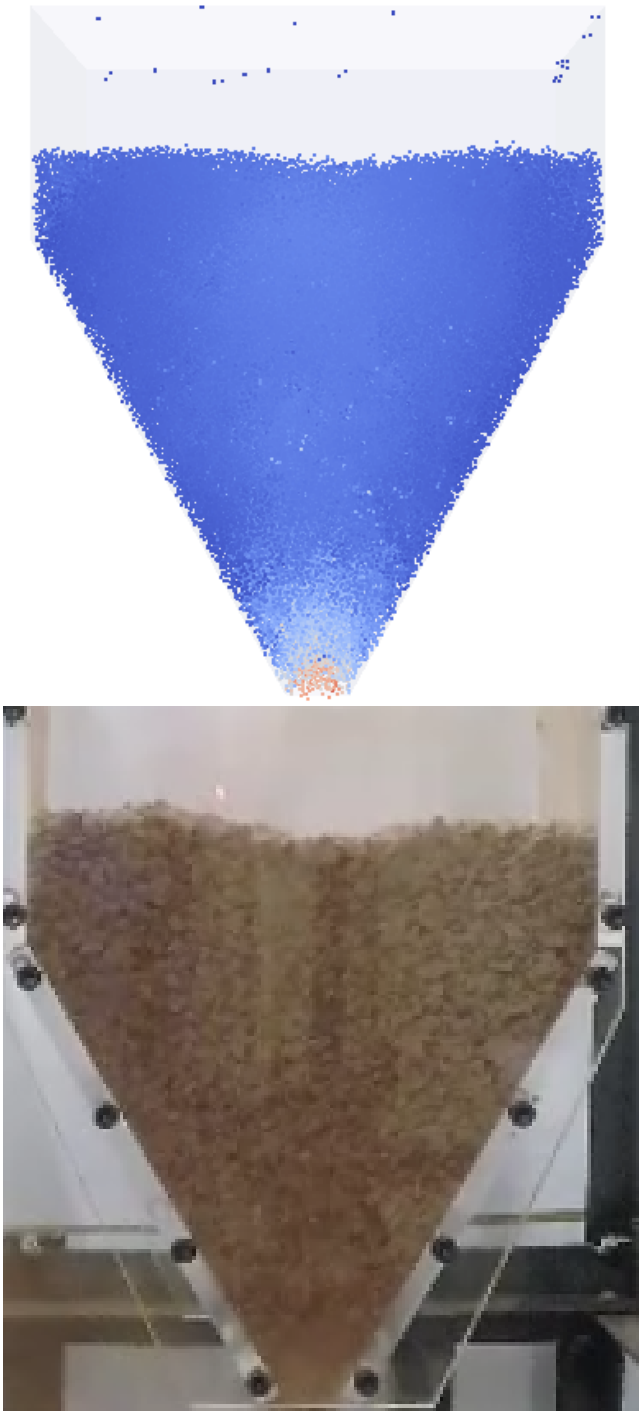


Figure 4.37: Flow profiles comparison, three quarters full silo, dry



Figure 4.38: Flow profiles comparison, half full silo, dry

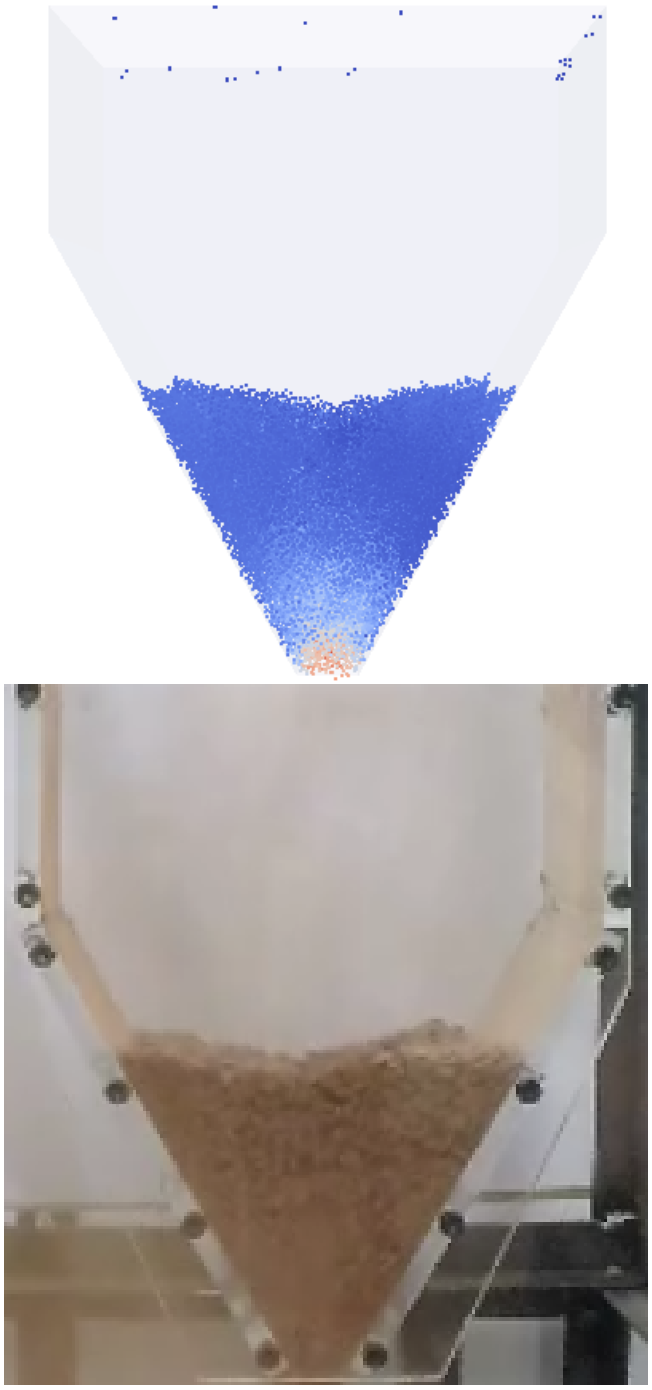


Figure 4.39: Flow profiles comparison, one quarter full silo, dry

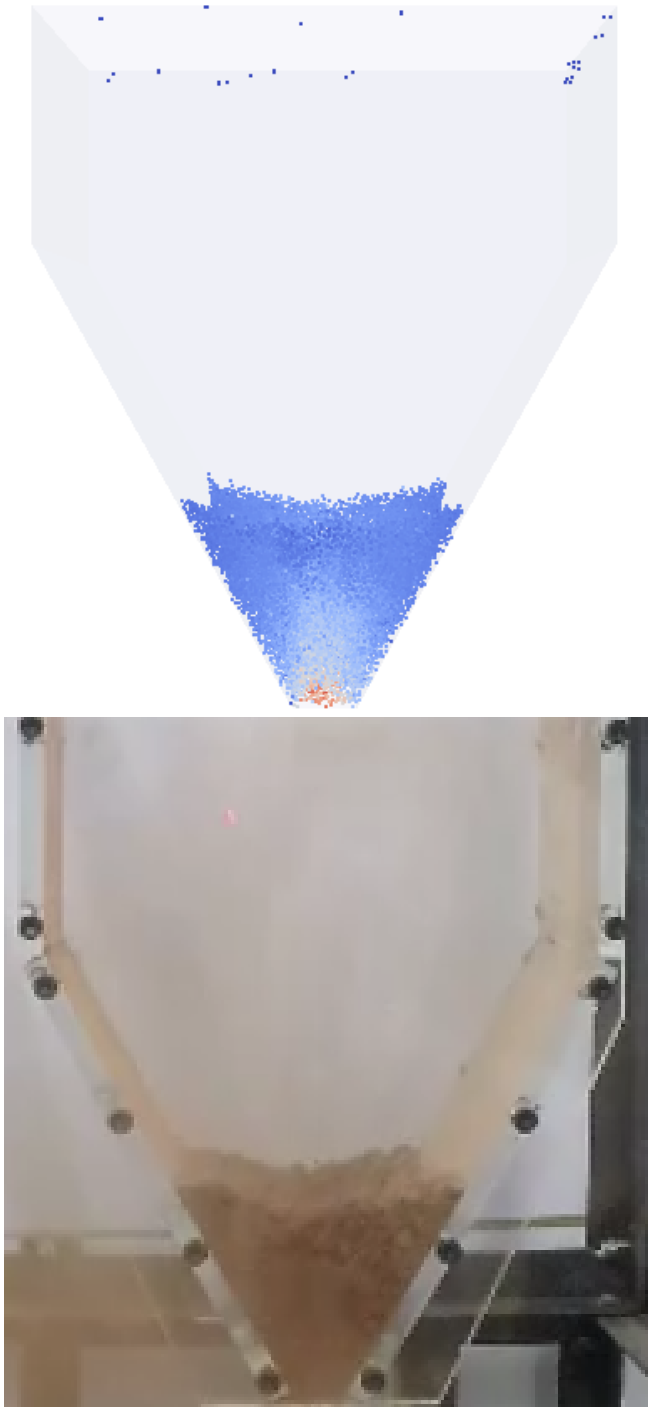


Figure 4.40: Flow profiles comparison, one eighth full silo, dry

The results show that DEM simulations using the calibrated input parameters predicted a higher mass flow rate as compared to the physically measured mass flow rate by 22.6%. However, the flow profiles at different positions of the DEM and physical material compared very well, as shown in Figures 4.36 to 4.40. The fact that material discharged faster in the DEM simulated flow

than in the physical flow meant there was more relative mobility of particles in the DEM test than in the physical test. Material mobility in the silo is a function of particle to particle and particle to wall coefficients of friction.

Given that during calibration experiments, the model equations for particle to particle coefficients of sliding and rolling friction (Equations 4.3 and 4.4) gave the least goodness of fit (0.97 and 0.93 respectively), compared to the particle to wall surface coefficient of sliding friction, the two inter-particle friction coefficients were each perturbed by 10% to observe their effect on the silo mass flow rate. Since DEM flow had shown more material mobility, the particle to particle coefficients of sliding and rolling friction were increased in order to reduce material mobility. Figures 4.41 and 4.42 shows the DEM mass variation in the silo when the particle to particle coefficients of sliding and rolling friction were increased, one at a time, by 10% to 0.80 and 0.31 respectively.

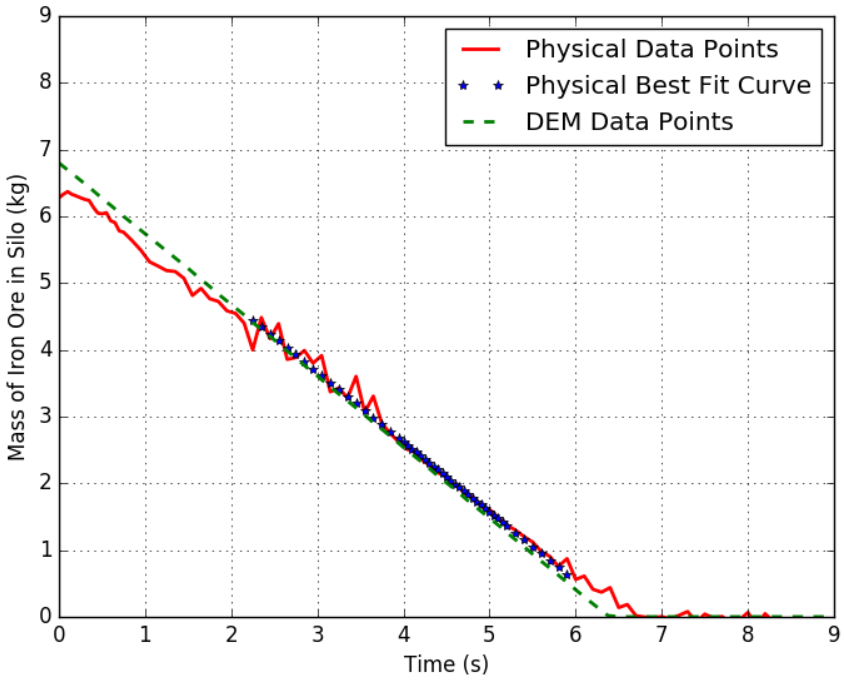


Figure 4.41: Silo flow mass variation with time, DEM $\mu_{pp,s} = 0.80$

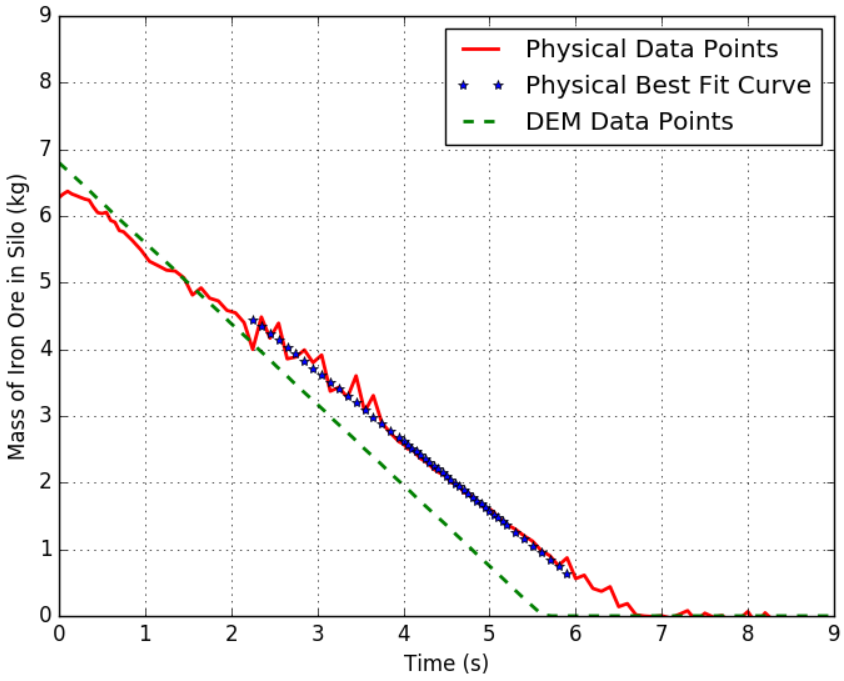


Figure 4.42: Silo flow mass variation with time, DEM $\mu_{pp,r} = 0.31$

Table 4.39 shows the comparison of the adjusted DEM parameters mass flow rate and the physically measured mass flow rate.

Table 4.39: Comparison of DEM and physical flow rates, adjusted parameters

DEM Measured $\mu_{\mathbf{pp,s}} = \mathbf{0.80}$ **(kg/s)**	**DEM Measured** $\mu_{\mathbf{pp,r}} = \mathbf{0.31}$ **(kg/s)**	**Load Cell Measured Mass Flow Rate (kg/s)**
1.07	1.21	1.03

The results show that an increase of the particle to particle coefficient of sliding friction by 10% reduced the DEM silo mass flow rate to 1.07 kg/s, which differs by 3.7% from the physically measured flow rate. However, an increase of the particle to particle coefficient of rolling friction only reduced the flow rate to 1.21 kg/s, which differs by 14.9% from the physically measured flow rate. These results show that silo flow rate is very sensitive to variations in the particle to particle coefficient of sliding friction. As such, calibration experiments for this parameter need to be precise. In this research, the angle of repose whose measurement had potential to introduce errors was used (see Section 5.3.1).

This reduced the accuracy of the fitted model, and consequently the predicted parameter values.

4.4.2 DEM silo flow sensitivity results

Silo flow sensitivity tests were performed on dry iron ore using the method described in Section 3.6.1, in order observe the effects of various input parameters on the quasi-static flow regime. The particle to particle coefficients of sliding and rolling friction, particle to wall coefficient of sliding friction, particle to particle coefficient of restitution and particle to wall coefficient of restitution were varied one at a time, while the rest of the input parameters were maintained at their calibrated values, given in Table 4.33.

Figure 4.43 shows the variations of mass remaining in the silo during material discharge for the varied input parameters. The gradient of each mass variation with time in the figure was computed, whose magnitude was the mass flow rate.

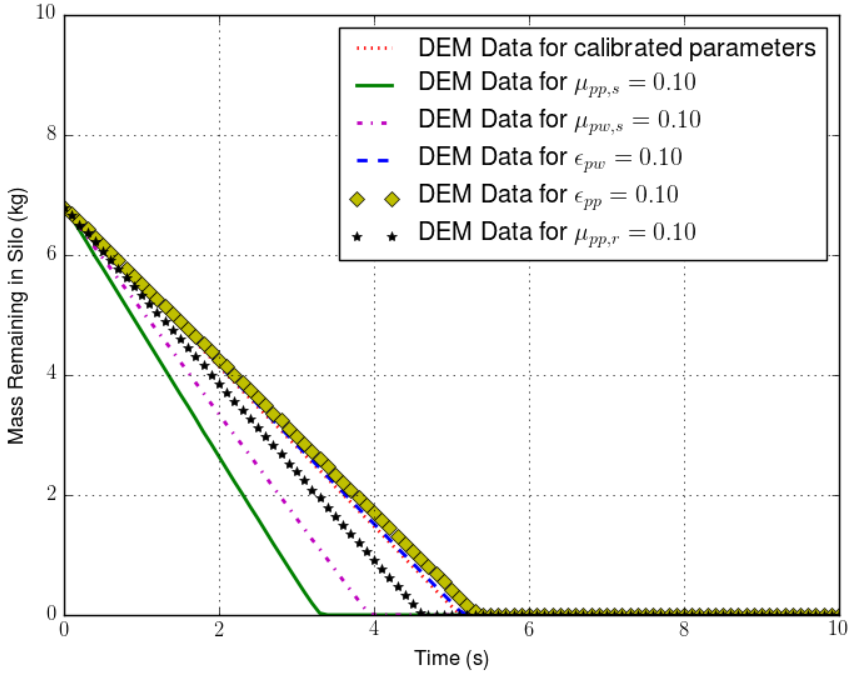


Figure 4.43: Silo flow mass rate sensitivity

Table 4.40 shows the tabulated DEM mass flow rates for each of the varied input parameters, and the deviation in percentage from the mass flow rate of 1.33 kg/s, obtained when all the input parameters were set at their calibrated values.

Table 4.40: Sensitivity of DEM silo mass flow rate

Adjusted Parameter Value	**Mass Flow Rate (kg/s)**	**Deviation (%)**
$\mu_{pp,s} = 0.1$	2.08	56.4
$\mu_{pp,r} = 0.1$	1.47	10.5
$\mu_{pw,s} = 0.1$	1.73	30.1
$\epsilon_{pp} = 0.1$	1.27	4.51
$\epsilon_{pw} = 0.1$	1.32	0.75

The largest variation in mass flow rate was observed when the particle to particle coefficient of sliding friction was changed from 0.73 to 0.1 where the flow rate changed from 1.33kg/s to 2.08kg/s. This change is 56.4% of the calibrated value. The increase in flow rate is consistent with the fact that reducing the coefficient of friction increases particle mobility.

Changing the particle to wall coefficient of sliding friction from the calibrated value of 0.47 to 0.1 resulted in the flow rate changing from 1.33kg/s to 1.73kg/s. This change is a 30.1% change from the calibrated value. Again the increased mass flow rate is consistent with the reduced coefficient of friction.

Changing the particle to wall coefficient of restitution from the calibrated value of 0.56 to 0.1 resulted in no significant change in the mass flow rate as it changed from 1.33kg/s to 1.32kg/s. This means that the particle to wall coefficient of restitution plays no significant role in the silo flow.

Changing the particle to particle coefficient of restitution from the calibrated value of 0.61 to 0.1 resulted in no significant change in the mass flow rate which changed from 1.33kg/s to 1.27kg/s. This points to the fact that the particle to particle coefficient of restitution is of no significance in the silo flow process.

Changing the particle to particle coefficient of rolling friction from the calibrated value of 0.28 to 0.1 resulted in a change of flow rate from 1.33kg/s to 1.47kg/s. This change is 10.5% of the calibrated value.

4.4.3 DEM silo flow test results, moist material

The procedure outlined in Section 3.6.1 was used with moist iron ore. The mass of iron ore remaining in the silo during discharge of material as a function of time was plotted as shown in Figure 4.44. The physically measured mass flow rate, and DEM mass flow rate with the particle to particle coefficient of sliding friction increased by 10% were plotted on the same graph.

The magnitudes of the gradients of the DEM plots during silo discharge were determined to be 0.94 kg/s and 0.86 kg/s for the calibrated parameters and 10% adjusted particle to particle coefficient of sliding friction respectively. These values represented the magnitudes of the two respective mass flow rates for DEM simulated moist iron ore in the silo.

Table 4.41 shows a comparison of the two DEM measured mass flow rates and the physically measured mass flow rate for moist iron ore.

Table 4.41: Comparison of DEM and physical flow rates, moist

DEM Measured Mass Flow Rate (kg/s)	**DEM Measured $\mu_{pp,s} = 0.80$ (kg/s)**	**Load Cell Measured Mass Flow Rate (kg/s)**
0.94	0.86	0.85

The results show that by using the calibrated parameters without any adjustments, the DEM mass flow rate is higher than the measured mass flow rate by 9.6%. However an increase in the calibrated particle to particle coefficient of sliding friction by 10% reduced the DEM mass flow rate to within 1.1% of the measured mass flow rate. The results show that the particle to particle coefficient of sliding friction was underestimated during calibration.

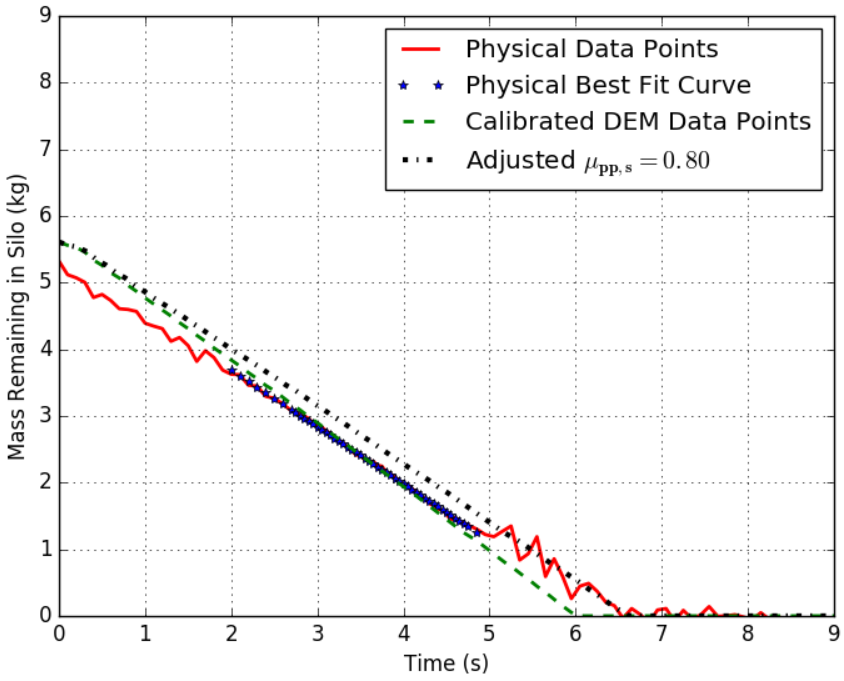


Figure 4.44: Silo flow mass variation with time, DEM moist

This underestimation may have stemmed from the angle of repose calibration experiments used to calibrate the particle to particle friction coefficients.

Figures 4.45 to 4.48 show comparisons of the DEM and physical moist iron ore flow profiles at specific corresponding positions during silo discharge. The flow profiles show a good correspondence between the DEM and the physical flows.

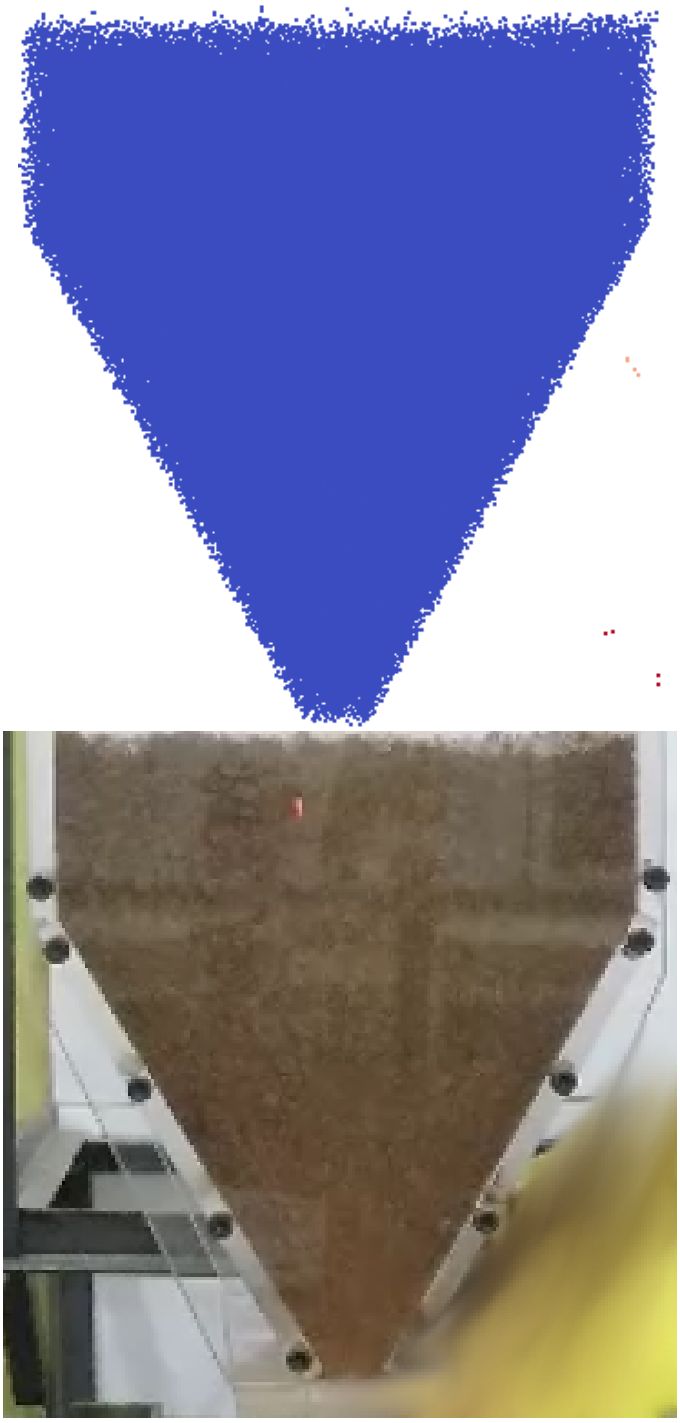


Figure 4.45: Flow profiles comparison, full silo, moist



Figure 4.46: Flow profiles comparison, half full silo, moist

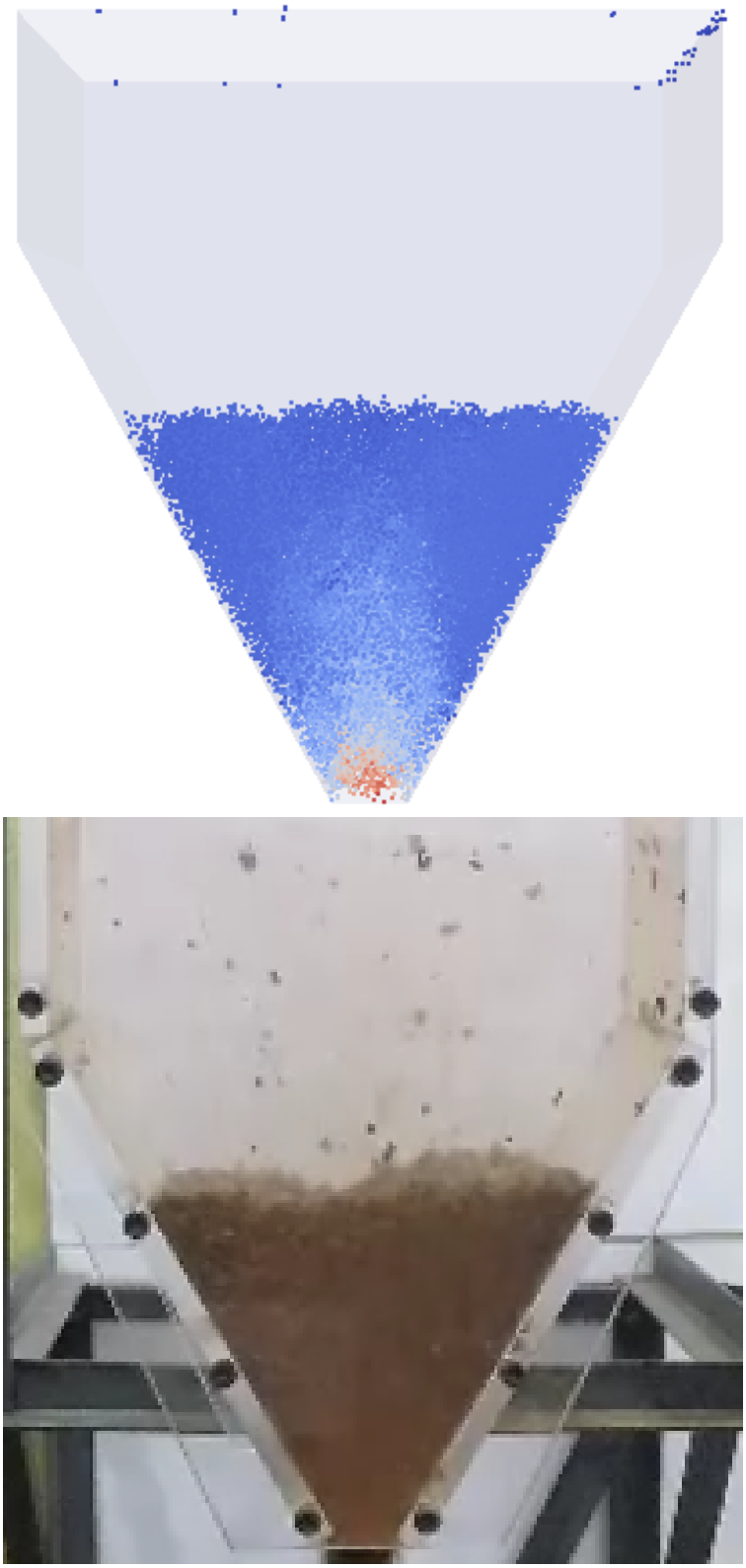


Figure 4.47: Flow profiles comparison, one quarter full silo, moist

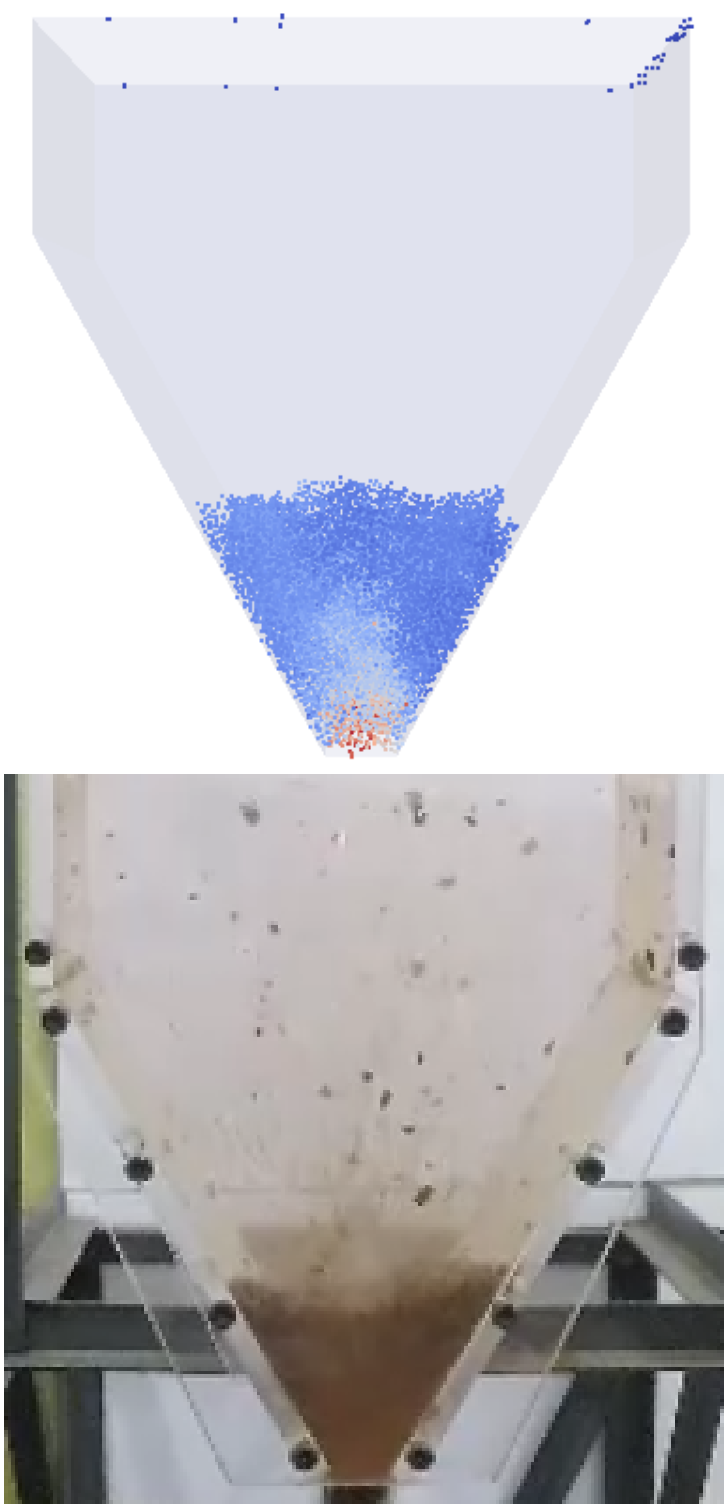


Figure 4.48: Flow profiles comparison, one eighth full silo, moist

4.4.4 DEM chute flow test results, dry material

The DEM chute flow procedure was carried out on dry iron ore to determine the mass of material that remained in the chute after flow had stopped, and the flow profiles. The procedure described in Section 3.6.2 was used.

The total mass of DEM material remaining in the chute after flow had stopped, using the calibrated parameter values was calculated as specified in the procedure to be 0.54 kg, which was less than the physically measured value of 0.83 kg by 34%. The calibrated value of particle to particle coefficient of sliding friction was increased by 10% from 0.73 to 0.80, and the DEM simulation predicted the remaining mass of 0.81 kg which was within 2.4% of the physically measured value. These results confirm the observations of under-estimation of the particle to particle coefficient of sliding friction made during silo flow experiments.

Figure 4.49 shows a comparison of the DEM flow profile using the calibrated parameter values and physical dry iron ore flow profiles during steady state flow. The two profiles showed a good correspondence.

Figure 4.50 shows the flow profiles when flow had ceased for the DEM flow using the calibrated parameter values at the top, DEM flow using particle to particle coefficient of sliding friction of 0.80 in the middle, and the physical flow profile at the bottom.

The results of the material profiles after flow had ceased show that the adjusted DEM particle to particle coefficient of sliding friction predicted a profile that corresponds well to the physically measured profile.

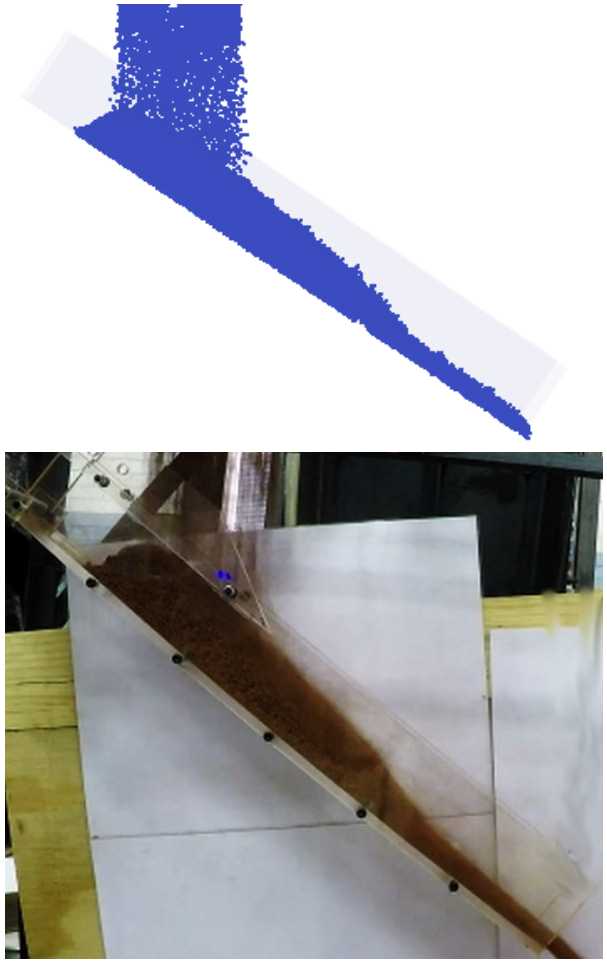


Figure 4.49: Chute flow profiles comparison, steady flow, dry

4.4.5 DEM chute flow sensitivity results

The procedure described in Section 3.6.2 was used to investigate the sensitivity of mass of material remaining in the chute after flow had stopped, with input parameter variations. In each experiment only one input parameter value was varied while all the other input parameters were set at their calibrated values, given in Table 4.33.

Table 4.42 shows the mass of DEM material remaining in the chute after flow had stopped, when specific input parameters were adjusted from their calibrated value. The table also shows the percentage deviation from the mass remaining of 0.544 kg, obtained when all the input parameters were set at their calibrated values.

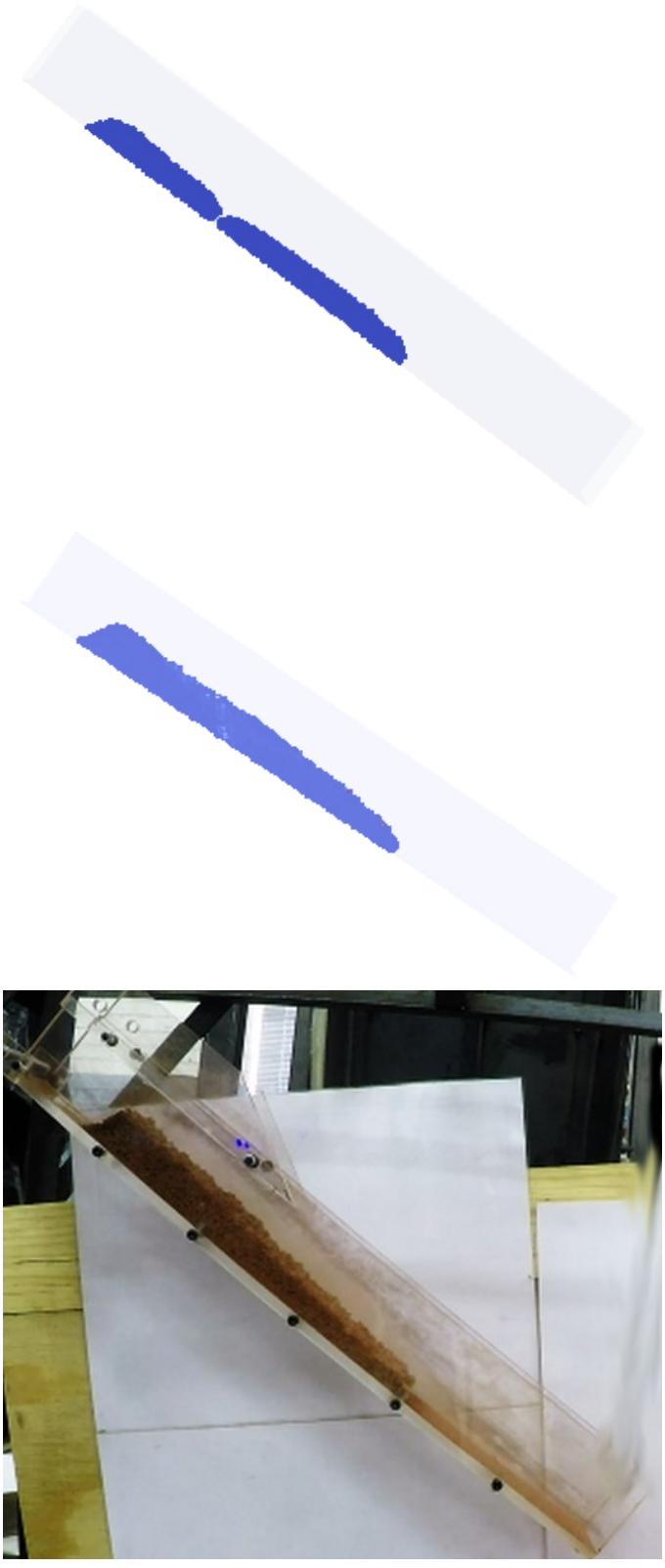


Figure 4.50: Chute flow profiles comparison, stationary, dry

Table 4.42: Sensitivity of DEM mass of material remaining on chute

Adjusted Parameter Value	**Remaining Mass (kg)**	**Deviation (%)**
$\mu_{pp,s} = 0.10$	0.122	77.6
$\mu_{pp,r} = 0.10$	0.284	47.8
$\mu_{pw,s} = 0.10$	0.148	72.8
$\mu_{pw,r} = 0.05$	0.516	5.15
$\epsilon_{pp} = 0.10$	0.554	1.84
$\epsilon_{pw} = 0.10$	0.478	12.1

The results of Table 4.42 show that the particle to particle coefficients of sliding and rolling friction have a significant effect on the chute flow. The particle to wall coefficient of sliding friction and particle to particle coefficient of restitution also show a significant effect on the bulk material flow in the chute. The particle to wall coefficient of rolling friction has a fairly insignificant effect on the chute flow, this observation is similar to observations made on the wall friction test (Section 4.2.7). This means material adjacent to a wall surface will slide instead of rolling when being confined. The impact of the coefficient of restitution on the flow was more significant as the coefficient of restitution approached 1.0 while it was insignificant as it approached 0.0. The dominant flow regime in this application was dynamic. These results therefore show that for dynamic flow regime, both the frictional and collisional parameters play a critical role in defining the flow mechanism, as such they must be accurately calibrated.

4.4.6 DEM chute flow test results, moist material

The DEM chute flow procedure was carried out on moist iron ore to determine the mass of material that remained in the chute after flow had stopped, and the flow profiles. The procedure described in Section 3.6.2 was followed.

The total mass of DEM material remaining in the chute after flow had stopped, using the calibrated parameter values was calculated as specified in the procedure to be 0.90 kg, which was less than the physically measured value of 1.11 kg by 18.9%. The calibrated value of particle to particle coefficient of sliding friction was increased by 10% from 0.73 to 0.80, and the DEM simulation predicted the remaining mass of 1.07 kg which was within 3.6% of the physically measured value. These results show that calibration experiments underestimated the value of the particle to particle coefficient of sliding friction.

Figure 4.51 shows a comparison of the DEM flow profile using the calibrated parameter values and physical dry iron ore flow profiles during steady state flow. The two profiles showed a good correspondence.

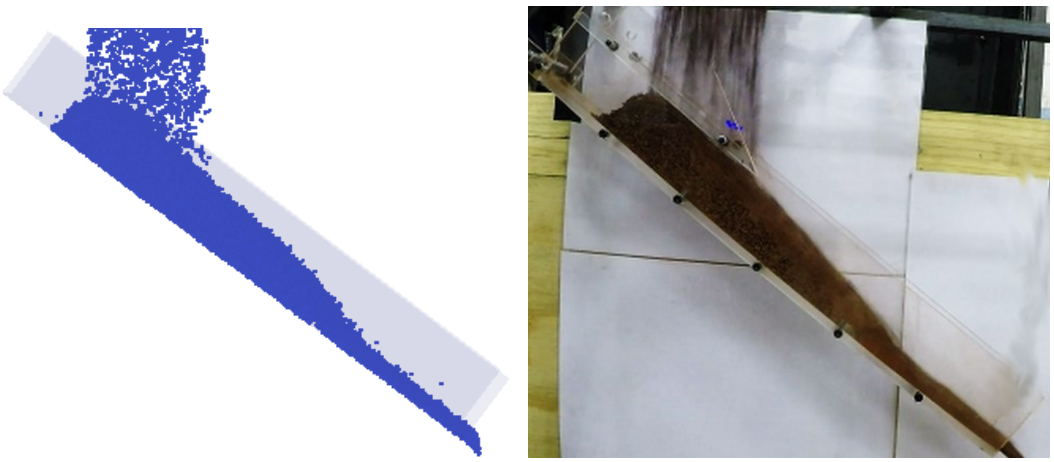


Figure 4.51: Chute flow profiles comparison, steady flow, moist

Figure 4.52 shows the flow profiles when flow had ceased for the DEM flow using the calibrated parameter values at the top, DEM flow using particle to particle coefficient of sliding friction of 0.80 in the middle, and the physical flow profile at the bottom.

As was the case with dry material flow, the results of the material profiles after flow had ceased show that the adjusted DEM particle to particle coefficient of sliding friction predicted a profile that corresponds well to the physically measured profile..

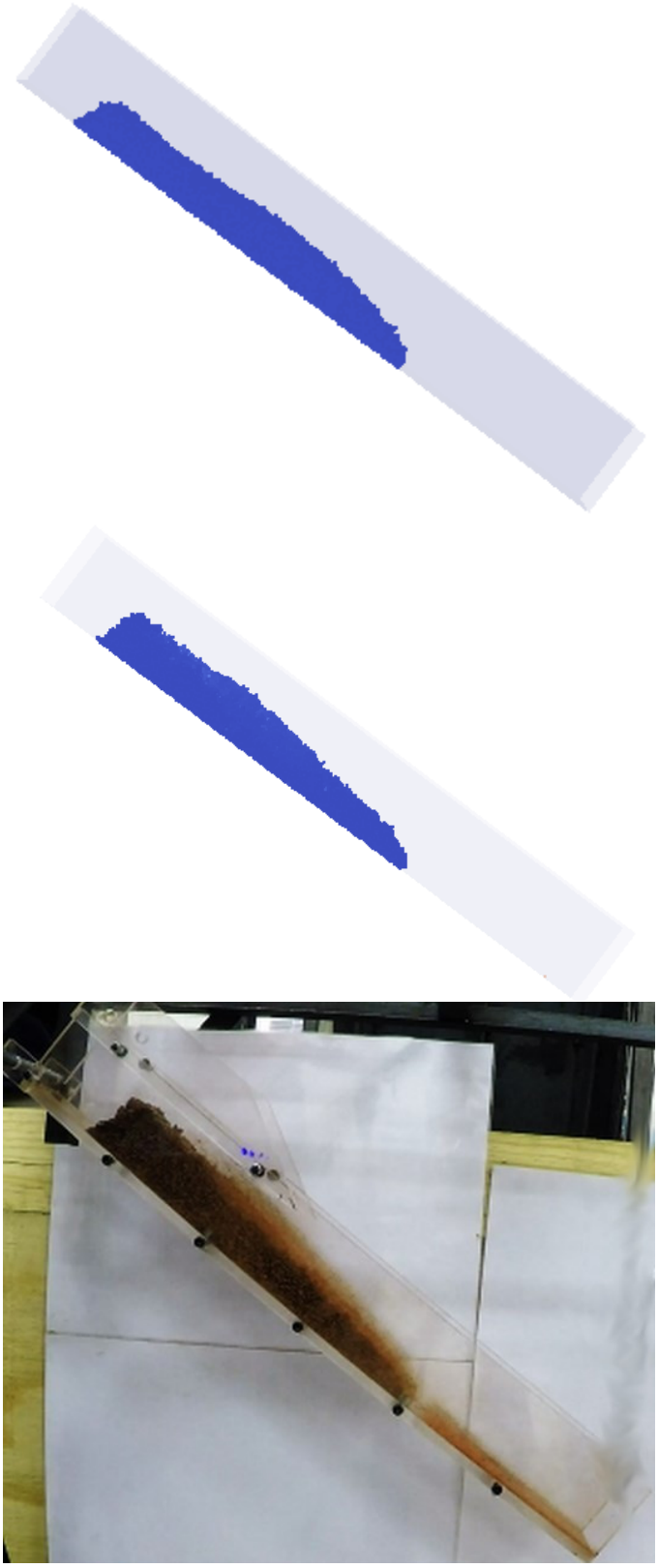


Figure 4.52: Chute flow profiles comparison, stationary, moist

5 Discussion

This chapter discusses the results of the experimental activities documented in Chapter 4. The discussion is organised into three main sections, namely the calibration framework in Section 5.1, calibration experiments in Section 5.2, and results validation in Section 5.3.

5.1 Calibration Framework

In order to simulate the behaviour of bulk material in a physical system, a number of input parameters are required. Previous work in DEM calibration relied on direct measurements or random parameter adjustment, but these approaches have not been satisfactory. The aim of this research was to develop a structured approach that would allow a dominant parameter to be calibrated in a specific sequence of experiments. This approach has been called a 'structured calibration framework' in this report.

Figure 5.1 shows the major components of the structured framework, which was used in the calibration of an iron ore DEM model in this research. It included parameters that could be measured or deduced from literature, as well as those determined in an experimental calibration programme. The logic behind the framework is as follows.

The framework begins with conducting direct measurements of the directly measurable input parameters in box 1, comprising the coefficients of restitu-

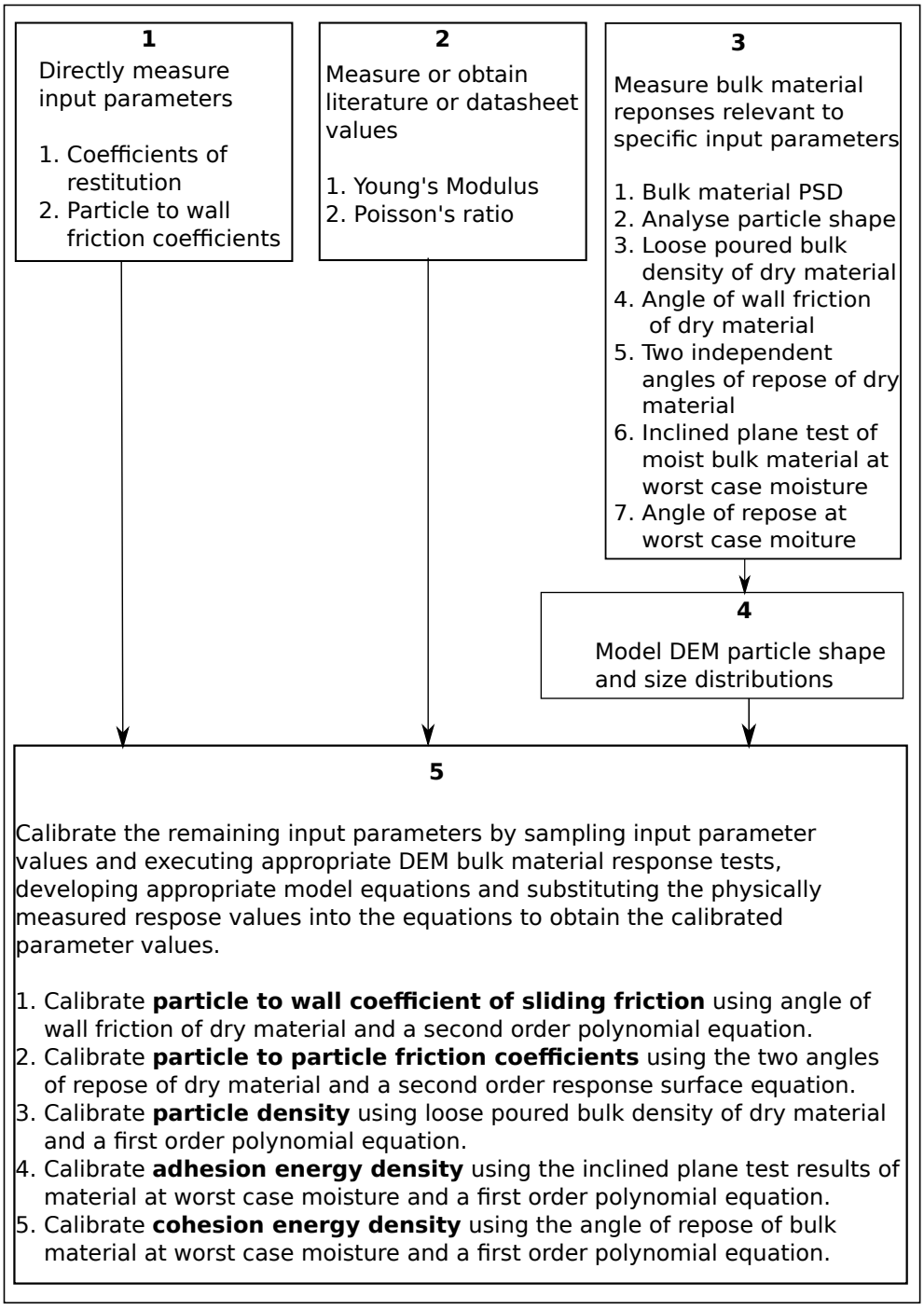


Figure 5.1: Structured DEM calibration framework

tion and the particle to wall surface coefficient of rolling friction. Literature acquired input parameters in box 2, comprising the Young's Modulus and Poisson's ratio are then obtained for both the particle and wall surfaces. These two categories of input parameters are independent of each other and could

be determined in any order. These parameters are determined before the onset of DEM calibration experiments begin, so that unknown variables may be reduced.

Next, specific experiments are identified which will yield bulk material responses (box 3). For this research, these included the bulk material PSD test, bulk density test, Jenike wall friction test, angle of repose tests, and the inclined plane test. These experiments are identified in relation to the DEM parameters to be determined (given in box 4 and 5), including the particle to wall surface coefficient of sliding friction, particle to particle friction coefficients, particle density, and for moist materials, adhesion and cohesion energy densities. The possible and commonly used bulk material responses are numbered 1 to 7 in box 3. The physical experiments in box 3 are not necessarily prescriptive and may be altered if other suitable bulk responses that can isolate the effects of input parameters in box 5 can be identified. The identified bulk experiments in box 3 are then carried out physically and may be done independently of the parameters in boxes 1 and 2; hence boxes 1, 2 and 3 can be conducted in any order.

The DEM particle shape and size distributions are modelled in box 4, based on the results of the physically measured PSD and shape analysis of real particles in box 3. This step is the primary reason for calibrating and not directly measuring all the input parameters because it introduces differences between the real material and the DEM material. These differences are inevitable due to the difficulty of modelling each shape and size of particle in DEM (as found in the real material), and would lead to significant difficulties associated with the limitations that are imposed by the available computational resources. The input parameter values that are obtained in box 5, are only valid for the particle shape and size distributions modelled at this stage. Because the PSD and shape influence the simulation time, the user may choose to conduct some preliminary tests to gauge the time required for the chosen DEM PSD and shape distributions. This approach for determining the optimal shape and size was reported and recommended by Grima and Wypych (2011*a*).

Using the results from boxes 1, 2, 3 and 4, the bulk material response calibrated input parameters are then determined in box 5, by simulating the physical experiments carried out in box 3. The input parameters in box 5 are calibrated in a sequential order that acknowledges the effect of the previously calibrated input parameters on the subsequent calibration experiments.

The first parameter to be calibrated is the particle to wall coefficient of sliding friction because it affects some of the downstream experiments such as the angle of repose, used in calibrating the the particle to particle coefficients of sliding friction, and the sliding angle used to calibrate adhesion energy density. The particle to particle friction coefficients (sliding and rolling) are then calibrated next because the particle to particle coefficient of sliding friction is known to significantly affect bulk density, which is then used in calibrating particle density. For dry materials, particle density is calibrated last. However, for moist material, adhesion energy density and cohesion energy density must also be calibrated. Of the two parameters, adhesion energy density is calibrated first because the angle of repose used to calibrate cohesion energy density is affected by the parameter, if using the double cell to calibrate cohesion energy density.

The structured framework that was developed was tested through a physical experiment and DEM calibration programme using iron ore.

5.2 Calibration Experiments

This section discusses the specific calibration experiments in relation to the input parameters they calibrate. The discussion follows the logical order given in Figure 5.1.

5.2.1 Coefficient of restitution

The coefficient of restitution measures the energy dissipation properties of bulk material particles at impact with each other or with a wall surface. This parameter is expected to significantly influence the flow behaviour of bulk materials under the dynamic flow regime because particles would be relatively free, with high kinetic energy. In the quasi-static flow regime, this parameter is expected to play an insignificant role because particles will have less kinetic energy, and are in enduring contact with each other.

In this research, simulations were conducted for quasi-static and dynamic flow regimes in relation to the coefficient of restitution. It was found that the parameter had no noticeable effect on the quasi-static flow regime, and only a marginal effect on the dynamic flow (see Sections 4.2.4, 4.2.12, 4.4.2 and 4.4.5). As such, this parameter should only be accurately calibrated in the dynamic flow regime, and can be assigned an average value of 0.5 in the quasi-static flow regime.

Challenges of obtaining an accurate value of the coefficient of restitution using the particle drop test were identified to be the use of an imperfect sphere, and parallax when estimating the rebound height of the particle. The impact of an imperfect sphere could be reduced by carrying out a sufficiently high number of tests, which is not less than 20 valid rebounds, in order to obtain statistically relevant results (Montgomery and Runger, 2014).

5.2.2 Particle to wall coefficient of rolling friction

The particle to wall coefficient of rolling friction measures the resistance force to particle rolling on a surface, given a normal applied force. Various sensitivity tests were carried out in this research, and it was shown that the particle to wall surface coefficient of rolling friction did not significantly affect either the quasi-static or dynamic flow regimes (see Sections 4.2.4, 4.2.7, 4.2.12, 4.4.2

and 4.4.5). The implication of these results is that this parameter does not require a high degree of accuracy, in order to accurately model the real flow behaviour in DEM. As such, in practice, the limitations of the method used in calibrating the parameter, identified in Section 4.1.2, can be safely tolerated.

5.2.3 Particle shape and size distributions

Particle shape and size distributions give a measure of the shapes and sizes existing in a bulk material sample. In real material, a small sample of material can contain hundreds of different sizes and shapes. This makes reproducing the real shapes and sizes in DEM a logistically and computationally impossible exercise. As such, an equivalent material is modelled in DEM to represent the real material, using a limited number of shapes and a limited size distribution. Hence the need for calibrating the DEM material, so that despite the differences in shape and sizes distributions, the DEM and real material would behave in a similar manner under the similar conditions. It follows therefore, that the input parameter values obtained are only valid for the modelled DEM particle shapes and sizes.

Researchers such as Barrios et al. (2013) and Coetzee (2016) investigated the effect of DEM particle shape accuracy and concluded that there is need to introduce some irregularity into the particle shape for simulated results to be representative of the real material behaviour. Coetzee (2016) also concluded that a particle made of 2-clumped spheres could accurately model real bulk material behaviour if properly calibrated. As such, in real applications, it is advisable to introduce some form of irregularity into the DEM particle shape, but the degree of irregularity should depend on the available computational resources.

5.2.4 Particle to wall coefficient of sliding friction

The particle to wall coefficient of sliding friction measures the resistance force exerted on a particle as it slides on a wall surface. This parameter is expected to play a significant role in applications where the bulk material flows over a wall surface, such as in silos, bins and segmented transfer chutes.

Various sensitivity tests of the quasi-static and dynamic flow regimes to this input parameter were conducted in this research, and it was found that both flow regimes were significantly affected by the parameter (see Sections 4.2.12, 4.4.2 and 4.4.5). Therefore, in practice, this parameter must be accurately determined.

Two available methods for determining the parameter are the inclined plane test (Section 4.1.2) and the Jenike shear test (Section 4.1.6). Both methods were used in this research, and it was found that the Jenike shear test gave results with less variability, in comparison to the inclined plane test. Therefore, the Jenike shear test should be the primary method for determining the parameter. However, conducting the Jenike wall friction test is time consuming. As such, the inclined plane test results can be used in applications such as in rock box chutes, in which the parameter has no significant effect, since particles would be primarily flowing over other particles, but in applications such as segmented or curved chutes, which have significant particle to wall interactions, it is necessary to obtain accurate values of the parameter.

Using the Jenike shear cell, the calibrated value of the particle to wall surface coefficient of sliding friction was determined in three steps. The first step was to physically measure the angle of wall friction (Section 4.1.6). The second step was to carry out DEM simulations to determine the angle of wall friction at different values of the particle to wall coefficient of sliding friction, from which a model empirical equation was developed (Section 4.2.5). The third step was enforcing equality of the physically measured angle of wall fric-

tion and the DEM angle of wall friction to determine the calibrated value of the particle to wall coefficient of sliding friction. Based on the goodness of fit value of $R^2 = 1.00$, a second order polynomial equation was shown to be able to model the relationship between the angle of wall friction and particle to wall surface coefficient of sliding friction with a high degree of accuracy. The non-linear relationship between the wall friction angle and the particle to wall surface coefficient of sliding friction was expected and consistent with the Mohr-Coulomb friction plotted in Figure 2.8. This means that theoretically three DEM experiments would suffice to calibrate the particle to wall surface coefficient of sliding friction using the wall friction angle. However, for the purposes of improving the accuracy of the model, a minimum of four experiments would be recommended.

Though the standard Jenike shear cell gives more accurate results, it is only designed for use with -4 mm size fractions, in order to maintain the relative dimensions of the cell to maximum particle size at a recommended ratio of 20 or more (Johnstone, 2010). When larger particle sizes are involved, the two alternatives would be to use either an inclined plane test or to construct a large test cell to accommodate the PSD to be tested. If a larger cell is constructed, it should have dimensions that would result in the relative ratio of cell to largest particle dimension of at least 20 being enforced, in order to get reliable results from the test. This would have consequences of heavier masses to be used for the applied normal load, and additional instrumentation and controls for shearing distance and speed.

Another alternative worth researching would be to investigate the effect of particle size on the angle of wall friction. If the results show that the wall friction angle is independent of particle size, then the standard shear cell would be used with a -4 mm sample obtained by size reduction of the large particles, and the results used in the calibration of large particle sizes in DEM.

5.2.5 Particle to particle coefficients of friction

The particle to particle coefficients of sliding and rolling friction measure the resistance to sliding and rolling respectively, when a particle slides or rolls on another particle. These two parameters are expected to play a significant role in applications where there is internal shearing of the bulk material; in both the dynamic and quasi-static flow regimes.

Various sensitivity tests were carried out in this research, and it was shown that both parameters significantly affected the flow behaviour in both flow regimes, with the coefficient of sliding friction being the one with the most dominant effect (see Sections 4.2.4, 4.2.12, 4.4.2 and 4.4.5). It therefore follows that these two parameters must be accurately calibrated if the DEM material is to be representative of the physical material.

These two parameters are calibrated simultaneously from the same bulk material responses; as such, two independent responses are required to uniquely determine the input parameter values. In this research, the full pipe and split pipe angles of repose were used to calibrate the parameters, in three steps. The first step involved physically measuring the angles of repose (Sections 4.1.7 and 4.1.8). The second step involved conducting DEM simulations at the CCD sampled points to determine the corresponding angles of repose, from which the non-linear model response surface equations were constructed, for each of the full and split pipe angles of repose (Sections 4.2.8 and 4.2.9). The third step involved enforcing equality of the physical and DEM angles of repose to determine the particle to particle coefficients of sliding and rolling friction (Section 4.2.10). Based on the goodness of fit values, the second order response surface equations were found to be able to model the relationship between the angle of repose and the two friction coefficients. Since the angle of repose is a function of particle to particle friction(hence the internal angle of friction), the non-linear relation between the angle of repose and the friction coefficients was expected (see Figure 2.8). The implication of this finding is

that the minimum number of DEM simulations required to construct a second order response surface using the CCD approach is known to be nine. Hence the number of DEM experiments required to calibrate the the parameters using the angles of repose should also be nine.

In comparison with the other model equations that were constructed for bulk density and wall friction angle, the obtained goodness of fit values of R^2 = 0.97 and 0.93 for the full pipe and split pipe angles of repose respectively, were relatively poor. The reason for the lower values of fit emanated from angle of repose measurement values in which there was variability in the material behaviour and subjectivity in the process of determining the angles. Coupled with subjectivity, when DEM simulations are conducted at low friction coefficients, the resulting angles of repose are shallow and difficult to measure. Also, in the physical experiment, the process of taking photographs for measurement in CAD software introduces potential parallax errors which could distort the true angle of repose.

These limitations of the angles of repose as calibration experiments have the potential to affect the obtained calibrated values of the particle to particle friction coefficients. One such effect was noticed in the validation experiments in which a 10% increase in the obtained particle to particle coefficient of sliding friction resulted in 19.5% change in the silo mass flow rate (see Section 5.3.1 for further discussion). As such, there is need to investigate other possible particle to particle friction coefficients calibration experiments, whose measurements are more objective and less error prone. One alternative test is the internal angle of friction using the Jenike shear cell, however, when using the standard shear cell, only -4 mm PSD may be tested and at low shearing speed. As with the particle to wall coefficient of sliding friction, to make the internal angle of friction realistic in DEM calibration, a larger shear cell with a relatively high shear rate would be needed. A larger shear cell would accommodate large particle sizes, while a high shear rate would minimise simulation time. If the standard shear cell were to be used as is to measure the internal angle of

friction, there would be a need to investigate the dependence of internal angle of friction on PSD. If it turns out that the angle is independent of PSD, then the internal angle of friction obtained from the standard shear cell can be be used to calibrate large particle sizes.

Alternative angles of repose may be obtained from the double cell equipment for calibrating the two input parameters. In this research, the double cell angles of repose were only used for verifying the calibrated input parameter values, due to their dependence on experimental conditions both physically and in DEM simulation.

A comparison of the physical double cell angles of repose at different upper cell depths showed that the drained angle of repose was relatively insensitive to variations in depth, while the poured angle of repose significantly changed with depth as seen by an increase of 32% in angle of repose when the depth in the upper cell was increased from 50 mm to 130 mm. This difference could be attributed to the change in flow regimes from quasi-static to dynamic with depth of material in the upper cell. The angles of repose at two different depths also showed that a smaller top cell depth resulted in a larger range of obtained values, while a larger depth reduced the range. This is because large material depth results in angles that can be more accurately measured because the resulting heaps are large. Therefore, it would be preferable to use larger top cell depths for calibration, subject to the limitations on simulation time of the equivalent DEM experiments.

Sensitivity tests of the double cell angle of repose, (Table 4.27), showed that the wall surfaces of the double cell significantly affected the flow behaviour. Zhou et al. (2002) in their investigation of angle of repose using a double cell also concluded that container width affected the angle of repose. Therefore, when the apparatus is used in calibration, the particle to wall friction coefficients should have previously been determined.

Given the dependence of the double cell angles of repose on too many experimental conditions both physically and in DEM, the method is not recommended because this can amplify the highlighted inherent uncertainties associated with the angle of repose in general. As such, the full pipe and the split pipe should be considered for use ahead of the double cell. A further advantage of the full and split pipe tests is that they have smaller volumes, which require less material to fill up, hence improved simulation time (see Appendix P).

5.2.6 Particle density

Particle density measures the mass per volume of the material. This parameter was found in this research to significantly affect the material's bulk density.

The DEM particle density was calibrated using the bulk density test in three steps. The first step involved physically measuring the bulk density of the real material (Section 4.1.5). The second step involved conducting DEM simulations to determine bulk density of the same physical configuration at different values of particle density, from which a model empirical equation was derived (Section 4.2.2). The third step involved enforcing equality between the DEM and physical bulk densities, in order to determine the calibrated value of particle density.

In the physical tests, two containers of different volumes were used to determine the bulk densities. The results showed an increase in the bulk density as the container volume increased due to the increase in consolidation pressure at the bottom of the larger container. The major implications of variation in the bulk density with container size are that the same container dimensions used in physical experiments should be used in simulations to ensure similar conditions and therefore same levels of consolidation. Comparing the standard deviations of iron ore bulk density in different size containers shows that as the container size increased the dispersion of measured bulk density decreased.

This can be observed from the small size container standard deviation which was 1.3% of the average bulk density, while the standard deviation from the large size container was 0.8% of the average bulk density. It therefore follows that the container size used in the bulk density experiment should be as large as possible as may be allowed by the available DEM simulation time, in order to increase the accuracy of the obtained average bulk density. However, larger container sizes would require more DEM particles in the equivalent DEM bulk density test, thereby increasing the simulation time.

The goodness of fit value ($R^2 = 1.00$) of the linear equation relating the DEM bulk density to particle density showed that a first order polynomial modelled the relationship between the two parameters with a high degree of accuracy. The reason for this relationship is that if PSD and container volume are maintained constant, bulk density is linearly related to the particle density as given by Equation 2.31. It therefore means theoretically the minimum number of DEM bulk density tests required to calibrate particle density is two. However, additional experiments above the theoretical minimum are necessary to improve the accuracy and confidence in the results, hence for practical purposes, a minimum of three experiments would be recommended. This finding makes it possible to plan the number of experiments required before the calibration process starts.

The calibrated particle density of 3609 kg/m^3 is higher than the measured average of real iron ore particle density of 3220 kg/m^3 for this particular material (which was determined for other research purposes). This is because of the higher voids ratio in DEM material caused by relatively larger particle size (Figure 4.6) as compared to the real material material PSD (Table 4.5). Because the voids ratio is higher in DEM material, its particle density would have to be higher than the real particle density so that the DEM and real material bulk densities maintain equality for a given volume (Equation 2.31). As the DEM particle shape and size distribution approaches that of the real material, the DEM particle density would approach the real particle density. Therefore,

the difference between the DEM and real particle densities can be used as an indicator of the accuracy of the DEM particle shape and size distribution in relation to the real particles.

Sensitivity of DEM bulk density to variations in other input parameters conducted in Section 4.2.4, showed that the rest of input parameters had negligible effect on the bulk density. However, the effect of particle to particle coefficient of sliding friction on the bulk density proved to be significant as shown by a variation of 11.4% in bulk density when it was reduced from 0.5 to 0.1. This means that, in the framework, the particle to particle coefficient of sliding friction should be calibrated before calibrating the particle density. This order of calibrating the parameters was also confirmed in Tables 4.28 and 4.29, which show that particle density has an insignificant effect on the angle of repose.

5.2.7 Adhesion energy density

Adhesion energy density measures the strength of the bond formed between the bulk material particles and the wall surfaces. This parameter plays a significant role in applications where moisture and small particle sizes are involved.

In this research, the DEM inclined plane test (Section 4.2.13), together with the physically measured sliding angle of a moist particle, was used to calibrate the adhesion energy using a first order polynomial equation. The goodness of fit value ($R^2 = 0.99$) of the first order polynomial showed that it could be used to model the relationship between the angle of sliding friction of adhesive material and the adhesion energy density. The reason why the relationship is linear is because the contact surface area between the particle and wall surface, on which the JKR adhesion energy depends, remained almost the same in all the simulations. This means theoretically the minimum number of DEM inclined plane tests required with moist material to calibrate adhesion energy density is two. However, additional experiments above the theoretical minimum are

necessary to improve the accuracy and confidence in the results, hence for practical purposes, a minimum of three experiments would be recommended.

The approach of using a single particle, as was done in this research, may result in the test particle losing some moisture when exposed to free air, and consequently testing it at a lower moisture content. This could be addressed by using a bulk material sample placed in a ring, as was the case in the shear test. This will ensure that the bulk material sample in contact with the wall surface is covered and hence retains its moisture. The downside of the latter approach is that additional simulation time would be required in comparison to the use of a single particle.

Since the sliding angle of the particle is a function of both the particle to wall surface coefficient of sliding friction and adhesion energy, the approach only gives valid results provided the particle to wall surface coefficient of sliding friction has been determined prior to the test. This was based on the assumption that all frictional effects were captured during tests with dry material. As such, any increase in sliding angle when using moist material would be a function of adhesion alone.

5.2.8 Cohesion energy density

Cohesion energy density measures the strength of the bond formed between particles of the bulk material. This parameter, just as adhesion energy density, plays a significant role in applications where moisture and small particle sizes are involved.

The DEM split pipe angle of repose (Section 4.2.14) was used together with the physically measured split pipe poured angle of repose of moist material to calibrate cohesion energy density. The relationship between the angle of repose and cohesion energy density was modelled by a first order polynomial with a goodness of fit value of $R^2 = 1.00$. The reason for the linear relationship

is that the contact surface area, on which cohesion energy density depends remained almost the same, since particle packing did not change in all the simulations. This means theoretically the minimum number of DEM angle of repose tests required with moist material to calibrate cohesion energy density is two. However, additional experiments above the theoretical minimum are necessary to improve the accuracy of the results, hence for practical purposes, a minimum of three experiments would be recommended.

This approach, however would require the particle to particle coefficients of friction to be determined first, since the angle of repose is also a function of these parameters. This was based on the assumption that all frictional effects are captured during tests with dry material. As such, any increase in the angle of repose when using moist material would be a function of cohesion alone. Another point to note with this approach is that, if an apparatus like the double cell is used, in which wall effects are significant, then the particle to wall coefficients of friction and adhesion energy density would need to be determined first.

5.2.9 Practical DEM calibration

Typical practical applications of DEM are in the design and modelling of transfer chutes, verification of flow profiles in silos, assessment of material landing position from a transfer chute onto conveyor belts, design of lifter bars in mills, design of mineral ore crushers etc. In transfer chutes, flow profiles and distribution of bulk materials can be predicted and used in optimisation of the chute geometry.

The developed systematic framework in Figure 5.1 is general and could be applied in practical DEM calibration scenarios with some variations in the calibration experiments, depending on the application conditions. These conditions pertain to the particle size distribution (PSD), flow regimes, and objectives of the simulation.

In this research, only a narrow PSD was used, however the framework applies to any PSD, as long as the correspondence between the DEM and the physical materials is established through appropriate calibration experiments for specific input parameters. Calibration experiments such as the wall friction and internal friction using the standard shear tester would only be applicable to -4 mm PSD. For +4 mm PSD, there may be a need to build and use larger shear testers that can accommodate the required PSD, with the constraint that the ratio of the cell diameter is at least 20 times the largest particle size (Johnstone, 2010).

For quasi-static flow conditions, the coefficient of restitution parameters may be assigned a rough value from as few as four valid drop tests or an average value such as 0.5. This is based on the results which showed that the parameter does not significantly affect the flow behaviour under quasi-static flow conditions. For dynamic conditions, however, there is need to accurately obtain parameter.

If the objective of DEM analysis is to obtain qualitative flow properties, the particle to particle friction coefficients may be calibrated from angle of repose tests. However, if the objective is to obtain quantitative flow properties, the angle of repose must be used with another more objective response, such as the internal angle of friction, to calibrate the particle to particle friction coefficients. However, this would require large shear cells with high shear speeds of approximately 10 mm/s, in order to obtain simulation results in realistic time frames.

Table 5.1 shows the DEM input parameters and the minimum number of DEM calibration experiments required to obtain each parameter.

In Table 5.1, the literature and direct measurement parameters are not included since their determination is not time intensive as compared to the input parameters calibrated from bulk material responses.

The calibration parameters in Table 5.1 should be conducted in a sequential order from the parameter at the top to the one at bottom. This is because, the

Table 5.1: Minimum number of DEM calibration experiments

Sequence	**Parameter**	**Recommended Minimum Number of Simulations**
1	$\mu_{pw,s}$	4
2	$\mu_{pp,s}$; $\mu_{pp,r}$	18 (9 per CCD)
3	ρ_p	3
4	ED_a	3
5	ED_c	3

parameters at the bottom require the top parameters to have been previously determined for their calibration. Theoretically, a first order polynomial may be constructed from two data points because it has two degrees of freedom, and a second order polynomial may be constructed from three data points because it has three degrees of freedom. However, to be able to detect any error that might happen during the process of acquiring one of the data points, an additional point above the minimum is necessary. As such, all the input parameters obtained from one dimensional equations are recommended to have one plus the theoretical minimum number of experiments. These parameters are the particle to wall surface coefficient of sliding friction, adhesion energy density and cohesion energy density. In order to construct a second order response surface equation using the CCD approach, at least nine data points are required for a single experimental set up. This means for two experimental setups required to obtain the particle to particle friction coefficients, a total of 18 experiments would be required.

5.3 Calibrated Parameters Validation

This section discusses the results documented in Section 4.3 and Section 4.4 which were obtained from carrying out physical and DEM validation experimental procedures. The specific validation experiments discussed are silo flow of dry and moist iron ore, and chute flow of dry and moist iron ore.

5.3.1 Silo flow

Experiments were physically conducted to measure the mass flow rates and flow profiles of dry and moist iron ore in a silo (Sections 4.3.1 and 4.3.2), where the results were compared with those obtained from equivalent DEM simulations that utilised the calibrated parameter values (Sections 4.4.1 and 4.4.3).

A comparison of the mass flow rates between the DEM and physical experiments showed that for both moist and dry materials, the DEM experiments overestimated the mass flow rates. For dry material, the DEM experiment overestimated the flow rate by 22.6%, while it overestimated the flow rate by 9.6% for moist material. A visual comparison of flow profiles for both dry and moist iron ore showed a very good agreement between the DEM and physical experiments. The discrepancy in the quantitative measurements meant that particles had more freedom to move in the DEM test as compared to the physical test, hence there were frictional properties that were underestimated during the DEM calibration process.

In order to investigate this deviation, particle to particle sliding and rolling coefficients were increased, one at a time, by 10% each. For dry iron ore, a 10% increase of the particle to particle coefficient of sliding friction reduced the DEM mass flow rate to within 3.7% of the physically measured value, and a 10% increase of the particle to particle coefficient of rolling friction reduced the DEM mass flow rate to within 14.9% of the physically measured value. For moist iron ore, a 10% increase of the particle to particle coefficient of sliding friction reduced the DEM mass flow rate to within 1.1% of the physically measured value. A comparison of flow profiles for both dry and moist iron ore after the 10% adjustments still showed a very good agreement between the DEM and physical experiments. The results confirm that the particle to particle coefficient of sliding friction was underestimated during calibration, and show that quantitative measurements are more sensitive to variations in the input parameters as compared to qualitative measures.

These results underscored the sensitivity of quasi-static flow to the particle to particle coefficient of sliding friction, and consequently the need to precisely obtain its calibrated value. The implication of this finding is that angle of repose is not a totally reliable experiment for use in the calibration of the particle to particle friction coefficients, where quantitative measurements are required. This is because the angle of repose measurements obtained during the tests are prone to errors, which arise due to variability in test results, parallax when taking photographs, and when deciding where to place the line from which the the angle of repose is measured. The friction coefficient is also sensitive to the angle of repose in that a 10% change in static friction amounted to a change of angle of repose of approximately 2.5°. The interpretation of angle of repose measurements and results is also amplified when the bulk material volume is small and/ or angles of repose to be measured are shallow. Though the volume of material may be increased to minimise the error, at the cost of more simulation time, shallow angles are unavoidable when the CCD sample points have low values of the friction coefficients. Because of the significance of the particle to particle coefficient of sliding friction, and the inherent limitations of the angle repose test, there is a need to investigate other tests to measure bulk responses more objectively than the angle of repose tests. One such response is the internal angle of friction from the direct shear test. However, appropriate modifications would need to be made to the standard shear tester, so that results are obtained more quickly and can cover wide size ranges.

In a related study, Coetzee (2017) independently calibrated the particle to particle friction coefficients using the shear cell and the angle of repose. On validating the calibrated parameters in a hopper, the angle of repose calibrated values overestimated hopper discharge, while the shear cell calibrated values correctly estimated hopper discharge. Coetzee then concluded that the angle of repose test may result in friction coefficients that are too low for applications with high friction levels.

These research results point to the need to relate the objectives of DEM analysis and calibration experiments to be used. If the primary objective of the DEM analysis is to obtain qualitative behaviour of material and not quantitative, then the angle of repose tests, because of their simplicity, can be used in calibrating the input parameters. An example where qualitative behaviour may be an objective is to assess whether flow in a silo or bin is mass or funnel flow. Mass flow happens when the entire material bed is in motion during discharge, while in funnel flow active flow happens above the outlet, with material in contact with the wall surfaces relatively stagnant. However, if the objective of DEM analysis is to obtain quantitative measurements, such as mass flow rate from a bin, then more precise calibration experiments are required to replace the angle of repose. The proposed larger Jenike shear cell should then be investigated.

When calibrating moist material, an assumption was made that the frictional effects of the material were adequately captured by tests on dry material. As such, any changes in the bulk response when using moist material was entirely due to cohesion or adhesion. The good correspondence between the physical silo experiment with moist material and the equivalent DEM simulation, has shown that the assumption made was not invalid.

Further sensitivity tests were conducted, where input parameters were systematically varied to observe their effect on quasi-static flow of dry iron ore. The results showed that quasi-static flow is sensitive to frictional parameters and insensitive to the coefficient of restitution. This observation is in agreement with sensitivity tests done on the angle of repose which showed that frictional parameters significantly affect the quasi-static flow regime while the coefficient of restitution does not. It therefore follows that generally, in applications where the flow is predominantly quasi-static, the frictional parameters need to be accurately calibrated, while the coefficient of restitution may be assigned an average value.

5.3.2 Chute flow

Physical chute flow experiments were conducted in Sections 4.3.3 and 4.3.4 with dry and moist iron ore respectively, and the results compared with those obtained from equivalent DEM experiments that utilised the calibrated parameter values in Section 4.4.4. For both material states, the flow profiles during steady flow and the remaining mass in the chute were compared. The flow profiles during steady flow showed a very good qualitative agreement between the DEM and physical experiments for both materials. However the remaining mass in the chute was less for the DEM test, by 34.0% for dry material and 18.9% for moist material. These results meant that in DEM, particles were less restrained as compared to the physical flow, hence there was less material remaining in the chute, in the DEM simulations. This means particle to particle friction was less in DEM experiment than in the physical experiment.

As was the case with silo flow, the particle to particle coefficient of sliding friction was increased by 10% for both dry and moist iron ore. The adjustment resulted in the remaining mass in the chute being within 2.4% of the physically measured mass for dry material, while it resulted in a deviation of 3.6% for moist material. This observation was in agreement with silo flow observations that the calibrated particle to particle coefficient of sliding friction was underestimated. A comparison of flow profiles during steady flow for both dry and moist material after the 10% adjustment showed no visible change from the unadjusted calibrated values.

These results mean that when quantitative measurements are the objective of DEM analysis, there is need for methods that can precisely calibrate the particle to particle coefficient of sliding friction, instead of the angle of repose. However, when the objective of DEM analysis is to obtain qualitative measurements, such as distribution of material in the flow volume, then small errors from the calibration experiments may be tolerated, and the angle of repose may be used. An example of a qualitative application could be to assess the

position where the bulk material from the chute is landing on a conveyor belt. If material is landing on the side of a belt, then belt tracking problems could arise.

Sensitivity of the dynamic flow to variations in various input parameters was also carried out. It was observed that both the frictional parameters and coefficient of restitution have significant impact on the dynamic flow regime. This observation agrees with observations made on the dynamic flow in the double cell in Section 4.2.12. It therefore follows that, in applications where the flow is predominantly dynamic, all the input parameters need to be accurately calibrated. The same observation was made by Gröger and Katterfield (2006).

6 Conclusions

This chapter concludes the research by reviewing the results obtained in relation to the original research objectives in Section 6.1, and some recommendations for further research in Section 6.2.

6.1 Summary of main findings

1. A systematic and sequential DEM calibration framework was developed as shown in Figure 5.1. The framework consists of categorising the DEM input parameters into three categories of determining the directly measured input parameters, obtaining the literature acquired input parameters, and linking physical experiments with DEM simulations to obtain the calibrated parameter values.

2. DEM calibration experiments that isolated the effects of specific input parameters were identified and integrated into the framework, in an order that acknowledged the effect of previously calibrated input parameters on subsequent experiments. The experiments, in their logical order, were:

    a) Particle drop test to directly measure coefficients of restitution.

    b) Inclined plane test to directly measure particle to wall surface coefficient of rolling friction.

    c) Jenike wall shear test to calibrate the particle to wall surface coefficient of sliding friction.

d) Full and split pipes angle of repose to calibrate the particle to particle coefficients of sliding and rolling friction.

e) Bulk density test to calibrate particle density.

f) Inclined plane test to calibrate adhesion energy density.

g) Full or split pipe angle of repose to calibrate cohesion energy density.

3. Validation of the input parameters obtained from the framework was conducted using laboratory-scale silo and chute flows, and the following conclusions were made:

   a) Quantitative predictions of bulk material flow are more sensitive to small variations in the input parameters, while qualitative predictions are less sensitive to small input parameter changes.

   b) The particle to particle coefficient of sliding friction significantly affects bulk material flow under both the quasi-static and dynamic flow regimes.

4. The angle of repose as a bulk response is not necessarily sufficiently accurate to calibrate the particle to particle coefficient of sliding friction, for obtaining quantitative results in DEM simulations.

6.2 Recommendations for Further Research

In order to further improve the accuracy of results obtained under the developed framework, experiments that are more accurate in isolating effects of specific parameters need to be investigated and integrated into the framework. Some of the recommended experiments are;

- Investigate the order of the model equation that relates the internal angle of friction to the particle to particle friction coefficients. This relationship can then be used to replace one of the angles of repose tests required to solve the simultaneous equations for the values of friction coefficients. The internal angle of friction is expected to result in an equation with a better fit since its value is determined more accurately than the angle of repose.

- Investigate the effect of PSD on the angles of internal and wall friction. If the these angles are independent of the PSD, then the standard shear cell can be used with -4 mm to obtain responses for calibrating +4 mm size fractions with a larger shear cell in DEM.

- In this research, adhesion and cohesion energy densities were calibrated using moist material, based on the assumption that all frictional effects were factored into the results by using dry material. Any further increase in the response value when using moist material was therefore a function of adhesion or cohesion alone. Investigate the validity of this assumption, and the consequences on DEM simulation time, by repeating the bulk response experiments with moist material.

- Investigate the order of the model equation that relates the dynamic angle of repose measured in a rotating drum to the particle to particle friction coefficients. The relationship can be used to replace one of the angles of repose used in this research. However the particle to wall surface coefficients of friction would need to be determined before executing this experimental setup.

- Instead of using the inclined plane test to calibrate adhesion energy density, the mass of material that remains stuck on an inclined chute can be used to calibrate the parameter. This can be achieved by establishing the relationship between the mass remaining on the chute and adhesion energy density.

- In this research, only one clumped particle was used so as to precisely measure bulk density in the DEM package used. Using a suitable simulation package, carry out the bulk density experiments with more than one sphere to determine the effect of number of clumps on the simulation.

References

Ai, J., Chen, J., Rotter, J. M. and Ooi, J. Y. (2011), 'Assessment of Rolling Resistance Models in Discrete Element Simulations', *Powder Technology* **206**, 269–282.

Asada, M. and Omori, Y. (1983), 'Determination of Young's Modulus and Poison Ratio of Lump Ores', *Journal of the Iron and Steel Institute of Japan* **65**, 739–745.

Asaf, Z., Rubinstein, D. and Shmulevich, I. (2006), 'Evaluation of link-track performances using DEM', *Journal of Terramechanics* **43**, 141–161.

Barrios, G. K., Carvalho, R. M., Kwade, A. and Tavares, L. M. (2013), 'Contact Parameter Estimation for DEM Simulation of Iron Ore Pellets', *Powder Technology* **248**, 84–93.

Brummer, J. (2010), Discrete Element Modelling with Varying Moisture for Sand, Master's thesis, University of Pretoria: South Africa.

Camborros, M., Feise, H. J., Zetzener, H. and Kwade, A. (2013), 'Segregation of Particulate Solids: Experiments and DEM Simulations', *Particuology* .

Campbell, C. S. (2006), 'Granular Material Flows - An Overview', *Powder Technology* **162**, 208–229.

CD-Adapco (2014), *StarCCM+ User Guide 9.06*.

CFDEM (2017), LIGGGHTS Documentation. INTERNET. http://www.cfdem.com/liggghts. Cited 23 October 2017.

Coetzee, C. and Els, D. (2009), 'Calibration of Discrete Element Parameters and the Modelling of Silo Discharge and Bucket Filling', *Computers and Electronics in Agriculture* **65**, 198–212.

Coetzee, C. J. (2016), 'Calibration of Discrete Element Method and the Effect of Particle Shape', *Powder Technology* **297**, 50–70.

Coetzee, C. J. (2017), 'Review: Calibration of the discrete element method', *Powder Technology* **310**, 104–142.

Curry, D., Favier, J. and LaRoche, R. D. (2009), A Systematic Approach to DEM Material Model Calibration, *in* 'The American Institute of Chemical Engineers (AIChE)', Tennessee: Nashvile.

Evonik-Industries (2017), Plexiglass GS Product Description, Technical report, Evonik Industries.

Favier, J. F., Abbaspour-Fard, M. H., Kremmer, M. and Raji, A. O. (2001), 'Modelling Non-Spherical Particles Using Multisphere Dicrete Elements', *J. Eng. Mech, ASCE* **127**, 971–977.

Grima, A. P., Fraser, T., Hastie, D. B. and Wypych, P. W. (2011), Discrete Element Modelling: Troubleshooting and Optimisation Tool for Chute Design, *in* 'Beltcon 16 Proceedings', Sun City, South Africa.

Grima, A. P. and Wypych, P. W. (2011*a*), 'Development and Validation of Calibration Methods for Discrete Element Modelling', *Granular Matter* **13**, 127–132.

Grima, A. and Wypych, P. (2011*b*), 'Investigation into Calibration of Discrete Element Model Parameters for Scale-Up and Validation of Particle Structure Interactions Under Impact Conditions', *Powder Technology* **212**, 198–209.

Grima, A., Wypych, P., Curry, D. and LaRoche, R. (2013), Predicting Bulk Flow and Behaviour for Design and Operation of Handling and Processing Plants, *in* '11th International Congress on Bulk Materials Storage, Handling

and Transportation', Newcastle, Australia: University of Newcastle, pp. 1–10.

Gröger, T. and Katterfield, A. (2006), On the Numerical Calibration of Discrete Element Models for the Simulation of Bulk Solids, *in* '16th European Symposium on Computer Aided Process Engineering and 9th International Symposium on Process Systems Engineering', Elsevier B.V.

Hanley, K. J., O'Sullivan, C., Oliveira, J. C., Cronin, K. and Byrne, E. P. (2011), 'Application of Taguchi Methods to DEM Calibration of Bonded Agglomerates', *Powder Technology* **210**, 230–240.

Hastie, D., Wypych, P., Grima, A., LaRoche, R. and Curry, D. (2012), Prediction of the Behaviour of Bulk Materials in the Design and Operation of Bulk Materials Handling and Processing Plants, Technical report, Australian Bulk Handling Review.

Horn, E. (2012), The Calibration of Material Properties for Use in Discrete Element Methods, Master's thesis, University of Stellenbosch: South Africa. Masters Dissertation.

Ileleji, K. E. and Zhou, B. (2008), 'The Angle of Repose of Bulk Stover', *Powder Technology* **187**, 110–118.

Johnstone, M. C. (2010), Calibration of DEM Models for Granular Materials Using Bulk Physical Tests, PhD thesis, The University of Edinburgh: UK. PhD Thesis.

Krügger, A. L. (2009), Discrete Element Modelling Validation and Modelling for Coal, Master's thesis, University of Pretoria: South Africa.

Langston, P. A., Tuzun, U. and Heyes, D. M. (1995), 'Discrete Element Simulation of Granular Flow in 2D and 3D Hoppers: Dependence of Discharge Rate and Wall Stress on Particle Interactions', *Chemical Engineering Science* **50**, 967–987.

Li, T., Peng, Y., Zhu, Z., Yu, Z. and Yin, Z. (2017), 'Effect of Lifting Velocity and Container Shape on Angle of Repose of Iron Ore Pellets', *Advances in Material Science and Engineering* **2017**.

Lommen, S., Schott, D. and Lodewijks, G. (2014), 'DEM Speed Up: Stiffness Effects on the Behaviour of Bulk Material', *Particuology* **12**, 107–112.

Maio, F. P. D. and Renzo, A. D. (2005), 'Modelling Particle Contacts in Discrete Element Simulations: Linear and Non-Linear Approach', *Chemical Engineering Research and Design* **83**, 1287–1297.

Mak, J., Chen, Y. and Sadek, M. (2012), 'Determining Parameters of a Discrete Element Model for Soil-Tool Interaction', *Soil & Tillage Research* **118**, 117–122.

Marigo, M. and Stitt, E. H. (2015), 'Discrete Element Method for Industrial Applications: Comments on Calibration and Validation for the Modelling of Cylindrical Pellets', *KONA Powder and Particle Journal* **32**.

Markauskas, D., Ramirez-Gomez, A., Kacianauskas, R. and Zdancevicious, E. (2015), 'Maize Grain Shape Approaches for DEM Modelling', *Computers and Electronics in Agriculture* **118**, 247–258.

Merkus, H. G. and Meesters, G. M. H. (2016), *Production, Handling and Characterization of Particulate Materials*, Springer International Publishing, Switzerland.

Montgomery, D. C. and Runger, G. C. (2014), *Applied Statistics and Probability for Engineers*, John Wiley & Sons, Inc, USA.

Myers, R. H., Montgomery, D. C. and Anderson-Cook, C. M. (2009), *Response Surface Methodology: Process and Product Optimization Using Designed Experiments*, A John Wiley & Sons, Inc, Hoboken, New Jersey.

Nordell, L. (1997), Particle Flow Modelling: Transfer Chutes and Other Applications, *in* 'International Materials Handling Conference (Beltcon 9)', South Africa: Johannesburg.

O'Sullivan, C. (2011), *Particulate Discrete Element Modelling: A Geomechanics Perspective*, Spon Press, New York, USA.

O'Sullivan, C., Cui, L. and Bray, J. D. (2004), *Three Dimensional Discrete Element Simulations of Direct Shear Tests* , Taylor & Francis Group, London, pp. 373–382.

Rackl, M. and Hanley, K. J. (2016), 'A methodical calibration procedure for discrete element models', *Powder Technology* **307**, 73–83.

ReliaSoft (2015), *Experiment Design & Analysis Reference*, ReliaSoft Corporation, Arizona, USA.

Renzo, A. D. and Maio, F. P. D. (2004), 'Comparison of Contact Force Models for the Simulation of Collisions in DEM based Granular Flow Codes', *Chemical Engineering Science* **59**, 525–541.

Rojek, J., Zarate, F., Agelet, C., Gilbourne, C. and Verdot, P. (2005), 'Discrete element modelling and simulation of sand mould manufacture for the lost foam process ', *International Journal for Numerical Methods in Engineering* **62**, 1421–1441.

Savage, S. B., Nedderman, R. M., Tuzun, U. and Houlsby, G. T. (1983), 'The Flow of Granular Materials - III', *Chemical Engineering Science* **38**, 189–195.

Thornton, C. (2015), *Contact Mechanics and Particle System Simulations: A DEM Study*, Springer International Publishing.

Thornton, C., Cummins, S. J. and Cleary, P. W. (2011), 'An Alternative of the Comparable Behaviour of Alternative Contact Force Models during Elastic Collisions', *Powder Technology* **210**, 189–197.

Tsuji, Y., Kawaguchi, T. and Tanaka, T. (1993), 'Discrete Particle Simulation of Two Dimensional Fluidised Bed', *Powder Technology* **77**, 79–87.

Wensrich, C. and Katterfield, A. (2012), 'Rolling Friction as a Technique for Modelling Particle Shape in DEM', *Powder Technology* **217**, 409–417.

Xu, Y., Kafui, K. D., Thornton, C. and Lian, G. (2002), 'Effects of Material Properties on Granular Flow in a Silo Using DEM Simulation', *Particle Science Technology* **20**, 109–124.

Zhou, G. G. D. and Sun, Q. C. (2013), 'Three Dimensional Numerical Study on Flow Regimes of Dry Granular Flows by DEM', *Powder Technology* **239**, 115–127.

Zhou, Y. C., Wright, B. D., Yang, R. Y., Xu, B. H. and Yu, A. B. (1999), 'Rolling Friction in the Dynamic Simulation of Sandpile Formation', *Physica* **269**, 536.

Zhou, Y. C., Xu, B. H., Yu, A. B. and Zulli, P. (2001), 'Numerical Investigation of Angle of Repose of Monosized Spheres', *Non-Linear Soft Matter Phys.* **64**.

Zhou, Y. C., Xu, B. H., Yu, A. B. and Zulli, P. (2002), 'An Experimental and Numerical Study of the Angle of Repose of Coarse Spheres', *Powder Technology* **125**, 45–54.

A Python Programs

A.1 Particle Density Calibration Code

```
import numpy as np
import matplotlib.pyplot as plt

rho = [2000, 3000, 4000, 5000]
m = [0.060151879, 0.09256051668, 0.12224033425,
   0.15272706708]

tbd = 1833  # target bulk density
# tbd = 1916  # target bulk density (larger bucket)

prho = np.array(rho)
pm = np.array(m)
vol = 6.01725e-5
brho = pm/vol
p = np.polyfit(prho, brho, 1)
f = np.polyval(p, prho)
pd = (tbd - p[1])/p[0]
print(pd)
pp = np.poly1d(p)
print(pp(pd))
print(brho)
```

```
plt.figure(1)
plt.plot(prho, brho, 'g*', linewidth=2)
plt.plot(prho, f, 'b-', linewidth=2)
plt.plot(pd, tbd, 'ro', linewidth=4)
plt.plot([0, pd], [tbd, tbd], 'r--', linewidth=2)
plt.plot([pd, pd], [0, tbd], 'r--', linewidth=2)
plt.axis([0, 5500, 0, 3000])
plt.xlabel('Particle Density (kg/m^3)')
plt.ylabel('Bulk Density (kg/m^3)')
plt.title('Bulk Density as a Function of Particle
   Density')
plt.grid(True)
plt.show()
```

A.2 Physical Wall Shear Data Processing

```
import csv
import math
import numpy as np
import matplotlib.pyplot as plt

g = 9.81
d = 0.095
A = math.pi*(d**2)/4
infile = open('csvs/sishen_wall_physical.csv','r')
table = []
for row in csv.reader(infile):
    table.append(row)
infile.close()
table = table[1:]
```

```
time = np.array([row[0] for row in table])
force_1 = np.array([row[1] for row in table])
force_2 = np.array([row[2] for row in table])
Ss_1 = force_1.astype(float)/(A*1000)
Ss_2 = force_2.astype(float)/(A*1000)
m = np.array([2.3, 4.3, 6.3, 8.3])
Nf = m*g
Ns = Nf/(A*1000)
Ss1_1 = np.array([np.mean(Ss_1[1:93]),
        np.mean(Ss_1[103:208]),
        np.mean(Ss_1[215:347]),
        np.mean(Ss_1[356:494])])
Ss1_2 = np.array([np.mean(Ss_2[1:120]),
        np.mean(Ss_2[129:231]),
        np.mean(Ss_2[246:358]),
        np.mean(Ss_2[377:494])])
p1 = np.polyfit(Ns,Ss1_1,1)
f1 = np.polyval(p1,Ns)
p2 = np.polyfit(Ns,Ss1_2,1)
f2 = np.polyval(p2,Ns)
plt.figure(1)
plt.plot(time,Ss_1,'b-',linewidth=1, label
   ='Experiment 1')
plt.plot(time,Ss_2,'r-',linewidth=1, label
   ='Experiment 2')
plt.title('Time vs Shear Stress')
plt.xlabel('Time (min)')
plt.ylabel('Shear Stress (KPa)')
plt.legend(loc='best')
plt.grid(True)
plt.show()
```

```
plt.figure(2)
plt.plot(Ns,Ss1_1,'b*',linewidth=2,\
         label='Experiment 1 Data Points')
plt.plot(Ns,f1,'b',linewidth=2,\
         label='Fitted Linear Curve Exp 1')
plt.plot(Ns,Ss1_2,'r*',linewidth=2,\
         label='Experiment 2 Data Points')
plt.plot(Ns,f2,'r',linewidth=2,\
         label='Fitted Linear Curve Exp 2')
plt.title('Normal Stress vs Shear Stress')
plt.xlabel('Normal Stress (kPa)')
plt.ylabel('Shear Stress (kPa)')
plt.legend(loc='best')
plt.grid(True)
plt.show()
mu1 = p1[0]
phi1 = math.atan(mu1)*(180/math.pi)
print(p1)
print(phi1,'\n\n')
mu2 = p2[0]
phi2 = math.atan(mu2)*(180/math.pi)
print(p2)
print(phi2,'\n\n')
phi = np.mean([phi1,phi2])
print(phi,'\n\n')
```

A.3 DEM Wall Shear Data Processing

```
import numpy as np
import matplotlib.pyplot as plt
from calibfuncs.quadratic import quadratic
```

```
mu = np.array([0.2, 0.4, 0.6, 0.9])
phi = np.array([11.2, 21.0, 27.7, 30.8])
p2 = np.polyfit(mu, phi, 2)
muu = np.linspace(0.1, 1.05, 1000)
f2 = np.polyval(p2, muu)
print(p2)
tbd = 23.7
pd = quadratic(p2[0], p2[1], p2[2]-tbd,\
     mu[0], mu[-1])
print('The predicted coefficient of static\
     friction is %.2f' % pd)
plt.figure(1)
plt.plot(mu, phi, 'b*', linewidth=2)
plt.plot(muu, f2, 'm', linewidth=2)
plt.plot([0, pd], [tbd, tbd], 'k--', linewidth=2)
plt.plot([pd, pd], [0, tbd], 'k--', linewidth=2)
plt.plot(pd, tbd, 'r*', linewidth=2)
plt.title('Wall Friction Angle vs Coefficient of\
           Static Friction')
plt.ylabel('Wall Friction Angle (Deg)')
plt.xlabel('Coefficient of Sliding Friction')
plt.legend(('DEM Data Points', 'Fitted Curve'),\
            loc='best')
plt.grid(True)
plt.axis([0, 1.1, 0, 31])
plt.show()
```

A.4 Double Cell Response Surface

```
from calibfuncs.statspara import *
# Double Cell - Withdrawal Angle of Repose
data = np.array([0.18, 0.60, 31.0, 0.30, 0.30, 35.0,
                 0.30, 0.90, 40.0, 0.60, 0.18, 37.0,
                 0.60, 0.60, 45.0, 0.60, 1.00, 46.0,
                 0.90, 0.30, 41.5, 0.90, 0.90, 48.5,
                 1.00, 0.60, 49.0])
# Data pre-processing
data = np.reshape(data, (-1, 3))
y = data[:, -1]
k = data.shape[0]
n = 2  # quadratic = 2, linear = 1
m = int(n + n*(n+1)/2)
X = np.ones((k, m+1))
# Compute the response surface equation coefficients
b = []
if n == 1 or n == 2:
    b = coefcalc(n, data, m, k, y, X)
    if len(b) == 3:
        print('F(x) = %.1f + %.1fx1 + %.1fx2' \
              % (b[0], b[1], b[2]))
    else:
        print('F(x) = %.1f + %.1fx1 + %.1fx2
           %.1fx1^2\
               %.1fx2^2 + %.1fx1x2'
              % (b[0], b[1], b[2], b[3], b[4], b[5]))
else:
    print("Please enter the value of n = 1 or n = 2")
```

```
# Compute coefficient of multiple determination and
   print
Rsquared = rsquared(k, y, b, X)
print('R^2 = %.3f' % Rsquared)
# Plot the response surface graph
plotsurface(b)
```

A.5 Full Pipe Response Surface

```
from calibfuncs.statspara import *
import matplotlib as mpl
mpl.rcParams['text.usetex'] = True
data = np.array([0.18, 0.60, 25.0, 0.30, 0.30, 30.0,
                 0.30, 0.90, 31.0, 0.60, 0.18, 32.0,
                 0.60, 0.60, 38.0, 0.60, 1.00, 39.0,
                 0.90, 0.30, 37.0, 0.90, 0.90, 42.0,
                 1.00, 0.60, 43.0])

# Data pre-processing
data = np.reshape(data, (-1, 3))
y = data[:, -1]
k = data.shape[0]
n = 1   # quadratic = 2, linear = 1
m = int(n + n*(n+1)/2)
X = np.ones((k, m+1))
# Compute the response surface equation coefficients
b = []
if n == 1 or n == 2:
    b = coefcalc(n, data, m, k, y, X)
    if len(b) == 3:
```

```
            print('F(x) = %.1f + %.1fx1 + %.1fx2' \
                  % (b[0], b[1], b[2]))
        else:
            print('F(x) = %.1f +%.1fx1 +%.1fx2 %.1fx1^2'
                  ' %.1fx2^2 +%.1fx1x2'
                  % (b[0], b[1], b[2], b[3], b[4], b[5]))
else:
    print("Please enter the value of n = 1 or n = 2")
# Compute coefficient of multiple determination
Rsquared = rsquared(k, y, b, X)
print('R^2 = %.3f' % Rsquared)
#  Plot the response surface graph
plotsurface(b)
```

A.6 Split Pipe Response Surface

```
import numpy as np
from calibfuncs.statspara import *
#Split Pipe - Poured Angle of Repose
data = np.array([0.18, 0.60, 17.0, 0.30, 0.30, 19.0,
                 0.30, 0.90, 20.5, 0.60, 0.18, 19.5,
                 0.60, 0.60, 22.0, 0.60, 1.00, 23.0,
                 0.90, 0.30, 21.0, 0.90, 0.90, 23.0,
                 1.00, 0.60, 23.0])
#Data pre-processing
data = np.reshape(data, (-1,3))
y = data[:,-1]
k = data.shape[0]
n = 2   #quadratic = 2, linear = 1
l = int(n + n*(n+1)/2)
X = np.ones((k,l+1))
```

```
# Compute the response surface equation coefficient
if n == 1 or n == 2:
    b = coefcalc(n,data,l,k,y,X)
    if len(b)==3:
      print('F(x) = %.1f + %.1fx1 + %.1fx2'\
            %(b[0],b[1],b[2]))
    else:
        print('F(x) = %.1f + %.1fx1 + %.1fx2 \
              %.1fx1^2 %.1fx2^2 + %.1fx1x2'
              %(b[0],b[1],b[2],b[3],b[4],b[5]))
else:
    print("Please enter the value of n = 1 or n = 2")
# Compute coefficient of multiple determination
Rsquared = rsquared(k,y,b,X)
print('R^2 = %.3f'%Rsquared)
# Plot the response surface graph
plotsurface(b)
```

A.7 Response Surface Equations Solver

```
from scipy.optimize import root
import numpy as np
# Double Cell - Withdrawal and Split Pipe - Poured
def dcw_sp(x):
    dcw = 14.1 + 46.8*x[0] + 29.4*x[1] - \
          27.8*x[0]**2 - 18.7*x[1]**2 + \
          5.6*x[0]*x[1] - 41
    sp = 11.9 + 17.9*x[0] + 7.1*x[1] - \
         11.1*x[0]**2 -3.7*x[1]**2 + \
         1.4*x[0]*x[1] - 21
```

```
    return [dcw, sp]
# Double Cell - Withdrawal and Full Pipe - Poured
def dcw_fp(x):
    dcw = 14.1 + 46.8*x[0] + 29.4*x[1] -\
          27.8*x[0]**2 -18.7*x[1]**2 +\
          5.6*x[0]*x[1]-41
    fp = 14.0 + 38.8*x[0] + 17.1*x[1] -\
         22.8*x[0]**2 -14.3*x[1]**2 +\
         11.1*x[0]*x[1] - 36
    return [dcw, fp]
# Full Pipe - Poured and Split Pipe - Poured
def fp_sp(x):
    fp = 14.0 + 38.8*x[0] + 17.1*x[1] -\
         22.8*x[0]**2 -14.3*x[1]**2 +\
         11.1*x[0]*x[1]- 36
    sp = 11.9 + 17.9*x[0] + 7.1*x[1] -\
         11.1*x[0]**2 -3.7*x[1]**2 +\
         1.4*x[0]*x[1] - 21
    return [fp, sp]
mu = root(dcw_sp, np.array([0.5, 0.5]), method='lm',\
          options={'maxiter': 3000})
mu = root(dcw_fp, np.array([0.5, 0.5]), method='lm',\
          options={'maxiter': 3000})
mu = root(fp_sp, np.array([0.5, 0.5]), method='lm', \
          options={'maxiter': 3000})
```

A.8 Response Surfaces Calculations and Plotting Module

```
# statspara.py

import numpy as np
from scipy import linalg
import matplotlib.cm as cm
from mpl_toolkits.mplot3d import Axes3D
import matplotlib.pyplot as plt

def coefcalc(n, data, l, k, y, xi):
    if n == 1:
        for m in range(0, k):
            for i in range(0, l):
                xi[m][i+1] = data[m][i]
    else:
        for m in range(0, k):
            for i in range(0, l-3):
                xi[m][i+1] = data[m][i]
            for i in range(l-3, l-1):
                xi[m][i+1] = data[m][i-2]**2
            for i in range(l-1, l):
                xi[m][i+1] =
                   data[m][i-4]*data[m][i-3]
    xxinv = linalg.inv(np.dot(xi.transpose(), xi))
    b = np.dot(np.dot(xxinv, xi.transpose()), y)
    return b

def firordercoef(data, l, k, y, xi):
    for m in range(0, k):
```

```
        for i in range(0, l):
            xi[m][i+1] = data[m][i]
    xxinv = linalg.inv(np.dot(xi.transpose(), xi))
    b = np.dot(np.dot(xxinv, xi.transpose()), y)
    return b

def secordercoef(data, l, k, y, xi):
    xxinv = []
    for m in range(0, k):
        for i in range(0, l-3):
            xi[m][i+1] = data[m][i]
        for i in range(l-3, l-1):
            xi[m][i+1] = data[m][i-2]**2
        for i in range(l-1, l):
            xi[m][i+1] = data[m][i-4]*data[m][i-3]
        xxinv = linalg.inv(np.dot(xi.transpose(),
           xi))
    b = np.dot(np.dot(xxinv, xi.transpose()), y)
    return b

def rsquared(k, y, b, xi):
    ymean = sum(y)**2/k
    yy = np.dot(y.transpose(), y)
    bxy = np.dot(np.dot(b.transpose(),
       xi.transpose()), y)
    sse = yy - bxy
    sst = yy - ymean
    rsquare = 1 - sse/sst
    return rsquare

def plotsurface(b):
```

```
    xx1 = np.linspace(0.1, 1.0, 50)
    xx2 = np.linspace(0.1, 1.0, 50)
    x1, x2 = np.meshgrid(xx1, xx2)
    if len(b) == 3:
        z = b[0] + b[1]*x1 + b[2]*x2
    else:
        z = b[0] + b[1]*x1 + b[2]*x2 + b[3]*x1**2 +
           b[4]*x2**2 + b[5]*x1*x2
    fig = plt.figure()
    ax = Axes3D(fig)
    ax.plot_surface(x1, x2, z, rstride=1, cstride=1,
       cmap=cm.rainbow)
    m = cm.ScalarMappable(cmap=cm.rainbow)
    m.set_array(z)
    ax.set_xlabel(r'$\mu_{s,pp}$')
    ax.set_ylabel(r'$\mu_{r,pp}$')
    ax.set_zlabel('Angle of Repose')
    plt.colorbar(m)
    plt.show()
```

A.9 Adhesion Data Processing

```
# print('\n'*500)
import csv
import numpy as np
import matplotlib.pyplot as plt
infile=open('sishen_iron_perspex_adhesion_1.csv','r')
table = []
for row in csv.reader(infile):
    table.append(row)
infile.close()
```

```
table = table[2:]
time = np.array([row[0] for row in table])
angle = []
angl = 0
for i in time:
    angl = float(i)*360./300
    angle.append(angl)
angle = np.array(angle)
ke0 = np.array([row[1] for row in table])
ke5000 = np.array([row[2] for row in table])
ke10000 = np.array([row[3] for row in table])
ke15000 = np.array([row[4] for row in table])
ke20000 = np.array([row[5] for row in table])
ke25000 = np.array([row[6] for row in table])

# SECTION 2: PLOT CURVES
plt.figure(1)
plt.plot(angle, ke0, 'r-', linewidth=2,\
         label='Adhesion = 0 kJ/m^3')
plt.plot(angle, ke5000, 'b-', linewidth=2,\
         label='Adhesion = 5 kJ/m^3')
plt.plot(angle, ke10000, 'k-', linewidth=2,\
         label='Adhesion = 10 kJ/m^3')
plt.plot(angle, ke15000, 'g-', linewidth=2,\
         label='Adhesion = 15 kJ/m^3')
plt.plot(angle, ke20000, 'm-', linewidth=2,\
         label='Adhesion = 20 kJ/m^3')
plt.plot(angle, ke25000, 'y-', linewidth=2,\
         label='Adhesion = 25 kJ/m^3')
plt.title('Kinetic Energy vs Rotation Angle')
```

```
plt.xlabel('Angle(Deg)')
plt.ylabel('Kinetic Energy (J)')
plt.ticklabel_format(style='sci',axis='y',\
                     scilimits=(0, 0))
plt.grid(True)
plt.legend(loc='best')
plt.show()
```

A.10 Adhesion Solution

```
import numpy as np
import matplotlib.pyplot as plt
from calibfuncs.quadratic import quadratic
ae = np.array([0, 5, 10, 15, 20, 25])
angle = np.array([25.7, 28.6, 32.8, 37.2,\
                  43.3, 47.4])
p = np.polyfit(ae, angle, 2)
f = np.polyval(p, ae)
print(p)
p1 = np.polyfit(ae, angle, 1)
f1 = np.polyval(p1, ae)
print(p1)
ta = 37  # target angle
tae = quadratic(p[0], p[1], p[2]-ta, ae[0], ae[-1])
print('Second Order predicted adhesion energy
   density\
       is %.0f kJ/m^3' % tae)
tae1 = (ta - p1[1])/p1[0]
print('First Order predicted adhesion energy density
   is\
      %.0f kJ/m^3' % tae1)
```

```
plt.figure(1)
plt.plot(ae, angle, 'g*', linewidth=2, label='Data
   Points')
plt.plot(ae, f, 'b-', linewidth=2, \
         label='Second Order Polynomial')
plt.plot(ae, f1, 'm-', linewidth=2, \
         label='First Order Polynomial')
plt.plot(tae, ta, 'ro', linewidth=4)
plt.plot([0, tae], [ta, ta], 'r--', linewidth=2)
plt.plot([tae, tae], [0, ta], 'r--', linewidth=2)
plt.axis([-0.001, 30, 10, 75])
plt.xlabel('Adhesion Energy Density (kJ/m^3)')
plt.ylabel('Inclination Angle (Deg)')
plt.grid(True)
plt.legend(loc='best')
plt.show()
```

A.11 Quadratic Equations Solution Module

```
# quadratic.py

from math import sqrt
def quadratic(a, b, c, e, f):
    try:
        sqrt_d = sqrt(b**2 - 4*a*c)
        x1 = 1/(2*a)*(-b+sqrt_d)
        x2 = 1/(2*a)*(-b-sqrt_d)
        if e <= x1 <= f:
            return x1
        else:
            if e <= x2 <= f:
```

```
                return x2
            else:
                print('No solution in the given
                   boundaries')
                return float('inf')

    except ValueError:
        print('No solution exists. Returned values
           not correct')
        return [float('inf'), float('inf')]

def quadratic2(a, b, c):
    try:
        sqrt_d = sqrt(b**2 - 4*a*c)
        x1 = 1/(2*a)*(-b+sqrt_d)
        x2 = 1/(2*a)*(-b-sqrt_d)
        return[x1, x2]

    except ValueError:
        print('No solution exists. Returned values
           not correct')
        return [float('inf'), float('inf')]
```

A.12 Cohesion Solution

```
import numpy as np
import matplotlib.pyplot as plt
from calibfuncs.quadratic import quadratic
ce = np.array([75, 100, 125, 150, 175, 200, 225])
angle = np.array([22.0, 23.5, 25.5, 27.5, 29.0,
   30.5, 32.0])
```

```
ce2 = []
angle2 = []
while True:
    try:
        a = input('Enter 1 to plot all points or 2
           to\
                  plot linear points only: ')
        a = int(a)
        x = [1, 2]
        if a not in x:
            raise ValueError
        if a == 1:
            ce2 = np.array([25, 50, 75, 100, 125,
               150,\
                           175, 200, 225])
            angle2 = np.array([21.0, 21.0, 22.0,
               23.5, 25.5,\
                               27.5, 29.0, 30.5,
                                  32.0])
        elif a == 2:
            ce2 = np.array([75, 100, 125, 150, 175,
               200, 225])
            angle2 = np.array([22.0, 23.5, 25.5,
               27.5, 29.0,\
                               30.5, 32.0])
        break
    except ValueError:
        print('Illegal value or character entered.\
                Please enter 1 or 2.')
p = np.polyfit(ce, angle, 1)
f = np.polyval(p, ce)
```

```
print(p)
if len(ce2) == 9:
    p2 = np.polyfit(ce2, angle2, 4)
else:
    p2 = np.polyfit(ce2, angle2, 2)
f2 = np.polyval(p2, ce2)
print(p2)
tar = 25  # target angle of repose
tce = (tar - p[1])/p[0]
print('\nFirst order polynomial prediction of
   cohesion \
        energy density is %.0f kJ/m^3' % tce)
if len(ce2) == 7:
    tce2 = quadratic(p2[0], p2[1], p2[2]-tar,
       ce2[0], ce2[-1])
    print('Second order polynomial prediction of
       cohesion \
           energy density is %.0f kJ/m^3' % tce2)
plt.figure(1)
plt.plot(ce, angle, 'g*', linewidth=2)
plt.plot(ce, f, 'b-', linewidth=3, label='First
   Order Polynomial')
plt.plot(tce, tar, 'ro', linewidth=3)
plt.plot([0, tce], [tar, tar], 'r--', linewidth=2)
plt.plot([tce, tce], [0, tar], 'r--', linewidth=2)
plt.axis([10, 230, 15, 35])
plt.xlabel('Cohesion Energy Density (kJ/m^3)')
plt.ylabel('Angle of Repose (Deg)')
plt.title('Angle of Repose vs Cohesion Energy
   Density')
plt.plot(ce2, angle2, 'g*', linewidth=2)
```

```
if len(ce2) == 9:
    plt.plot(ce2, f2, 'm-', linewidth=3,\
             label='Fourth Order Polynomial')
else:
    plt.plot(ce2, f2, 'm-', linewidth=3,\
             label='Second Order Polynomial')
plt.grid(True)
plt.legend(loc='best')
plt.show()
```

B LIGGGHTS Input Files

B.1 Bulk Density Test

```
### Particle Density Calibration
atom_style                  granular
atom_modify                 map array
boundary                    f f f
newton                      off
units                       si
communicate                 single vel yes
processors                  1 1 1
# Declare domain
region                      domain block -0.1 0.1 -0.4
                            0.1 -0.009 0.1 units box
create_box                  2 domain
# Neighbor listing
neighbor                    0.003 bin
neigh_modify                delay 0
#Material properties required for new pair styles
fix     m1 all property/global youngsModulus
        peratomtype 1.e7 1.e7
fix     m2 all property/global poissonsRatio
        peratomtype 0.25 0.37
fix     m3 all property/global coefficientRestitution
```

```
       peratomtypepair 2 0.5 0.5 0.5 0.5
fix    m4 all property/global coefficientFriction
       peratomtypepair 2 0.5 0.73 0.73 0.5
fix    m5 all property/global
       coefficientRollingFriction
       peratomtypepair 2 0.5 0.5 0.5 0.5
#Import mesh from CAD:
fix    cad1 all mesh/surface file
       meshes/cylinder.stl type 2 scale 0.001
fix    cad2 all mesh/surface file
       meshes/scrapper.stl type 2 scale 0.001
#Particles, generation and insertion:
fix    pts all particletemplate/multisphere
       123457 atom_type 1 density constant 3609
       nspheres 2 ntry 1000000
       spheres 0. 0. 0. 0.0015 0.002 0. 0. 0.0005
       type 1
fix    pdd all particledistribution/discrete
       63243 1 pts 1.0
region factory cylinder z 0 0 0.03 0.02 0.07 units
       box
fix    ins all insert/rate/region seed 123481
       distributiontemplate pdd nparticles 4000
       particlerate 7500 insert_every 1000
       overlapcheck yes vel constant 0. 0. -0.001
       region factory ntry_mc 100000
#Contact laws
pair_style  gran model hertz tangential history
            rolling_friction cdt
pair_coeff  * *
fix         geometry all wall/gran model hertz
```

```
            tangential history mesh n_meshes 2
            meshes cad1 cad2
fix         integrate all multisphere
#Gravity
fix     gravi all gravity 9.81 vector 0.0 0.0 -1.0
#Timestep
timestep    0.00001
#Thermo setting
variable          t equal time
compute           1 all erotate/multisphere
compute           m all multisphere property masstotal
compute           k all ke/multisphere
thermo_style      custom step time atoms c_k c_1
thermo            1000
thermo_modify     lost ignore norm no
# Check time step and initialize dump file
fix     ctg all check/timestep/gran 1 0.2 0.2
run     1
unfix   ctg
# Create imaging information
dump    dmp all custom 1000 post/dump*.density
        id type type x y z ix iy iz vx vy vz
        fx fy fz omegax omegay omegaz radius
dump    dmpstl all mesh
# Fill the cup
run             100000 upto
# Move the scrapper and unfix it
fix         movecad2 all move/mesh mesh cad2
            linear 0. -0.16 0
run         170000 upto
undump      dmpstl
```

```
dump          dmpstl all mesh/stl 1000 post/dump*.stl
              cad1
unfix         movecad2
run           200000 upto
```

B.2 Wall Shear Test

```
shell rm csvs/wshear_047_15.csv
atom_style     granular
atom_modify    map array
newton         off
communicate    single vel yes
processors     2 2 1
read_restart   restart/wall_ringfill.rsrt
# Neighbor listing
neighbor        0.001 bin
neigh_modify    delay 0
# Material and interaction properties required
fix    m1 all property/global youngsModulus
       peratomtype 1.e7 1.e7
fix    m2 all property/global poissonsRatio
       peratomtype 0.25 0.37
fix    m3 all property/global coefficientRestitution
       peratomtypepair 2 0.61 0.56 0.56 0.5
fix    m4 all property/global coefficientFriction
       peratomtypepair 2 0.73 0.47 0.47 0.5
fix    m5 all property/global
   coefficientRollingFriction
       peratomtypepair 2 0.28 0.1 0.1 0.5
# Import mesh from cad:
fix    cad1 all mesh/surface/stress file
```

```
      meshes/liner.stl type 2 scale 0.001
      stress on
fix   cad2 all mesh/surface/stress file
      meshes/ring.stl type 2 scale 0.001
      stress off
# Use the imported mesh as granular wall

fix   geometry all wall/gran model hertz tangential
      history rolling_friction cdt mesh n_meshes 2
      meshes cad1 cad2
# Define the physics for particle-particle
   interactions
pair_style  gran model hertz tangential history
            rolling_friction cdt
pair_coeff  * *
### Detailed settings
# Integrator
fix    integrate all multisphere
# Gravity
fix        grav all gravity 9.81 vector 0.0 0.0 -1.0
# Timestep
timestep        0.00001
reset_timestep  0
run             10
# Import the top lid - load carrier mesh
unfix           geometry
fix             cad3 all mesh/surface/stress/servo
                file meshes/top.stl type 1 scale
                0.001 com 0 0 0.0663 ctrlPV force axis
                0. 0. 1. target_val -14.175
                vel_max 10.0
```

```
fix           geometry all wall/gran model hertz
          tangential history mesh n_meshes 3 meshes
          cad1 cad2 cad3
# Thermodynamic and other output settings
variable    t equal "step*dt"
variable    k equal ke
variable    F equal f_cad1[1]
variable    N equal (-1.*f_cad1[3])
variable    d equal "(step*dt - 0.0)*0.00042*1000"
thermo_style    custom step atoms ke cpu v_t v_d v_F
                v_N
thermo          10000
thermo_modify   norm no lost ignore
fix             out2 all print 10000 "$t,$d,$N,$F"
                append csvs/wshear_047_15.csv screen
                yes title "Time (s),
                   Displacement(mm),
                Normal Force (N),Shear Force (N)"
# Create imaging information
dump    dmp all custom 10000 post/dump*.shear id type
        type x y z ix iy iz vx vy vz fx fy fz omegax
        omegay omegaz radius
dump    dmpstl all mesh/stl 10000 post/dump*.stl
        cad1 cad2 cad3
# Move the base in shearing motion
fix     movecad1ahead all move/mesh mesh cad1
        linear -0.00042 0 0
run     1000000 upto
# Save the simulation state to a restart file
write_restart    restart/wall_shear_1000000.rsrt
```

B.3 Double Cell Repose

```
atom_style    granular
atom_modify   map array
newton        off
communicate   single vel yes
processors    2 2 1
read_restart restart/doublefill_in.rsrt
# Neighbor listing
neighbor       0.001 bin
neigh_modify   delay 0
# Material and interaction properties required
fix   m1 all property/global youngsModulus
      peratomtype 1.e7 1.e7
fix   m2 all property/global poissonsRatio
      peratomtype 0.25 0.37
fix   m3 all property/global coefficientRestitution
      peratomtypepair 2 0.61 0.56 0.56 0.5
fix   m4 all property/global coefficientFriction
      peratomtypepair 2 0.73 0.47 0.47 0.5
fix   m5 all property/global
      coefficientRollingFriction peratomtypepair
      2 0.28 0.1 0.1 0.5
# Import mesh from cad:
fix   cad1 all mesh/surface file
      meshes/lower_cell.stl type 2 scale 0.001
fix   cad2 all mesh/surface file
      meshes/upper_cell.stl type 2 scale 0.001
fix   cad4 all mesh/surface file
      meshes/gate.stl type 2 scale 0.001
# Use the imported mesh as granular wall
```

```
fix  geometry all wall/gran model hertz
     tangential history rolling_friction cdt
     mesh n_meshes 3 meshes cad1 cad2 cad4
# Define the physics for particle - particle
pair_style   gran model hertz tangential history
             rolling_friction cdt
pair_coeff   * *
# Integrator
fix   integrate all multisphere
# Gravity
fix   grav all gravity 9.81 vector 0.0 0.0 -1.0
# Time step
timestep   0.00001
# Thermodynamic and other output settings
variable   t equal "step*dt"
compute    k all ke/multisphere
variable   a equal atoms
thermo_style  custom step atoms ke cpu v_t
thermo        10000
thermo_modify norm no lost ignore
# Check time step and initialize dump file
fix     ctg all check/timestep/gran 1 0.01 0.01
run     1
unfix   ctg
# Create imaging information
dump    dmp all custom 10000 post/dump*.repose
        id type type x y z ix iy iz vx vy vz fx
        fy fz omegax omegay omegaz radius
dump    dmpstl all mesh/stl 10000
        post/dump*.stl cad1 cad2
# Remove the gate and run the simulation
```

```
unfix    geometry
fix      geometry all wall/gran model hertz
         tangential history rolling_friction cdt
         mesh n_meshes 2 meshes cad1 cad2
reset_timestep  0
run             500000 upto
# Save the simulation state to a restart file
write_restart restart/doublecell073028_500000.rsrt
```

B.4 Full Pipe Repose

```
atom_style    granular
atom_modify   map array
newton        off
communicate   single vel yes
processors    2 2 1
read_restart restart/pipefill_in.rsrt
# Neighbor listing
neighbor      0.001 bin
neigh_modify delay 0
# Material and interaction properties required
fix    m1 all property/global youngsModulus
       peratomtype 1.e7 1.e7
fix    m2 all property/global poissonsRatio
       peratomtype 0.25 0.37
fix    m3 all property/global
       coefficientRestitution peratomtypepair
       2 0.61 0.56 0.56 0.5
fix    m4 all property/global coefficientFriction
       peratomtypepair 2 0.73 0.47 0.47 0.5
fix    m5 all property/global
```

```
      coefficientRollingFriction peratomtypepair
      2 0.28 0.1 0.1 0.5
# Import mesh from cad:
fix   cad1 all mesh/surface file
      meshes/cylinder_repose.stl type 2
      scale 0.001
fix   cad2 all mesh/surface fil
      meshes/floor.stl type 2 scale 0.001
# Use the imported mesh as granular wall
fix   geometry all wall/gran model hertz
      tangential history rolling_friction
      cdt mesh n_meshes 2 meshes cad1 cad2
# Define the physics for particle - particle
pair_style  gran model hertz tangential
            history rolling_friction cdt
pair_coeff  * *
# Integrator
fix         integrate all multisphere
# Gravity
fix   grav all gravity 9.81 vector 0.0 0.0 -1.0
# Time step
timestep     0.00001
# Thermodynamic and other output settings
variable      t equal "step*dt"
compute       k all ke/multisphere
variable      a equal atoms
thermo_style  custom step atoms ke cpu v_t
thermo                  10000
thermo_modify   norm no lost ignore
# Check time step and initialize dump file
fix    ctg all check/timestep/gran 1 0.01 0.01
```

```
run     1
unfix   ctg
# Create imaging information
dump    dmp all custom 10000 post/dump*.repose
        id type type x y z ix iy iz vx vy vz fx
        fy fz omegax omegay omegaz radius
dump    dmpstl all mesh/stl 10000
        post/dump*.stl cad1 cad2
# Remove the gate and run the simulation
fix    movecad1 all move/mesh mesh cad1
       linear 0 0 0.005
reset_timestep  0
run    1400000 upto
# Save the simulation state to a restart file
write_restart restart/pipefull073028_1400000.rsrt
```

B.5 Split Pipe Repose

```
atom_style      granular
atom_modify     map array
newton          off
communicate     single vel yes
processors      2 2 1
read_restart    restart/pipefill_in.rsrt
# Neighbor listing
neighbor        0.001 bin
neigh_modify    delay 0
# Material and interaction properties required
fix   m1 all property/global youngsModulus
      peratomtype 1.e7 1.e7
fix   m2 all property/global poissonsRatio
```

```
     peratomtype 0.25 0.37
fix  m3 all property/global
     coefficientRestitution peratomtypepair
     2 0.61 0.56 0.56 0.5
fix  m4 all property/global coefficientFriction
     peratomtypepair 2 0.73 0.73 0.73 0.5
fix  m5 all property/global
     coefficientRollingFriction peratomtypepair
     2 0.28 0.1 0.1 0.5
# Import mesh from cad:
fix  cad1 all mesh/surface file
     meshes/cylinder_repose.stl type 2
     scale 0.001
fix  cad2 all mesh/surface file
     meshes/floor.stl type 2 scale 0.001
# Use the imported mesh as granular wall
fix  geometry all wall/gran model hertz
     tangential history rolling_friction cdt
     mesh n_meshes 2 meshes cad1 cad2
# Define the physics for particle - particle
pair_style    gran model hertz tangential history
              rolling_friction cdt
pair_coeff    * *
# Integrator
fix       integrate all multisphere
# Gravity
fix grav all gravity 9.81 vector 0.0 0.0 -1.0
# Time step
timestep    0.00001
# Thermodynamic and other output settings
variable      t equal "step*dt"
```

```
compute       k all ke/multisphere
variable      a equal atoms
thermo_style  custom step atoms ke cpu v_t
thermo        5000
thermo_modify norm no lost ignore
# Check time step and initialize dump file
fix     ctg all check/timestep/gran 1 0.01 0.01
run     1
unfix   ctg
# Create imaging information
dump    dmp all custom 5000 post/dump*.repose
        id type type x y z ix iy iz vx vy vz
        fx fy fz omegax omegay omegaz radius
dump    dmpstl all mesh/stl 5000 post/dump*.stl
        cad1 cad2
# Execution and further settings
reset_timestep  0
run             1000 upto
# Remove the cylinder instantaneously
unfix   geometry
fix     geometry all wall/gran model hertz
        tangential history rolling_friction
        cdt mesh n_meshes 1 meshes cad2
undump  dmpstl
dump    dmpstl all mesh/stl 5000 post/dump*.stl
        cad2
run     150000 upto
# Save the simulation state to a restart file
write_restart  restart/pipesplit073028_150000.rsrt
```

B.6 Adhesion Inclined Plane

```
shell rm csvs/adhesion_15000.csv
units          si
atom_style     granular
atom_modify    map array
boundary       f f f
newton         off
communicate    single vel yes
processors     2 2 1
# Declare domain
region      domain block -0.2 0.2
            -0.1 0.1 -0.01 0.2 units box
create_box  2 domain
# Neighbor listing
neighbor       0.001 bin
neigh_modify   delay 0
# Material and interaction properties required
fix   m1 all property/global youngsModulus
      peratomtype 1.e7 1.e7
fix   m2 all property/global poissonsRatio
      peratomtype 0.25 0.37
fix   m3 all property/global coefficientRestitution
      peratomtypepair 2 0.61 0.56 0.56 0.06
fix   m4 all property/global coefficientFriction
      peratomtypepair 2 0.73 0.47 0.47 0.5
fix   m5 all property/global
      coefficientRollingFriction peratomtypepair
      2 0.28 1.0 1.0 0.5
fix   m7 all property/global cohesionEnergyDensity
      peratomtypepair 2 0 15000 15000 0
```

```
# Import mesh from cad:
fix  cad1 all mesh/surface/stress file
     meshes/inclinoplane.stl type 2 scale 0.001
# Use the imported mesh as granular wall
fix  geometry all wall/gran model hertz
     tangential history cohesion sjkr
     rolling_friction cdt
     mesh n_meshes 1 meshes cad1 limitForce on
# Define the physics for particle - particle
pair_style  gran model hertz tangential history
            cohesion sjkr rolling_friction cdt
            limitForce on
pair_coeff  * *
# Particle insertion
fix  pts all particletemplate/multisphere
     15485863 atom_type 1 density constant 3609
     nspheres 2 ntry 1000000
     spheres 0. 0. 0. 0.0015 0.002 0. 0. 0.0005
     type 1
fix  pdd all particledistribution/discrete
     49979687 1 pts 1.0
region  factory cylinder z 0.1 0 0.03 0.001 0.03
        units box
fix     ins all insert/rate/region seed 32452843
        distributiontemplate pdd nparticles 1
        particlerate 1000 insert_every 1000
        overlapcheck yes vel constant 0. 0. -0.01
        region factory ntry_mc 100000
# Integrator
fix     integrate all multisphere
# Gravity
```

```
fix   grav all gravity 9.81 vector 0.0 0.0 -1.0
# Time step
timestep  0.00001
# Thermodynamic and other output settings
variable      t equal "step*dt"
variable      k equal ke
thermo_style  custom step atoms ke cpu
thermo        5000
thermo_modify norm no lost ignore
fix  out2 all print 5000 "$t,$k" append
     csvs/adhesion_15000.csv screen yes title
     "Time (s), Kinetic Energy (J)"
# Create imaging information
dump   dmp all custom 5000 post/dump*.wshear
       id type type x y z ix iy iz vx vy vz fx
       fy fz omegax omegay omegaz radius
dump   dmpstl all mesh/stl 5000 post/dump*.stl
       cad1
### Execution and further settings
run     50000 upto
fix     rotatecad1 all move/mesh mesh cad1
        rotate origin 0. 0. 0. axis 0. 1. 0.
        period -300.0
run     6000000
```

B.7 Cohesion Split Pipe Repose

```
atom_style      granular
atom_modify     map array
newton          off
communicate     single vel yes
```

```
processors      2 2 1
read_restart    restart/pipefill_in.rsrt
# Neighbor listing
neighbor        0.001 bin
neigh_modify    delay 0
# Material and interaction properties required
fix  m1 all property/global youngsModulus peratomtype
     1.e7 1.e7
fix  m2 all property/global poissonsRatio
     peratomtype 0.25 0.37
fix  m3 all property/global coefficientRestitution
     peratomtypepair 2 0.61 0.56 0.56 0.5
fix  m4 all property/global coefficientFriction
     peratomtypepair 2 0.73 0.73 0.73 0.5
fix  m5 all property/global
   coefficientRollingFriction
     peratomtypepair 2 0.28 0.1 0.1 0.5
fix  m7 all property/global cohesionEnergyDensity
     peratomtypepair 2 118000 0 0 0
# Import mesh from cad:
fix  cad1 all mesh/surface file
     meshes/cylinder_repose.stl type 2
     scale 0.001
fix  cad2 all mesh/surface file
     meshes/floor.stl type 2 scale 0.001
# Use the imported mesh as granular wall
fix  geometry all wall/gran model hertz tangential
     history cohesion sjkr mesh n_meshes 2 meshes
     cad1 cad2
# Define the physics for particle - particle
pair_style  gran model hertz tangential history
```

```
            cohesion sjkr rolling_friction cdt
pair_coeff  * *
# Integrator
fix         integrate all multisphere
# Gravity
fix grav all gravity 9.81 vector 0.0 0.0 -1.0
# Timestep
timestep    0.00001
# Thermodynamic and other output settings
variable    t equal "step*dt"
compute     k all ke/multisphere
variable    a equal atoms
thermo_style custom step atoms ke cpu v_t
thermo     5000
thermo_modify  norm no lost ignore
# Check time step and initialize dump file
fix ctg all check/timestep/gran 1 0.01 0.01
run         1
unfix       ctg
# Create imaging information
dump    dmp all custom 5000 post/dump*.repose
        id type type x y z ix iy iz vx vy vz fx
        fy fz omegax omegay omegaz radius
dump    dmpstl all mesh/stl 5000 post/dump*.stl
        cad2
# Execution and further settings
reset_timestep    0
run               1000 upto
# Remove the cylinder instantaneously
unfix             geometry
fix  geometry all wall/gran model hertz
```

```
      tangential history cohesion sjkr mesh
      n_meshes 1 meshes cad2
run   150000 upto
```

C Drawings

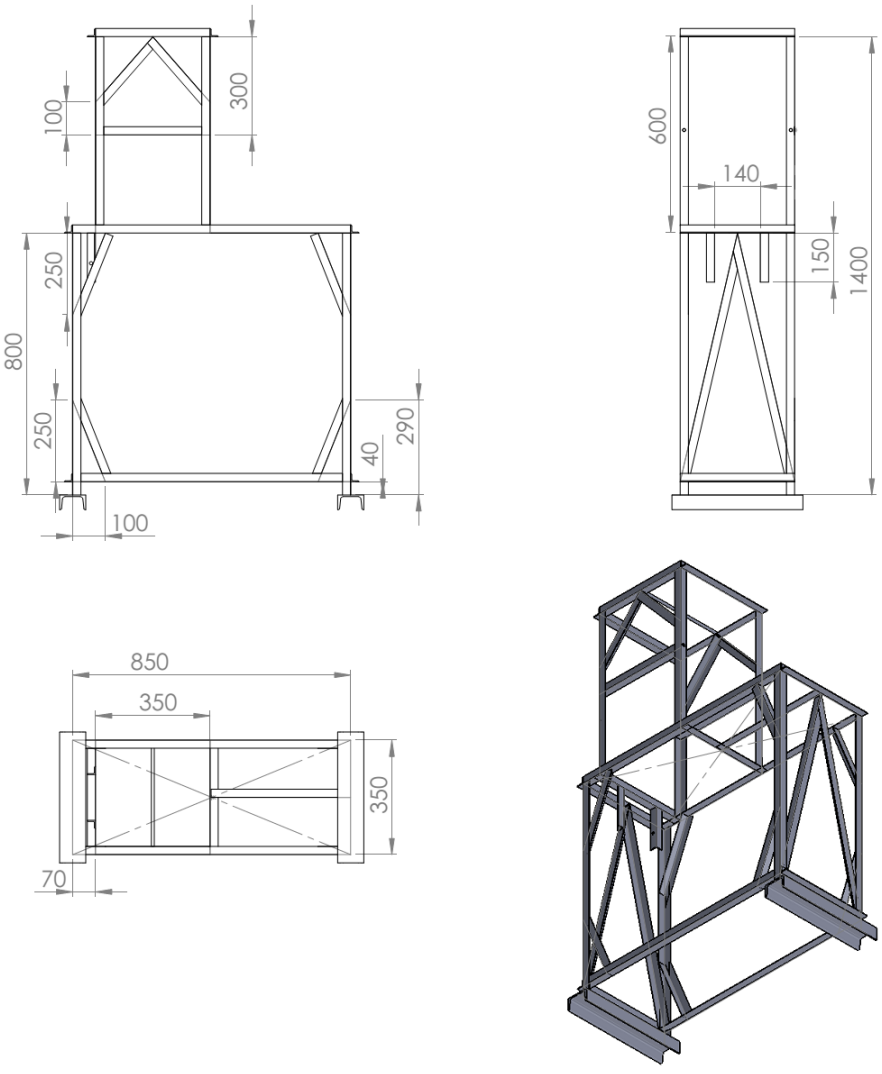


Figure C.1: Steel frame drawings

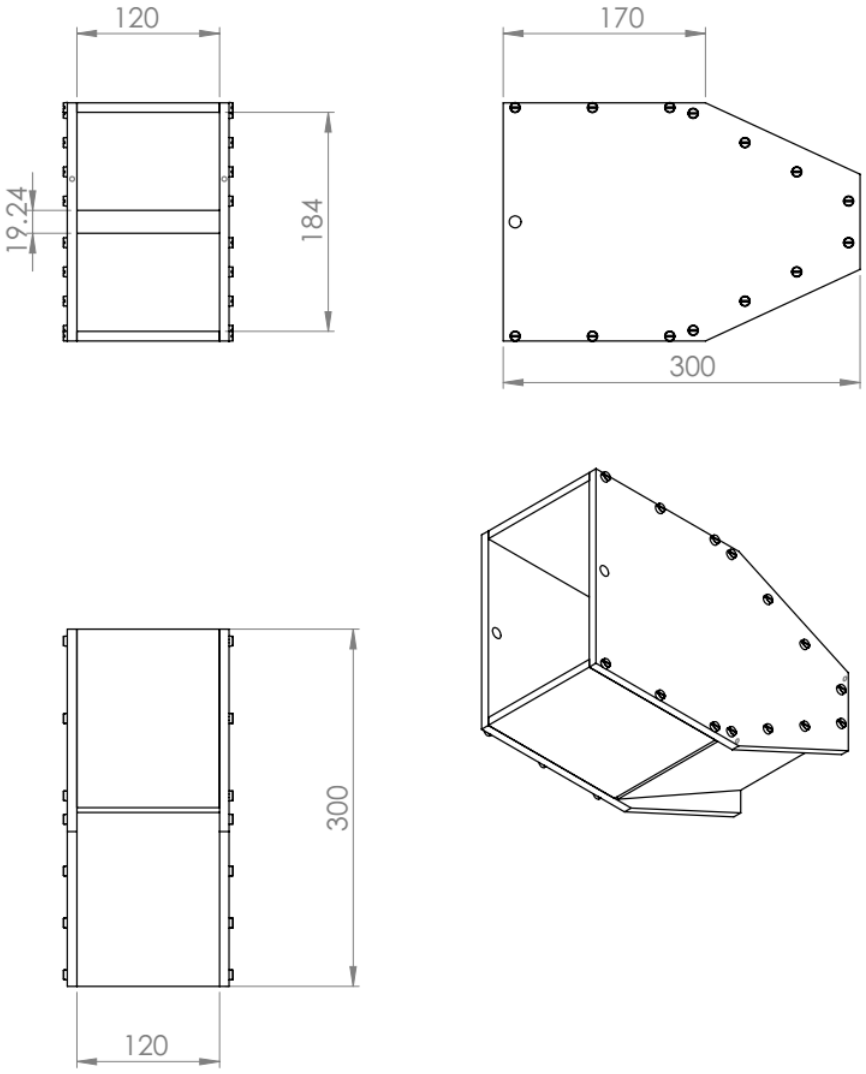


Figure C.2: Silo drawings

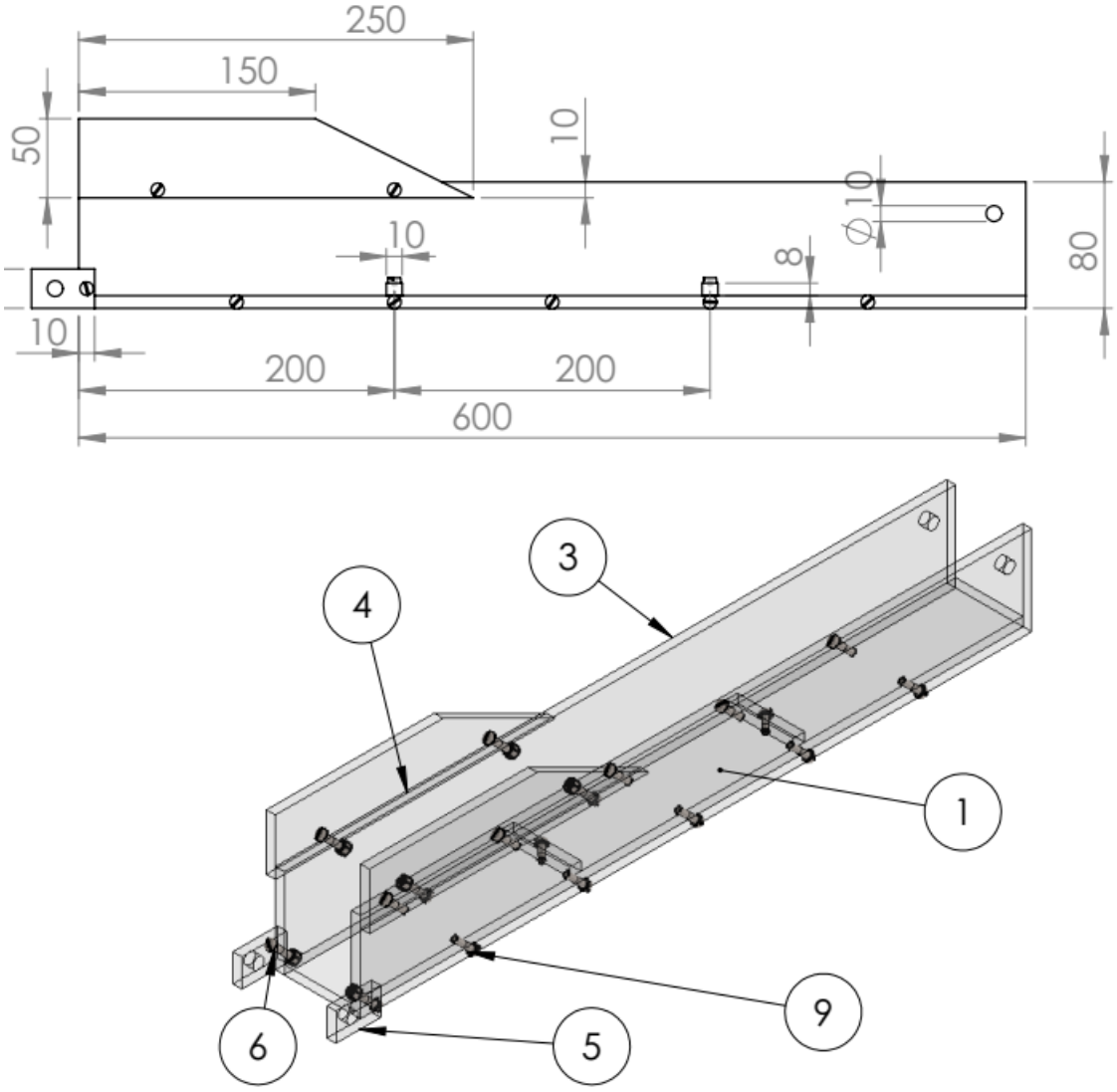


Figure C.3: Chute drawings

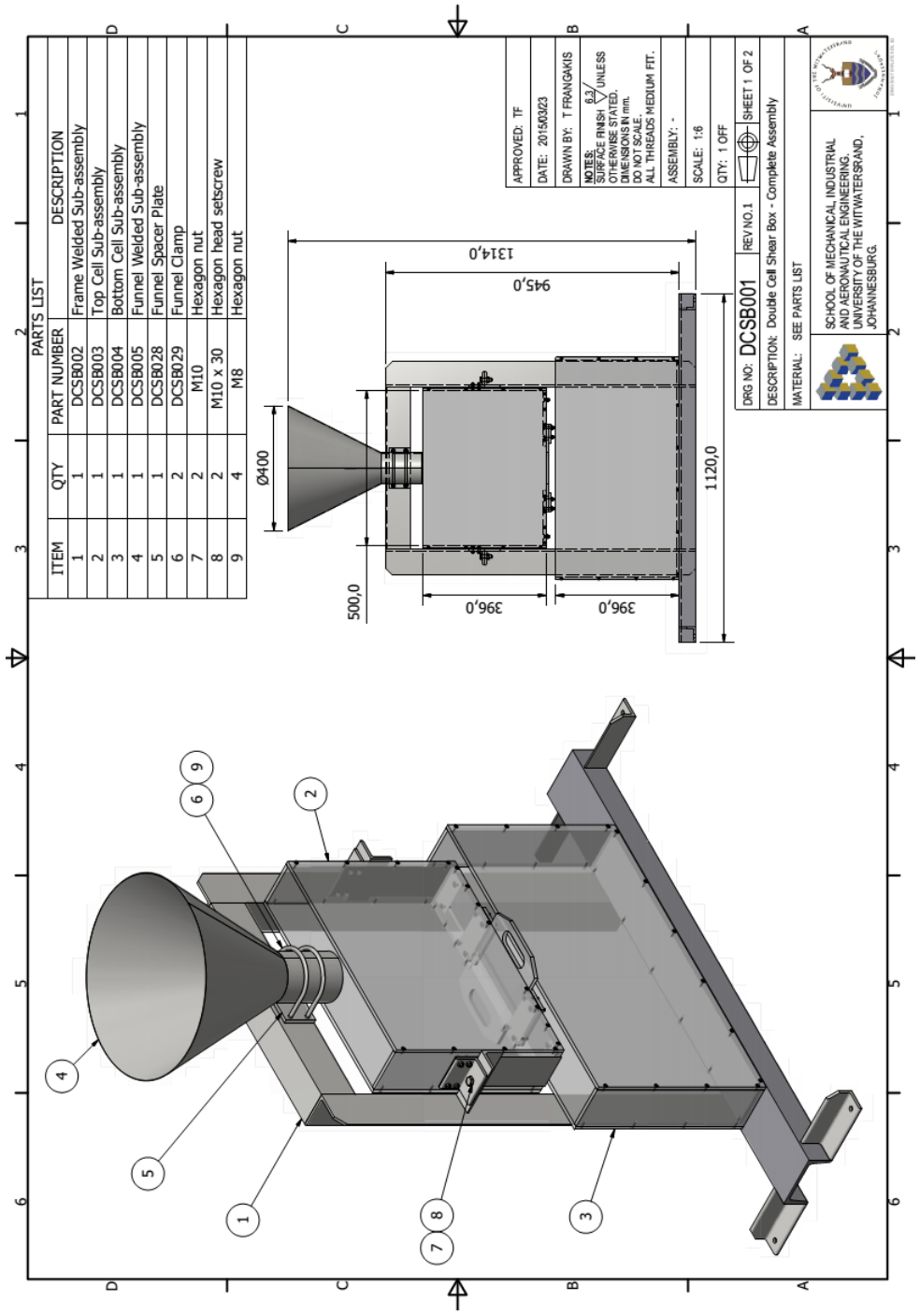


Figure C.4: Double Cell Angle of Repose Tester

D Moisture Content procedures

D.1 Bulk Material Moisture Elevation Procedure

Moisture content experimental procedure is carried out to determine the existing moisture in the dry bulk material. The result is used to determine the amount of water to be added into the bulk material in order to bring the moisture content to the desired moisture content of 1.2%.

Bulk material at 1.2% moisture content was used for the purposes of calibrating cohesion energy density. This value of moisture content was chosen based on the flow property tests of the same material, which was determined to exhibit highest level of cohesion at 1.2%.

For this procedure, the drying ovens in TBSA laboratory were used. The following experimental procedure was followed:

1. The oven was preheated to a temperature of 105 ^{o}C.

2. The drying tray was cleaned, weighed on a scale and the mass recorded.

3. A bulk material sample was placed into the tray and evenly spread to maximise surface area of bulk material exposed to free air flow.

4. The mass of the tray and bulk material was measured on the scale and recorded.

5. The tray with bulk material was placed into the drying oven and left for

15 minutes. The tray was taken out and the mass mass measured.

6. The process was repeated at 15 minutes intervals until two consecutive readings have less than 0.3 grams difference in mass.

7. The total mass of expelled moisture was calculated by subtracting the final mass in step (6) from the starting mass in step (4).

8. The total moisture content was calculated as the ratio of mass of the expelled moisture in step (7) and the starting mass in step (4)

9. The mass of a sample of bulk material was measured on a scale for elevation to the desired moisture content of 1.2%.

10. The amount of water for adding into the bulk material sample was calculated using Equation D.1.

11. The amount of water determined in step (10) was measured and added into the bulk material sample in step (9)

12. The bulk material and the added water were thoroughly mixed.The mixed sample was tightly closed to ensure moisture retention.

D.2 Bulk Material Moisture Elevation Test Results

Bulk material moisture elevation of dry iron ore was carried out according to the procedure outlined in Section D.1. Table D.1 shows the experiment observations and the existing moisture content.

The total bulk material sample prior to addition of water was 5.5 kg. The amount of water added was calculated using Equation D.1 to be 55.7 g for a total moisture content 0f 1.2% on a wet basis.

Table D.1: Existing moisture content

Time (min)	**Material Mass (g)**	**Change in Mass (g)**
0	386.9	-
15	386.2	0.7
30	386.1	0.1
45	386.1	0.0
Moisture Content (%)	0.2	

D.3 Bulk Material Moisture Elevation Calculations

Sometimes it is desirable to raise the moisture content of the bulk material by addition of water. Given the existing moisture content, MC_c, the desired moisture content, MC_t, and the total mass of the bulk material sample, m_t, Equation D.1 gives the mass of water required, m_{aw}, to bring the bulk material sample to the desired moisture content from the existing moisture content.

$$m_{aw} = \frac{m_t(MC_t - MC_c)}{100 - MC_t} \tag{D.1}$$

The mass of dry bulk material, m_s, can be calculated given the existing moisture content and mass of the bulk material sample, using Equation D.2.

$$m_s = \frac{m_t(100 - MC_c)}{100} \tag{D.2}$$

The total moisture content of a bulk material sample can be calculated given the mass of dry bulk material, m_s, and mass of water, m_w, in the sample, using Equation D.3

$$MC_c = \frac{100m_w)}{m_w + m_s} \tag{D.3}$$

E Coefficient of Restitution

Table E.1: Coefficient of restitution, particle to particle

Test #	**Start Height (mm)**	**Rebound Height (mm)**	**Coefficient of Restitution**
1	200	55	0.52
2	200	55	0.52
3	200	85	0.65
4	200	110	0.74
5	200	55	0.52
6	210	50	0.49
7	210	45	0.46
8	210	95	0.67
9	210	100	0.69
10	190	55	0.54
11	220	80	0.60
12	210	95	0.67
13	200	70	0.59
14	210	110	0.72
15	230	90	0.63
16	230	80	0.59
17	230	85	0.61
18	240	105	0.66
19	230	90	0.63
20	230	85	0.61
21	230	80	0.59
22	240	105	0.66
23	240	50	0.46
24	230	110	0.69
25	230	80	0.59
26	230	80	0.59
27	230	110	0.69
Average			0.61
Minimum			0.46
Maximum			0.74
Standard Deviation			0.08

Table E.2: Coefficient of restitution, particle to wall surface

Test #	**Start Height (mm)**	**Rebound Height (mm)**	**Coefficient of Restitution**
1	200	30	0.30
2	200	40	0.45
3	200	60	0.55
4	210	60	0.53
5	200	30	0.39
6	210	50	0.49
7	220	70	0.56
8	220	60	0.52
9	220	60	0.52
10	230	60	0.51
11	220	70	0.56
12	220	70	0.56
13	220	80	0.60
14	220	75	0.58
15	210	60	0.53
16	210	65	0.56
17	210	65	0.56
18	220	60	0.52
19	220	65	0.54
20	220	70	0.56
21	210	50	0.49
22	220	60	0.52
23	220	60	0.52
24	220	100	0.67
25	220	85	0.62
26	230	90	0.63
27	220	80	0.60
28	210	70	0.58
29	210	75	0.60
30	200	65	0.57
31	210	60	0.53
32	210	75	0.60
33	200	60	0.55
34	210	85	0.64
35	200	70	0.59
36	210	80	0.62
37	210	90	0.65
38	210	60	0.53
39	210	80	0.62
40	200	75	0.61
41	210	70	0.58
42	210	65	0.56
43	200	50	0.50
Average			0.56
Minimum			039
Maximum			0.67
Standard Deviation			0.06

F Inclined Plane Tests

F.1 Coefficient of Sliding and Rolling Friction Results

Table F.1: Coefficients of sliding and rolling friction, particle to wall

Test #	Sliding Angle (°)	Coefficient of Sliding Friction	Rolling Angle (°)	Coefficient of Rolling Friction
1	24	0.45	8	0.14
2	26	0.49	7	0.12
3	26	0.49	5	0.09
4	24	0.45	5	0.09
5	24	0.45	6	0.11
6	26	0.49	5	0.09
7	27	0.52	4	0.07
8	25	0.47	5	0.09
9	24	0.45	5	0.09
10	26	0.49	8	0.14
11	25	0.47	9	0.16
12	24	0.49	4	0.07
13	24	0.45	4	0.07
14	25	0.47	8	0.14
15	26	0.49	6	0.11
16	24	0.45	9	0.16
17	25	0.47	4	0.07
18	24	0.45	6	0.11
19	24	0.45	4	0.07
20	26	0.49	6	0.11
Average		0.47		0.10
Minimum		0.45		0.07
Maximum		0.51		0.16
Standard Deviation		0.02		0.03

F.2 Moist Iron Ore Sliding Angle

Table F.2: Moist particle sliding angle

Test #	**Sliding Angle (°)**
1	36
2	37
3	39
4	34
5	35
6	38
7	33
8	40
9	32
10	37
11	38
12	35
13	39
14	38
15	40
16	33
17	38
18	37
19	40
20	34
Average	37
Minimum	32
Maximum	40
Standard Deviation	2.5

G Bulk Density Test Results

Table G.1: Bulk density, small container

Parameter	**Test 1**	**Test 2**	**Test 3**	**Test 4**	**Test 5**	**Test 6**
Container Volume (m^3)	$6.017\,15 \times 10^{-5}$					
Material Mass (kg)	0.1099	0.1122	0.1107	0.1093	0.1083	0.1114
Bulk Density (kg/m^3)	1826	1865	1840	1816	1800	1851
Average						1833
Minimum						1800
Maximum						1865
Standard Deviation						24

Table G.2: Bulk density, large container

Parameter	**Test 1**	**Test 2**	**Test 3**	**Test 4**	**Test 5**	**Test 6**
Container Volume (m^3)	$9.715\,69 \times 10^{-4}$					
Material Mass (kg)	1.8750	1.8600	1.8400	1.8500	1.8350	1.8650
Bulk Density (kg/m^3)	1930	1914	1894	1904	1889	1920
Average						1908
Minimum						1899
Maximum						1930
Standard Deviation						16

H DEM Wall Friction Test Results

This Appendix shows the DEM wall friction observations and results plotted and calculated from the csv files saved during the simulations. The processing was done using a Python program in Appendix A.3. The shear and normal stress on the shear plane were all averaged between shearing distances of 3 mm and 4 mm, for $\mu_{pw,s}$ from 0.2 to 0.9.

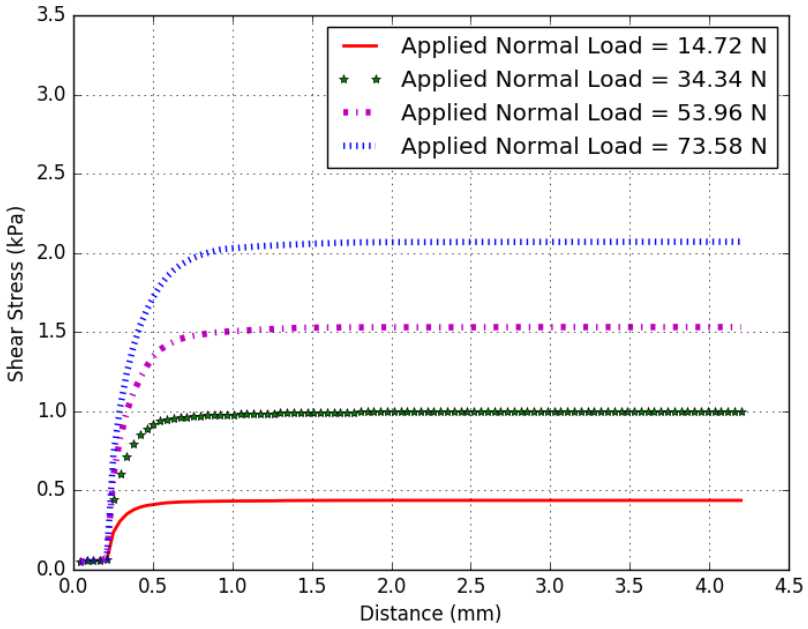


Figure H.1: Variation of shear stress with displacement for $\mu_{pw,s} = 0.2$

The fitted linear curve in Figure H.2 has a gradient of 0.197. The corresponding angle of wall friction is therefore the arctangent of the gradient which is equal to 11.2 °.

Table H.1: Average limiting shear and normal stresses, $\mu_{pw,s} = 0.2$

	Normal Load (N)			
	14.7	**34.3**	**54.0**	**73.5**
Average Shear Stress @ 3mm - 4mm Displacement (kPa)	0.44	1.00	1.53	2.07
Average Normal Stress @ 3mm - 4mm Displacement (kPa)	2.20	5.02	7.73	10.5

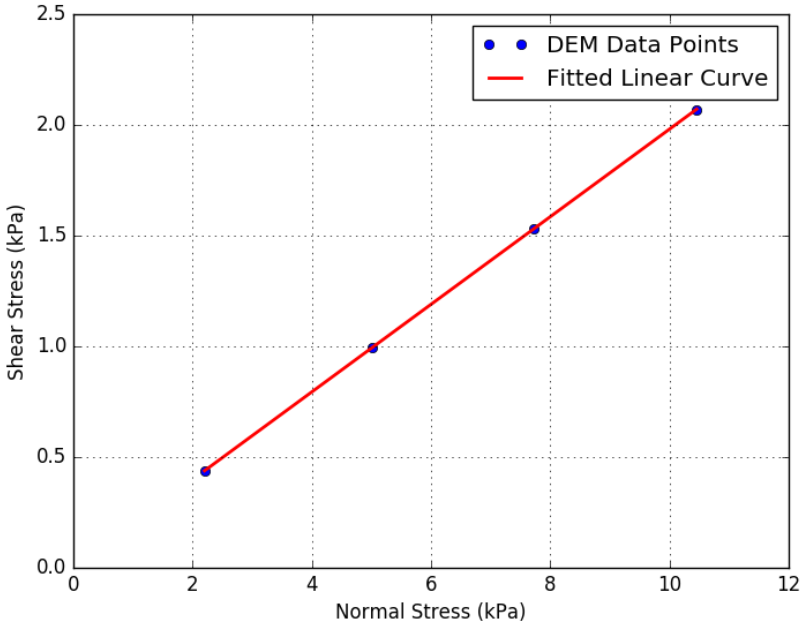


Figure H.2: Variation of shear stress with normal stress for $\mu_{pw,s} = 0.2$

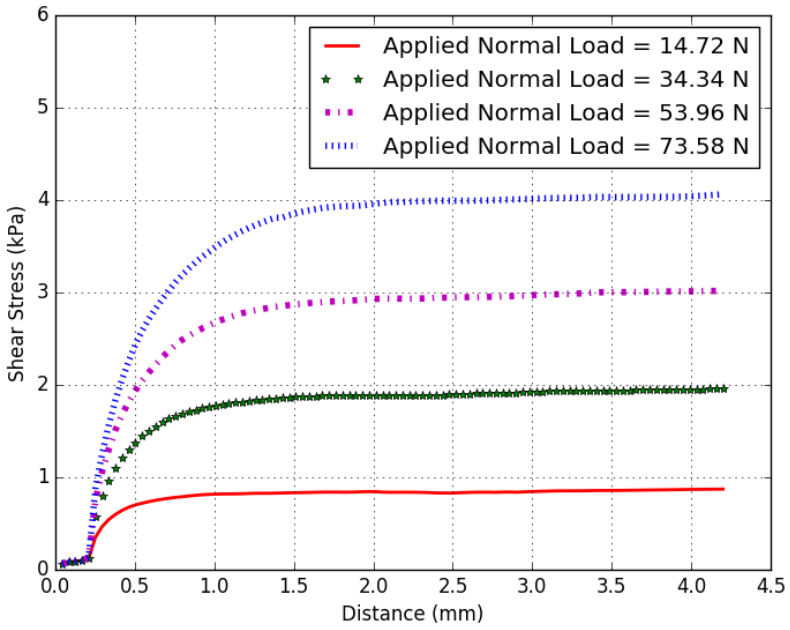


Figure H.3: Variation of shear stress with displacement for $\mu_{pw,s} = 0.4$

Table H.2: Average limiting shear and normal stresses, $\mu_{pw,s} = 0.4$

	Normal Load (N)			
	14.7	**34.3**	**54.0**	**73.5**
Average Shear Stress @ 3mm - 4mm Displacement (kPa)	0.85	1.95	3.01	4.04
Average Normal Stress @ 3mm - 4mm Displacement (kPa)	2.22	4.98	7.76	10.5

The fitted linear curve in Figure H.4 has a gradient of 0.383. The corresponding angle of wall friction is therefore the arctangent of the gradient which is equal to 21.0 °.

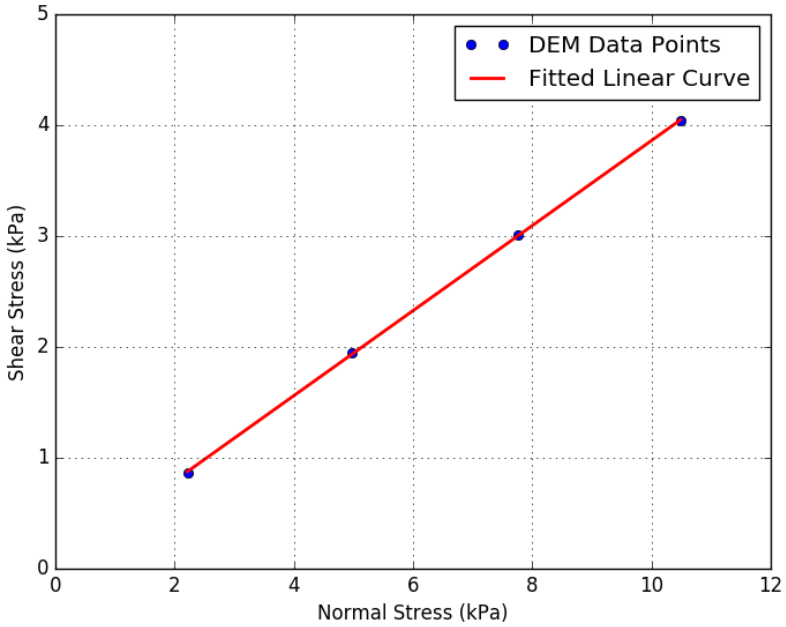


Figure H.4: Variation of shear stress with normal stress for $\mu_{pw,s} = 0.4$

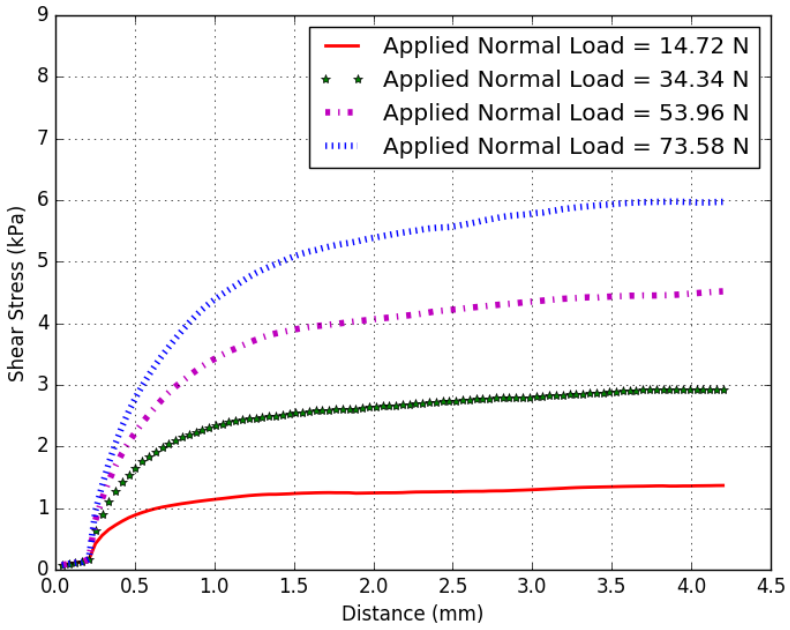


Figure H.5: Variation of shear stress with displacement for $\mu_{pw,s} = 0.6$

Table H.3: Average limiting shear and normal stresses, $\mu_{pw,s} = 0.6$

	Normal Load (N)			
	14.7	**34.3**	**54.0**	**73.5**
Average Shear Stress @ 3mm - 4mm Displacement (kPa)	1.36	2.91	4.66	5.96
Average Normal Stress @ 3mm - 4mm Displacement (kPa)	2.47	5.40	8.33	11.3

The fitted linear curve in Figure H.6 has a gradient of 0.524. The corresponding angle of wall friction is therefore the arctangent of the gradient which is equal to 27.7 °.

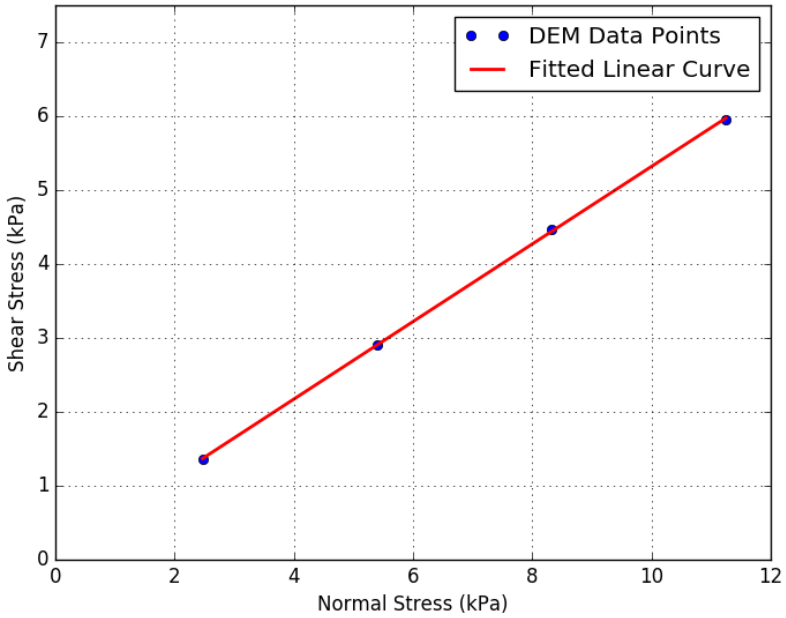


Figure H.6: Variation of shear stress with normal stress for $\mu_{pw,s} = 0.6$

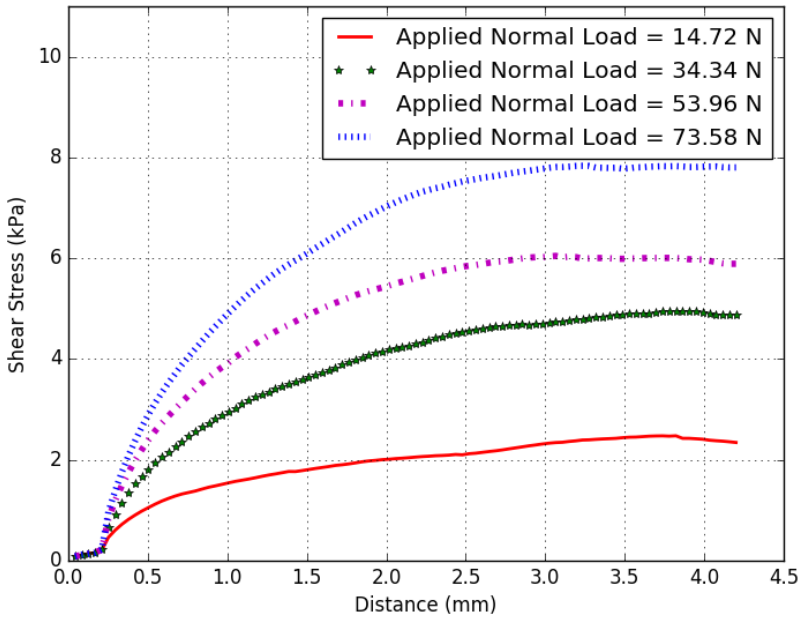


Figure H.7: Variation of shear stress with displacement for $\mu_{pw,s} = 0.9$

Table H.4: Average limiting shear and normal stresses, $\mu_{pw,s} = 0.9$

	Normal Load (N)			
	14.7	**34.3**	**54.0**	**73.5**
Average Shear Stress @ 3mm - 4mm Displacement (kPa)	2.43	4.01	5.98	7.81
Average Normal Stress @ 3mm - 4mm Displacement (kPa)	3.42	7.26	9.30	12.42

The fitted linear curve in Figure H.8 has a gradient of 0.595. The corresponding angle of wall friction is therefore the arctangent of the gradient which is equal to 30.8 °.

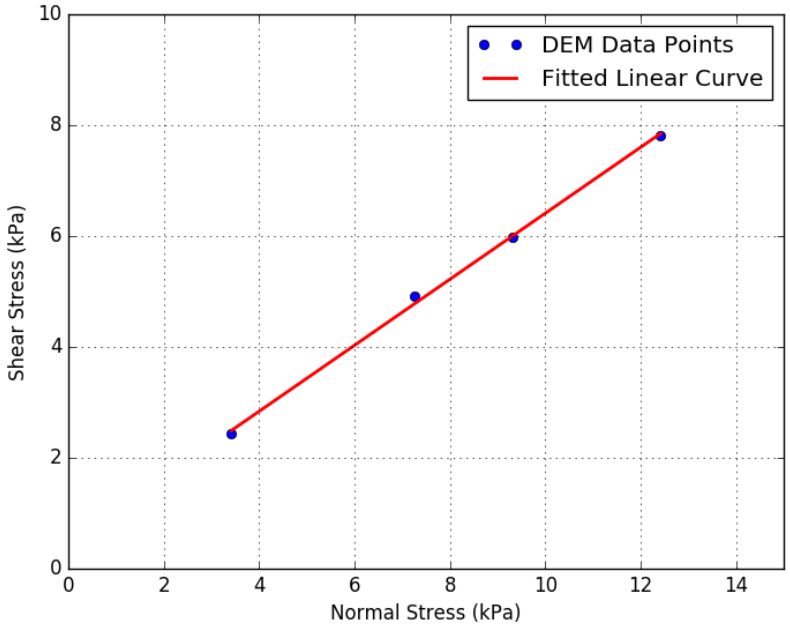


Figure H.8: Variation of shear stress with normal stress for $\mu_{pw,s} = 0.9$

I Central Composite Design Sampling

I.1 Central Composite Design Sampling Procedure

The Central Composite Design was used to select sample points for use in DEM simulation experiments used to calibrate the particle to particle coefficients of sliding and rolling friction. This approach was adopted because of its efficiency in selecting the minimum number of sample points required for experiments in which a specific response variable is a function of two or more independent variables (Myers et al., 2009; ReliaSoft, 2015).

In this research, the response variables were the angles of repose obtained from the double cell, full pipe and split pipe experiments carried out on dry bulk material. These angles of repose are all functions of the particle to particle coefficients of sliding and rolling friction. Each sample point was defined by a unique set of the two particle to particle friction coefficients. The results of the DEM simulations at sample points were the angles of repose.

Using the results of DEM simulations at the sample points, empirical equations were developed that related a specific angle of repose to the particle to particle coefficients of sliding and rolling friction, using the response surface methodology. For an experiment whose response variable is a function of two

independent variables, as in this case, nine sample points are required by the CCD approach, and are found using the criteria shown in Fig. 2.13 (Myers et al., 2009). As such, nine sample points were selected using the CCD in the range 0.0 to 1.0 for each of the two independent variables, for use in the subsequent DEM angle of repose experiments.

The following detailed procedure was followed in determining the sample points for each of the two variables.

1. Two points were arbitrarily selected from a range of 0.0 to 1.0 to be equivalent to -1 and 1 in Fig. 2.13 respectively.

2. The two selected points were named x_{lower} and x_{upper} respectively

3. The two selected points x_{lower}, and x_{upper}, were averaged and the result named x_{aver}

4. x_{lower} was subtracted from x_{upper}, and the result divided by 2. The resulting answer was named x_{less}

5. The remaining points (x_i) were then computed using Equation I.1, for i in $(-\sqrt{2}, -1, 0, 1, \sqrt{2}\ )$

$$x_i = i * x_{less} + x_{aver} \tag{I.1}$$

I.2 Central Composite Design Sampling Results

Sampling of points in the two dimensional space defined by the particle to particle coefficients of sliding and rolling friction was carried out as described in Section I.1.

Two points, 0.30 and 0.90, were arbitrarily selected to be equivalent to -1 and 1 respectively. Using Equation I.1, 0.18, 0.60 and 1.0 were computed to be equivalent to $-\sqrt{2}$, 0, and $\sqrt{2}$ respectively.

Table I.1 shows the sample points for use in subsequent experiments for calibration of the iron ore to iron ore coefficients of sliding and rolling friction.

Table I.1: CCD sample points

Sample Point Number	$\mu_{pp,s}$	$\mu_{pp,r}$
1	0.18	0.60
2	0.30	0.30
3	0.30	0.90
4	0.60	0.18
5	0.60	0.60
6	0.60	1.00
7	0.90	0.30
8	0.90	0.90
9	1.00	0.60

J Full Pipe Angle of Repose Results

J.1 Full Pipe Physical Calibration Test Results



Figure J.1: Full pipe angle of repose, dry, physical test 1 @ 94 mm



Figure J.2: Full pipe angle of repose, dry, physical test 2 @ 94 mm

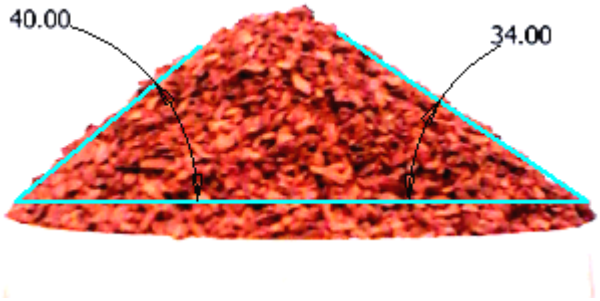


Figure J.3: Full pipe angle of repose, dry, physical test 3 @ 94 mm



Figure J.4: Full pipe angle of repose, dry, physical test 1 @ 110 mm



Figure J.5: Full pipe angle of repose, dry, physical test 2 @ 110 mm



Figure J.6: Full pipe angle of repose, dry, physical test 3 @ 110 mm

J.2 Full Pipe DEM Calibration Test Results

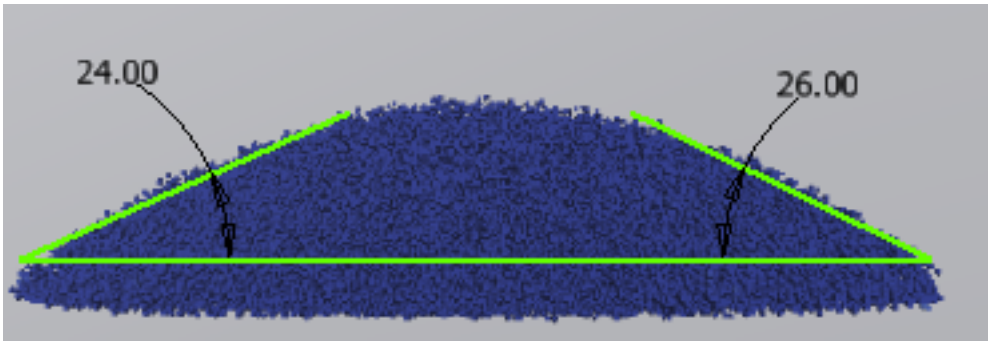


Figure J.7: Full pipe angle of repose, DEM $\mu_{pp,s} = 0.18$, $\mu_{pp,r} = 0.60$

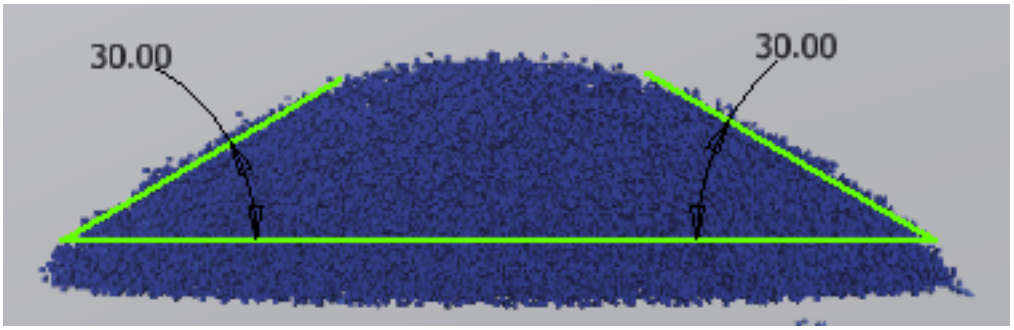


Figure J.8: Full pipe angle of repose, DEM $\mu_{pp,s} = 0.30$, $\mu_{pp,r} = 0.30$

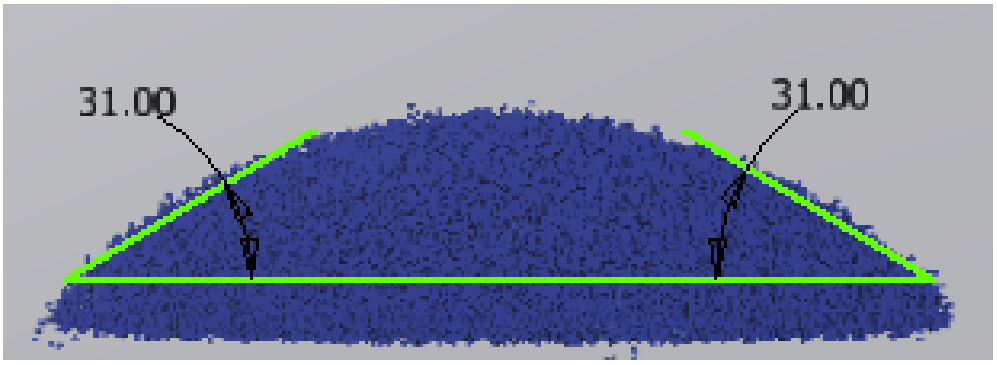


Figure J.9: Full pipe angle of repose, DEM $\mu_{pp,s} = 0.30$, $\mu_{pp,r} = 0.90$

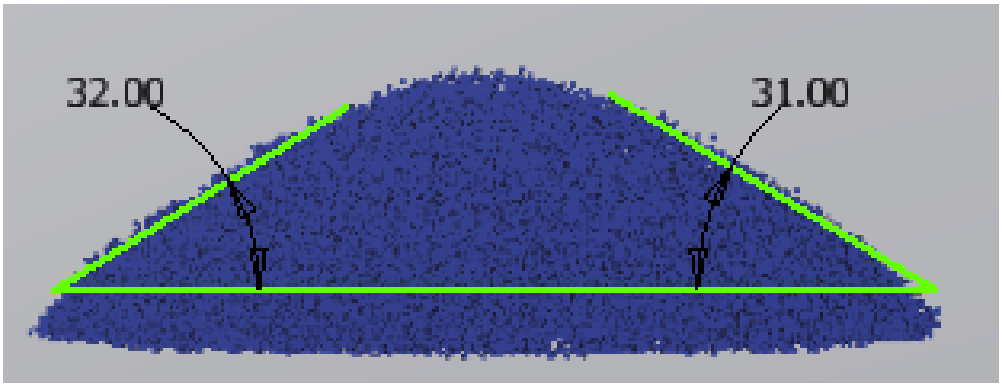


Figure J.10: Full pipe angle of repose, DEM $\mu_{pp,s} = 0.60$, $\mu_{pp,r} = 0.18$

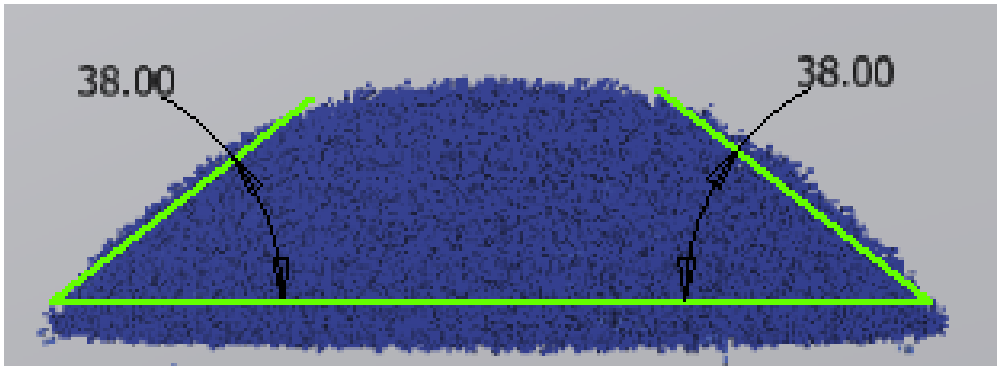


Figure J.11: Full pipe angle of repose, DEM $\mu_{pp,s} = 0.60$, $\mu_{pp,r} = 0.60$

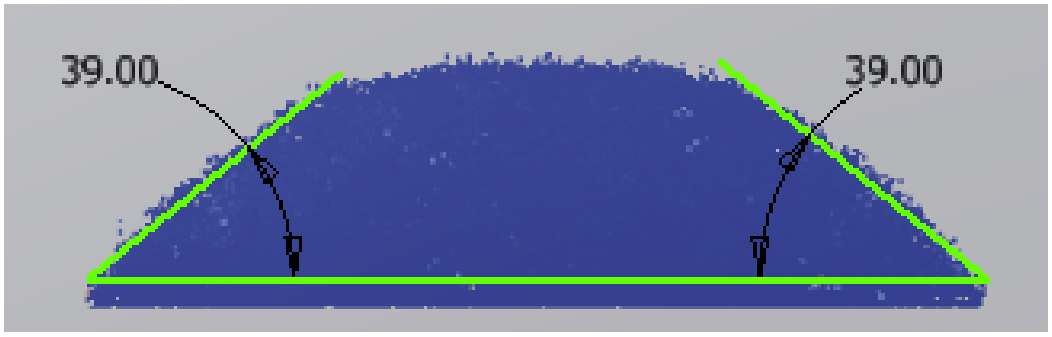


Figure J.12: Full pipe angle of repose, DEM $\mu_{pp,s} = 0.60$, $\mu_{pp,r} = 1.00$

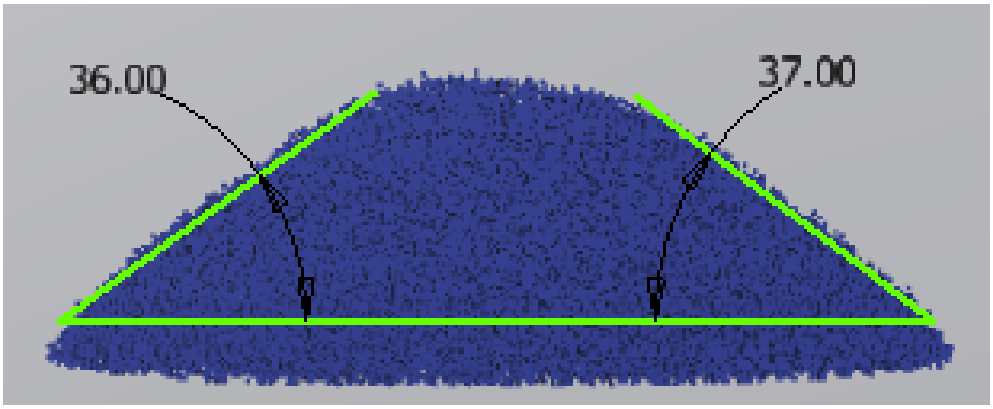


Figure J.13: Full pipe angle of repose, DEM $\mu_{pp,s} = 0.90$, $\mu_{pp,r} = 0.30$

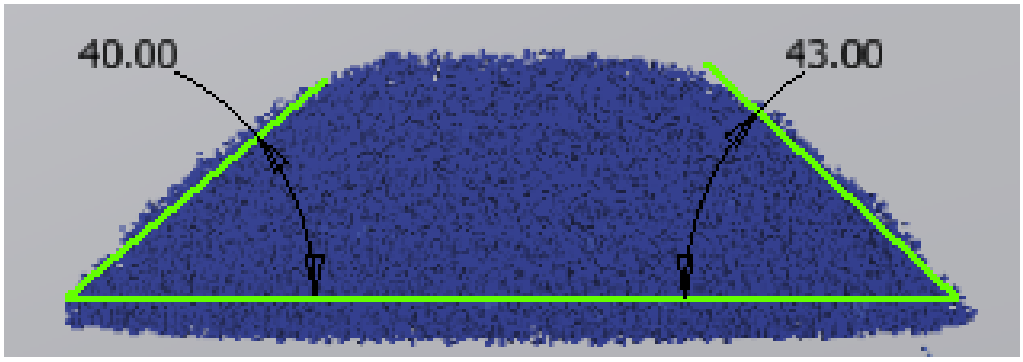


Figure J.14: Full pipe angle of repose, DEM $\mu_{pp,s} = 0.90$, $\mu_{pp,r} = 0.90$

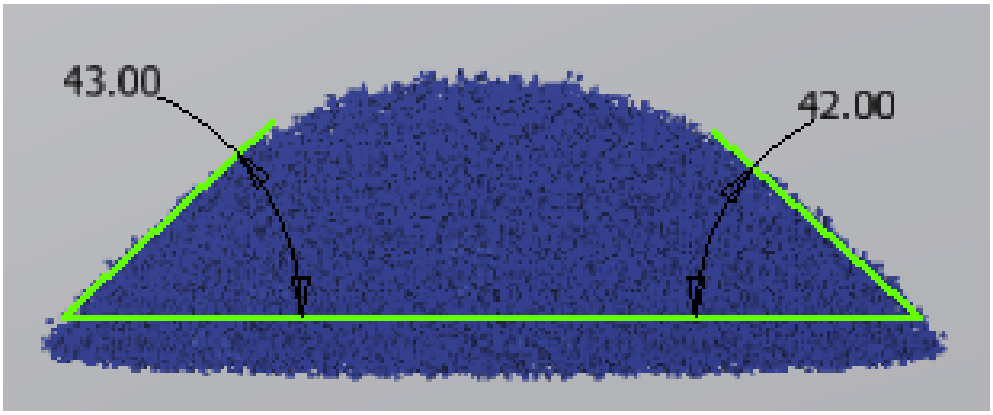


Figure J.15: Full pipe angle of repose, DEM $\mu_{pp,s} = 1.00$, $\mu_{pp,r} = 0.60$

J.3 Full Pipe DEM Verification Test Results

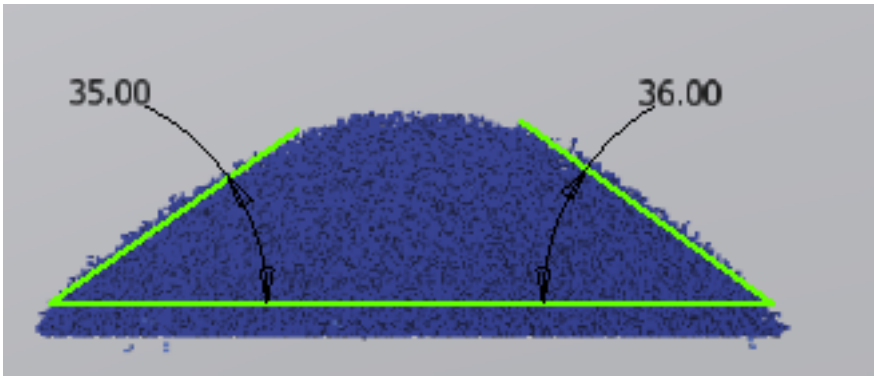


Figure J.16: Full pipe angle of repose, DEM $\mu_{pp,s} = 0.73$, $\mu_{pp,r} = 0.28$

J.4 Full Pipe DEM Sensitivity Test Results

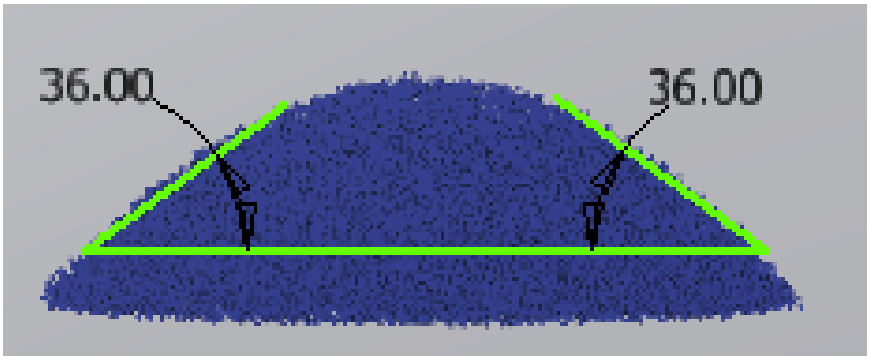


Figure J.17: Full pipe angle of repose sensitivity, DEM $\epsilon_{pp} = 0.10$

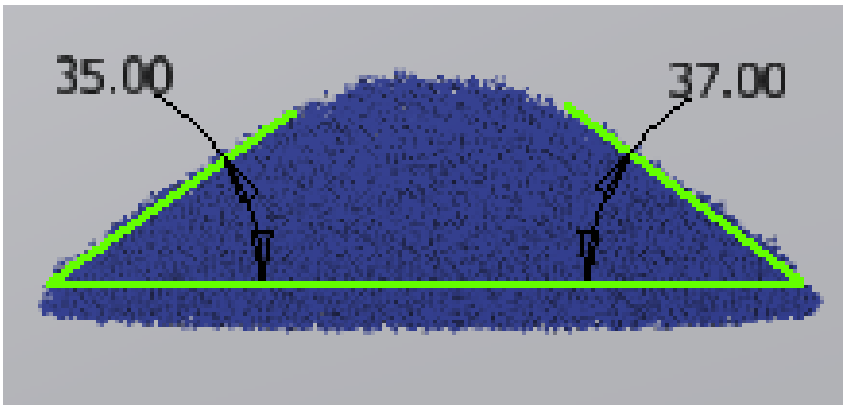


Figure J.18: Full pipe angle of repose sensitivity, DEM $\epsilon_{pp} = 1.00$

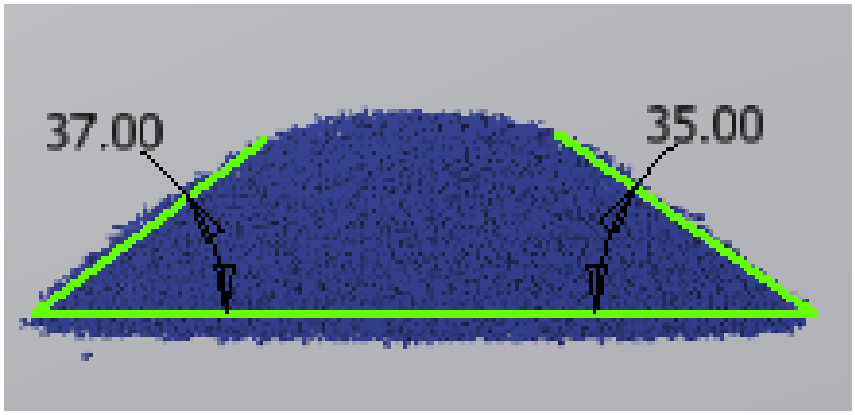


Figure J.19: Full pipe angle of repose sensitivity, DEM $\mu_{pw} = 0.10$

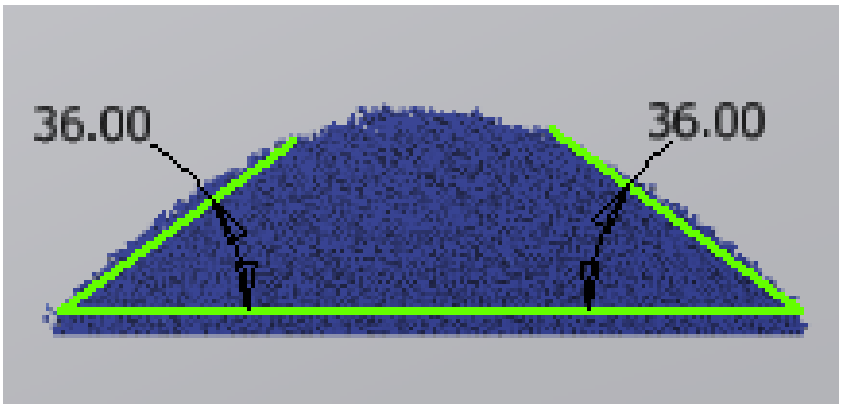


Figure J.20: Full pipe angle of repose sensitivity, DEM $\rho = 2000$ kg/m^3

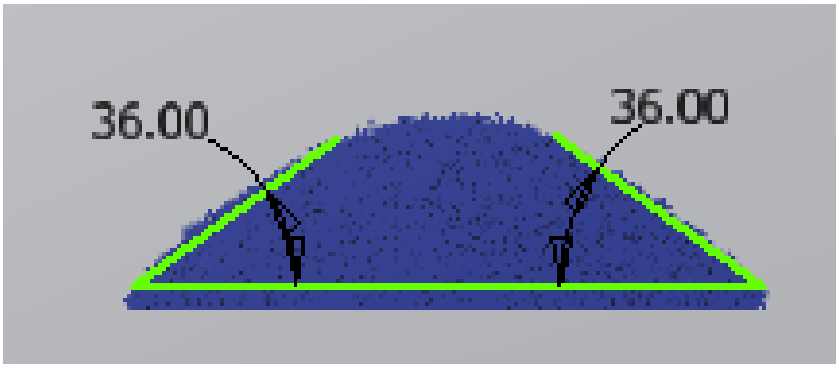


Figure J.21: Full pipe angle of repose sensitivity, DEM $\rho = 5000$ kg/m^3

K Split Pipe Angle of Repose Results, Dry Material

K.1 Split Pipe Physical Calibration Test Results



Figure K.1: Split pipe angle of repose, dry, physical test 1

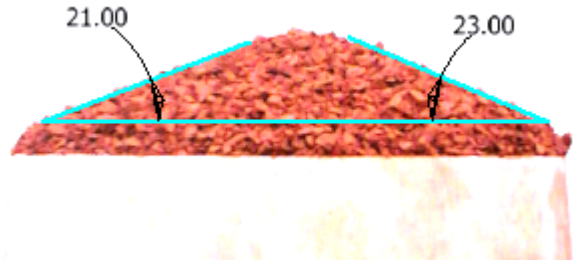


Figure K.2: Split pipe angle of repose, dry, physical test 2



Figure K.3: Split pipe angle of repose, dry, physical test 3

K.2 Split Pipe DEM Calibration Test Results

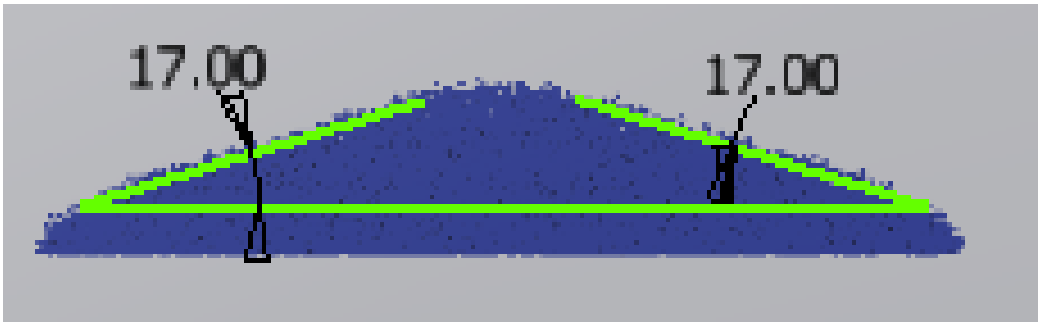


Figure K.4: Split pipe angle of repose, DEM $\mu_{pp,s} = 0.18$, $\mu_{pp,r} = 0.60$

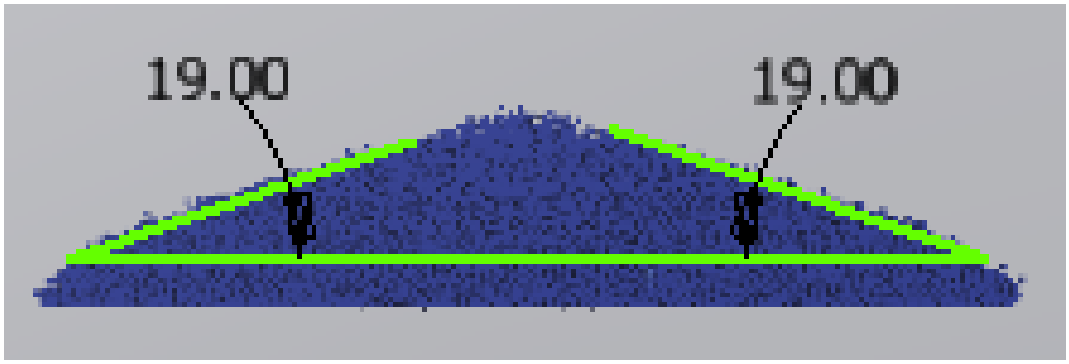


Figure K.5: Split pipe angle of repose, DEM $\mu_{pp,s} = 0.30$, $\mu_{pp,r} = 0.30$

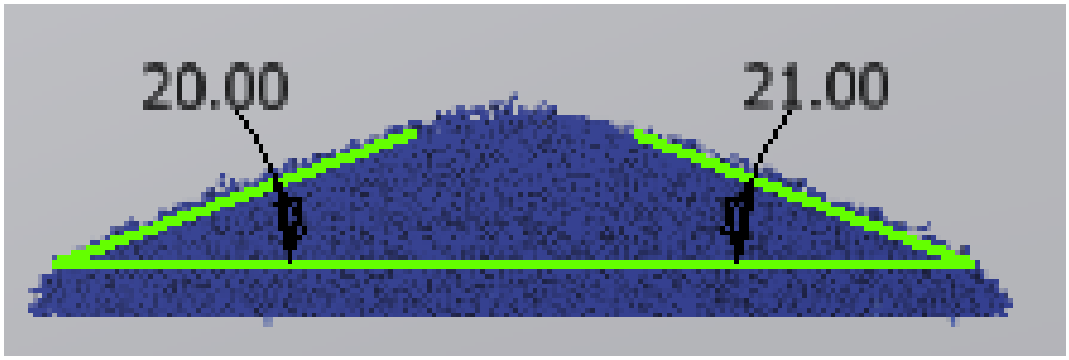


Figure K.6: Split pipe angle of repose, DEM $\mu_{pp,s} = 030$, $\mu_{pp,r} = 0.90$

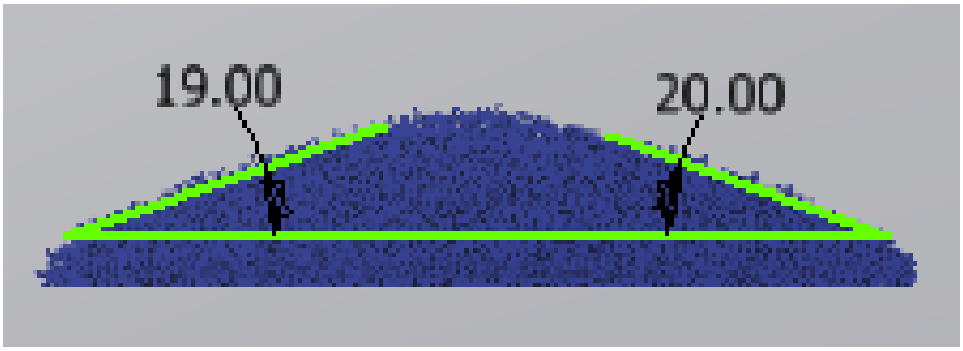


Figure K.7: Split pipe angle of repose, DEM $\mu_{pp,s} = 0.60$, $\mu_{pp,r} = 0.18$

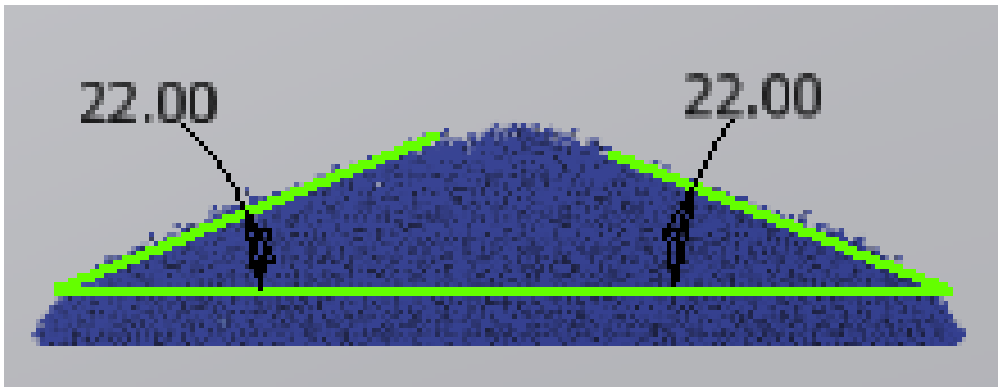


Figure K.8: Split pipe angle of repose, DEM $\mu_{pp,s} = 0.60$, $\mu_{pp,r} = 0.60$

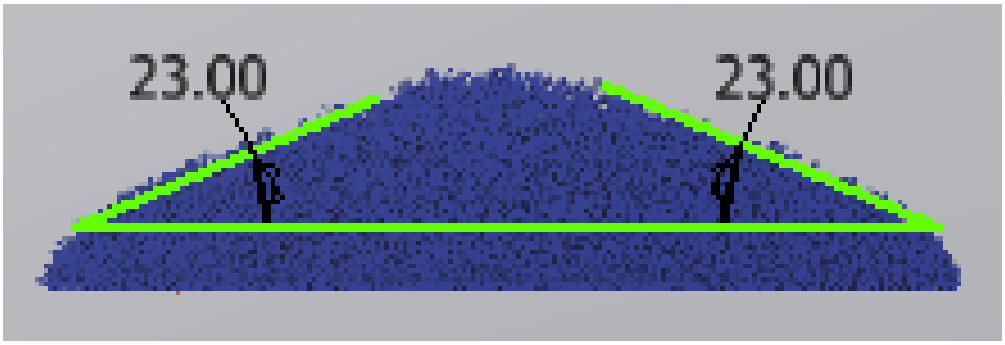


Figure K.9: Split pipe angle of repose, DEM $\mu_{pp,s} = 0.60$, $\mu_{pp,r} = 1.00$

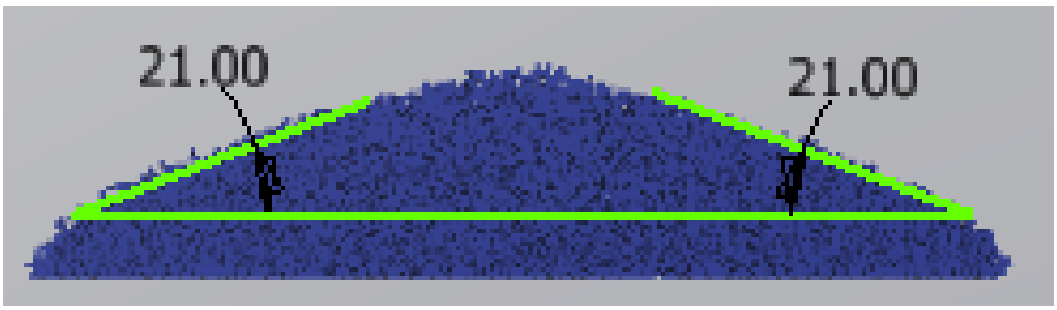


Figure K.10: Split pipe angle of repose, DEM $\mu_{pp,s} = 0.90$, $\mu_{pp,r} = 0.30$

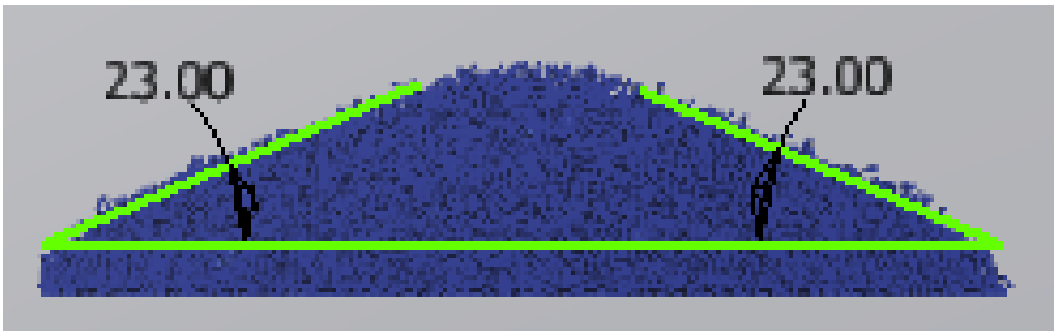


Figure K.11: Split pipe angle of repose, DEM $\mu_{pp,s} = 0.90$, $\mu_{pp,r} = 0.90$

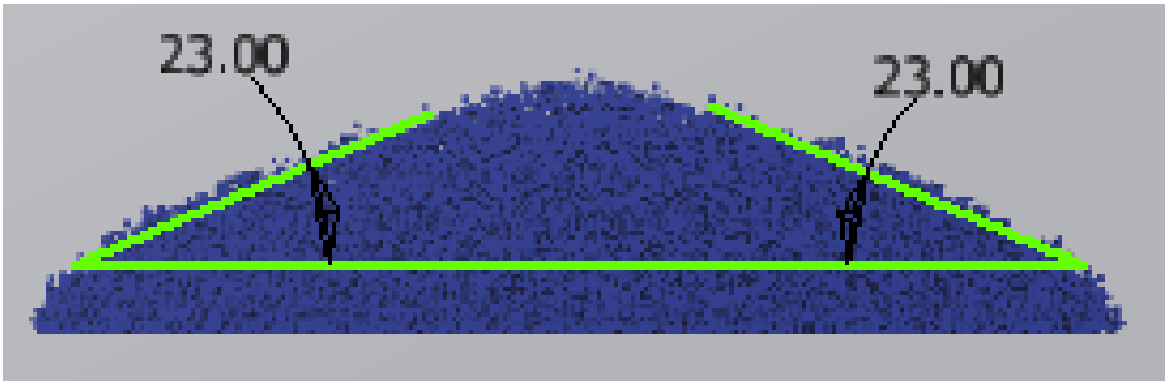


Figure K.12: Split pipe angle of repose, DEM $\mu_{pp,s} = 1.00$, $\mu_{pp,r} = 0.60$

K.3 Split Pipe DEM Verification Test Results

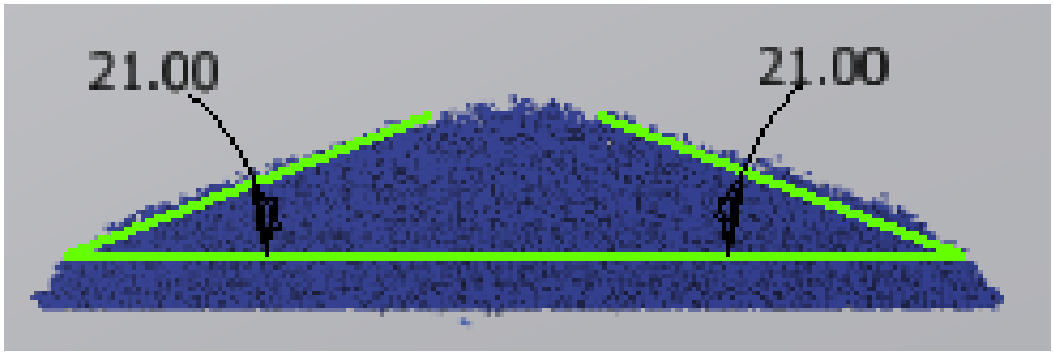


Figure K.13: Split pipe angle of repose, DEM $\mu_{pp,s} = 0.73$, $\mu_{pp,r} = 0.28$

L Double Cell Angle of Repose Results

L.1 Double Cell physical Calibration Test Results

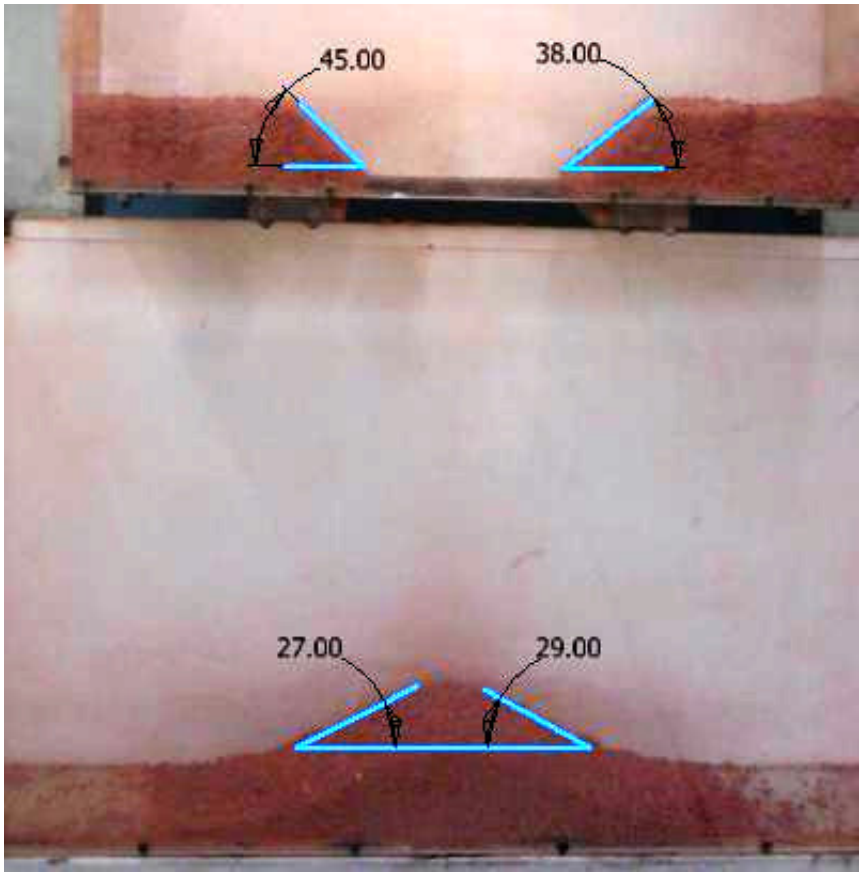


Figure L.1: Double cell angle of repose, dry, physical test 1 @ 50mm

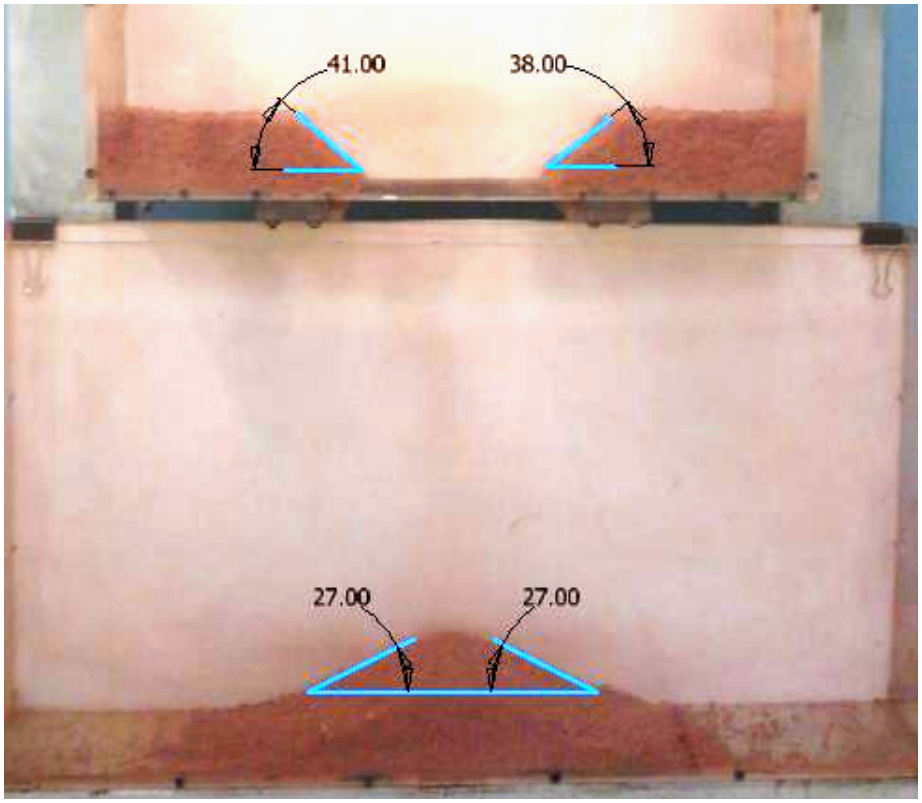


Figure L.2: Double cell angle of repose, dry, physical test 2 @ 50mm

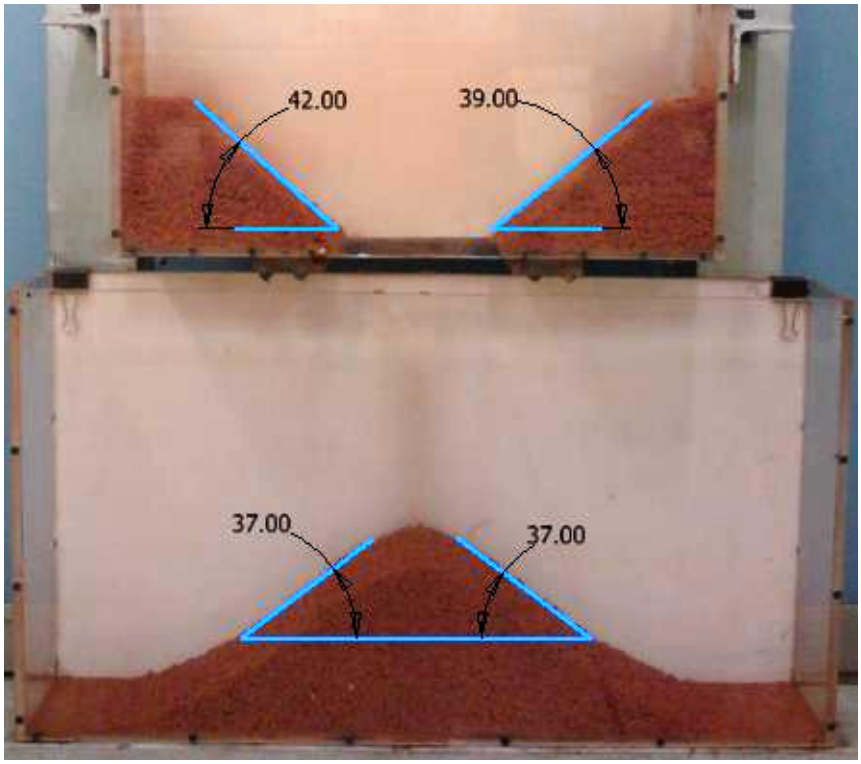


Figure L.3: Double cell angle of repose, dry, physical test 1 @ 130mm

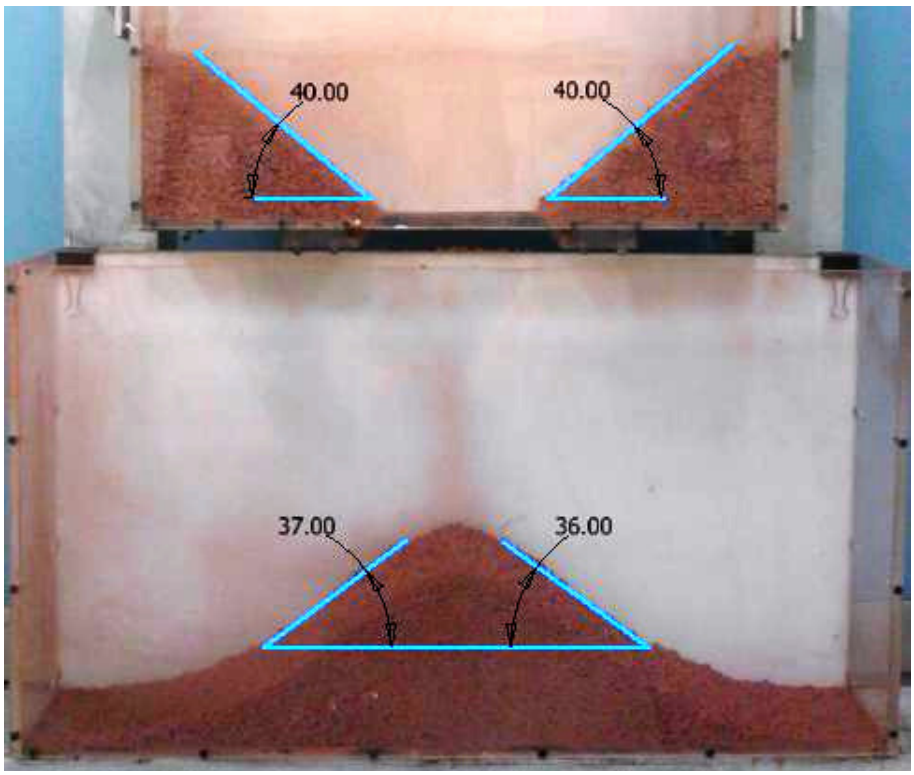


Figure L.4: Double cell angle of repose, dry, physical test 2 @ 130mm

L.2 Double Cell DEM Verification Test Results

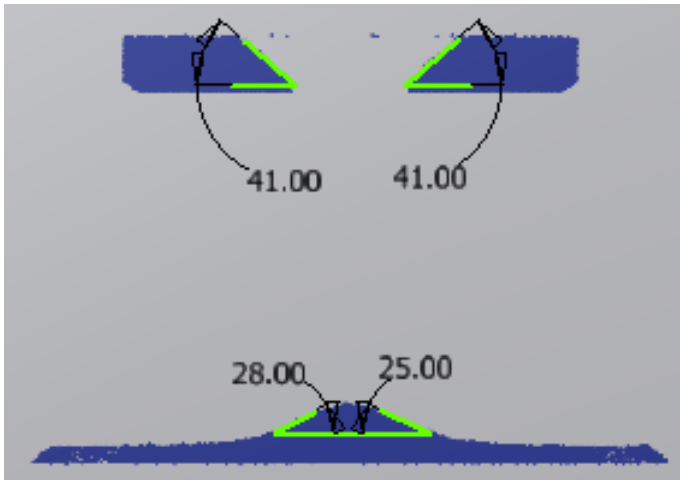


Figure L.5: Double cell angle of repose, DEM $\mu_{pp,s} = 0.73$, $\mu_{pp,r} = 0.28$

L.3 Double Cell DEM Sensitivity Test Results

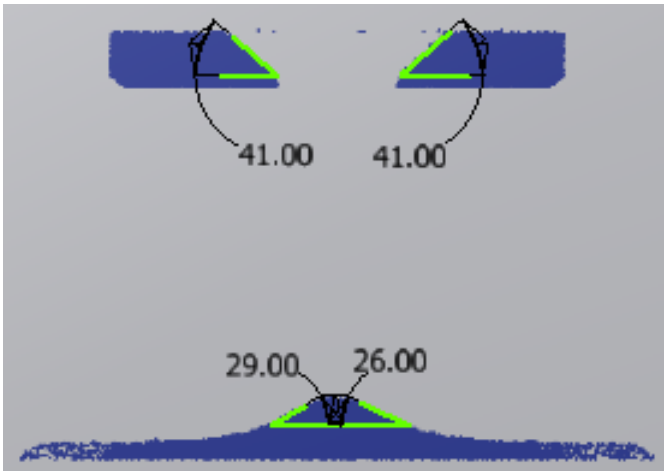


Figure L.6: Double cell angle of repose sensitivity, DEM $\epsilon_{pp} = 0.10$

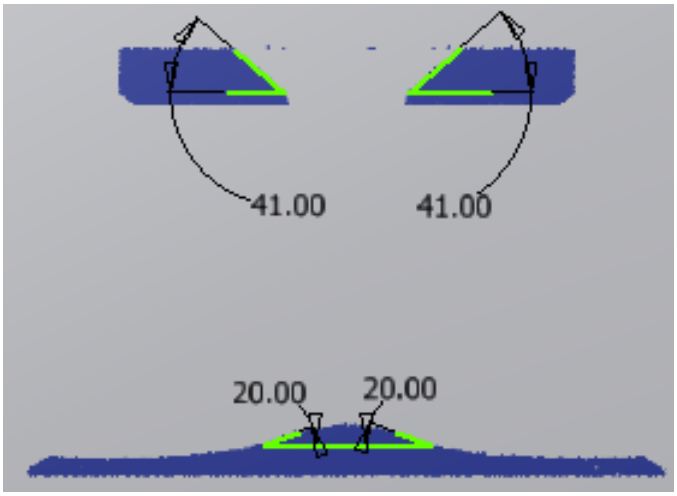


Figure L.7: Double cell angle of repose sensitivity, DEM $\epsilon_{pp} = 1.00$

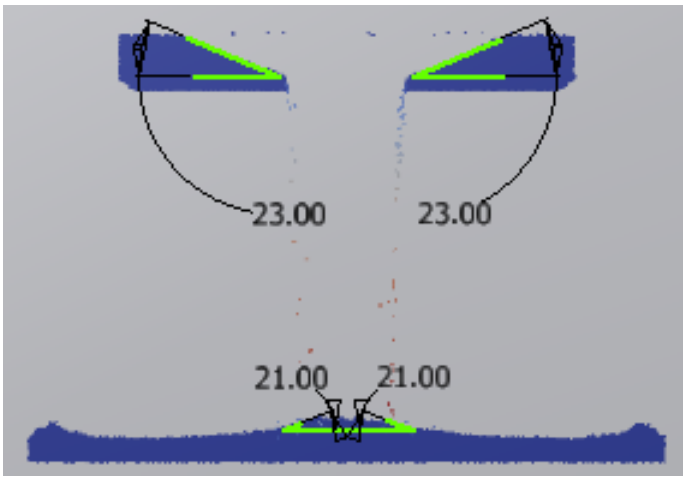


Figure L.8: Double cell angle of repose sensitivity, DEM $\mu_{pw} = 0.10$

M Split Pipe Angle of Repose Results, Moist Material

M.1 Cohesion Energy Physical Calibration Results



Figure M.1: Split pipe angle of repose, moist, physical test 1

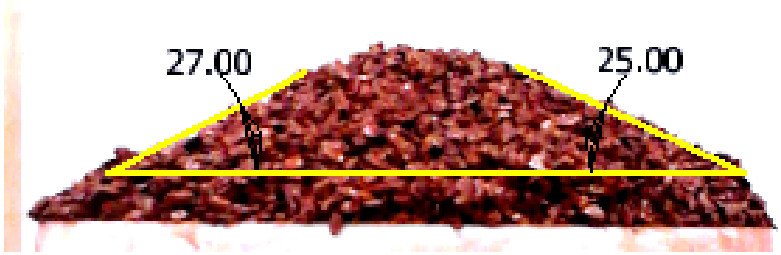


Figure M.2: Split pipe angle of repose, moist, physical test 2



Figure M.3: Split pipe angle of repose, moist, physical test 3

M.2 Cohesion Energy DEM Calibration Results

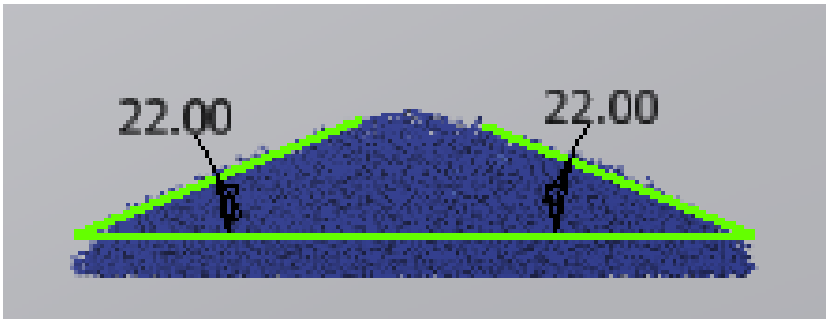


Figure M.4: Split pipe angle of repose, DEM cohesion density=75 kJ/m^3

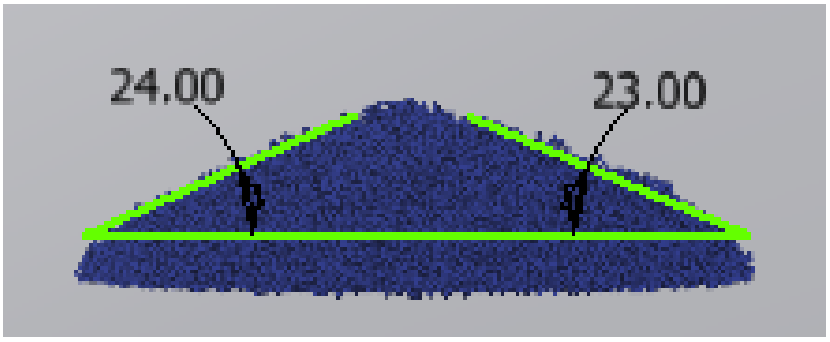


Figure M.5: Split pipe angle of repose, DEM cohesion density=100 kJ/m^3

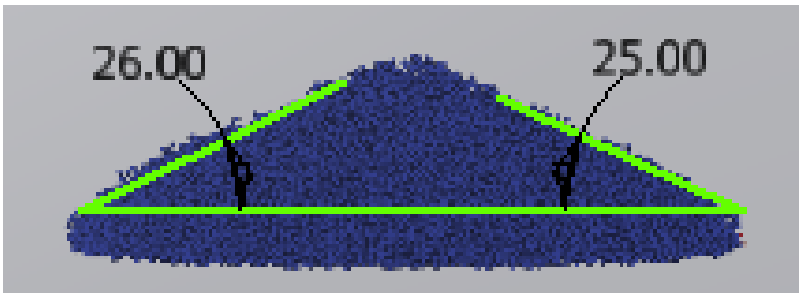


Figure M.6: Split pipe angle of repose, DEM cohesion density=125 kJ/m^3

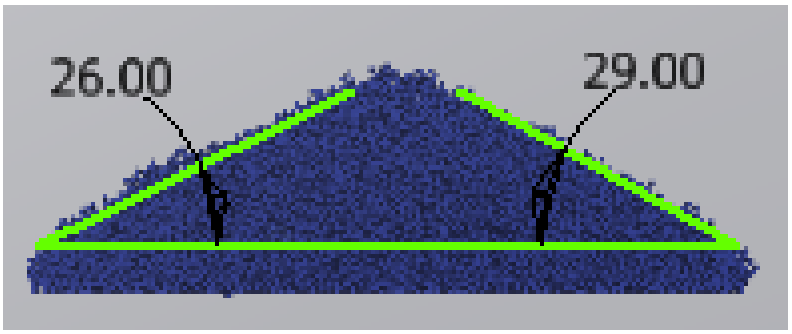


Figure M.7: Split pipe angle of repose, DEM cohesion density=150 kJ/m^3

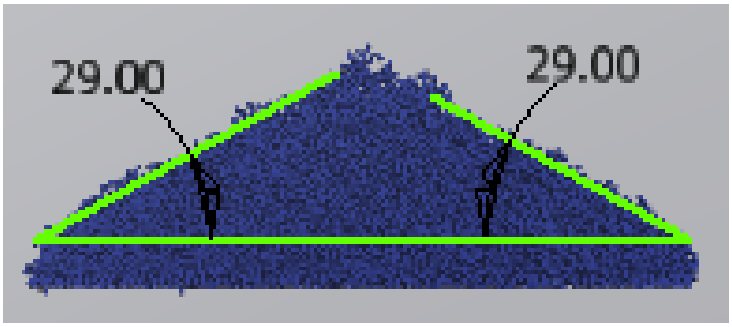


Figure M.8: Split pipe angle of repose, DEM cohesion density=175 kJ/m^3

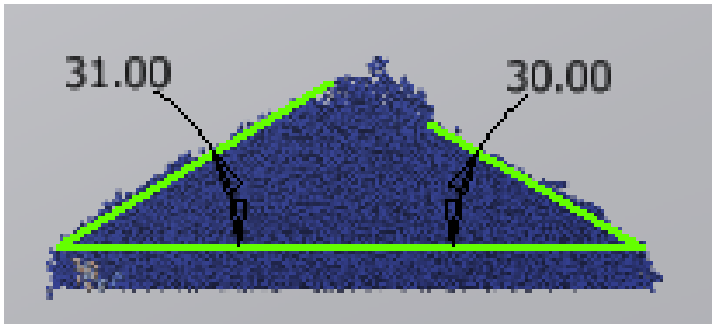


Figure M.9: Split pipe angle of repose, DEM cohesion density=200 kJ/m^3

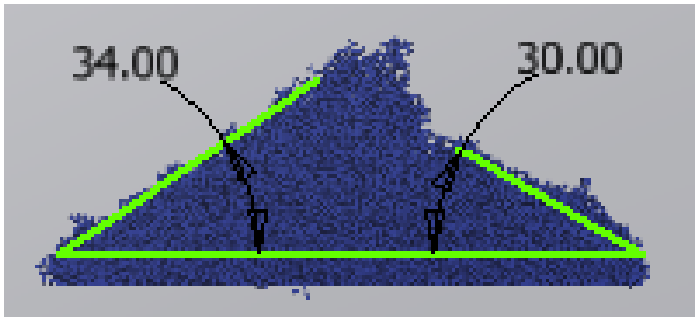


Figure M.10: Split pipe angle of repose, DEM cohesion density=225 kJ/m^3

M.3 Cohesion Energy DEM Verification Results

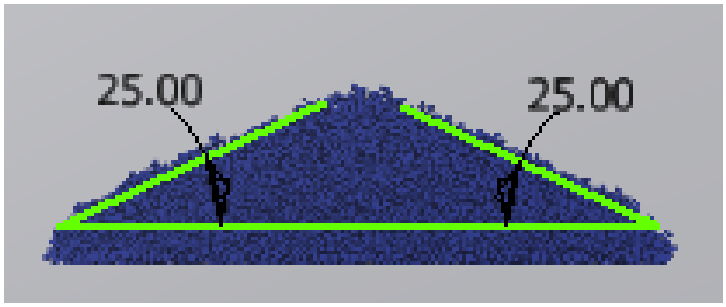


Figure M.11: Split pipe angle of repose, DEM cohesion density=117 kJ/m^3

N Loadcell Information

N.1 Loadcell Linearity Checking Procedure

A loadcell was used to measure the instantaneous mass of the bulk material sample in the silo as the silo was being emptied. For this purpose, the loadcell was first checked for linearity of the output voltage values within the range of possible of masses to be carried. An equation relating voltage output to mass was also established for use in converting voltage readings into equivalent mass. The detailed procedure used was as follows:

1. The minimum and maximum masses were selected for use in checking loadcell output voltage linearity. The selected masses were 0 and 10 kg respectively.

2. The loadcell was placed on a flat surface in a vertical position.

3. The loadcell output terminals were connected to a powered amplifier with a display screen for measuring voltage. A digital multimeter was connected to the amplifier output for verifying the voltage readings from the amplifier display.

4. The voltage reading from the digital multimeter and amplifier display with no load applied on the load cell were recorded.

5. A mass of 0.5 kg was added and the voltage readings from the digital multimeter and the amplifier display recorded. Consecutively the mass

was increased by 0.5 kg while recording the voltage readings in each case, until the load reached 5 kg. The load was incremented by 1 kg increments until the load reached 10 kg while recording the voltage for each increment.

6. A graph of voltage against mass was plotted and a linear equation of best fit was fitted to the data (Figure N.1).

7. The voltage reading for no load was verified to be zero and the data points were evaluated if they fall in the line of best fit using the R^2. The loadcell needed no adjustment if the output reading was zero for no load, and data points fell into the line of best fit.

N.2 Loadcell Linearity Checking Results

The loadcell for use in the verification experiments was checked for linearity in the region of interest using the procedure outlined in Section N.1. Masses between 0 kg and 10 kg were placed on the load cell and output voltages recorded. The load cell voltage readings for each mass placed on the load cell were plotted and a line of best fitted as shown in Figure N.1. Equation N.1 defines the linear relationship between voltage output and mass on the load cell,

$$V = 0.0606m - 0.0027 \tag{N.1}$$

where V is the voltage signal in volts and m is the mass in kilograms. The goodness of fit value for the linear equation was determined to be $R^2 = 0.99994$, showing the equation adequately described the voltage and mass relationship between 0 kg and 10 kg.

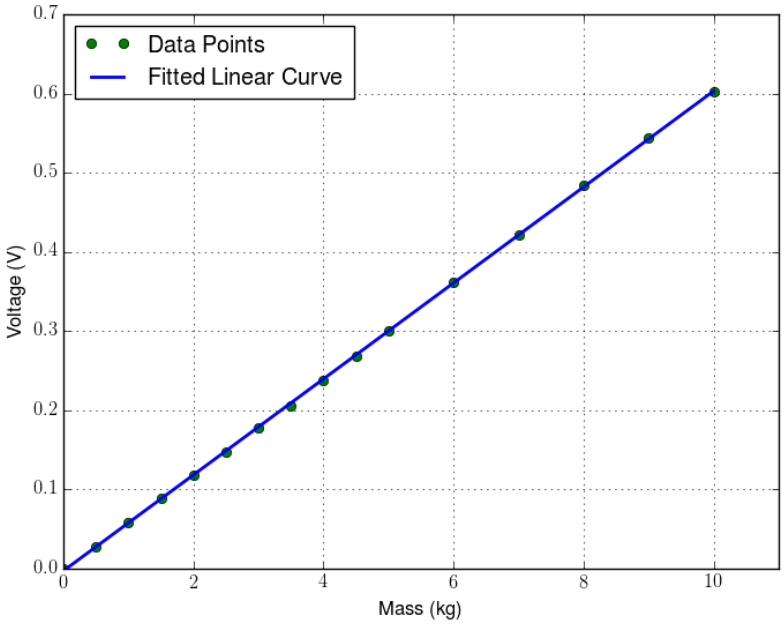


Figure N.1: Loadcell linearity check

N.3 Loadcell Specifications

LT 400

LOADTECH
LOAD CELLS



Model LT400 load cells are manufactured from aircraft grade annodised aluminium or high grade electroless nickel plated steel.

The 'S' design can be used in tension or compression, but is best suited to tension applications where the side forces can be contained.

IP66 protection ensures long operating life in indoor and outdoor applications.

Commercial applications include mechanical scale conversions and small hanging scales. Industrial applications include packaging machines, belt conveyors, and small batching systems.

Model LT 400 low cost, high accuracy "S" type load cell.

Capacities 50 kg to 2 000 kg

Annodised aluminium 50-500 kg

Electroless nickel plated steel 1 000 - 2 000 kg

IP66 protection

Cost effective solution for scale conversions and small industrial weighing systems

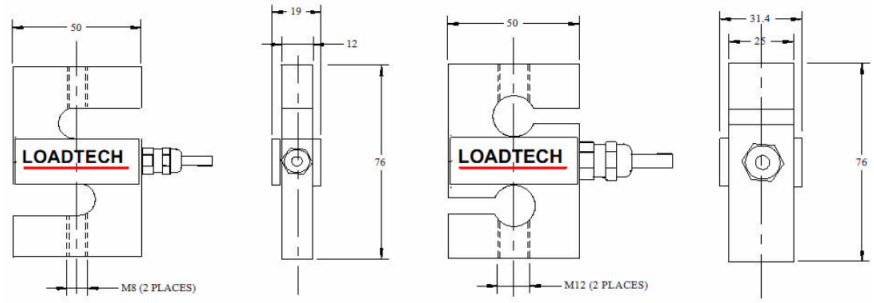
Manufactured by :

LOADTECH LOAD CELLS (PTY) LTD
134 Sarel Baard Crescent
Gateway Industrial Park
Centurion, Gauteng
P.O. Box 9947, Centurion 0046

Tel : 012 661 0830
Fax : 012 661 0816
E-mail : sales@loadtech.co.za

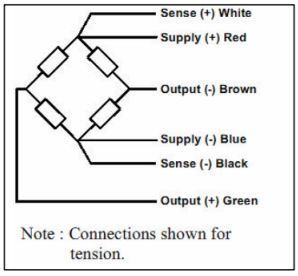
LT400 SPECIFICATIONS

ACCURACY CLASS	0.1%	0.05%	0.03%	UNITS
Rated capacities	50,75,100,200,300,500,1000,1500 and 2000			kg
Rated output		3.0 + / - 0.1%		mV/V
Total error	0.1	0.05	0.03	+ - % of Applied load
Creep at rated capacity: Zero return	0.1	0.05	0.03	+ - % of Applied load
Zero Balance	0.5	0.5	0.5	+ - % of Rated Output
Temperature Range : Operating	-30C to + 80			C
: Compensated	0C to + 40			
Temperature Effect : On Output	0.007	0.004	0.003	+ - % of Applied Load/C
: On Zero	0.015	0.007	0.003	+ - % of Rated Output/C
Safe Overload	120			+ - % of Rated Capacity
Ultimate Overload	250			+ - % of Rated Capacity
Exciatation: Recommended	10			Volts AC or Dc
: Maximum	15			Volts AC or Dc
Input Impedance	350 + / -3			Ohms
Output Impedance	350 + / -3			Ohms
Insulation Resistance	>1000			Mega ohms
Deflection at rated capacity	< 0.4			mm
Weight 50, 75 and 100 kg	0.5			kg
200,300 and 500 kg	0.5			kg
1000,1500 and 2000 kg	1.5			kg
Construction material 50-500 kg	Annodised Aluminium			
1000-2000 kg	Electroless Nickel Plated Tool Steel			
Environmental protection	IP66			
Cable	5 meter 6 wire screened			



50-100 kg Load Cells

200-2000 kg Load Cells



Note : Connections shown for tension.

MANUFACTURED BY :

134 Sarel Baard Cresent
Gateway Industrial Park
Centurion Gauteng
P.O. Box 9947`
Centurion 0046
Tel : 012 661 0830
Fax : 012 661 0816
E-mail : sales@loadtech.co.za

Note : These specifications are Subject to change without notice

O Silo Flow Validation Results

O.1 Physical Silo Flow of Dry Iron Ore

Table O.1: Silo mass flow rates, scale, dry

Test	Mass (kg)	Flow Time (s)	Flow Rate (kg/s)
1	7.09	6.93	1.02
2	7.13	6.99	1.02
3	7.10	7.00	1.01

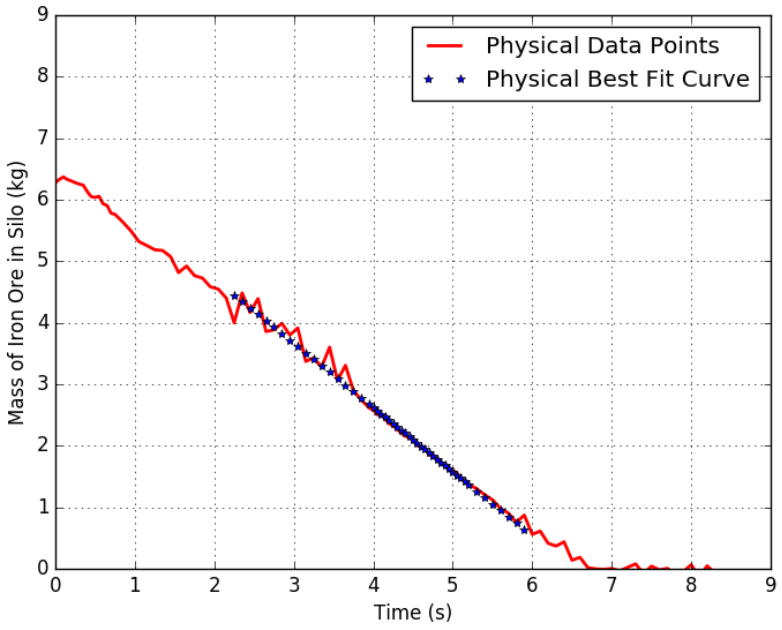


Figure O.1: Dry silo mass flow rate, loadcell measured, test 1

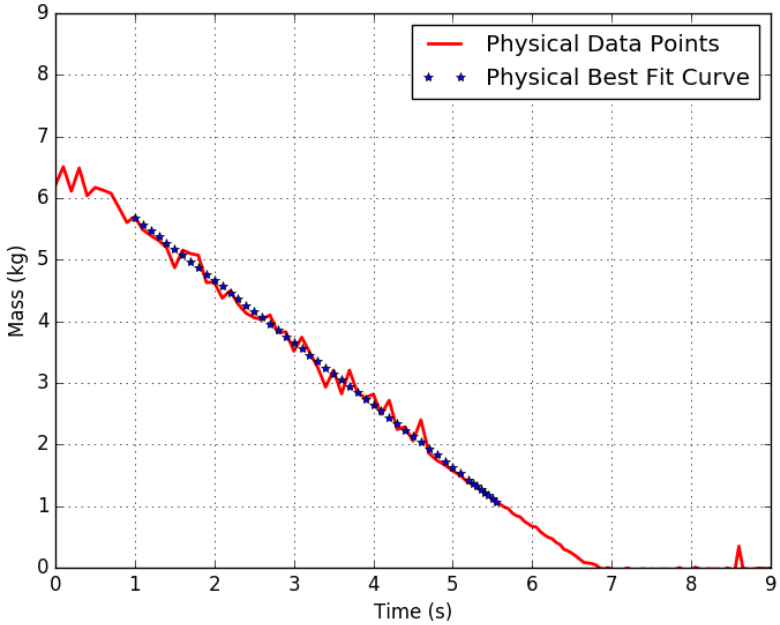


Figure O.2: Dry silo mass flow rate, loadcell measured, test 2

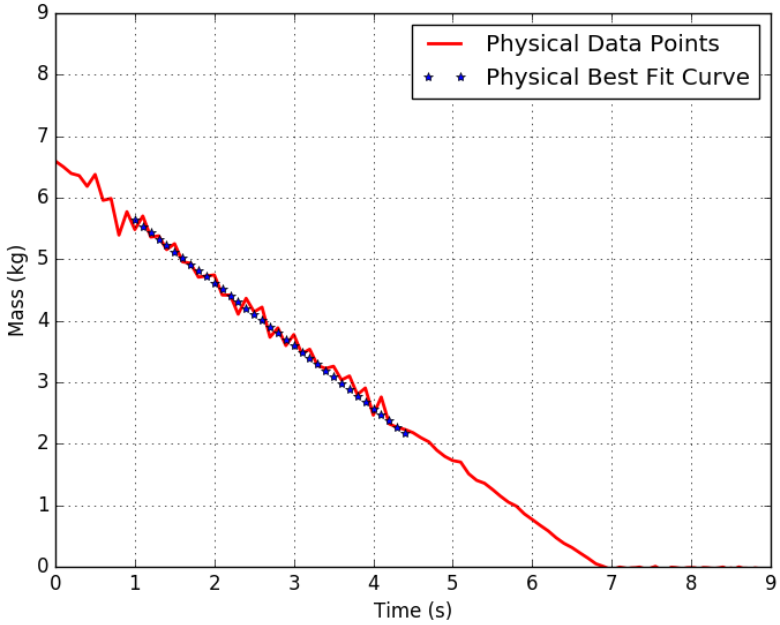


Figure O.3: Dry silo mass flow rate, loadcell measured, test 3

O.2 Physical Silo Flow of Moist Iron Ore

Table O.2: Silo mass flow rates, scale, moist

Test	Mass (kg)	Flow Time (s)	Flow Rate (kg/s)
1	5.88	6.7	0.87
2	5.87	6.7	0.88

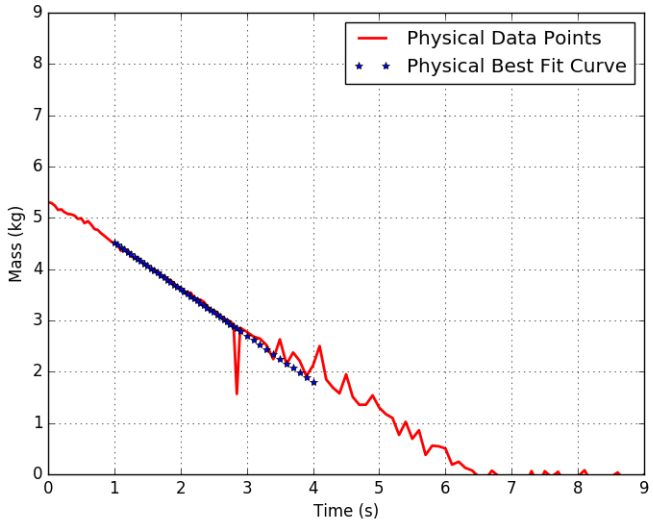


Figure O.4: Moist silo mass flow rate, loadcell measured, test 1

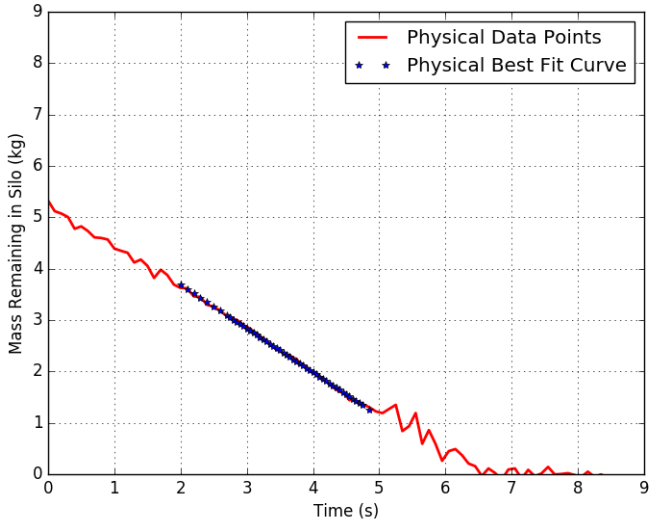


Figure O.5: Moist silo mass flow rate, loadcell measured, test 2

P Simulation Time

Table P.1 shows the DEM simulation times in hours for a single execution of each experimental setup. The hardware used was a Dell Latitude with an Intel Processor Corei7-3520M @ 2.9GHz x 4, and 4GB memory.

Table P.1: Minimum number of DEM calibration experiments

Experiment	**Number of Particles**	**Simulation Time Per Execution (Hrs)**
Bulk density test	2823	2
Wall shear test	6867	3
Full pipe angle of repose	36449	5
Split pipe angle of repose	36449	5
Double cell angle of repose	92232	13
Inclined plane	1	0
Cohesion split pipe angle of repose	36449	6
Silo	128409	19
Chute	128409	22

Q LIGGGHTS Installation

LIGGGHTS is an open source software code, which is provided as a directory of C++ source files. The following procedure is used to build LIGGGHTS on Linux Ubuntu operating system.

1. Install g++ and git-core libraries

    - sudo apt-get install libvtk5-dev libvtk6-dev libeigen2-dev libopenmpi-dev g++ git-core

    - sudo install openmpi-bin libopenmpi-dev libvtk6.2 libvtk6-dev

2. Download LIGGGHTS onto the machine

    - git clone https://github.com/CFDEMproject/LIGGGHTS-PUBLIC.git

3. Build LIGGGHTS executable

    - On the terminal, navigate to the src directory in the downloaded LIGGGHTS PUBLIC folder

    - Within the src folder, type 'auto '. The compilation is supposed to produce an executable called lmp_auto. If it fails, go to the next step.

    - open MAKE/Makefile.user with your any text editor and uncomment VTK_INC_USR=-I/home/liggghts/vtk/include and TK_LIB_USR=-L/home/liggghts/vtk/lib

- Run ‘make auto ’. After the compilation is finished you will obtain a executable named lmp_auto

4. Install LPP for postprocessing

   - sudo apt-get install python-numpy
   - sudo git clone https://github.com/CFDEMproject/LPP.git $HOME-/LPP

5. Install syntax highlighting

   - cd
   - swget https://sites.google.com/site/rahuliitdhn/files-1/language-specs.tar.gz?...
   - sudo mv $HOME/language-specs/liggghts.lang /usr/share/gtksourceview-3.0/language-specs

6. Install Paraview

   - sudo apt-get install paraview